Tempered Glass

Bolted Connections and Related Problems

Nielsen, Jens Henrik

Publication date:
2009

Document Version
Publisher's PDF, also known as Version of record

Over the last couple of decades there has been a trend towards using glass for structural load-carrying elements. Unfortunately, glass is a brittle material and small unavoidable flaws in the surface make the tensile strength relatively low and unreliable. However, the presence of residual stresses in tempered glass increases the apparent strength considerably but also introduces a spatial variation. A numerical model for predicting the residual stress state has been developed and validated. This model has been used for a parametric study of the residual stresses near holes in tempered glass in order to estimate the strength of e.g. pinned joints.

The thesis furthermore presents work on the fragmentation of tempered glass and the behavior of mechanically reinforced glass beams.

DTU Civil Engineering
Department of Civil Engineering
Technical University of Denmark

Brovej, Building 118
2800 Kgs. Lyngby
Telephone 45 25 17 00

www.byg.dtu.dk

ISBN: 9788778772824
ISSN: 1601-2917

Jens Henrik Nielsen

Tempered Glass - bolted connections and related problems

Report R-204 2009

DTU

Tempered Glass

-bolted connections and related problems

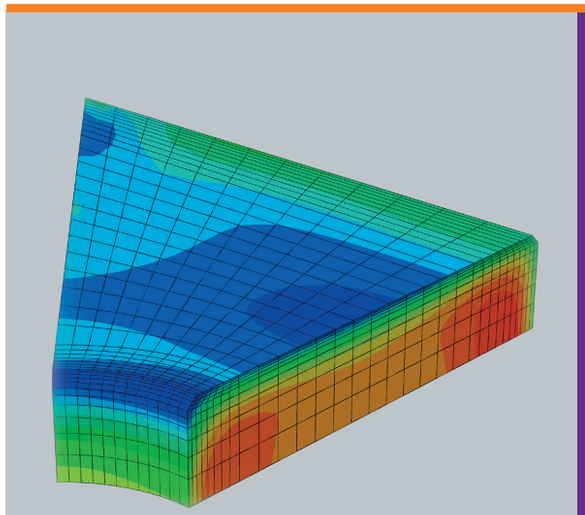

Jens Henrik Nielsen

PhD Thesis

Department of Civil Engineering
2009

DTU Civil Engineering Report R-204 (UK)
September 2009

DTU Civil Engineering
Department of Civil Engineering

Tempered Glass

– Bolted Connections and Related Problems

Jens Henrik Nielsen

Ph.D. Thesis

Department of Civil Engineering
Technical University of Denmark

2009

Tempered Glass
– Bolted Connections and Related Problems

Printed by DTU-Tryk
Department of Civil Engineering
Technical University of Denmark
ISBN: 9788778772824
ISSN: 1601-2917

Preface

This thesis is submitted as a partial fulfilment of the requirements for the Danish Ph.D. degree. The first part introduces the research field, highlights the major findings and provides an overview of the work along with a discussion. The second part is a collection of papers which constitute the basis of the work and describe the work in greater detail.

Lyngby the 6$^{\text{th}}$ of April 2007

Jens Henrik Nielsen

Preface to published version of thesis

The thesis was defended at a public defence on Monday the 14$^{\text{th}}$ of September 2009. Official opponents were Professor Jeppe Jönsson, Technical University of Denmark, Lecturer Mauro Overend, University of Cambridge and Principal Technologist Paul David Warren, Science Support Group, Pilkington plc. Subsequently the Ph.D. degree was awarded from the Technical University of Denmark.

Compared to the original submitted version of the thesis a number of minor editorial corrections have been implemented and the status of some of the papers on which the thesis is based has changed from submitted to accepted or from accepted to published.

Lyngby the 25$^{\text{th}}$ of January 2010

Jens Henrik Nielsen

Acknowledgements

I gratefully acknowledge the support from my supervising team: Professor Henrik Stang, associate professor John Forbes Olesen and associate professor Peter Noe Poulsen, all from the Department of Civil Engineering, Section for Structural Engineering at the Technical University of Denmark. Furthermore, Leif Otto Nielsen, also from the Department of Civil Engineering, Section for Structural Engineering at the Technical University of Denmark, is greatly acknowledged.

Former and present students who have performed experiments useful for my work is greatly acknowledged, in particular Andreas Breum Ølgaard.

Finally, Bent Bondo is greatly acknowledged for proofreading the manuscript.

Abstract

Glass has been used for the building envelope for centuries. Over the last couple of decades there has been a trend towards using glass for load-carrying elements.

Glass has many excellent properties such as high compressive strength and a superior environmental resistance compared to more common building materials. Unfortunately, glass is a brittle material and small unavoidable flaws in the surface make the tensile strength relatively low and unreliable. The apparent tensile strength[1] can be improved considerably by tempering the glass; however, the fracture characteristic at failure is changed.

Experimental and numerical investigations on the residual stresses induced by the tempering process have been conducted during the project.

Large variations of the residual stresses within the specimens were found experimentally using photoelastic measurements. The measured residual stress state was compared to a fragmentation test similar to what is specified in Eurocode. This investigation showed that the fragmentation test was not able to reveal spots in a specimen with a low residual stress. Moreover, the residual stresses were found to vary with the specimen thickness.

In order to investigate the process of fragmentation further, high-speed recordings of the fragmentation process and analysis of the fracture surfaces was carried out. From these investigations, a hypothesis for the local fragmentation process was suggested.

A state-of-the-art model of the tempering process was described and implemented for solid elements in a commercial Finite Element code. The model was used for a parametric study of the residual stresses near holes in tempered specimens and for investigating the residual stress state dependence on the thickness and cooling rate.

Charts and a simple method for estimating the lowest compressive residual stress at a hole for different geometries and degrees of tempering are given. This provides a unique knowledge of the apparent strength at holes in tempered glass.

Such knowledge is valuable when designing pinned joints in tempered glass. A parametric study on the maximum tensile stresses at the hole in an in-plane loaded pinned joint was conducted. The study covers parameters regarding the insert material, the interface behaviour and the influence from nearby edges. Significant differences in the principal tensile stresses at the holes were found for varying parameters.

A hypothesis of estimating the strength of a pinned joint is validated by comparison with experiments.

Although the tempering process increases the apparent strength, the material is still

[1]The apparent strength is the strength originating from both residual stresses and the material. In other words, the strength measured by direct testing.

brittle and ductility must be sought in the design of the structural elements. Investigations on mechanically reinforced float glass beams were carried out and reported.

It is shown experimentally that ductility can be obtained by adding the right amount of reinforcement to the beam. Analytical formulas and a numerical model for estimating the beam behaviour are developed. These tools can be used for estimating the amount of reinforcement needed.

Resumé

Gennem århundreder har glas været brugt i bygningers klimaskærm. Det er dog gennem de seneste par årtier blevet mere udbredt at benytte glas i lastbærende bygningselementer. Glas har, som kontruktionsmateriale, mange fremragende egenskaber såsom høj trykstyrke og suveræn modstandsdygtighed i aggressive miljøer. Desværre er glas et sprødt materiale med en relativt lav og upålidelig trækstyrke pga. små uundgåelige overfladefejl. Den tilsyneladende trækstyrke kan dog forbedres væsentligt ved termisk hærdning, hvorved enkelte af glassets egenskaber ændres.

Under dette studie er der udført eksperimentelle og numeriske undersøgelser af egenspændingsstilstanden i hærdet glas. Store variationer af egenspændingerne er eksperimentielt observeret ved brug af fotoelastiske målemetoder. Den målte egenspændingstilstand er sammenlignet med resultater fra en fragmenteringstest. Denne undersøgelse viser, at fragmenteringstesten ikke er i stand til afsløre mindre områder med lave egenspændinger. Ydermere viste egenspændingerne sig at variere med tykkelsen af glasset.

For at undersøge fragmenteringsprocessen yderligere blev processen filmet med højhastighedskameraer, og brudfladerne blev analyseret. Fra disse undersøgelser blev fragmenteringshastigheden fundet, og der blev opstillet en hypotese for brudmekanismen.

En state-of-the-art model af hærdeprocessen er beskrevet og implementeret for 3D elementer i et kommercielt Finit Element Metode program. Denne model er blevet brugt til et parameterstudie af egenspændingerne ved huller i hærdede emner samt undersøgelse af egenspændingernes afhængighed af tykkelse og kølehastighed.

Diagrammer og en simpel metode til bestemmelse af den laveste trykegenspænding ved et hul, for forskellige geometrier og hærdegrader, er givet. Dette giver en unik viden om den tilsyneladende hulrandsstyrke for en hærdet glasskive.

Denne viden er nødvendig i forbindelse med beregning og design af dornsamlinger i hærdet glas. Et parameterstudie af største trækspænding på hulranden for en boltesamling belastet i planen er udført. Studiet omfatter materiale- og interface-parametre samt betydningen af kantafstande. En signifikant forskel i den maksimale trækspænding på hulranden blev fundet under parametervariationen.

En hypotese for at beregne styrken af en given samling blev eftervist ved sammenligning med forsøg.

Selvom hærdeprocessen forøger glassets tilsyndeladende styrke, forbliver materialet sprødt, og duktilitet skal findes i designet af de strukturelle elementer. Undersøgelser af en mekanisk armeret glasbjælke er derfor udført i sidste kapitel. Det er eksperimentielt eftervist, at duktiliteten kan opnås ved at tilføje den rette armeringsmængde. Analytiske formler og en numerisk model til bestemmelse af bjælkeopførslen er givet. Disse redskaber kan bruges til bestemmelse af den rette mængde armering.

Table of Contents

Additional work (not included in the thesis)

[1] Nielsen J.H.: 'Modeling of Residual Stresses in Toughened Glass'. In proceedings: *6th Int. PhD symposium in Civil Eng., 2006, Zürich (Schweiz).*

[2] Nielsen J.H., Olesen J.F., Stang H., Poulsen P.N.: 'An implementation of 3D viscoelatic behavior for glass during toughening '. In proceedings: *Glass Performance Days., 2007, Tampere (Finland).*

[3] Nielsen J.H., Olesen J.F.: 'The use and Properties of Toughened Glass'. Chapter in: *The Future of Civil Engineering, 2007.*

[4] Nielsen J.H., Stang H.: 'Connections in Glass Structures'. *Lecture Notes, 2007.*

[5] Nielsen J.H., Olesen J.F., Stang H.: 'Experimental Investigation of Residual Stresses in Toughened Glass'. In proceedings: *Challenging Glass 2008.*

[6] Ølgaard A.B., Nielsen J.H., Olesen J.F., Stang H.: 'Properties of an Adhesive for Structural Glass Applications'. In proceedings: *Challenging Glass 2008, Delft (Holland).*

Part I

Introduction and summary

Chapter 1

Introduction

1.1 Structural Use of Glass

Over the last couple of decades, glass as a building material has undergone a transformation from being used exclusively for the building envelope to also being a part of the load-carrying structure. However, glass is brittle and lacks the stress-redistribution capability which more common building materials possess. The stress concentrations occurring under loading therefore become a major issue for the designer. Furthermore, the tensile strength of glass is, due to its brittleness, dependent on the size and distribution of surface flaws, the load duration, the ambient conditions and the residual stress state[1].

Although the issues of strength and stress concentrations complicate the design, load-carrying structures in which the strength of glass is utilised to some extent are often seen. Staircases, canopies, floors and small pedestrian bridges are all examples on built structures where the load capacity of glass has been utilised, see e.g. Figure 1.1. Most of these structures are transferring forces by means of standard structural elements like beams, columns, discs and plates made of glass, see e.g. Saunders (1999), Nijsse (2004) or Schittich et al. (1999).

Most conspicuous are the large facades of glass seen on many modern buildings. However, many of these facades are suspended on a steel frame carrying the load. In some cases the designer has utilised the strength of the glass to carry the horizontal load by vertical glass beams – the so-called fins, see Figure 1.2. Unfortunately, fins made entirely of glass are brittle and do not show any warnings or ductility before failure[2]. However, ductility for a glass beam can be achieved by mechanical reinforcement, without ruining the transparency of the beam. Reinforced float glass beams is the subject of Chapter 4.

Manufacturing and transportation is limiting commercially available sizes of glass panels and the maximum dimensions are typically $3.21\,\mathrm{m}\times6.00\,\mathrm{m}$. Since facades often span several floors, load-transferring joints between glass panes are essential. An example of a facade where glass has been used is "Den Norske Opera & Ballett", which is located at Oslo harbour in Norway, see Figure 1.2.

[1] In tempered glass, a superficial compressive residual stress is established and the apparent strength is increased considerably.

[2] Post buckling behavior yields a kind of ductile behavior. ESP (Engineered Stress Profile) glass can also provide some warning before failure Green et al. (1999).

(a) Small glass bridge (Saunders, 1999) (b) Glass staircase

Figure 1.1: *Examples of the use of glass for load-carrying applications.*

The figure shows that the fins are assembled from four pieces of glass using bolted joints. Most often the strength of a load-transferring joint is governing the load capacity of the structure. Due to inadequate codes, full-scale testing and/or detailed numerical analysis of joints are needed in order to verify the strength.

In general, there is a lack of knowledge of designing load-carrying structures using glass. In particular, calculations and optimisation of the load-carrying capacity of joints can be difficult to handle for the practicing engineer. It is therefore of great importance to develop and provide design tools for estimating the load capacity of joints in tempered glass.

The focus of the thesis is to provide a tool for estimating the load capacity of pinned joints in tempered glass and thereby contribute to an expansion in the use of glass for structural applications.

The primary hypothesis for this project is that the strength of a given joint in tempered glass can be estimated from the residual stresses and the stresses originating from the applied load. The thesis treats the hypothesis mainly from a numerical point of view; however, comparisons with experiments are also carried out.

A state-of-the-art model of the tempering process is developed and implemented in a FE-code. The model is capable of estimating both transient stresses and the steady-state residual stresses in almost arbitrarily complex geometries of glass. It has been used for investigations of some of the parameters of the tempering process and for holes at varying locations in tempered glass panels.

The stresses arising at the holes due to the external load of a pinned joint are investigated numerically. A parametric study on such joints is carried out. The hypothesis for the project is verified by comparison with experimental results.

The next section will be used for describing and defining the material, glass. Hereafter, a section on the principal methods for assembling glass panels will be given and finally a "road map" to the thesis is given at the end of this chapter. The following sections will constitute most of the terminology and definitions used throughout the thesis.

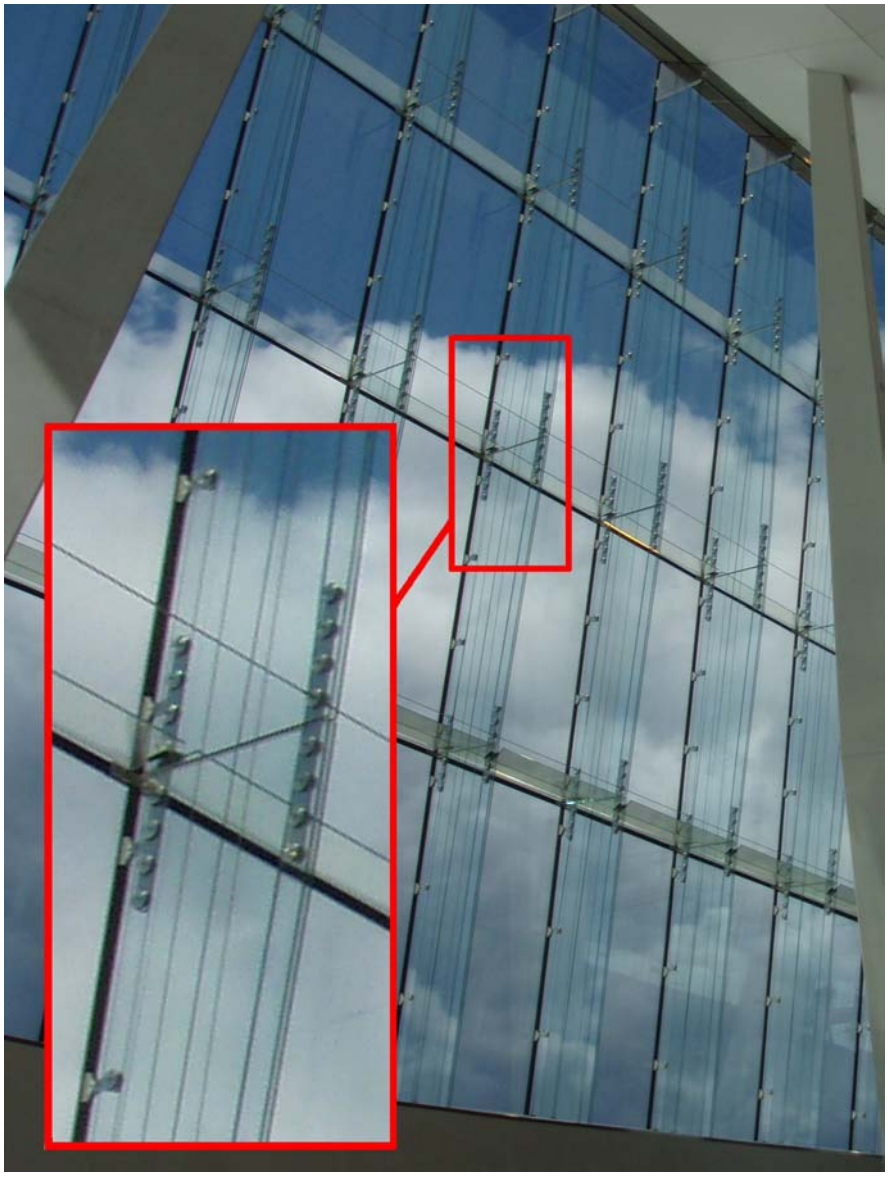

Figure 1.2: *The in-side of the facade from "Den Norske Opera & Ballett" in Oslo. Note that each fin consists of four assembled glass panes.*

1.2 Definition and Properties of Glass

The term "glass" is widely used for all materials which, at a reasonably low cooling rate, transform from liquid state to solid state without crystallisation. This indicates that the atomic structure of a glass is similar to that of a liquid, and in many ways it is reasonable to regard glass as a frozen liquid.

By referring to the glass-forming material, the so-called *glass former*, a subdivision of glass can be made. Commercially common glass formers are boric oxide, silica and phosphoric oxide, but many other materials such as alumina or arsenic can act as glass formers. However, the most well-known glass former is silica (SiO_2), which is the only one considered here. Additives for reducing the melting temperature, changing properties and reducing the content of bubbles in the glass are often added to the melt and the chemical composition of the same type of glass may vary. The glass system used for windows and building glass is called *soda-lime-silica glass*; however, throughout this thesis the term *glass* is used for this system. A typical composition of such a glass is given in Table 1.1.

Table 1.1: *Chemical composition of soda-lime-silica glass (EN572-2, 2004).*

Chemical compound		*Weight-%*	*Remarks*
Silicium oxide (silica)	SiO_2	69-74	Glass former
Calcium oxide (lime)	CaO	5-14	
Sodium oxide (soda)	Na_2O	10-16	Reduces melting temperature
Magnesium oxide (magnesia)	MgO	0-6	
Aluminium oxide (alumina)	Al_2O_3	0-3	
others (e.g. Fe^{2+} or Fe^{3+})		0-5	

Glass is considered a perfectly linear elastic solid even for temperatures well above 100°C. The mechanical properties can be considered time-independent for most structural applications[3]. The mechanical properties can be found in general texts such as Haldimann et al. (2008); Hess (2004). However, some of the most common properties at room temperature are given in Table 1.2.

During the production and tempering of glass, temperatures well above 500°C are present and the glass can no longer be considered an elastic solid. At high temperatures, glass should be treated as a viscous liquid. The viscosity is increasing for decreasing temperatures until the viscosity becomes so high that the glass can be treated as a solid. The transformation from liquid to solid state is utilised in the tempering process. The behaviour of glass at high temperatures is therefore important for the work presented. A short review of the material behaviour, the float process and the mechanisms of the tempering process is presented in the following.

The temperature range in which the molted glass is solidifying is called the *glass transformation range* and is, for all glasses, dependent on the cooling rate, see e.g. Shelby (2005). The change of viscosity with temperature is utilised in the tempering process and

[3]Care should be taken when considering fire in buildings. However, this is not within the scope of this thesis.

Table 1.2: *Commonly used properties for glass at room temperature (from Haldimann et al., 2008).*

Property	*Symbol*	*Unit*	*Value*
Young's modulus	E	GPa	70
Poisson's ratio	ν	-	0.23
Thermal expansion coefficient	α	$10^{-6}\mathrm{K}^{-1}$	9.10
Tensile strength[a](float glass)	f_t	MPa	20 to 100
Compressive strength[b]	f_c	MPa	>800
Density	ρ	$\mathrm{kg/m}^3$	2500
Specific thermal capacity	c_p	$\mathrm{J/(kg\,K)}$	720
Thermal conductivity	λ	$\mathrm{W/(m\,K)}$	1

[a] The strength depends on several parameters and values not included in the interval can be observed.
[b] Large variations of the compressive strength have been reported in the literature.

is therefore an important aspect even though the behaviour of glass at room temperature is regarded as linear elastic.

During the cooling of a melt, certain temperatures are defined by the viscosity of the melt. In Figure 1.3 a typical plot of ($\log_{10}$)viscosity as function of the temperature is shown. In the plot some of the more common temperatures are shown and their name and reference viscosity can be found in Table 1.3.

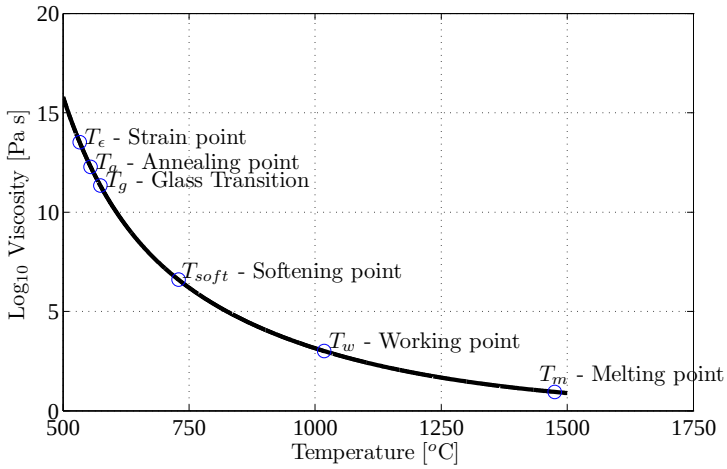

Figure 1.3: *Viscosity as a function of temperature for soda-lime-silica glass after Shelby (2005). The values named in Table 1.3 are marked in the figure.*

The term *practical melting temperature (T_m)* is used to distinguish between the melting temperature of a crystal and this melting temperature defined at a certain viscosity. At the *working point (T_w)*, the glass is fluid enough to be deformed (worked) under relatively low

Table 1.3: *Viscosity reference temperatures after Shelby (2005).*

Name of reference temperature	*Symbol*	*Temp.* [°C]	*Viscosity* [Pa s]
Practical melting temperature[a]	T_m	1475	5
Working point	T_w	1020	1×10^{3}
Softening point	T_{soft}	730	$1 \times 10^{6.6}$
Glass transition temperature	T_g	575	$1 \times 10^{11.3}$
Annealing point[b]	T_a	550	$1 \times 10^{12.4}$
Strain point	T_ϵ	530	$1 \times 10^{13.5}$

[a] Values ranging from 1 Pa s to 10 Pa s.
[b] Sometimes the value of 1×10^{12} Pa s is used.

stresses. When the glass elastically can carry its own weight, the *softening point*[4] *(T_{soft})* is reached. The *glass transition temperature (T_g)* can be seen as the temperature where the glass becomes solid; in spite of the fact that the solidification happens gradually and not instantly as implied by this definition. T_g can be found from measurements of e.g. the thermal expansion coefficients, but it is dependent on the cooling rates, sample size etc. and an often used term is therefore the glass transition temperature range. However, the term is convenient and widely used. The *annealing point (T_a)* is defined as the point where residual stresses induced during the cooling process are relieved after a few minutes and the *strain point (T_ϵ)* is defined as the point where such stresses are relieved after several hours.

Extrapolating the curve in Figure 1.3 to lower temperatures and comparing with more well-known fluids (see Table 1.4), it is seen that the assumption of glass behaving as an elastic solid at room temperature (and well above) is reasonable.

Table 1.4: *Viscosity for different materials.*

Material	*Temperature* [°C]	*Viscosity* [Pa s]
Water[a]	25	89×10^{-5}
Olive oil[a]	25	81×10^{-3}
Glass (soda-lime-silica)	1500	78×10^{-1}
Honey[a,b]	25	60×10^{-1}
Glass (soda-lime-silica)	1000	$1 \times 10^{3.2}$
Glass (soda-lime-silica)	500	$1 \times 10^{15.8}$
Glass (soda-lime-silica)[c]	100	1×10^{351}
Glass (soda-lime-silica)[c]	25	1×10^{740}

[a] Source: Wikipedia (2008).
[b] The viscosity for honey is ranging from 2 to 10 Pa s.
[c] Values are extrapolated from the curve in Figure 1.3.

[4] often referred to as the Littleton softening point after the test used to determine this point (Shelby, 2005).

1.2.1 The Float Glass Process

The most common process for producing sheets of glass is the float process. The raw materials are melted at approximately 1500 °C depending on the composition. The melt is then poured out on a bath of molten tin. This part of the process provides the glass panels with very smooth surfaces and thereby eliminates the need for polishing in order to achieve a satisfactory transparency. The thickness of the glass panel is controlled by the rate at which the melt is poured onto the molten tin. It should be noted that the manufacturers often deliver sheets of glass with a thickness close to the lower limit of the tolerances specified by e.g. Eurocode(EN12150-1, 2004)[5]. In the tin bath, the glass is cooled to about 600 °C where it is entering the annealing oven. Here the glass is slowly cooled further down in order to reduce the residual stresses to make cutting and drilling possible. A sketch of the float process can be seen in Figure 1.4.

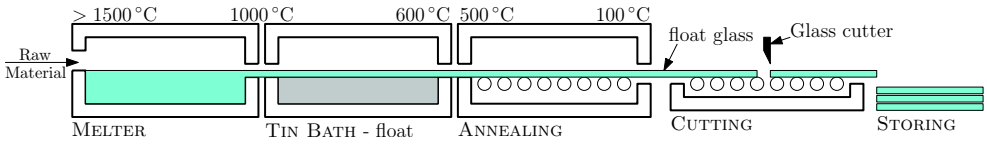

Figure 1.4: *Sketch of the process line for float glass.*

Due to the manufacturing process and the handling of the glass, flaws are always present at the surfaces and the tensile strength of the glass is therefore relatively low.

Acid treatments have shown a great improvement of the strength by reducing the crack length, rounding the crack tip and thereby minimising the stress intensities at the small surface cracks (Varner and Oel, 1975). However, if the material is scratched again, the strength is lost again. Furthermore, acid treatments leave the surface matt and some of the transparency is thereby lost. Another possibility is to close the surface flaws by inducing superficial compressive stresses. This can be done by either thermal tempering[6] or chemical toughening where existing small ions (Na^+) in the surface are substituted by larger ions (K^+). This method provides a thin surface layer with high superficial compressive stress. For structural use the glass panes are always relatively thick and thermal tempering is the most common process and is the only one considered in this work.

1.2.2 Tempered Glass

This section describes the process of tempering glass and the principal mechanisms related to the generation of the residual stresses.

The Process of Tempering Float Glass

The process line for tempering float glass is sketched in Figure 1.5. Due to the equilibrated residual stress state in tempered glass, cutting and drilling must be done before quenching

[5] Schneider (2001) measured more than 400 specimens from three different manufacturers with a nominal thickness of 10 mm and showed that none of these panels had a thickness above the nominal thickness. Most of the measurements were actually close to (and even a few below) the lower limit of 9.8 mm.

[6] Thermal tempering is sometimes called toughening or thermal toughening.

the glass. After such pretreatment, the glass is cleaned and thereafter heated to above the glass transition temperature, T_g. When the specimen has a uniform temperature above T_g it is moved on rollers to the quench, see Figure 1.5. In the quench, the specimen is cooled rapidly by air jets while rolling back and forth in order to minimise the isolating effect from the rollers. Tempered glass is often slightly curved due to asymmetric cooling and the rollers might produce so-called *roller-waves* in the glass. Roller-waves originates from sagging of the soft glass between the rollers and can be seen as a regular distortion of images reflecting in the glass surface (Saunders, 1999).

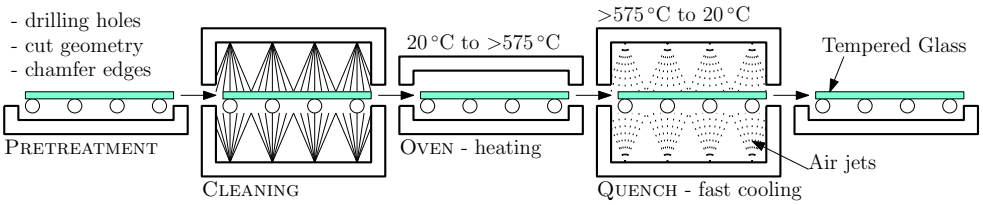

Figure 1.5: *Sketch of the process line for tempering float glass.*

A certain amount of tempered glass breaks spontaneously after the tempering. This breakage is due to phase changes in small nickel-sulfide (NiS) particles which can be found in glass. The NiS particles are expanding during the phase transformation and might cause spontaneous breakage of the tempered glass. According to Brungs and Sugeng (1995) NiS inclusions occur at a frequency of approximately one per 8 tonnes of raw glass. The time to failure has been investigated by Jacob (2001). Here it is shown that the cumulative number of failures vs. the time to failure can be estimated using a Weibull distribution. This distribution shows that approximately 60 % of the failures happen within the first five years. After ten years, 90 % of the failures will have occurred.

In modern tempering facilities, the tempered glass is *heat-soaked*. In this process, the tempered glass is heated to approximately 290°C, which will speed up the phase changes of NiS, thereby causes failure before the glass unit is installed. The heat-soak test reduces the problem; however, the designing engineer should take this phenomenon into consideration when designing load-carrying structures in tempered glass.

Generation of Residual Stresses

Several mechanisms are involved in the generation of residual stresses in tempered glass. Considering all mechanisms at once tend to complicate the explanations and in the following a simplified mechanism is given. More detailed information on the mechanisms is given later.

Figure 1.6 shows a typical temperature distribution through the thickness of a panel far from any edges at different times[7] during cooling. Along with the temperature, the stress distribution in the panel is shown for two cases. First the panel is assumed to be made of an elastic material and it is seen that when the temperature distribution through the thickness is constant, no stresses exist. It is also seen that the largest stresses are occurring when the temperature gradients are largest and that tension is present at the

[7]The times indicated in the figure are typical values for the tempering process in a 19 mm thick panel.

relatively cold surfaces. This is intuitively reasonable, since the material tends to expand at high temperatures and contract at low temperatures.

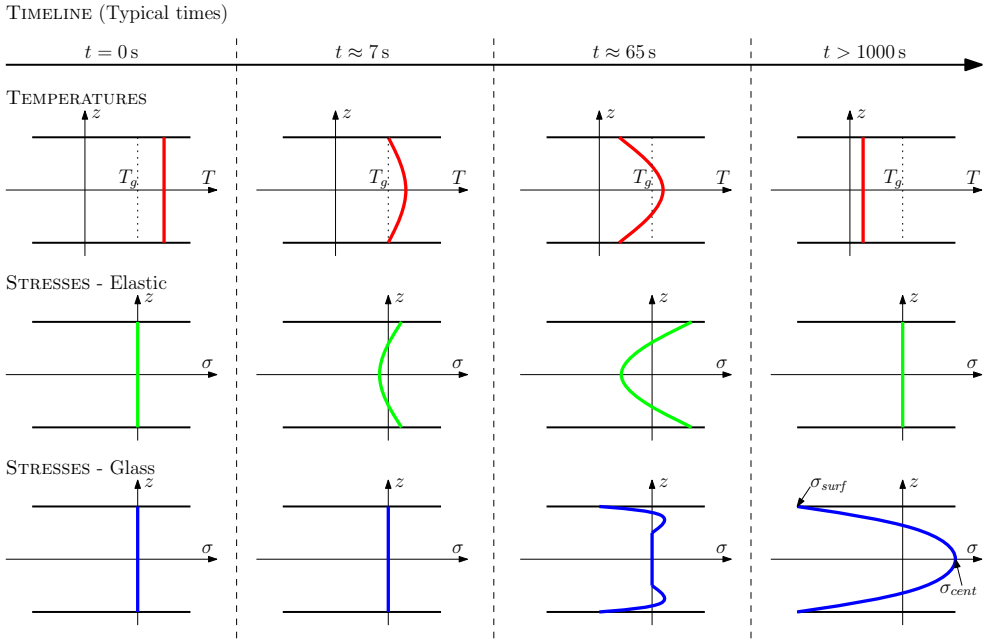

Figure 1.6: *Sketch of the temperature profile and the matching stress profile for an elastic material and a glass during cooling. The glass is assumed to have an instant shift from liquid to solid at T_g.*

The second case considers the material of the panel to be glass and it is seen from Figure 1.6 that the behaviour is quite different. The glass is relatively soft, unable to carry any stresses, at temperatures above T_g. Due to the temperature distribution where the surfaces are cooler than the interior, the surfaces will solidify first. Considering the glass in terms of layers, the outermost layer will solidify without generating noteworthy stresses due to the lack of stiffness in the other layers. When the next (toward the centre) layer cools down, solidifies and cools further down it will contract and apply compressive stresses to the first layer. The temperature in the first layer is now lower than in second layer and the second layer will therefore, in total, contract more during cooling than the first layer. The first layer will resist this contraction and thereby end in a state of compression. This process is progressing toward the centre of the specimen, all amplifying the effect.

Considering the development over time of the surface stresses, σ_{surf}, and the interior stresses at the centre plane, σ_{cent}, the maximum stresses in the elastic material are achieved when the maximum temperature difference between the surface and the interior is present. For the glass the maximum stresses are obtained at the end of the process. In Figure 1.7 the difference between the temperature at the surface and in the centre, ΔT, is shown in

the graph at the top. The development of σ_{surf} and σ_{cent} for both glass and the elastic material is seen in the lower graph.

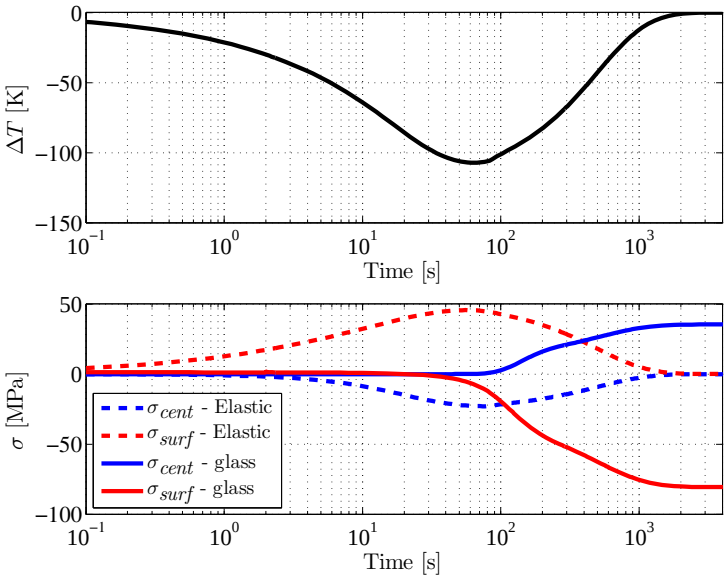

Figure 1.7: *Development of temperature difference between the centre and the surface during the tempering process and the development of stresses in an elastic solid and in glass. Data obtained by the numerical model described in Chapter 2.*

In the following, the stress states found during the tempering process will be referred to as *transient* stresses while the permanent stresses found in the glass after tempering are referred to as *stedy-state* stresses.

The real mechanism is a bit more complex than described above since the transition between the fluid state and the elastic state is not instantaneous and various time- and temperature-dependent processes are present. These effects give rise to transient superficial tensile stresses which are not shown in Figure 1.6. However, the more complex part of the tempering process is described in Paper II and Chapter 2.

The maximum transient tensile stress at the surface is denoted $\sigma_{surf,max}$. A more detailed graph showing the development of surface and centre stresses during tempering of glass is seen in Figure 1.8. This figure also shows the transient and steady-state zone along with the maximum tensile transient surface stress, $\sigma_{surf,max}$. Furthermore, σ_{surf} and σ_{cent} are also shown.

The residual stress profile shown in Figure 1.6 for $t > 1000\,\mathrm{s}$ is often approximated with a second-order parabola, see e.g. Barsom (1968). The expression for such a parabola is easily obtained by assuming symmetry about the panel mid-plane and equilibrium. Such an approximation provides a few rules of thumb for the residual stresses far from edges or holes.

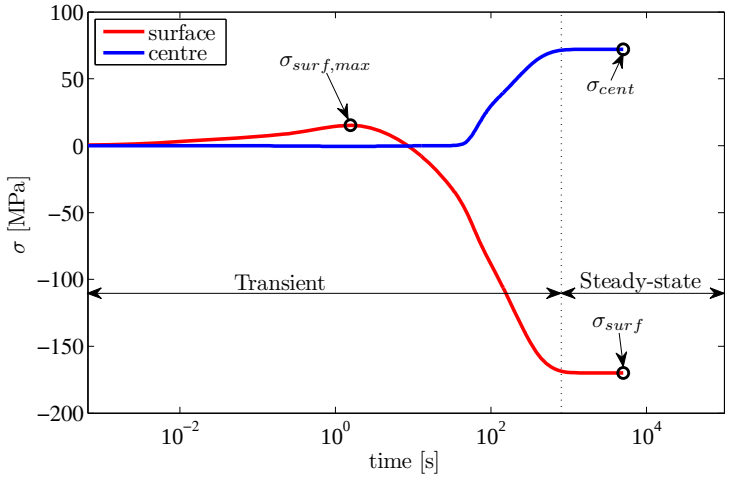

Figure 1.8: *Development of surface and centre stresses ($h = 250\,\mathrm{W/m^2\,K}$).*

- The compressive surface stress is twice the interior tensile stress in magnitude ($|\sigma_{surf}| = 2|\sigma_{cent}|$).
- The depth from the surface at which the residual stress is zero (the zero-stress zone) is approximately 21 % of the total thickness, l_z.

Due to the superficial compressive stresses, the apparent tensile strength is several times what is observed for float glass and the apparent strength becomes practically independent of the load duration.

1.3 Load-Transferring Joints in Glass

The three basic joints used for transferring in-plane loads between glass panes are described here: The adhesives joint, the friction joint and the pinned joint.

1.3.1 Adhesive Joint

Utilising adhesives to connect panes of glass can be advantageous, especially for the aesthetic of the structure since the surfaces can be kept smooth and the joints are almost invisible. Many adhesives show some yield capacity and can thereby redistribute and lower the stress concentrations arising in the joint. However, some adhesives exhibit extensive creep behaviour[8] and long-term effects are still an issue that requires more research. The short-term strength of an adhesive joint is very sensitive to the condition of the glued surfaces. Any grease or dirt on the surfaces when glued might result in an area of less adherence and thereby provide a initiation site for failure. This circumstance complicates any on-site assembly of glass panes using an adhesive.

[8] Creep tests on a dog-bone specimen is seen in Figure 4.10 and other tests are described in Ølgaard et al. (2008b).

The single-lap joint, which is shown in Figure 1.9, is a common adhesive joint. This connection type has been used in the early airplane industry and an analytical expression for the linear elastic joint can be derived (Volkersen, 1938). More elaborated models including the eccentricity of the connection and plastic behaviour of the adhesive can be found in the literature, see e.g. Goland and Reissner (1944), Hart-Smith (1973) and Kinloch (1981).

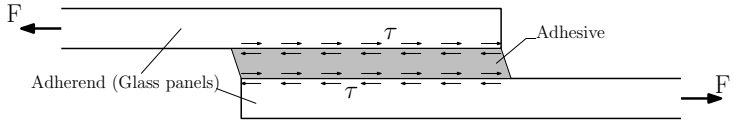

Figure 1.9: *Adhesive single-lap joint.*

1.3.2 Friction Joint

The friction joint utilises the fact that in order for one material to slide on another, the sliding force has to be equal to a fraction of the normal force applied. This fraction is referred to as the *coefficient of friction* and is denoted μ. In Figure 1.10 a friction joint is sketched where p is the pressure arising from the normal forces and the horizontal forces, F, are transferred as shear stresses, τ, at the interface between the two materials. In order to protect the glass a soft interlayer between the glass is used.

It is clear that determination of μ is essential for predicting the strength of the design; however, this coefficient is depending on the two materials in contact, the temperature and the time p is applied before loading (Morcant et al., 2005) and conservative values are often used. The pressure, p, is often established by pretensioned bolts; however, the pretension might be lost if the interlayer is not carefully selected to be a material without any creep behaviour. An advantage of the friction joint is that it provides a stiff connection compared to the pinned joint. Unfortunately, the friction joints are often large and might spoil the aesthetic appearance of the structure.

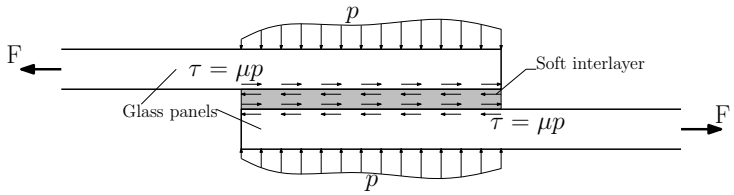

Figure 1.10: *Friction joint.*

1.3.3 Pinned Joint

In the pinned joint, the forces are transferred from the main glass to the lap-plates by contact pressure, p, between the pin and the surface of the hole[9] as indicated in Figure 1.11.

[9]The contact stresses may vary across the thickness due to e.g. bending of the pin.

This contact pressure leads to local high compressive stresses at the point of contact but also large tensile stresses will be present on the boundary of the hole. In order to avoid contact between the glass and the steel pin, an *insert* of a soft material such as aluminium or certain types of plastic is utilised as shown in Figure 1.11. Furthermore, a soft interlayer between the lap-plates and the main glass panel may be used in order to minimise scratches in the glass arising from small particles.

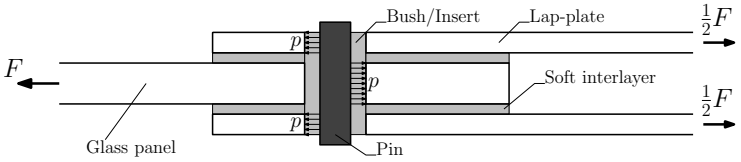

Figure 1.11: *Pinned joint.*

The advantage of the pinned joint is its relatively high and reliable strength. It is not as invisible as the adhesive connection, but it is typically smaller than the friction joint. The pinned joint is the preferred type of connection in glass structures today.

Many authors have investigated this type of connection. However, emphasis has been on the stresses arising from the external loading conditions and the contact problem, see e.g. Maniatis (2005) or Siebert (2004). The aim of this project is to establish a reasonable procedure for calculating the strength of a given pinned joint. The importance of the apparent strength of the material is recognised and is, to a high degree, included in the procedure. The procedure is validated by experiments.

1.4 Overview of the Thesis

Chapter 2 contains an experimental and a numerical part investigating the residual stress state in tempered glass. The residual stress distribution through the thickness of the test panels was measured by a photoelastic method. A fragmentation test was performed and compared to the standard test given in Eurocode. This investigation indicates that the Eurocode test method might be unsafe. The fragmentation process is studied further by means of digital high-speed cameras. These studies have estimated the fragmentation velocity with high accuracy and a hypothesis on the fragmentation mechanism is given.

The second part of Chapter 2 considers a numerical treatment of the tempering process in order to determine the residual stress state and thereby estimate the apparent strength. A state-of-the-art model has been implemented for solid 3D elements in a FE-code and is capable of calculating the stresses for arbitrarily complex geometries. The mechanism and implementation of the model is described and numerical convergence tests are performed. The model is also utilised for a parametric study of the stress state at holes far away from edges.

Chapter 3 describes the stress distribution due to the external load arising from the loading of a pinned connection. Numerical models are used to determine the effect of different inserts and the location of the hole relative to the edges. It has been recognised that the force applied is scaling almost linearly with the maximum tensile stress at the hole and design charts, independent of the magnitude of the load, can therefore be made.

Furthermore, the procedure for calculating the strength of a pinned joint is demonstrated in two examples. The examples were verified experimentally and a discussion on the results is given.

Chapter 4 investigates the possibility of reinforcing float glass beams and through the reinforcement obtain a ductile structural element. The concept is proven by experimental work and numerical modelling. Furthermore, design formulas are given and the long-term loading behaviour is discussed on the basis of creep tests on the adhesive.

It should be noted that this thesis consist of two parts, where Part I is a summary of the work done and primarily reported in the papers given in Part II. Furthermore it should be noted that not all references made in the papers are listed in the bibliography of the summary and vice versa.

Chapter 2

Residual Stresses

The residual stress state in tempered glass is described and investigated throughout this chapter. First an experimental investigation of the residual stresses in commercially fully tempered glass is carried out. The measured stresses are compared with a fragmentation test, leading to an investigation of the fracture process of tempered glass. Hereafter, the development and implementation of a state-of-the-art numerical model of the tempering process is described. This model is capable of predicting both the transient- and steady-state stresses arising during the process. Applications for the model is given in terms of optimising the tempering process and estimating the strength of tempered glass panels with holes at varying locations.

2.1 Measurement of Residual Stresses

The present section begins by describing the principles of the method used in Paper I for measuring the stress distribution far from edges and holes. Afterwards, the main results presented in Paper I are reviewed and commented upon.

2.1.1 Measurement Technique

Various methods for determining the residual stresses in glass exist. However, many of these methods are only capable of measuring the stresses at the surface of the glass and some techniques are limited to measurements only on the tin side of the glass (Aben et al., 2008). More methods, based on photoelasticity, have recently been developed (Anton and Aben, 2003) and a review of similar methods for different shapes of glass is given in Aben et al. (2008).

The device used for the measurements reported here is a so-called *SCAttered Light Polariscope* (SCALP) developed by GlasStress in Tallinn, Estonia (Anton and Aben, 2003). The SCALP is capable of measuring the stress distribution throughout the thickness of the glass panel; however, there are certain limitations to the method. In order to understand the limitations, the principle of the method is examined in the following.

When a laser beam penetrates a specimen of glass, a scatter of the light in the plane orthogonal to the laser beam will occur. The retardation of the scatter changes according to the stress/strain state in the glass due to the so-called lattice effect (Aben and Guillemet, 1993). This effect is utilised in the SCALP, which uses a laser beam inclined

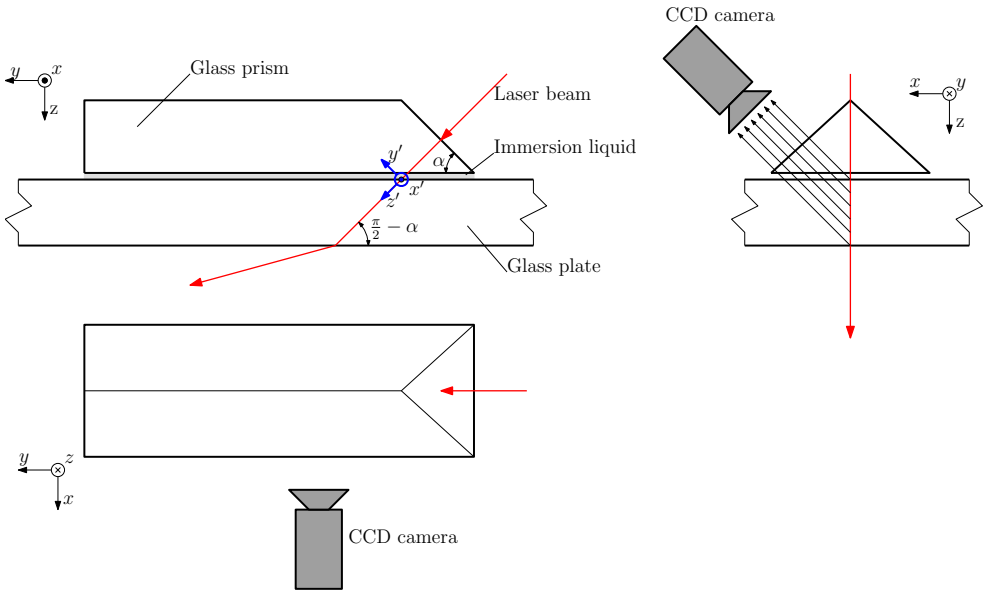

Figure 2.1: *Principle sketch of the technique used by the SCALP.*

at an angle $(\frac{\pi}{2} - \alpha)$ to the surface (Figure 2.1). The scatter of the laser is recorded by a camera and the retardation along the path of the laser beam, $\delta(z')$, is found. Assuming plane stress, the integral version of the so-called Wertheim law (see e.g. Aben and Guillemet, 1993) can be utilised to determine the stress components along the path of the laser beam, z', from the distribution of the retardation, $\delta(z')$. In order to determine the stresses in the panel plane (x,y-plane) the stress transformation formula for plane stress is used (the last equal sign in (2.1)).

$$\delta(z') = C \int_0^{z'} (\sigma_{x'} - \sigma_{y'}) dz' = C \int_0^{z'} \left(\sigma_x - \sigma_y \cos^2 \alpha\right) dz' \tag{2.1}$$

One measurement of the retardation, $\delta(z')$, does not provide information enough for solving (2.1) for both stress components. Theoretically, a plane hydrostatic residual stress state ($\sigma_x = \sigma_y$) exists far from edges. Using this assumption, the second equation needed for solving (2.1) is given. However, variations in the residual stresses in the panel plane are present in commercially tempered glass, even far from edges. It is therefore recommended to obtain the second equation for solving (2.1) by a second measurement at the same spot orthogonal to the first measurement. Due to the inclination of the laser beam, the path, z', cannot coincide for the two orthogonal measures and large stress gradients might yield inaccurate measurements. Each individual observation given in Paper I is based on two orthogonal measurements, where the beam entered the glass at the same point in order to minimise the error of the surface stress estimate.

In order to verify the stress distribution found by the SCALP, measurements on an externally loaded glass panel were carried out. Comparing measured changes in stresses

with analytical solutions, it was possible to determine how the SCALP performed for changes in the load. This verification test revealed that the measurements were consistent; however, the photoelastic constant, C, deviated from what was given by the manufacturer (see Paper I). Similar tests have later on been carried out by Ankergren and Bak-Jensen (2008) with similar results and estimates of C for tempered glass (Table 2.1). It is seen that for tempered glass the measured value of C is approximately 10 % larger than for float glass. Using C for float glass in tempered glass causes a misinterpretation of the measured retardation, yielding measured stresses which are 10 % too low.

Table 2.1: *Photoelastic constant, C, for float glass and tempered glass.*

Glass type	C [TPa^{-1}]	*Reference*
Float glass	2.70	SCALP manual - Anton (2006)
Float glass	2.75	Ankergren and Bak-Jensen (2008)
Tempered glass	3.01	Paper I
Tempered glass	3.10	Ankergren and Bak-Jensen (2008)

Many parameters are affecting C; a review on how the current temperature and the temperature history influences C can be found in Aben and Guillemet (1993). As an example it can be mentioned that pure silica has a photoelastic constant of 3.45 TPa^{-1} while the addition of other compounds reduces it to approximately 2.70 TPa^{-1} for float glass. Furthermore, the photoelastic constant is dependent on the density of the glass due to a phenomenon known as the "lattice effect". A low density yields a high value of C and since the density of tempered glass is approximately 0.1-0.3% lower than the density of annealed float glass, the differences shown in Table 2.1 might be partly explained by this.

2.1.2 Experimental Observations

In Paper I, 32 specimens, divided into four groups as shown in Table 2.2, were investigated. All specimens were ordered as (fully) tempered from a commercial manufacturer.

The residual stress state was measured in nine points on each specimen, located as shown in Figure 2.2. Two measurements were carried out at each point as described in Section 2.1.1 and therefore the stresses at the top surface are most accurately determined due to the intersection of the laser beams.

The average stresses measured for each group is shown in Table 2.2. It is seen that the measurements in both directions are similar when the average of the whole group is considered. Furthermore, an increase in the average stress is seen for a decreasing panel thickness.

A plot showing the stresses measured at the top surface can be seen in Figure 2.3. This clearly shows the increase in compressive surface stresses for decreasing thickness.

Similar observations are reported in Haldimann et al. (2008) for heat-strengthened glass[1]. For tempered glass the same tendency is reported between 10 mm and 15 mm

[1]Heat-strengthened glass is similar to tempered glass; however, the residual stress state is lower and it does not fragmentise upon failure.

Group:	*A*	*B*	*C*	*D*
No. of specimens	8	8	8	8
Thickness, l_z [mm]	19	19	12	8
Low iron content	No	Yes	No	No
Avg. σ_x *(top)* [MPa]	−68	−64	−81	−95
Avg. σ_y *(top)* [MPa]	−69	−65	−81	−95
Avg. σ_x *(mid)* [MPa]	38	36	45	45
Avg. σ_y *(mid)* [MPa]	38	36	45	45
Avg. σ_x *(bot)* [MPa]	−63	−55	−77	−101
Avg. σ_y *(bot)* [MPa]	−66	−57	−77	−101

Table 2.2: *Grouping, data and average measured stresses for investigated specimens.*

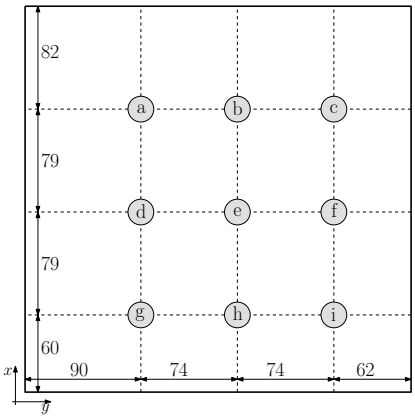

Figure 2.2: *Measurement points for investigated specimens. Dimensions are in* mm.

specimens; however, the results shown in Haldimann et al. (2008) for 6 mm tempered glass deviate from this tendency. The variation of residual stresses with the panel thickness indicates an inadequate adjustment of the tempering process[2].

Figure 2.3 shows scatter in the measurements. However, as described earlier, the data is obtained at nine different locations on each specimen and the scatter therefore indicates an uneven distribution of the residual surface stresses in each specimen. The maximum deviation between two measurement points found in a single specimen was 35.3 MPa. Table 2.3 provides the maximum surface stress deviation in each specimen.

Table 2.3: *Differences between highest and lowest measured compressive surface stress (in MPa) for each specimen.*

	1	*2*	*3*	*4*	*5*	*6*	*7*	*8*	*Mean*	*Max.*
A	34.7	35.3	22.9	30.5	25.9	35.0	27.7	19.8	29.0	35.3
B	26.7	34.3	6.2	4.9	29.7	7.5	22.0	6.1	17.2	34.3
C	12.3	9.4	8.2	8.1	15.4	6.8	11.5	7.3	9.9	15.4
D	11.6	23.0	15.8	15.0	9.1	8.1	15.2	13.8	13.9	23.0

A variation of residual stresses within a commercially tempered specimen was also reported by Lochegnies et al. (2005). He measured the stresses along a line crossing the specimen and showed that the residual compressive surface stress varied from 70 MPa to about 145 MPa for a 5.5 mm thick specimen. Furthermore, a difference of 50 MPa in the residual surface stress between two points located approximately 10 mm from each other was found.

[2]In Section 2.4 a numerical model of the tempering process is used for deriving graphs showing the forced convection constants needed in order to obtain equal residual surface stresses for different thicknesses of the glass.

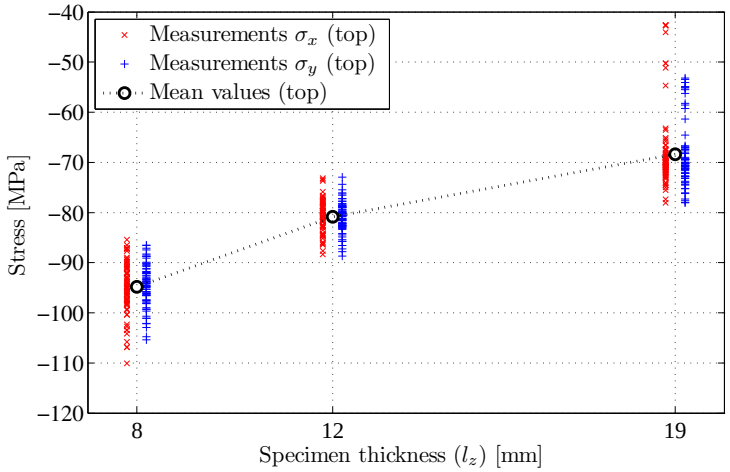

Figure 2.3: *Measurements from Group A, Group C and Group D. Note that all measurements for stresses in the x-direction are to the left of the vertical line representing the nominal thickness while the y-direction measurements are to the right of it.*

Such large variations in the tempering stresses must be due to nonuniform cooling and it is of great importance to lower these variations in order to optimise the performance of the tempered glass, without compromising the safety of the design. Models describing the tempering process are important tools for optimisation and development within this research area. Numerical models of the tempering process will be the topic of the next section; however, these optimisation problems are not within the scope of the present work.

In Eurocode the characteristic residual compressive surface stress is implicitly assumed to be at least 75 MPa, see e.g. Paper I or Haldimann et al. (2008). From Figure 2.3 it is seen that only a few of the measurements for $l_z = 19$ mm comply with this.

In Paper I a fragmentation count is made on one of the specimens from group A. The number of fragments were counted within an area of 50 mm × 50 mm centrally located at each of the nine measurement points.

The results from the fragmentation tests compared with the measured stresses can be seen in Figure 2.4, where N_{frag} is the number of fragments and, σ_x and σ_y are residual surface stresses (top) in orthogonal directions measured by SCALP. The measured values are normalised with values found in EN12150-1 (2004)[3], $N_{frag,EC} = 30$ and $\sigma_{Res,EC} = -75$ MPa, respectively.

From the figure it is seen that the counted number of fragments is more than 25 % higher, for all areas, than what is specified by Eurocode. This indicates that the glass can be regarded as fully tempered. However, when the corresponding measured stresses are

[3]It should be noted that the Eurocode fragmentation test procedure was not followed exactly regarding the size of the panel and the initiation.

considered, it is seen that they are too low for the glass to be regarded as fully tempered. Furthermore, it is seen that there is no correlation between the number of fragments counted locally and the residual stresses measured.

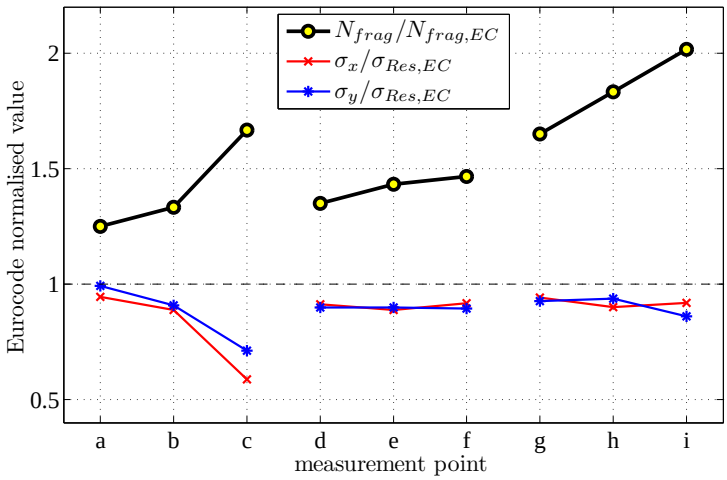

Figure 2.4: *Residual surface stresses (top) from SCALP and a fragmentation test. Results are normalised using the minimum residual surface stress and number of fragments specified in Eurocode.*

The fragmentation test is based on analytical considerations and experimental verification (Barsom, 1968). However, several assumptions on the fragmentation mechanism had to be made in order for the analytical derivation to be correct. Such assumptions are regarding the mechanism of the fracture propagation. In the following, the fracture of tempered glass is investigated by means of high-speed digital images, showing that not all assumptions are fulfilled.

2.2 The Fracture Process in Tempered Glass

The residual stresses in tempered glass are self-equilibrated; however, if this equilibrium is disturbed sufficiently the tempered glass will fragmentise.

Due to the high fracture velocity and correspondingly short process time (for reasonably sized specimens), investigations on the fracture process are rare. The present work is based on pictures obtained by means of digital high-speed cameras, measured residual stresses and visual inspection of the fracture surfaces (fractography), see Paper IV.

2.2.1 Whirl-Fragments

The process of fragmentation was initiated by drilling a hole from the narrow side of a tempered specimen into the tensile zone. This method was selected in order to minimise the energy added from external sources. The fragmentation progresses in a polar manner

from two origins as seen from Figure 2.5. Each origin is characterised by a relatively large fragment on the side towards the drill. These fragments are termed the *whirl-fragments* (see e.g. Paper IV) and can be separated by several centimetres. The two larger fragments are also seen when the initiation of the fragmentation process is done on the large surface (parallel to the panel-plane); however, in such cases there is no distance between the two characteristic fragments.

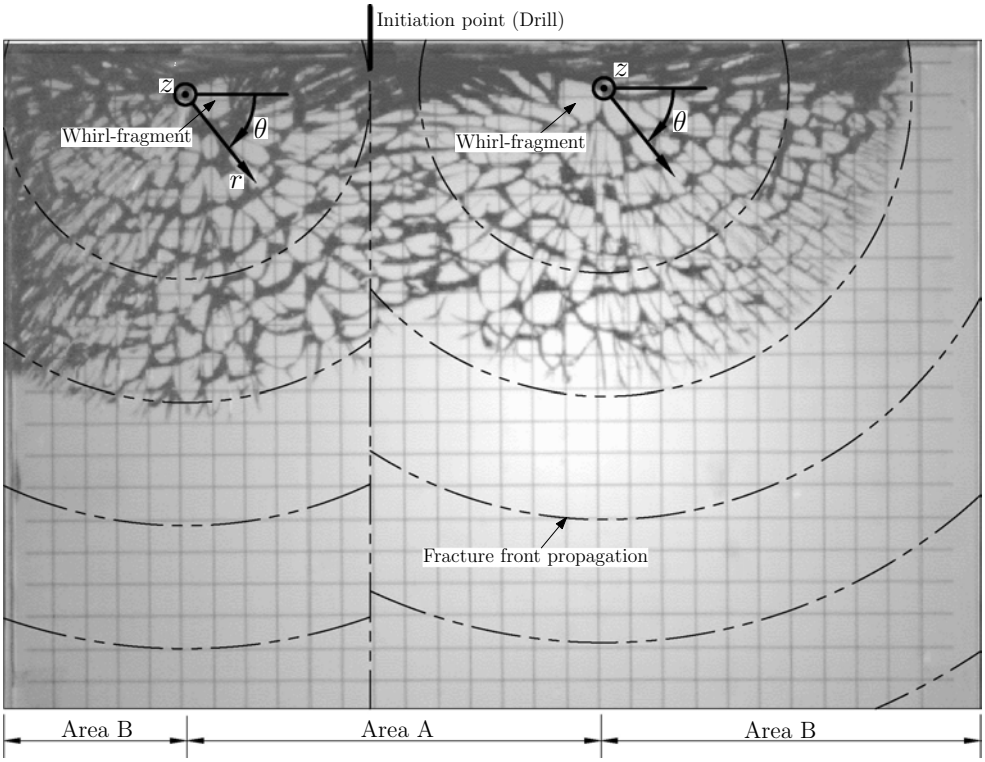

Figure 2.5: *The polar crack front propagation from the two whirl-fragments. The grid is* 10 mm × 10 mm.

The generation of a whirl-fragment was recorded using a frame rate of 150 000 fps (frames per second) and a shutter time of 4.5×10^{-6} s (Figure 2.6). In the beginning of the process, the primary direction of the fragmentation is approximately parallel to the edge of the glass where the initiation was done. The distance to this edge is corresponding to the depth of the zero-stress zone[4]. At some point the direction is changed and the cracks are running away from the edge. Hereby the whirl-fragment is created by bifurcation.

For crack velocities higher than 60 % of the elastic shear-wave speed[5], the maximum principal stress is located at an angle of 60° to the direction of crack propagation (Yoffe,

[4]The zone where the residual stress is changing from compressive to tensile.

[5]The elastic shear-wave speed for glass is $v_{shear} = \sqrt{\frac{G}{\rho}} = \sqrt{\frac{28.7\,\text{GPa}}{2500\,\text{kg/m}^3}} = 3387\,\text{m/s}$.

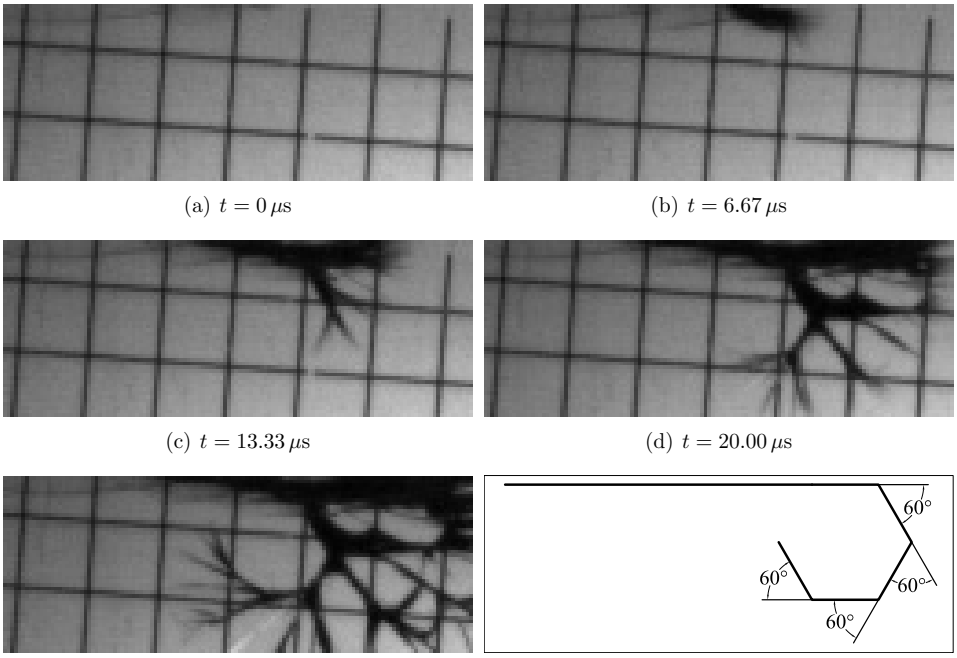

(a) $t = 0\,\mu$s (b) $t = 6.67\,\mu$s

(c) $t = 13.33\,\mu$s (d) $t = 20.00\,\mu$s

(e) $t = 26.67\,\mu$s (f) 60° bifurcation

Figure 2.6: *A close view to the formation of a whirl-fragment. The drill initiates the fragmentation just to the left of the pictures.*

1951; Freund, 1990). Figure 2.6(f) shows a drawing of a whirl-fragment created by 60° angles. By comparison with the picture in Figure 2.6(e) it is seen that similar angles are observed experimentally.

2.2.2 Velocity of the Fracture Front

An estimate of the radial fracture front velocity, v_r, could be made from the high-speed recordings within an accuracy of 1.0 %. The average velocities were estimated in 11 specimens with known residual stress states. A correlation between the fracture front velocity and the residual stress state has been reported by others (Takahashi, 1999; Acloque, 1962). However, plotting v_r as a function of the average centre stress, $\sigma_{cent,avg}$, in each specimen does not support such correlation. It should be mentioned that the range of residual stresses investigated here is relatively small, which might explain the apparent lack of correlation.

From Figure 2.7 it is seen that the average of the velocities is 1466 m/s. This is approximately 43 % of the elastic shear-wave speed for glass, v_{shear}. The velocity found is representing the fragmentation front. The velocity of a single crack between each branching might not be constant and the peak velocity might attain 60 % of the shear-wave speed.

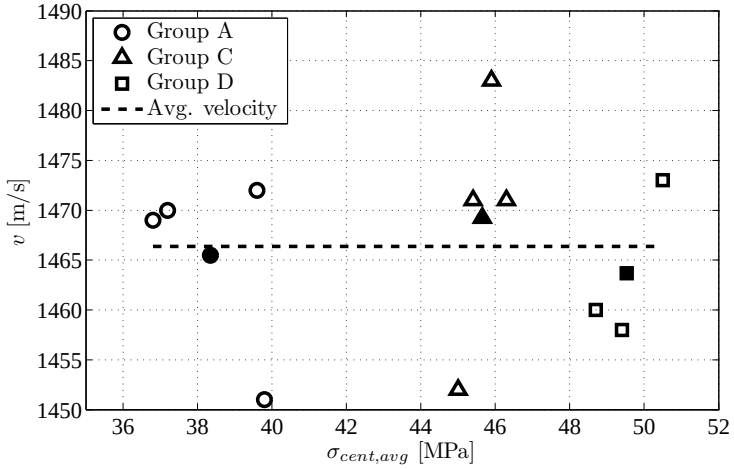

Figure 2.7: *True fracture front velocity vs. residual stresses. The filled markers are representing the average value within the respective groups.*

The maximum velocity was estimated to be 1550 m/s from the fracture surfaces by Acloque (1962). Acloque (1962) also estimated the velocity to be 1460 m/s by high-speed observations, which is a deviation of 0.4 % from the velocity estimated in the present project (Paper IV).

2.2.3 In-Plane Shape of the Fracture Front

The in-plane shape[6] of the fragmentation front has previously been determined by fractographic methods, i.e. visual inspection of the fracture surfaces. By such a method Acloque (1962) estimated a shape of the in-plane fracture front; however, photographs of the in-plane shape of the fracture front during propagation have never been reported before.

In these tests, the cameras were filming through the narrow side of the glass panel, i.e. parallel to the panel midplane. Glass with a low iron content[7] was used in order to transmit enough light for the pictures.

The pictures in Figure 2.8 show the development of the in-plane fragmentation front from the stage of initiation. In Figure 2.8(a) the drill and the surface of the specimen are seen. Figure 2.8(b) shows the initiation of the fragmentation process, where the crack seems to follow the zero-stress zone in the thickness direction. Figure 2.8(c) shows the crack propagation along the edge where the fragmentation was initiated, just before the whirl-fragments are generated. Figure 2.8(d) shows the beginning of the radial fragmentation process and the shape of the fragmentation front appears. Figure 2.8(e) shows a clear shape of the fragmentation front after 95.24 μs. Figure 2.8(f) shows the in-plane

[6]The in-plane shape is the shape of the fracture front in the panel plane, e.g. as seen through the narrow side of the panel.

[7]A low iron content yields a higher transmittance of visible light.

fragmentation front at a later stage in the same specimen, recorded with a second camera.

Two parallel horizontal lines are seen on the photos. These lines originate from the chamfered edges at the side opposite the cameras and are, due to the perspective, located inside the picture.

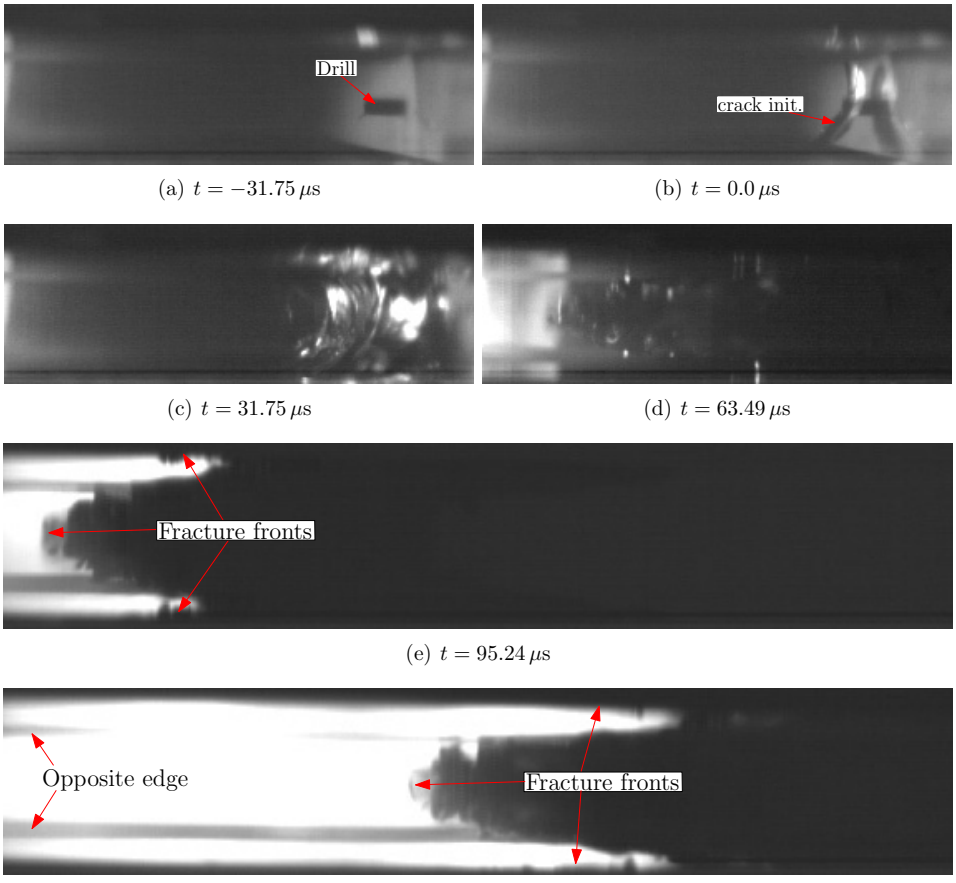

(a) $t = -31.75\,\mu s$ (b) $t = 0.0\,\mu s$

(c) $t = 31.75\,\mu s$ (d) $t = 63.49\,\mu s$

(e) $t = 95.24\,\mu s$

(f) $t = 127.0\,\mu s$

Figure 2.8: *Shape of the in-plane fracture front.*

The shape derived using fractography (Acloque, 1962) and the shape observed from these experiments are seen in Figure 2.9. Due to the depth in the picture, the location of the zero-stress depth is marked as a band in Figure 2.9(b)

It is seen that the observed shape is different from what was suggested by Acloque (1962) in that it has two secondary fragmentation fronts near the surfaces. One of the assumptions made for the analytical derivation of a correlation between the fragment size and the residual stress in Barsom (1968) was based on a crack front only propagating in the tensile zone.

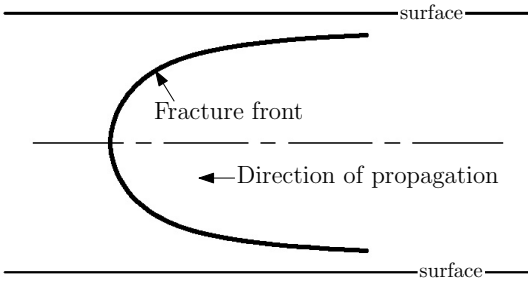

(a) Shape suggested by Acloque (1962)

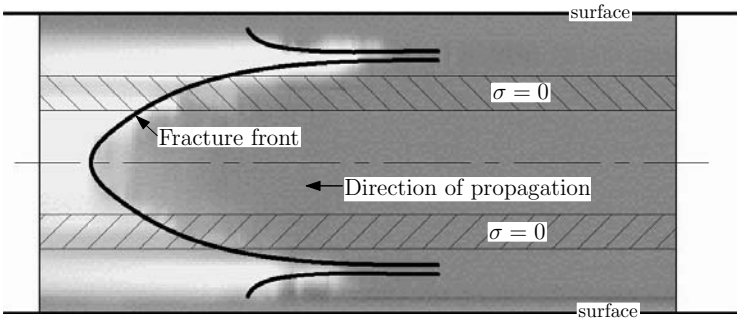

(b) Shape - High-speed observation

Figure 2.9: *The in-plane shape of the crack front. (a) is suggested from fractography by Acloque (1962), (b) is based on high-speed observations in the present work.*

2.2.4 Hypothesis for the Fragmentation Mechanism

Investigating the fracture surfaces, certain features may indicate the local direction of the crack propagation (Hull, 1999). Considering the near-surface parts of the fracture front so-called *river lines* are found and the local crack direction can be determined to reach from the surface towards the centre, see Figure 2.10.

The observations done for the in-plane fragmentation front yields the following hypothesis on the mechanism of fracture propagation in tempered glass: The fragmentation process is primarily driven by the tensile stresses in the interior. When the primary front propagates in the tensile zone, the tensile stresses are released and the material contracts locally. Thereby compressive surface stresses are released dynamically and tensile stresses may occur shortly at the surface. This initiates a secondary crack propagating from the surface towards the centre. When the secondary crack approaches the primary crack an amount of interference occurs and the local mode of the crack opening becomes partly mode III as indicated by the "river lines" in Figure 2.10. This process is then repeated and thereby the appearance of three fracture fronts propagating in the same direction occurs.

A sketch of the hypothesis is given in Figure 2.11, which shows the same section at different times (note that the time increases when reading from right to left). The primary

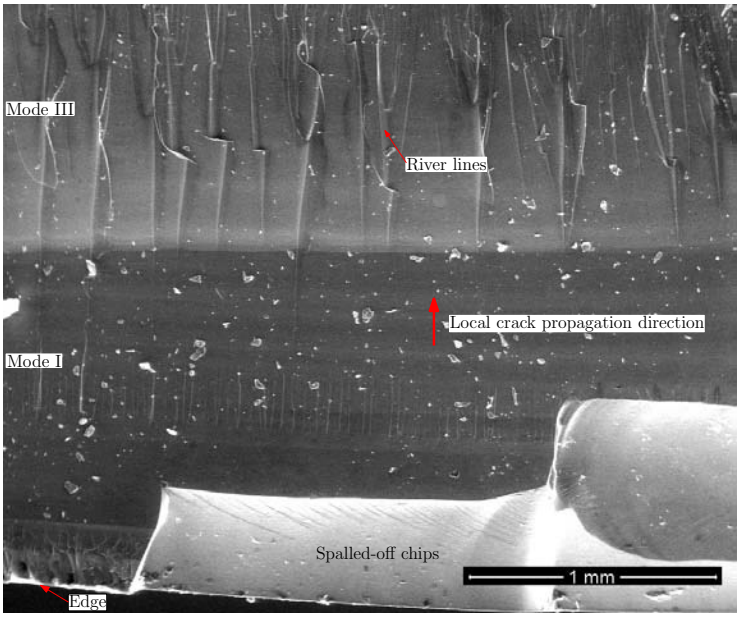

Figure 2.10: *Scanning electron microscope images of a fracture surface.*

front (black) is seen to be slightly ahead of the secondary fronts that are built up from several fronts (blue, green and red) moving perpendicular to the direction of the primary front propagation.

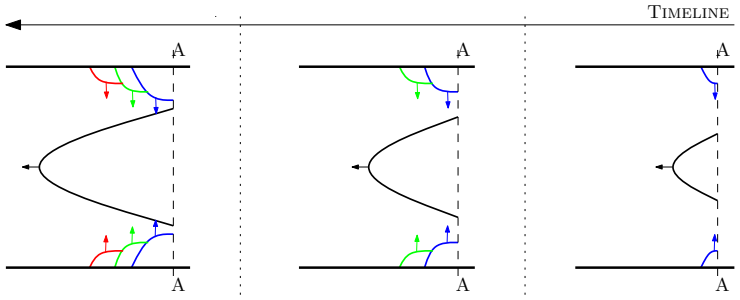

Figure 2.11: *In-plane crack propagation mechanism (to be read from right to left).*

2.3 Modelling of the Tempering Process

Knowledge of the residual stresses is essential when utilising tempered glass for carrying load. The distribution of the residual stresses is complex, which gives rise to a similarly complex variation of the apparent strength within a specimen. A tool for calculating the residual stresses in arbitrary geometries is presented in the following.

A numerical model of the stress-generating part of the tempering process (quenching) is presented. The model is implemented in a commercial Finite Element software and used for a numerical study of residual stresses in tempered glass.

Due to the complex behaviour of glass quenched from above T_g, reasonable estimates of the residual stresses can only be obtained by means of numerical methods. The mechanisms involved during the cooling are time-, temperature- and cooling-rate-dependent.

The tempering process was, according to Narayanaswamy (2001), patented in 1877 and several models for estimating the residual stresses have been reported over the last 90 years. At the beginning of the 20th century, Adams and Williamson (1920) suggested a simple hypothesis, which stated that *"the strain remaining in a block of glass is equal and opposite in sign to the reverse strain lost by viscous yielding in the early stages of the cooling process"*. After that, the theories for estimating the residual stresses were progressively developed by several authors. From the instant freeze model (Bartenev, 1948) over a thermoviscoelastic model proposed by Lee and Rogers (1965) to a model which also accounts for the so-called structural relaxation (Narayanaswamy, 1971). A more elaborate review of the evolution of tempering models can be found in Paper II, Narayanaswamy (2001) and Uhlmann and Kreidl (1980).

At the time of the development of the models, a lack of computational power restrained the solutions to 1D only (through the thickness far from edges). However, present computers are powerful enough to handle complex 3D geometries and thereby investigate the residual stresses at e.g. holes, edges and corners.

In order to determine the residual stress state for complicated geometries, a full 3D implementation of the tempering model is needed. Paper II describes an implementation of such a model in a user-subroutine for use in commercial FE software such as ABAQUS.

The model basically consists of a thermorheologically simple material model where the thermal expansion coefficients are determined by the structural relaxation. The description of the implementation is therefore divided into two parts:

1. The thermorheologically simple behaviour.

2. The structural relaxation.

2.3.1 Thermorheologically Simple Behaviour

Thermorheologically simple materials are viscoelastic materials where the variation of the relaxation moduli at different temperatures can be accounted for by a simple scaling of time, t. For varying temperatures, $T(t')$, an integration is needed to determine the scaled

time[8], ξ.

$$\xi = \int_0^t \phi\left(T(t')\right) dt' \tag{2.2}$$

Here t' is a running (time) parameter and ϕ is the temperature-dependent time-scaling function. There are several different time-scaling functions; however, the one used here can be derived from the Arrhenius equation (see Paper II)

$$\ln \phi(T) = \frac{H}{R_g}\left(\frac{1}{T_B} - \frac{1}{T}\right) \tag{2.3}$$

where H is the activation energy for glass, R_g is the universal gas constant and T_B is the base temperature at which the master relaxation curves are specified and therefore $\xi(T_B) = t$.

The viscoelastic behaviour is implemented using the hereditary integral approach. In index notation, the governing equations in 3D can be written as

$$\sigma_{ij}(t) = \underbrace{2\int_0^t G(\xi - \xi')\frac{de_{ij}(t')}{dt'}dt'}_{\text{Deviatoric stress, } s_{ij}} + \delta_{ij}\underbrace{\int_0^t K(\xi - \xi')\frac{d\varepsilon_{ii}(t')}{dt'}dt'}_{\text{Hydrostatic stress, } \sigma_{ii}} \tag{2.4}$$

where σ_{ij} represents the stress tensor, G and K are the time-dependent shear and bulk modula respectively, e_{ij} is the deviatoric strain tensor, ε_{ii} is the trace of the strain tensor, t is the time, and δ_{ij} is Kronecker's delta. The first term in (2.4) is seen to correspond to the deviatoric part, and the second term to the hydrostatic part, of the material behaviour.

It is seen from (2.4) that the complete strain history is needed in order to evaluate the integral. Such integration in each time step would be expensive in terms of computational power. Furthermore, the storage of the complete strain history for all considered material points would be expensive for full 3D models.

It turns out that by choosing the functions G and K wisely, an integration of the complete strain history can be avoided (see Paper II). It is therefore a huge advantage to write the relaxation modula as series of exponential functions – the so-called Prony series[9].

$$G(t) = \sum_{n=1}^{N_G} g_n \exp\left(-\frac{t}{\lambda_n^g}\right) \qquad \text{and} \qquad K(t) = \sum_{n=1}^{N_K} k_n \exp\left(-\frac{t}{\lambda_n^k}\right) \tag{2.5}$$

A stress response to a load increment is sketched in Figure 2.12, where it is seen that the stress increment consists of a viscoelastic stress increment considering the load applied, $\Delta\check{\sigma}_{ij}$, and the relaxation of the actual stress state, $\Delta\tilde{\sigma}_{ij}$. Linearising the applied strain increment, $\Delta\check{\sigma}_{ij}$ can be found analytically from (2.4). Similar operations can be carried out for $\Delta\tilde{\sigma}_{ij}$ utilising that the strain increment is zero.

From Figure 2.12 it is seen that the total stress at the end of the increment, $\sigma_{ij}(t+\Delta t)$, equals the sum of the "viscoelastic loading" and the "relaxation of stress history". By

[8]The scaled time is often referred to as the shifted time. This is due to its derivation, where a logarithmic time traditionally is used, see e.g. Christensen (2003).

[9]Such series are also known as a generalised Maxwell material.

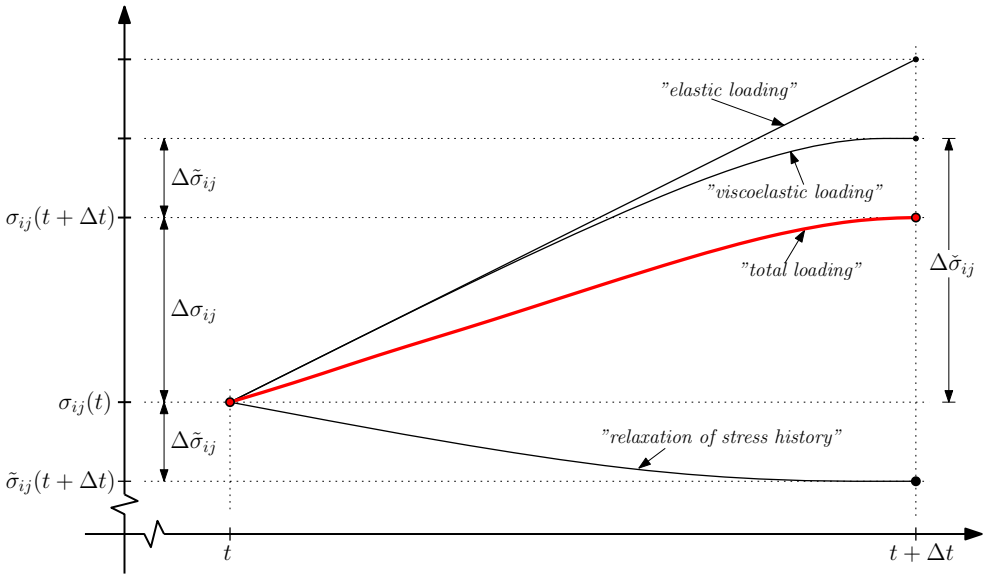

Figure 2.12: *Sketch of responses to an increment in time and load.*

separating the stresses further into in a deviatoric part, s_{ij}, and a hydrostatic part, σ_{ii}, the total stress, $\sigma_{ij}(t+\Delta t)$, can be expressed as

$$\sigma_{ij}(t+\Delta t) = \underbrace{\sum_{n=1}^{N_G}\left(\Delta\check{s}_{ij}^{(n)} + \tilde{s}_{ij}^{(n)}(t+\Delta t)\right)}_{\text{Deviatoric stress, } s_{ij}} + \delta_{ij}\underbrace{\sum_{n=1}^{N_K}\left(\Delta\check{\sigma}_{ii}^{(n)} + \tilde{\sigma}_{ii}^{(n)}(t+\Delta t)\right)}_{\text{Hydrostatic stress, } \sigma_{ii}} \tag{2.6}$$

A uniaxial analytical solution for a thermorheologically simple material has been derived in Paper II and used for validating this part of the model. The comparison between the implementation and the exact solution showed only small deviations even for relatively large time steps.

2.3.2 Structural Relaxation

The next "layer" in the model is the so-called structural relaxation. The term "structural relaxation" refers to the arrangement of the microstructure[10] of the material, which is changing over time. If glass is cooled slowly, the microstructure tends toward a more organised form and thereby a change in certain material properties. For the residual stresses generated during the process of cooling, the most important property is the volumetric contraction. The effect of structural relaxation is therefore often referred to as volume relaxation.

The sketch in Figure 2.13 illustrates the effect of structural relaxation on the volume. Many materials crystallise when cooled from above the melting point, T_m. However,

[10]Books on material science often refer to the "long-range order" of a material structure.

glass is characterised by its ability to prevent crystallisation and, for realistic cooling rates, it will become a supercooled liquid. From Figure 2.13 it is seen that an increasing cooling rate yields a high specific volume. This effect will be accounted for in the volume relaxation model proposed by Narayanaswamy (1971).

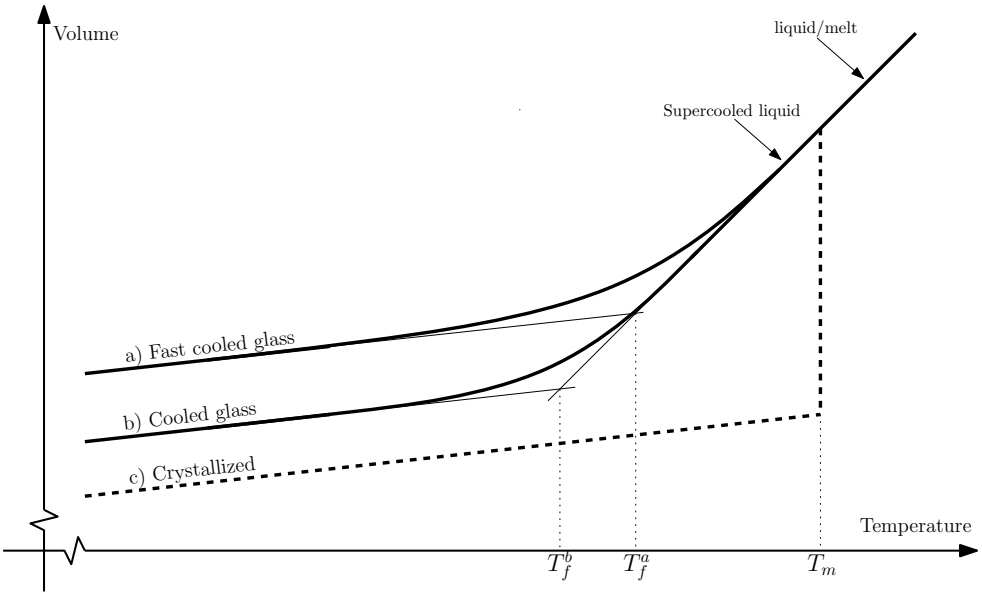

Figure 2.13: *Volume as function of temperature during cooling.*

In order to describe the state of the microstructure in glass, the concept of fictive temperature, T_f, was introduced by Tool (1946). From Figure 2.13 it is seen that T_f is found at the intersection between the extensions of the solid-state line and the liquid-state line. A high cooling rate is seen to yield a high fictive temperature ($T_f^a > T_f^b$). During cooling, T_f will equal the real temperature, T, in the liquid state but tend to lack behind when the solid state is approached, and finally it will be constant in the solid state. In general T_f is dependent on the property considered; however, this text only considers the volume contraction.

A general mathematical model of the structural relaxation was formulated by Narayanaswamy (1971). In this formulation the integral equation in (2.7) needs to be solved for T_f.

$$T_f(t) = T(t) - \int_0^t M(\xi(t,T_f) - \xi'(t,T_f))\frac{\partial T(t')}{\partial t'}dt' \tag{2.7}$$

Here M is the so-called response function for the given property (the volume), ξ is again used for the scaled time. However, the activation energy in the time-scaling function, ϕ, is now divided into a temperature part, H_g, and a part associated with the atomic structure, H_s (described by the fictive temperature, T_f). Substituting $H = H_g + H_s$ in (2.3), the

time-scaling function to use when including structural volume relaxation is obtained:

$$\ln \phi(T) = \frac{H_g}{R_g}\left(\frac{1}{T_B} - \frac{1}{T}\right) + \frac{H_s}{R_g}\left(\frac{1}{T_B} - \frac{1}{T_f}\right) \tag{2.8}$$

For the implementation, equation (2.7) is solved by an algorithm proposed by Markovsky and Soules (1984).

As mentioned before, the tempering model was implemented in a commercial FE-software and the complete code for the user subroutine is given in Appendix A. A more elaborate description of the implementation can be found in Paper II.

2.3.3 Convergence

In Paper II it is shown that the parameters needed for convergency are dependent on the stresses considered. In general, more restricted parameters are needed for estimating the maximum tensile transient stresses, $\sigma_{surf,max}$ compared to the steady-state stresses, σ_{surf} and σ_{cent} defined in Figure 1.8. The cooling rate only showed a minor effect on the convergency rates.

Model Description - String Model

For the convergence tests, a model describing the panel cross-section far from edges is primarily used. Such a model can be simply built from solid elements if the right boundary conditions are applied. In Figure 2.14 a sketch of this so-called string model is shown.

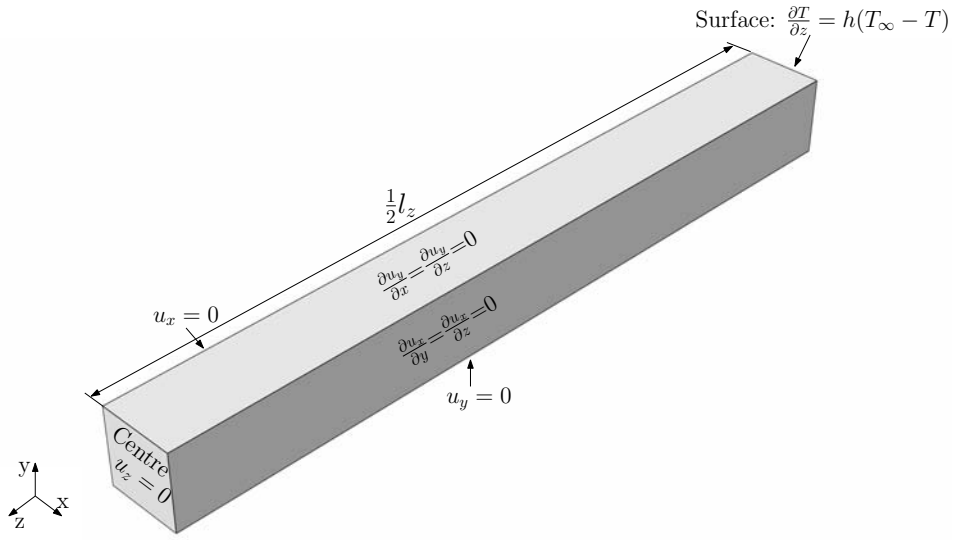

Figure 2.14: *The string model with all thermal and mechanical boundary conditions.*

Due to symmetric cooling, only half the thickness needs to be modelled ($1/2l_z$). Therefore, the face in the centre plane is a symmetry plane and zero displacements in the plane

normal direction ($u_z = 0$) is prescribed. Rigid body motions are prevented by prescribing $u_x = 0$ and $u_y = 0$ on two orthogonal faces as shown in Figure 2.14.

In order to model the surrounding material from the large panel, the two remaining surfaces can only be allowed to move in their respective normal direction. However, the surfaces must remain plane without changes in the direction of the normal. Choosing the faces with the x-axis and y-axis as outward normals, the conditions can be written as:

$$\frac{\partial u_x}{\partial y} = \frac{\partial u_x}{\partial z} = 0 \quad \wedge \quad \frac{\partial u_y}{\partial x} = \frac{\partial u_y}{\partial z} = 0 \tag{2.9}$$

respectively, where u is the displacement.

Due to limitations in the FE-software used, such boundary conditions can only be specified on one of the faces. An investigation on the significance of only supporting one of the faces showed a deviation in the strains of 3.8 %. In the following the model with boundary conditions on only one face is used for the string model. It should be noted that the 3D models described later do not suffer from this lack of boundary conditions.

On the surface, the thermal boundary conditions are prescribed by forced convection. For the surface where the normal direction is coincident with the z-direction, the thermal boundary condition can be written as:

$$\frac{\partial T}{\partial z} = h(T_\infty - T) \tag{2.10}$$

where T is the temperature, T_∞ is the ambient temperature and h is the *convection heat-transfer coefficient*. It is seen that h is governing the cooling rate, and it will later be used as a measure of the cooling rate. The thermal boundary conditions on all other surfaces are adiabatic.

The number of elements and their distribution required for obtaining convergence in the results is investigated in the following. Due to the symmetry, the number of elements always refers to how many elements are used through half the thickness of the panel. In order to increase the mesh density at the surface, the bias ratio is defined as the ratio between the length of the element at the centre and the length of the element at the surface, as shown in Figure 2.15. The figure shows four models with 10 elements and different bias ratios.

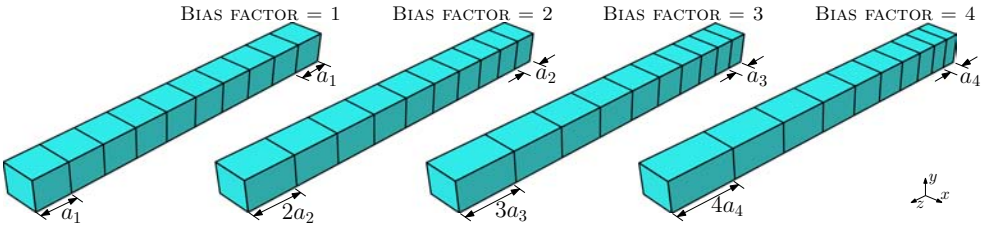

Figure 2.15: *Mesh with 10 elements shown for different bias ratios.*

The solution is independent of the dimensions in the x- and y-directions. However, these dimensions are chosen so that the elements will become perfectly cubic for a bias ratio equal to one.

Convergence for the String Model

Comparing the convergency rates for elements with first- and second-order displacement fields[11], it is seen, as expected, from Figure 2.16 that the higher-order elements are superior to the lower-order elements. This is reasonable due to the near-parabolic shape of the steady-state residual stress. It would be interesting to investigate the convergency rate for elements with a third-order displacement field since such an element is capable of reproducing a parabolic stress distribution; however, such elements were not tested here. From the figure it is seen that convergency for the steady-state stresses is obtained for relatively few elements, while the transient stresses require considerably more elements. This is due to the complex transient stress distribution arising during the cooling, see e.g. Figure 1.6 on page 11.

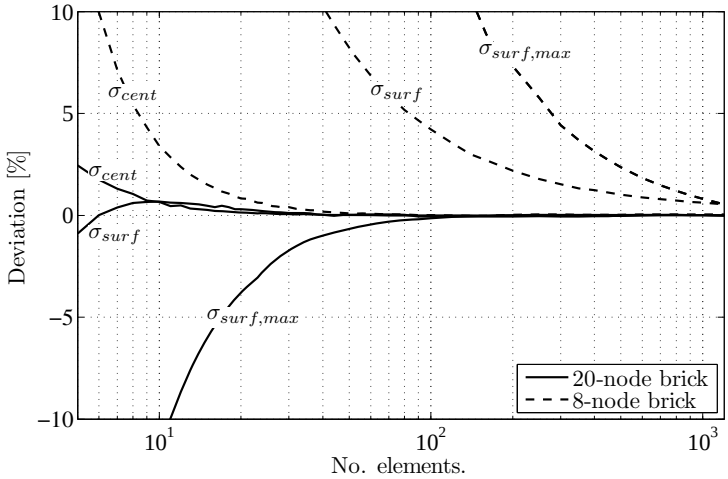

Figure 2.16: *Uniformly distributed elements, convergency for 20-node and 8-node hexahedron elements. Deviation from a model using 1200 20-node elements*

From Figure 2.16 it is seen that in order to estimate the steady-state residual stresses far from edges (the string model), no more than 5 elements through half the thickness are required for a reasonable convergency (Figure 2.16). In order to model the transient stresses with similar accuracy, approximately 30 elements through half the thickness are needed. However, if the elements are biased towards the surface, 10 elements may provide a reasonable accuracy. This accuracy is found for a bias factor between 4 and 8 as seen in Figure 2.17. Increasing the bias factor further spoils the determination of σ_{cent}. This phenomenon is seen in Figure 2.17, where the solutions are compared to 1200 elements uniformly distributed through half the thickness and the biased solutions do not converge towards zero.

[11] with the corresponding constant and first-order temperature fields.

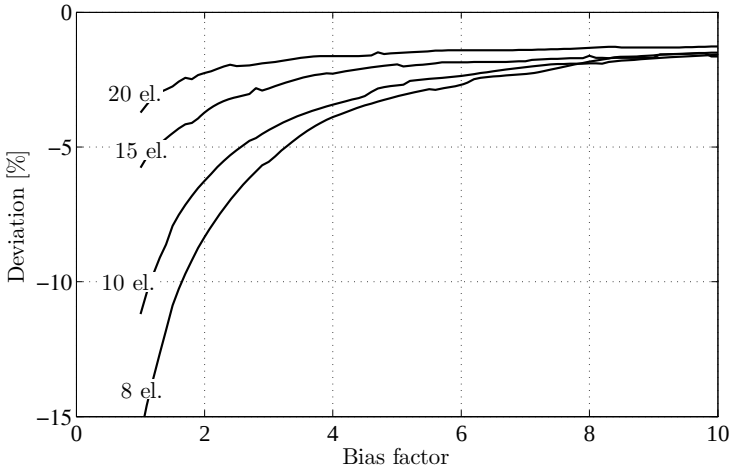

Figure 2.17: *Biased element convergence for $\sigma_{surf,max}$ compared to a solution obtained for 1200 uniformly distributed elements.*

Due to the large variations in material stiffness during the cooling, it is beneficial to vary the size of the time steps throughout the analysis. In the analysis presented here, the step size is controlled by a maximum allowable temperature change in the model, ΔT_{max}. An investigation on this measure for the step size showed that setting $\Delta T_{max} < 5\,\mathrm{K}$ gives results with deviations less than 2 % compared to a converged solution ($\Delta T_{max} = 0.1\,\mathrm{K}$), see Paper II.

2.4 Parametric Study of the Tempering Process

Paper II includes a parametric study on cooling rates and thicknesses far from edges, corners and holes. Paper III is an investigation on the residual stresses at holes for different geometries. Before proceeding, certain terms needs to be defined.

The term σ_{rc} is defined as *"the **r**esidual **c**ompressive in-plane stress at the surface of the hole"* (positive in compression). The minimal value of σ_{rc} is the most critical value regarding the apparent strength and is denoted σ_{rc}^{min}.

The far-field stress, σ_∞, for a given specimen is defined as *"the undisturbed compressive surface stress observed far from edges or holes in a specimen of equal thickness and cooling history"*.

The following non-dimensional measures are defined for later use:

$$\hat{\sigma}_{rc}^{min} = \frac{\sigma_{rc}^{min}}{\sigma_\infty} \tag{2.11}$$

Hereby the actual residual stress state at the hole is related to the far-field stress, σ_∞.

2.4.1 Cooling Rates and Thickness

The residual surface stresses, σ_∞, obtained for varying cooling rates were investigated. In Figure 2.18 the results for the most common glass thicknesses are seen. The figure shows

that a high cooling rate (expressed by h) yields a high σ_∞ and that thick specimens do not need as high a cooling rate as thin specimens in order to obtain equal σ_∞ . These curves can be utilised for adjusting the tempering process in order to obtain equal residual stresses regardless of the panel thickness.

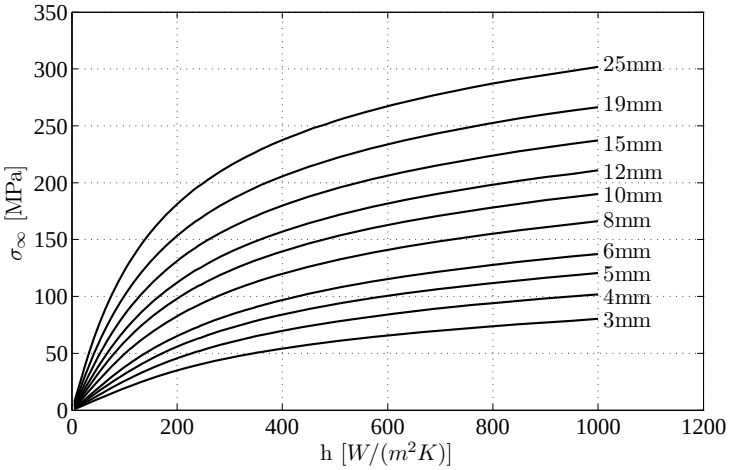

Figure 2.18: *The far-field residual stress as a function of the cooling rate expressed by the forced convection coefficient. The initial temperature used was* 650 °C

.

During the process of quenching, transient tensile stresses at the surface, $\sigma_{surf,max}$, arise. These transient stresses increase with the cooling rate, and the glass may shatter if the cooling rate is high. Investigations on these stresses are also carried out in Paper II and Figure 2.19 shows the results for different thicknesses. It is seen that for constant h, an increase in thickness also increases the transient stresses. Thus, in order to compare the maximum steady-state stresses for different panel thicknesses, the transient stresses ($\sigma_{surf,max}$) need to be considered. The simplest way to do this is to limit the value of $\sigma_{surf,max}$.

From Figure 2.18 and Figure 2.19 it is possible to estimate the maximum obtainable steady-state residual stress, $\sigma_{\infty,max}$, for a limiting value of $\sigma_{surf,max}$.

Figure 2.20 shows $\sigma_{\infty,max}$ as a function of the thickness for four different limits of $\sigma_{surf,max}$. It is seen that for an increasing thickness of the glass panel, the maximum obtainable steady-state surface stress ($\sigma_{\infty,max}$) is also increased.

Using the model developed and the graphs presented above, the measured surface stresses presented in Section 2.1.2 can be analysed for their history of tempering. In Table 2.4 the average of the measured surface stresses for each group is used for estimating h and the maximum transient tensile stress, $\sigma_{surf,max}$. From the table it is seen that h is increasing for decreasing panel thickness, which is expected according to Figure 2.18. An optimisation of the tempering process would be to keep $\sigma_{surf,max}$ constant regardless of the panel thickness. The last two rows in Table 2.4 are found by prescribing that $\sigma_{surf,max} =$ 10 MPa. It is seen that $\sigma_{\infty,max,10}$ is higher than what was found by measurements and

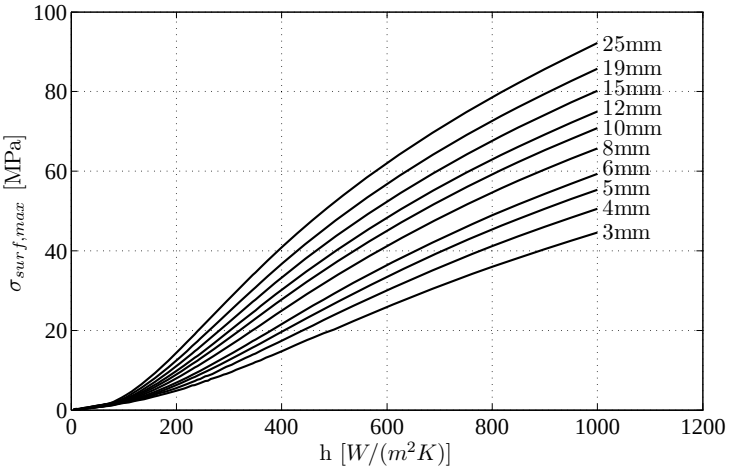

Figure 2.19: *The maximum transient tensile stress during tempering as a function of the cooling rate (expressed by the forced convection coefficient).*

that the stress is decreasing with a decreasing thickness, opposite to what is found in the measurements.

The graphs presented above can be utilised for optimising the process and in Table 2.4 maximum obtainable compressive surface stresses for $\sigma_{surf,max} = 10\,\text{MPa}$ and corresponding values of h are given. From the results it is seen that an optimisation of the tempering process could provide glass panels with a much higher apparent strength.

Table 2.4: *Inverse analysis on measured residual stresses.*

Group	*A*	*B*	*C*	*D*
Thickness [mm]	19	19	12	8
σ_∞ [MPa][a]	−68.5	−64.5	−81	−95
h [W/(m^2 K)][b]	60.7	56.5	121.4	252.7
$\sigma_{surf,max}$ [MPa][c]	1.3	1.2	3.6	12.1
$\sigma_{\infty,max,10}$ [MPa][d]	−144.1	−144.1	−112.8	−89.2
h_{10} [W/(m^2 K)][e]	178.0	178.0	201.9	226.7

[a] Averaged measurements from Table 2.2 using the top surface measurements.
[b] Found from Figure 2.18. [c] Found from Figure 2.19. [d] Found from Figure 2.20 using $\sigma_{surf,max} = 10\,\text{MPa}$. [e] Values of h corresponding to $\sigma_{\infty,max,10}$.

The maximum transient stresses in a panel of finite size might not be located far from edges as assumed by the string model. On the other hand, the chosen limit for the transient tensile stress, $\sigma_{surf,max}$, has been chosen to be less than the value estimated for group D.

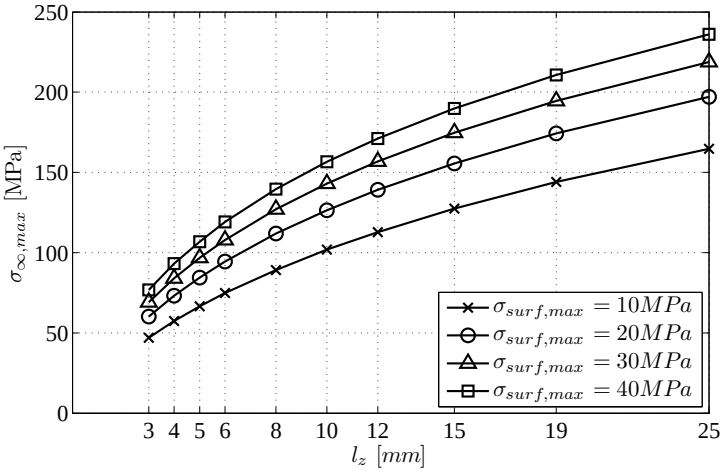

Figure 2.20: *The maximum far-field residual stress when limiting the cooling rate due to transient tensile stresses, $\sigma_{surf,max}$, as a function of the panel thickness, l_z.*

2.4.2 Geometric Location of Holes

Paper III describes the minimum compressive residual stress, σ_{rc}^{min}, found at holes considering different geometries. Such results can be used for estimating the apparent strength of the glass at the hole, which is a valuable parameter when designing pinned joints in tempered glass.

Description of Models

In order to investigate the residual stresses near holes and how these are affected by boundaries, the string model cannot be applied. It is therefore necessary to model the full 3D domain. However, wherever it has been possible, symmetry has been utilised.

In the following a model with a typical mesh and the boundary conditions used is described. This model represents a square panel with a centrally located hole. Due to symmetry only 1/16 of the geometry needs to be modelled (assuming symmetric cooling), see Figure 2.21(a). However, such a high degree of symmetry is only found for a few of the examples modelled.

A typical mesh near the hole, the edge and the corners can be seen in Figure 2.21(b). This figure also defines the three locations on the surface of the hole. The edge of the hole at the surface of the panel is denoted *surf*. The edge where the chamfered edge meets the vertical hole surface is denoted *cham* and the edge along the perimeter in the panel mid-plane is denoted *mid*.

For the model different convection heat-transfer coefficients have been used on the surface, h_1, the faces of the chamfered edges, h_2, the vertical faces of the hole, h_3, and the vertical free faces along the edges, h_4, see Figure 2.21(b). Unless otherwise specified, the values used are: $h_1 = 77\,\mathrm{W/m^2\,K}$, $h_2 = 76\,\mathrm{W/m^2\,K}$, $h_3 = 60\,\mathrm{W/m^2\,K}$ and $h_4 =$

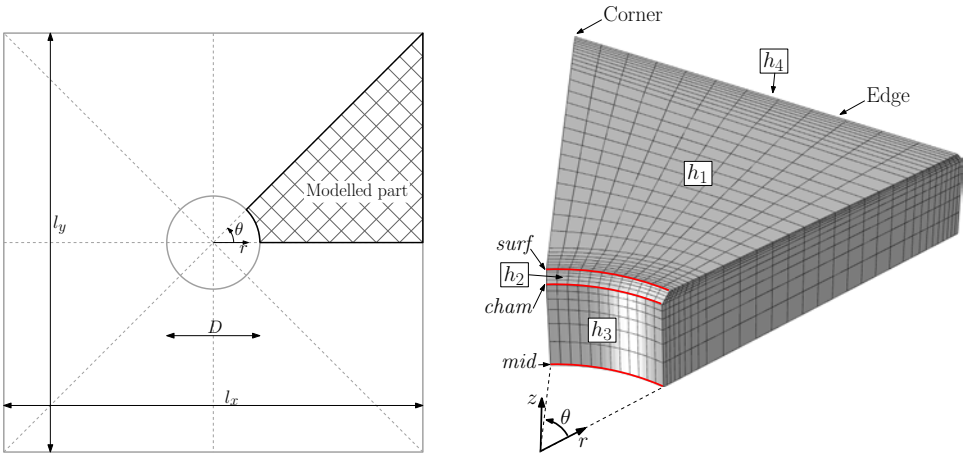

(a) Utilised symmetry (b) Typical mesh

Figure 2.21: *Model of a square panel with a centrally located hole. a) shows the utilisation of symmetry for this particular model. b) shows a typical mesh and the different convection heat-transfer coefficients, h_1, h_2, h_3 and h_4.*

$62\,\mathrm{W/m^2\,K}$ which are based on the investigations carried out by Bernard et al. (2001).

In the previous section, the convergence for the stresses far from edges was investigated for a varying number of elements through the thickness. In order to test the convergence for the stresses at a hole, a model as shown in Figure 2.21 is investigated for a different number of elements through the thickness. The considered geometry is for $l_x = l_y = 120\,\mathrm{mm}$, $l_z = 19\,\mathrm{mm}$ and $D = 30\,\mathrm{mm}$ (Figure 2.21(a)).

The convergence for steady-state stresses and maximum transient stresses were investigated on three locations on the surface of the hole. The locations are *surf*, *cham* and *mid* for $\theta = 0°$ and the results are presented in Figure 2.22. The results are normalised using the solutions obtained with most elements.

In Figure 2.22 it is seen that solutions are converged to within a few percent for more than 8 elements through half the thickness. The following parametric investigations were carried out using 10 elements through half the thickness.

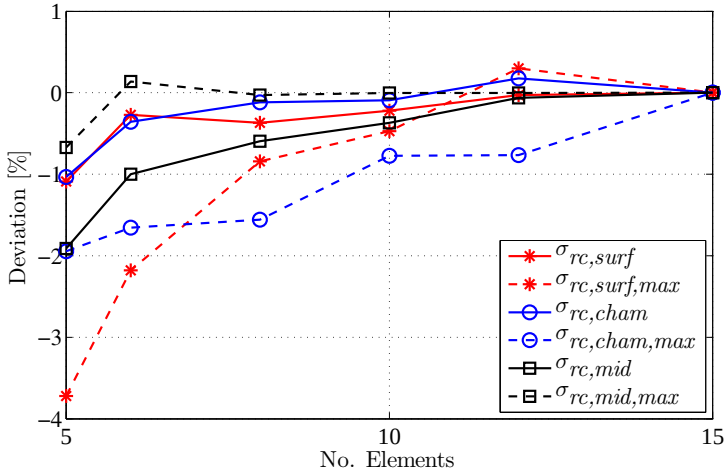

Figure 2.22: *Convergence for no. of elements through thickness for the stresses at the hole. Deviation from the solution using 15 elements through the thickness.*

Generation of Residual Stresses Near Holes

Before continuing with varying geometric parameters in the model, the generation of residual stresses at the hole is considered. In Figure 2.23 the tangential stresses, σ_θ, are shown for a 19 mm thick square panel ($l_x = l_y = 120$ mm) with a centrally located hole ($D = 30$ mm).

Figure 2.23(a) shows the stress state after approximately 20 s of quenching. It is seen that tensile stresses are found at the edges where the cooling is fastest. The largest transient tensile stress is located on the edge halfway between two corners.

Due to the fast cooling at the edges, the stresses are developed near these areas at first. From Figure 2.23(b) and Figure 2.23(c) it is seen that the stresses in these areas are increasing towards the central part of the cut shown. This is indicated by the arrows on the figure.

The residual stress state after the tempering process is shown in Figure 2.23(d). Here it is seen that the fast-cooled areas are also the areas with the highest state of compressive stress. However, a structural stiffness is also needed in order to carry the stresses and therefore the residual stresses near the corners are low. Thus, the residual stress state is governed by two things: 1) the cooling rate and 2) the amount of material to carry the stress (structural stiffness).

These effects are not trivial and in the following the residual stresses at holes are investigated for different geometries in order to estimate the apparent strength of the tempered glass for use in pinned connections.

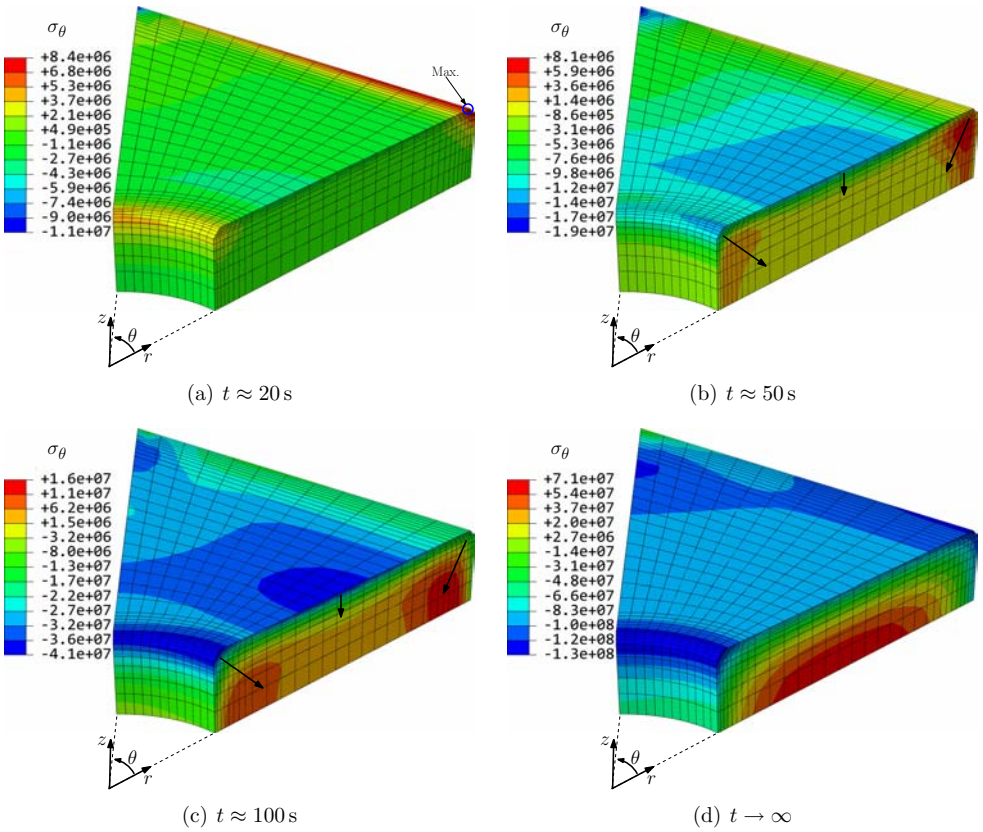

(a) $t \approx 20\,\mathrm{s}$ (b) $t \approx 50\,\mathrm{s}$

(c) $t \approx 100\,\mathrm{s}$ (d) $t \to \infty$

Figure 2.23: *Different stages during the tempering process for a square panel with a centrally located hole.*

Parametric investigation

A geometry as shown in Figure 2.24 was investigated for varying widths of the specimen, l_x. Three different values for the hole-to-edge distances, $l_{y,e}$, were investigated. The diameter of the hole, D, was constant (30 mm); however, it was shown in Paper III that a change in D only had a weak effect on σ_{rc}^{min}. The distance between the hole and the line of symmetry in the y-direction, $l_{y,s}$, was 350 mm. Using this distance, σ_{rc}^{min} would be relatively unaffected by the boundary conditions at the symmetry line. The thickness of the specimens was $l_z = 19\,\mathrm{mm}$.

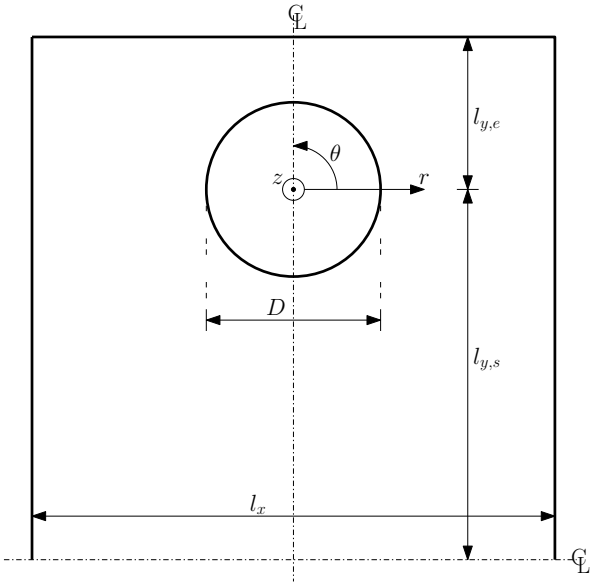

Figure 2.24: *Geometry of a model for a hole near an edge.* $D = 30\,\text{mm}$, $l_y, s = 350\,\text{mm}$ *and* $l_z = 19\,\text{mm}$

The plot in Figure 2.25 shows $\hat{\sigma}_{rc}^{min}$ as a function of the specimen width, l_x, for different values of $l_{y,e}$. It is shown in Paper III that the variation of σ_{rc}^{min} with far-field stress σ_∞ is linear and it is therefore possible to determine the residual stress state for a relatively wide range of σ_∞ . The stresses in Figure 2.25 are therefore normalised with σ_∞ .

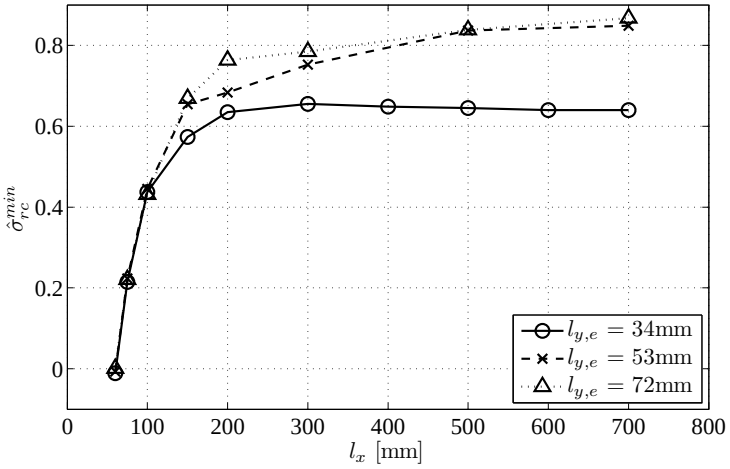

Figure 2.25: *Variation of* l_x *for three values of* $l_{y,e}$*. The far-field stress used for normalising the plot is* $\sigma_\infty = 83\,\text{MPa}$.

The graphs in Figure 2.26 show the results for a variation in the distance from the hole to the edge ($l_{y,e}$) for two different widths of the panel (l_x).

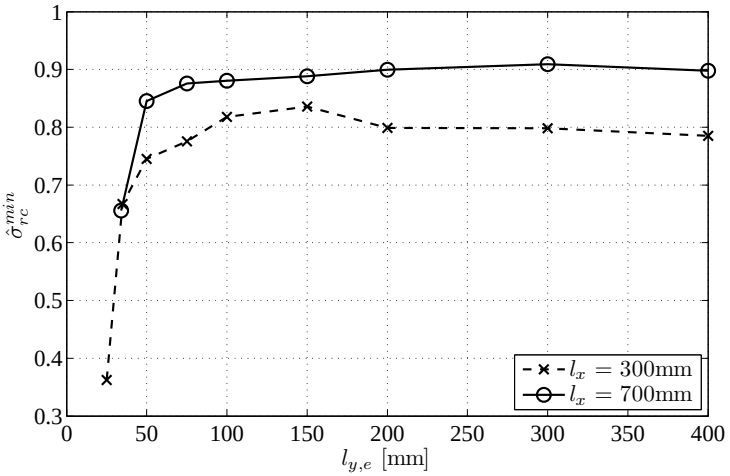

Figure 2.26: *Variation of $l_{y,e}$ for two values of l_x. The far-field stress used for normalising the plot is $\sigma_\infty = 83$ MPa.*

From Figure 2.26 it is seen that for $l_{y,e} > 100$ mm the effect of $l_{y,e}$ is vanishing; however, the width of the panel might still be important. In general, the apparent strength of a glass panel is dependent on the geometry and the location of holes.

In Paper III geometries with a hole approaching a corner and two holes in different positions were investigated. From these investigations relations between distances and $\hat{\sigma}_{rc}^{min}$ were derived, see Table 2.5 and Table 2.6. These tables can be used for estimating the reduction in apparent strength for a given geometry. The only guidelines available for edge distances are provided by EN12150-1 (2004) and do not state anything about strength reduction. For the designing engineer, tables like Table 2.5 and Table 2.6 provide much more freedom in the design than the distances specified in Eurocode. It should be noted that the * in the tables, indicates a value not covered by EN12150-1.

$\hat{\sigma}_{rc}^{min}$	$l_{e,min1}$ [mm]	$l_{e,min2}$ [mm]	$l_{xy,min}$ [mm]
0.90	350	200	400
0.85	350	53	250
0.80	150	100	170
0.75	150	53	150
0.65	75	53	90*

Table 2.5: *Reduction in apparent strength for a single hole.*

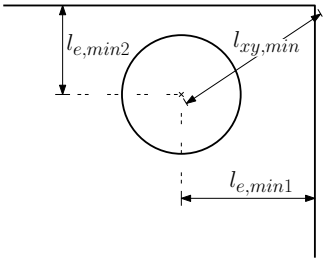

Figure 2.27: *Sketch of the measures in Table 2.5*

$\hat{\sigma}_{rc}^{min}$	l_h [mm]	$l_{e,min1}$ [mm]	$l_{e,min2}$ [mm]
0.90	150	350	350
0.85	130	350	53
0.85	130	53	350
0.80	90	350	53
0.80	90	53	350
0.75	75	350	53
0.75	75	53	350
0.60	50*	350	53

Table 2.6: *Reduction in apparent strength for two holes. The * indicates a value not covered by EN12150-1.*

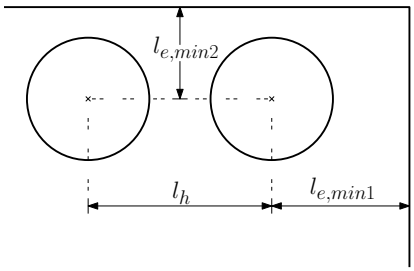

Figure 2.28: *Sketch of the measures in Table 2.6*

Table 2.5 and Table 2.6 are only guidelines for very specific dimensions and other combinations of the measures might provide similar results. In general it is recommended to use a numerical tool for the design considered if it is not covered in the tables above.

In general it is difficult to extract concise conclusions of general character for the influence from the geometry on the residual stress state at holes in tempered glass. However, the following provides the conclusions derived from the parametric investigation described in Paper III.

- Two phenomena seem to govern the magnitude of σ_{rc}^{min} : 1) The rate of cooling, 2) The structural stiffness (the amount of material available to carry stresses).

- The value of $\hat{\sigma}_{rc}^{min}$ converges towards 0.9 for a hole centrally located in a panel of infinite size.

- The value of σ_{rc}^{min} is primarily governed by the total size of the panel over the size of the hole.

- The lowest in-plane compressive residual stress at the hole, σ_{rc}^{min} , is always located along the mid-plane perimeter and is always less than 50 % of the corresponding stresses along the surface plane perimeter. However, the 50 % limit is only valid for 19 mm thick panels; in thinner panels the effect is less distinct.

- For hole geometries, the change in σ_{rc}^{min} is proportional to σ_∞ with an almost unique proportionality factor. This provides a possibility to easily obtain results for panels with a different far-field stress.

- Scaling of σ_{rc}^{min} with the geometry is not possible due to the complex tempering process. However, when scaling down the total geometry or the thickness alone, an increase in σ_{rc}^{min} is found for constant σ_∞ .

The parametric study in Paper III considers 19 mm thick specimens primarily. It is shown that a simple scaling of the geometry is impossible. A numerical investigation on the geometric scaling might expand the use of the design graphs provided in Paper III. However, such an investigation is not given here.

Chapter 3

Pinned Joints - In-Plane Loaded

The previous chapter considers the residual stresses in tempered glass. Charts providing the lowest compressive residual stress at the hole for varying geometries were given. In this chapter, these results are applied in order to estimate the strength of an in-plane loaded pinned joint. This is done using the assumption that the strength of a pinned joint can be calculated by superpositioning the stresses arising from the tempering process and the external loading and then comparing with the inherent glass strength.

Investigations of the stresses arising at the hole in a pinned joint due to contact forces are carried out. These stresses are dependent on numerous parameters such as the material properties of the insert, the friction at the interfaces between pin/insert and insert/glass and the location relative to edges. An exploded view of a pinned joint with all typical components is seen in Figure 3.1.

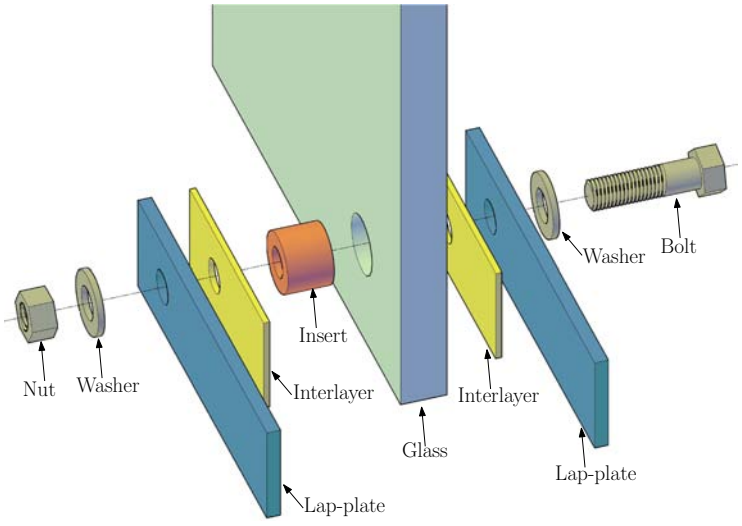

Figure 3.1: *Exploded view of the components in a typical pinned joint.*

3.1 Introduction to Pinned Joints

Due to the brittleness of glass, a relatively soft and ductile material should be used for the insert. The insert material therefore deforms relatively easily and absorbs rough parts of the hole surface, decreasing the local stress peaks. Furthermore, the stress concentration from small eccentricities and bending of the pin is lowered. According to Maniatis (2005) and Haldimann et al. (2008), typical materials used for insert are: Aluminium, Polyamide (PA), Polyoximethylen (POM), Ethylene propylene diene monomer (EPDM) and Polyether ether ketone (PEEK).

Many of these materials exhibit non-linear stress-strain behaviour and, furthermore, the contact behaviour between the parts is inherently non-linear, complicating the calculation of stresses further. Closed-form solutions are therefore rare, however, To et al. (2007) and To and He (2008) have derived solutions for a reinforced pinned joint. The practical use of these formulas, however, is dubious due to their complexity.

According to Haldimann et al. (2008), only a minor effect on the tensile stresses at the hole boundary is caused by the insert material. Maniatis (2006) experimentally investigated inserts of aluminium and POM and reported only small differences in the principal stresses near the hole. However, the numerical studies presented here show differently. The discrepancies might originate from the fact that the stresses cannot be measured experimentally at the boundary of the hole and that the effect is local.

Methods for estimating the stresses at the hole have been suggested by Fay (2001) and Feldmann et al. (2008). These methods are based on superposition of stress concentration factors from the literature (e.g. Pilkey, 1997). However, these approaches do neither include the effect of friction between the materials nor the stiffness properties of the insert. In the following, FEM models are used for investigating both geometric and material parameters.

3.2 Parametric Investigations

This section describes a 2D numerical study of some of the parameters affecting the maximum principal stress at the hole. The hole diameter, the material and interface properties are investigated in a large panel without any influence from the edges. The investigated parameters are:

- Elastic material parameters of the insert
- Friction between bolt/insert and insert/glass
- Ratio between hole diameter in glass and bolt diameter
  - Varying stiffness of the insert
- Hole-to-edge distance
  - Varying panel width

The models used for the parametric study can be subdivided into three groups. The first group is concerning the material of the inserts and the interface parameters. This group covers the first two bullets in the list above. The second group is considering the diameter of the glass hole compared to the diameter of the bolt and is covering the third bullet. The last group is concerning the distance from the hole to the edge and is covering the last bullet in the list.

The parameters varied within the different groups can be found in Table 3.1. In total more than 1400 models constitute the basis for the results and conclusions presented in the following.

Table 3.1: *Data for the parametric studies. The subscripts g, b and i refer to glass, bolt and insert, respectively.*

Parameter	*Material/Interface*	*Hole diameter*	*Hole-to-edge distance*
F, [kN]	120	60	120
E_g, [GPa]	70	70	70
E_b, [GPa]	210	210	210
E_i, [GPa]	[1,2,5,10,20,30,50,70,90]	[1,5,10,20,...,80]	1
ν_g	0.23	0.23	0.23
ν_b	0.30	0.30	0.30
ν_i	[0.30, 0.48]	0.3	0.48
μ_{ig}	[0.0,0.1,0.2,0.3,0.5]	0.2	0.0
μ_{bi}	[0.0,0.1,0.2,0.3,0.5]	0.2	0.0
l_x, [mm]	1550	1550	1550
$l_{x,e}$, [mm]	1025	1025	[50,60,...,960]
l_y, [mm]	2000	2000	[125, 250, 500, 1000, 2000]
D_g, [mm]	50	[25,26,...,80]	30
D_b, [mm]	20	20	20

See Figure 3.2 for the geometric measures.

Figure 3.2 shows an illustration where the geometric measures for the parametric investigations are defined. Due to symmetry, only half the joint is shown in the sketch.

In the following, the maximum tensile stress at the hole boundary is selected as the measure of interest for the different parameter variations mentioned above. It turns out that the force applied and this measure are (almost) linearly related and the results are therefore normalised with the force. In order to present the results as dimensionless, both the panel thickness, l_z, and the diameter of the bolt are used for the normalisation. This gives a measure, K_b, for the stress as defined in (3.1).

The stiffness of the insert is also normalised with the stiffness of the glass, and thereby we define the measure $E_{i,rel}$ as shown in (3.1).

$$K_b = \sigma_I \frac{D_b \cdot l_z}{F} \qquad \text{and} \qquad E_{i,rel} = \frac{E_i}{E_g} \tag{3.1}$$

Here σ_I is the maximum principal stress at the hole, D_b is the diameter of the bolt, l_z is the panel thickness, F is the load applied, E_i and E_g are the stiffness of the insert and

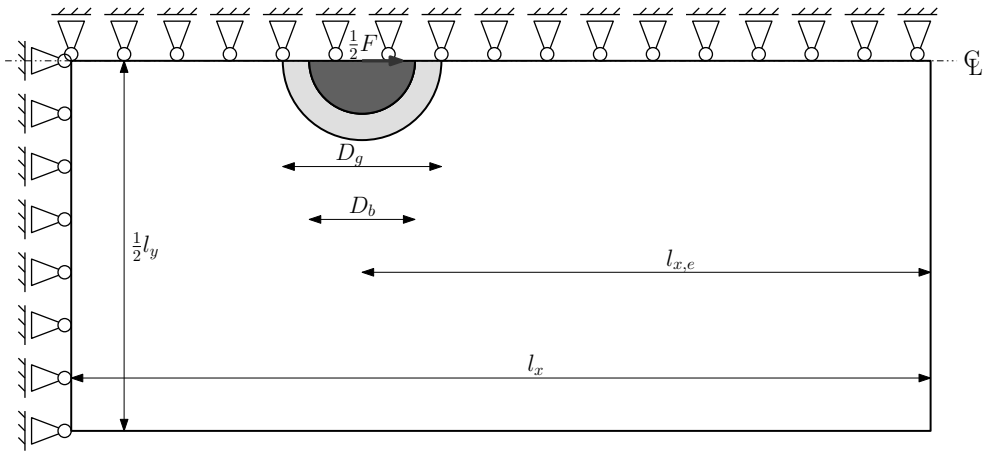

Figure 3.2: *Sketch of the geometry, support and load used for the parametric studies. Values for the measures and the forces are given in Table 3.1.*

the glass respectively.

3.2.1 FE-Model (Plane Stress)

Due to the inherently non-linear contact constrains, the modelling of the external loading can be a cumbersome process. In particular 3D models with relatively soft inserts and non-linear material behaviour are both difficult and time-consuming. An alternative approach is to assume plane stress, thereby neglecting the bending of the pin, the friction in the thickness direction and the compatibility conditions (see Section 3.4). This way it is possible to use 2D elements and computational costs are reduced significantly. Furthermore, the handling of contact is less complicated and convergency problems in ABAQUS are reduced considerably. In Section 3.4 a discussion on the plane stress assumption is given.

This section describes the FE-model used for the parameter study presented above. The commercial FE-software ABAQUS (v6.7 and v6.8) was used.

Three different models were used in the parametric studies. The first type covers the material and interface behaviour. The second covers a geometric variation of the hole diameter and the third investigates the influence from nearby edges.

The geometry for the material/interface study and the hole diameter study is chosen in such a way that doubling the distances to the edges yields a change in the stresses at the hole of less than 5 %.

The load applied is force-controlled by applying a concentrated force at the centre of the bolt as indicated in Figure 3.3. The elements used are LST (Linear Strain Triangles) for the glass and CST (Constant Strain Triangles) for the bolt and the insert. The high mesh density along the hole perimeter is needed for the results to converge. This is due to the fact that ABAQUS does not increase the integration order for the iso-parametric elements and thereby the integration becomes inaccurate.

The penalty method was used for modelling the contact behaviour. For the insert/glass interface, the glass was chosen as the master surface while the insert was chosen as the slave surface. For the bolt/insert interface, the bolt was chosen as the master surface and the insert as the slave surface.

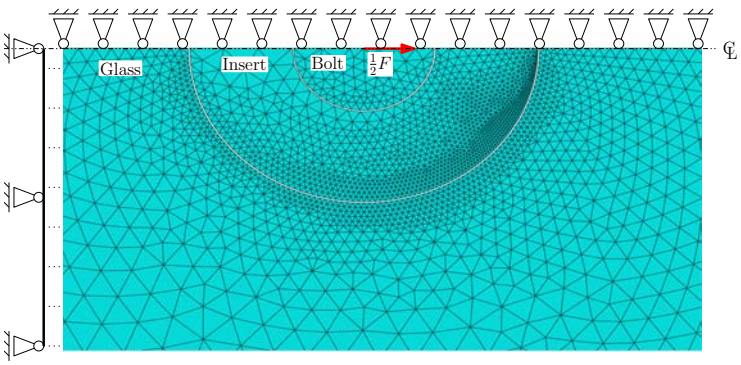

Figure 3.3: *Typical mesh for the parametric variations. The indicated supports are applied outside the figure as indicated by the space. Symmetry conditions are applied along the centre line.*

The material parameters, the loading and the geometries used for the models are given in Table 3.1.

3.2.2 Material and Interface

The parameters specified in Table 3.1 for the material/interface column were investigated. The investigations were carried out far enough from the edges to eliminate any interaction. The tensile stresses found at the hole were depending on all parameters and Figure 3.4 shows a band containing all the results. The curves for each material/interface variation can be found in Appendix B.

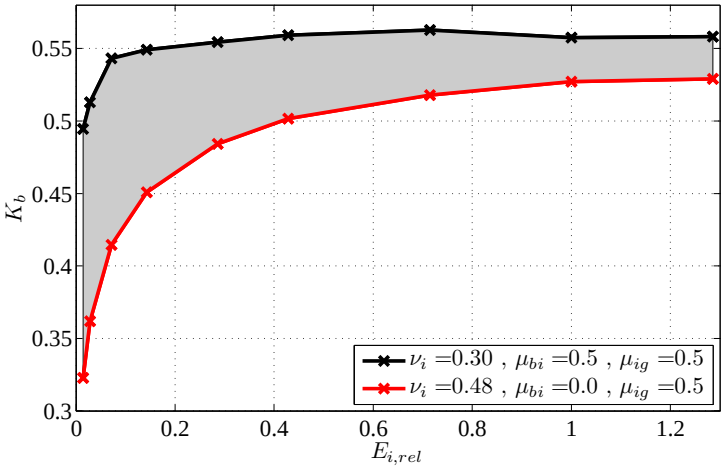

Figure 3.4: *Variation of K_b as a function of the insert stiffness for different values of ν_i, μ_{bi} and μ_{ig}.*

From Figure 3.4 it is seen that a high Poisson's ratio and low friction in the bolt/insert interface along with high friction at the insert/glass interface yield the lowest tensile stresses at the hole. The strength of a connection is therefore increased under these conditions. This indicates that gluing the insert to the glass is beneficial for the strength of the joint. To et al. (2007) describe a reinforced pinned joint where a steel ring is glued to the glass. Such an arrangement must be benefitting from the shear stresses transferred in the adhesive.

3.2.3 Glass Hole Diameter

In order to determine the influence of the diameter of the glass hole, a second investigation far from edges is carried out. In this investigation the diameter of the hole in the glass is varied and the outer diameter of the insert is adjusted accordingly. This investigation shows that the stresses are lowered with an increasing hole diameter.

Figure 3.5 shows the variation in K_b for varying ratios between the diameter of the hole in the glass, D_g, and the diameter of the bolt, D_b, for the two extreme material

combinations found in Figure 3.4. It is seen that for low ratios, $\frac{D_g}{D_b}$, a significant decrease in K_b is found for a small increase in the ratio. The plot shows an area representing all the investigations carried out. More detailed plots are given in Appendix B, where it is seen that for low ratios the effect of a soft insert material is highest. It is furthermore seen that this effect is rapidly vanishing for increasing insert stiffness.

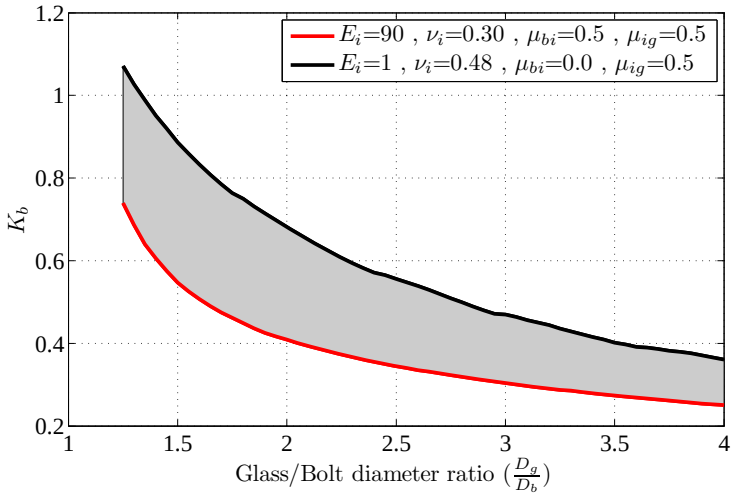

Figure 3.5: *Variation of the hole diameter.*

3.2.4 Hole-to-Edge Distance

Figure 3.6 shows the stress concentration factor for varying hole-to-edge distances and different panel widths, l_y. From the figure it is seen that if the hole is near the edge in the direction of the force ($l_{x,e}$ is low), high tensile stresses are present at the hole. This seems reasonable due to the fact that the resistance for deforming the hole is lower due to the nearness of the boundary (a low structural stiffness). The further decrease seen for the narrow panel ($l_y = 125\,\text{mm}$) when $l_{x,e}$ is approaching 1500mm can be explained by the more uniform stress state due to the short distance between the hole and the support. The wider panels are stiff enough for building up stress concentrations at the hole; however, this phenomenon is not of any practical interest.

From the figure it is seen that for $l_{x,e} < 200\,\text{mm}$ a considerable increase in the maximum stress is found.

In Eurocode (EN12150-1, 2004) the specified minimum allowable value for $l_{x,e}$ is given by

$$l_{x,e} \geq 2l_z + \frac{1}{2}D_g \tag{3.2}$$

From Figure 3.6 it is seen that even for thick panels, this specified distance yields a considerable increase in stresses. Furthermore, it must be noted that the panel thickness only yields a small influence on the tensile stresses arising at the hole boundary. Again

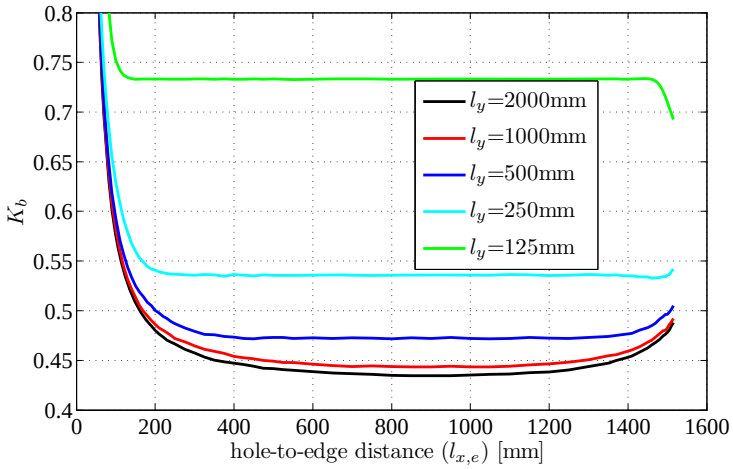

Figure 3.6: *Variation of hole-to-edge distance in* 1550 mm *long specimens with different widths, for* $\mu_i g = \mu_{bi} = 0.0$, $E_i = 1\,\text{GPa}$ *and* $\nu_i = 0.48$.

it is emphasised that applying Eurocode in the process of designing pinned joints will be insufficient.

Expanding the parametric studies might yield valuable charts for the designer. Isolating the effect from different parameters and thereby extending the method of stress concentration factors should be interesting. However, this is not further pursued in this work.

3.3 Examples

This section provides two examples on how to estimate the load capacity of a pinned joint in tempered glass. First the residual stresses at the hole are considered. Then the tensile stresses arising from the external load are found and compared to the residual stresses. As mentioned previously, the load capacity of these examples is also determined experimentally.

3.3.1 Experiments

The geometries for the two examples of in-plane loaded pinned joints are seen in Figure 3.7.

In order to verify the strength of the joints, 12 joints of each design were tested by applying an in-plane load until failure (Køppen and Munck, 2005). The average failure load determined for Example 1 and Example 2 respectively was 35 kN and 77 kN. Test results for all specimens are shown in Table 3.2.

In order to determine the strength of the hole, 12 panels of float glass with a hole were tested in pure tension. The failure stress was derived from the failure load and can be found in Table 3.2. An average failure stress of 46.1 MPa was found.

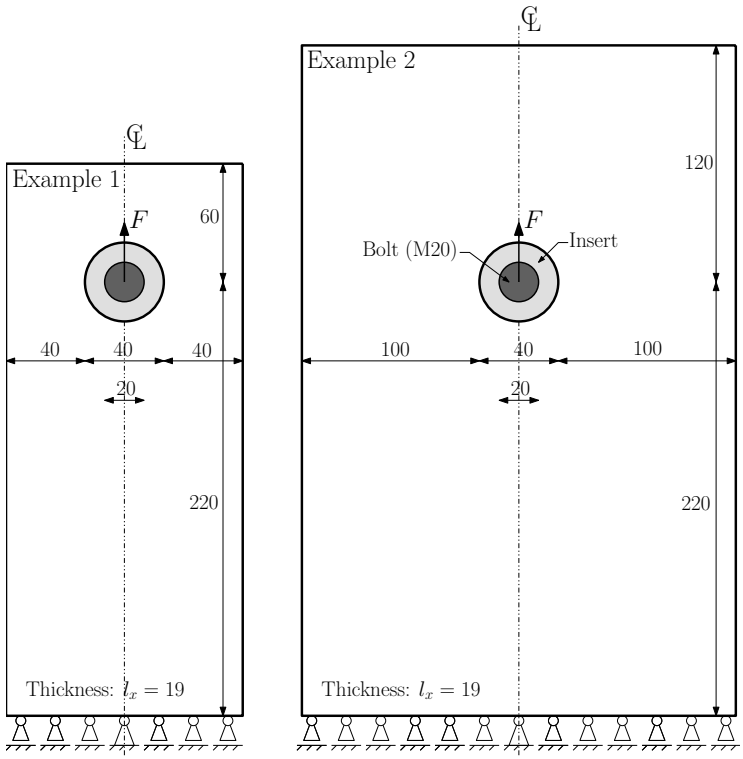

Figure 3.7: *Sketch of the two examples. All measures are in* mm.

The insert material is nylon and by experiments and inverse analysis Køppen and Munck (2005) find a bi-linear plastic stress-strain relation as given in Table 3.3.

However, the model utilised for the inverse analysis is not capable of modelling the sliding in the interfaces and therefore the estimated plastic material behaviour might be dubious. In spite of this, results utilising both a purely linear material behaviour and the bi-linear behaviour are given in the following.

Table 3.2: *Experimentally obtained failure loads for the examples and strengths for a hole in annealed glass (Køppen and Munck, 2005).*

Example 1				*Example 2*				*Hole in tension*			
No.	[kN]	*No.*	[kN]	*No.*	[kN]	*No.*	[kN]	*No.*	[MPa]	*No.*	[MPa]
1	40.2	7	43.0	1	75.3	7	75.6	1	54.5	7	38.7
2	42.4	8	32.0	2	82.7	8	74.9	2	57.6	8	34.5
3	27.6	9	35.2	3	80.4	9	79.3	3	49.3	9	45.5
4	25.4	10	38.3	4	75.5	10	68.7	4	41.1	10	51.4
5	31.4	11	40.2	5	76.3	11	73.5	5	51.3	11	45.9
6	33.1	12	30.8	6	83.0	12	80.7	6	44.4	12	39.2
Avg.		35.0			77.2				46.1		
Std. dev.		5.8			4.2				6.95		

Table 3.3: *Insert material behaviour - found by inverse analysis (Køppen and Munck, 2005).*

E [MPa]	ν	f_y [MPa]	E_{tan} [MPa]
900	0.40	48	85

f_y is the yield stress, E_{tan} is the slope of the hardening.

3.3.2 FE-Model (Plane Stress)

The geometries and boundary conditions for the two examples are given in Figure 3.7.

The models used for the examples are similar to the models used for the parametric variation (see Section 3.2.1). However, in the examples the insert was modelled both plastic and linear elastic using the material parameters described in Table 3.3. The plasticity model used was von Mises plasticity with isotropic hardening.

The friction was chosen to be 0.2 for both interfaces.

3.3.3 Strength Calculations

The procedure for determining the strength of a pinned connection in tempered glass can be divided into three major steps.

- Determine the highest principal stress originating from the external loading, σ_{ext}.
- Determine the lowest residual compressive stresses at the hole, σ_{rc}^{min} in order to estimate the apparent strength.
- Compare the residual stresses with the principal stresses from the external loading and thereby using the inherent strength as an extra safety.

This might be written as:

$$\begin{aligned} &\sigma_{rc}^{min} + \sigma_{ext} \leq f_{inherent} = f_{annealed} + f_{other} \quad , \quad f_{inherent} = 0 \\ &\sigma_{rc}^{min} + \sigma_{ext} \leq 0 \end{aligned} \tag{3.3}$$

where f_{other} is the strength originating from e.g. crack healing. Conservatively the material strengths are assumed zero, as shown in the second line of (3.3).

This section will follow the three steps above and discuss the results.

External Stresses

From Section 3.2 it is seen that the stresses arising at the hole are dependent on many different parameters. Design charts could be derived from analysis of the different parameters; however, the results presented in Section 3.2 are not extensive enough for deriving such charts. It is therefore necessary to model each joint and a description of the model used can be found in Section 3.3.2. The results from FE-models of the two examples are given in Table 3.4.

Table 3.4: *Applied load and corresponding maximum stresses at the hole for the two examples.*

Geometry	F [kN][a]	σ_{ext}^{plast} [MPa][b]	σ_{ext}^{elast} [MPa][c]
Example 1	35	81	88
Example 2	77	114	128

[a] Load, see Section 3.3.1. [b] Bi-linear plastic material behaviour for the insert. [c] Linear elastic material behaviour for the insert.

From the table it is seen that modelling the inserts with a plastic material behaviour yields lower tensile stresses than the corresponding linear elastic model. This is in accordance with the parametric study where it was seen that a soft insert material would lower the tensile stresses (Figure 3.4).

Residual Stresses

The results from a 3D FE-model of the tempering process for the specific geometry of the examples is given in Table 3.5. The results are compared with estimates obtained from the design charts given in Section 2.4. For the specimen in Example 1, Figure 2.25 was used with $l_x = 120\,\text{mm}$ and $l_{y,e} = 53\,\text{mm}$. The residual stress for Example 2 was estimated using Figure 2.26 with $l_{y,e} = 120\,\text{mm}$ and $l_x = 300\,\text{mm}$. The results and deviations from the exact model are given in Table 3.5. In spite of the differences in the geometries used

Table 3.5: *Residual stresses at the hole for the examples.*

Geometry	σ_{rc}^{min} [MPa][a]	σ_{rc}^{min} [MPa][b]	*Deviation* [%]
Example 1	49	46	6.1
Example 2	70	69	1.6

[a] Values obtained by a FE-model of the exact geometry.
[b] Values obtained from the graphs in Section 2.4.

for the design charts and the examples, the deviations of the residual stress estimates are low. In particular the residual stresses of Example 1 are difficult to read on the design chart due to the steep curve.

The residual stresses in the specimens used for the experiments were not measured and the estimate of the residual stresses is made from the FEM model using the assumption that the far-field stress was 83 MPa.

Superposition

The apparent strength used in design situations is often, conservatively, assumed to originate from the residual stresses alone (Haldimann et al., 2008). Applying this assumption yields a maximum allowable tensile stress of 49 MPa and 70 MPa for Example 1 and Example 2 respectively (Table 3.5).

From Table 3.4 it is seen that the plastic material model for the insert lowers the maximum tensile stresses at the hole approximately 10 % compared to the linear elastic behaviour.

In Table 3.6 the stresses originating from the load (plastic insert) and the residual stress are shown.

Table 3.6: *Residual stresses (based on* σ_∞ =83 MPa*) and external stresses.*

Geometry	σ_{rc}^{min} [MPa]	σ_{ext} [MPa]	*Difference* [MPa]
Example 1 (elastic)	49	88	39
Example 2 (elastic)	70	128	58
Example 1 (plastic)	49	81	32
Example 2 (plastic)	70	114	44

The difference between the values in the first two columns represents the estimated material strength and is shown in last column. From the hole-in-tension tests an average strength of a hole in float glass was found to be 46.1 MPa (see Section 3.3.1), which is similar to the difference calculated in Table 3.6. Such a comparison might be partly questionable due to the fact that the apparent strength of the tempered glass originates from both the material strength of the annealed glass, crack healing from the heating and the residual stress, see e.g. Haldimann et al. (2008).

Furthermore, the weakest point on the hole perimeter might not be coincident with the location of the maximum tensile stress originating from the external loading. These facts are also sources of uncertainties in the estimates of the load capacity of the joint. It is therefore in general recommended to compare the lowest compressive residual stress with the maximum principal stress at the hole, regardless of the location on the perimeter.

3.4 Plane Stress Versus Solid modelling

A 2D and a 3D example for an insert material with Poisson's ratio $\nu_i = 0.4$ and coefficients of friction equal to $\mu = \mu_{ig} = \mu_{bi} = 0.2$ were compared and it turned out that the 2D model yielded maximum principal stresses 7.7 % lower than the 3D model. This deviation can be ascribed to several parameters such as bending in the pin, friction in the thickness direction and the lack of fulfilling the compatibility condition when using plane stress elements.

The compatibility condition for plane stress can be written as

$$\frac{\partial^2 \varepsilon_x}{\partial y^2} + \frac{\partial^2 \varepsilon_y}{\partial x^2} = 2\frac{\partial^2 \gamma_{xy}}{\partial x \partial y} \tag{3.4}$$

$$\frac{\partial^2 \varepsilon_z}{\partial x^2} = \frac{\partial^2 \varepsilon_z}{\partial y^2} = \frac{\partial^2 \varepsilon_z}{\partial x \partial y} = 0 \tag{3.5}$$

where γ_{xy} is the shear strain. Using plane stress elements, ε_x, ε_y and γ_{xy} are determined and (3.4) can be fulfilled. However, ε_z is not determined and it is, in general, not possible to fulfill (3.5) unless the variation of $\sigma_x + \sigma_y$ is linear or constant.

This lack of fulfilment leads to an error. In Figure 3.8 solutions for an in-plane loaded panel with a hole are seen. The figure shows the stress as a ratio between the solution using solid elements (σ_{3D}) and the solution using the plane stress assumption (σ_{2D}).

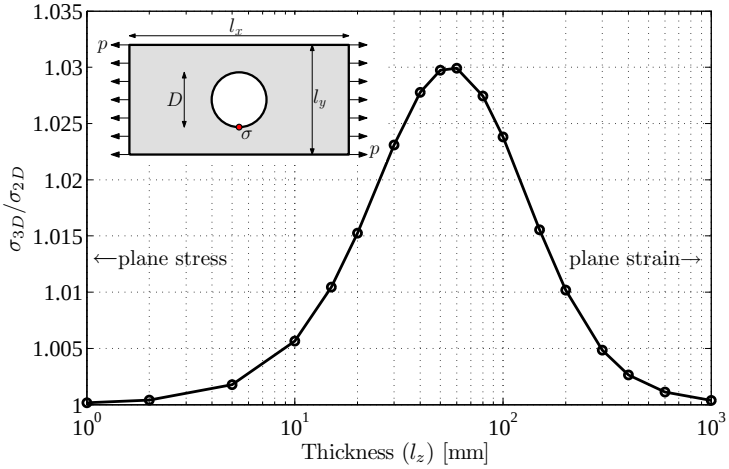

Figure 3.8: *Ratio between stresses obtained using plane stress elements and solid elements,* $l_x = 600\,\text{mm}$, $l_y = 300\,\text{mm}$ *and* $D = 50\,\text{mm}$.

From the figure it is seen that for very thin and very thick panels the solutions converge towards the plane stress solution. At a first glance it might seem odd that the solution converges towards plane stress for very thick specimens; however, the classical solution for the problem (using infinite panel size) is equal for both plane stress and plane strain (see e.g. Timoshenko and Goodier, 1970). It is also seen that the deviation for this particular problem can be 3 % depending on the thickness. This shows that part of the 7 % deviation mentioned before is due to the lack of fulfilment of the compatibility condition. This also indicates that for large panels the plane stress assumption is likely to improve further.

The elements used for the 3D models were 20-node brick elements for the bolt and insert and 15-node wedge elements for the glass, see Figure 3.9 for the mesh used. In order to avoid numerical problems due to the high-order elements, ABAQUS automatically uses a mid-face node on the contact elements, see e.g. ABAQUS (2008) and Jepsen and Svendsen (2006).

The geometries for the two models are given in Figure 3.7. Symmetry was utilised and thereby only 1/4 of the joint was modelled.

The loading was displacement-controlled by prescribing the movement of a single node on the bolt as indicated in Figure 3.9.

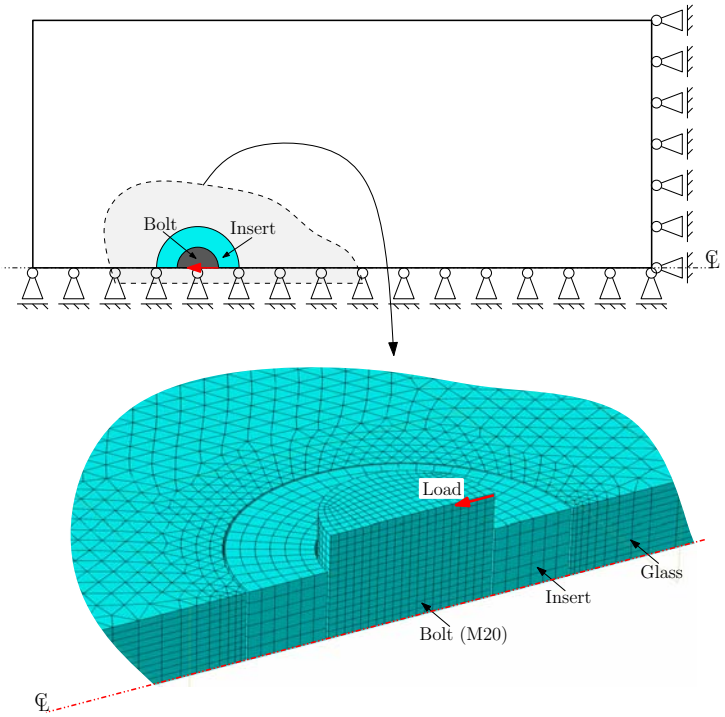

Figure 3.9: *Typical mesh for the two 3D models. The displacement load of the bolt is indicated by the red arrow. The indicated supports are applied outside the figure as indicated by the space. Symmetry conditions are applied on the face coincident with the centre line.*

Material and interface parameters are identical to the ones used for the models described in Section 3.3.2.

Chapter 4

Mechanically Reinforced Float Glass Beams

In the previous chapters, tempered glass has been considered and it has been demonstrated how the apparent strength can be increased. However, the tempering process does not introduce any ductility. The present chapter deals with the possibility of introducing a ductile behaviour in a transparent glass beam by reinforcement.

A principle sketch of such a beam layout is seen in Figure 4.1. It is seen from the sketch that such a reinforcement arrangement only slightly changes the appearance of the pure glass beam. Due to the complete fragmentation (and thereby loss of integrity) of tempered glass, float glass has been used for the beams considered. The use of tempered glass for reinforced glass beams has never been reported in the literature.

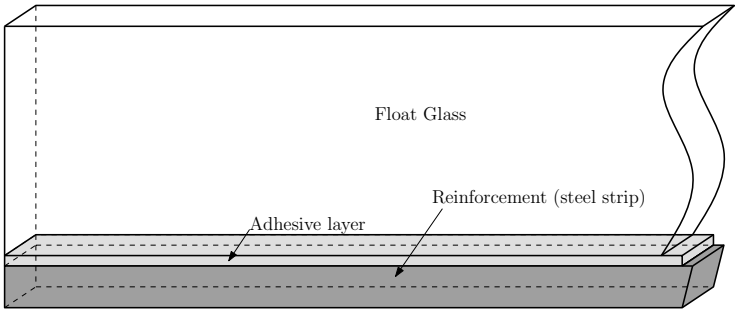

Figure 4.1: *Sketch of principal beam layout.*

Most of the research in this area has been done recently at TUDelft, where experimental research on reinforced glass beams was conducted (Bos et al., 2004; Louter et al., 2005; Louter and Veer, 2007). Studies on the adhesive behaviour were reported in Louter et al. (2007) and Louter and Veer (2008). Post tensioned reinforcement has also been reported; however, local breakage of the glass at the concentrated forces is a major problem with such a design (Louter et al., 2006). A glass-concrete composite has also been reported by Freytag (2004).

4.1 Mechanism and Failure Modes

The concept of the reinforced beam is that in case of glass failure, the reinforcement alone is carrying the tensile stresses. By a further increase in load the reinforcement starts yielding and a ductile behaviour of the beam is obtained, where the hardening of the reinforcement provides a further increase in load capacity. However, this is not the only failure mode and in Paper V four different modes are identified and associated with different degrees of reinforcement and anchorage capacity.

- *Anchorage:* The beam fails due to delamination of the adhesive before yielding of the reinforcement - i.e. failure of the adhesive.
- *Over-reinforced:* The reinforcement does not yield before crushing of the compression zone.
- *Normal-reinforced:* Yielding of the reinforcement begins after cracking of the glass and before failure of the compression zone.
- *Under-reinforced:* The reinforcement fails together with the glass and the maximum load capacity is the same as for the un-reinforced glass beam.

The failure modes are illustrated in Figure 4.2 for displacement-controlled loading.

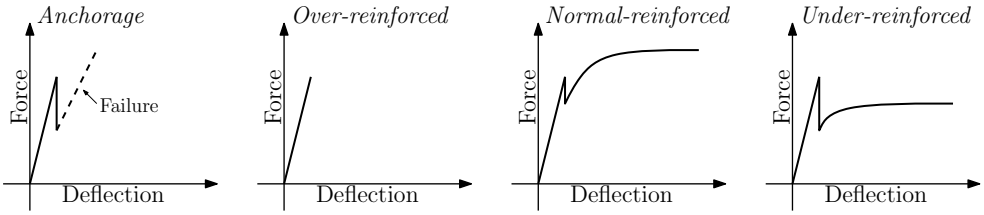

Figure 4.2: *The four different failure modes (displacement-controlled loading).*

From the conducted experiments reported in the literature, the over-reinforced beam failure with crushing of the glass in the compression zone has not been observed. This is possibly due to the high compressive strength of glass. The other three failure modes are more often found.

The failure mode depends on several parameters, such as the adhesive strength, the glass strength and the yield stress of the reinforcement. It is therefore obvious that a thorough knowledge of the material and interface behaviour is needed for estimating the load capacity and failure mode.

4.1.1 Design Formulas

This section presents design formulas for estimating the points where cracking of the glass occurs and the point of yielding in the reinforcement. The derivation of design formulas for estimating the beam behaviour in the "un-cracked state", the "cracked state" and the "yield state" is given in Appendix C.

Cracking of glass

The cross-section is treated as a composite, i.e. each part of the cross-section is weighted with its own stiffness relative to a chosen reference. The analysis is simplified by assuming zero thickness of the adhesive layer. It is assumed that the strain distribution is linear and that all materials behave linear elastically.

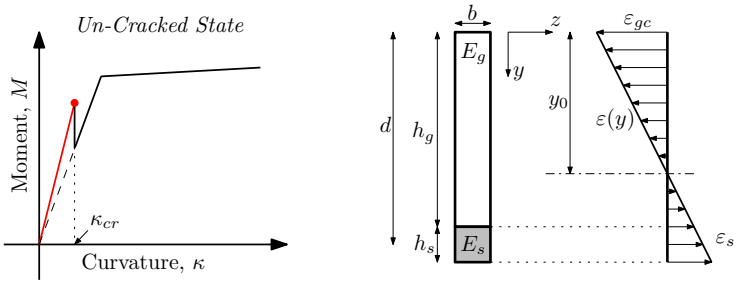

Figure 4.3: *Composite cross-section for the un-cracked state.*

Equation (4.1) can be used for estimating the curvature in the glass at fracture as indicated in Figure 4.3.

$$\kappa_{cr} = -\frac{f_{tg}}{E_g(y_0 - h_g)} \quad , \quad y_0 = \frac{S_t}{A_t} = \frac{h_g^2 + 2h_s d}{2\,(h_g + n h_s)} \tag{4.1}$$

where f_{tg} is the tensile strength of the glass, E_g is Young's modulus of the glass. From Figure 4.3, y_0 is seen to be the depth of the neutral axis and h_g is the height of the glass.

Yielding of Reinforcement

The cross-section is assumed to be partly cracked and it is furthermore assumed that no tensile stresses are transferred in the glass. Again the linear strain distribution is assumed; however, the force in the reinforcement is assumed to be located in the centre of the reinforcement in order to simplify the equations further.

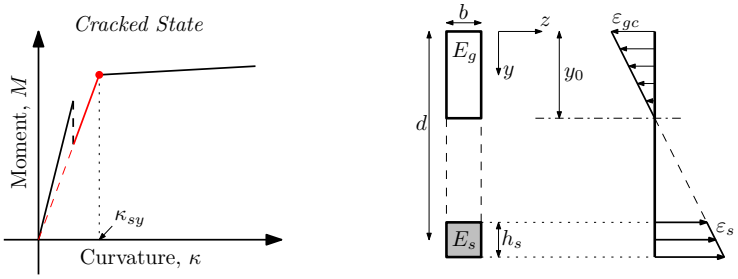

Figure 4.4: *Composite cross-section for the cracked and linear state.*

Figure 4.4 shows the cross-section and the point on the curve to be determined is marked with a red circle. In Appendix C formulas for the red curve are also derived.

$$\kappa_{sy} = \frac{f_y}{E_s\,(d - y_0)} \quad , \quad y_0 = nh_s\left(-1 + \sqrt{1 + \frac{2d}{nh_s}}\right) \tag{4.2}$$

where f_y is the yield stress of the reinforcement, E_s and E_g are Young's modulus of the reinforcement and glass respectively. The geometric parameters y_0, h_s and d are seen from Figure 4.4.

4.1.2 Anchorage Failure

A simple failure criterion for the adhesive is to specify a maximum shear stress. A modified Volkersen[1] formula for the adhesive layer is used for estimating the shear stresses under the assumption that all materials behave linear elastic, that the glass and reinforcement only deform in the longitudinal direction, and that the adhesive only deforms in pure shear.

Considering a cracked part of the beam (Figure 4.5), an equation for the shear stress in the adhesive can be derived (see Appendix C).

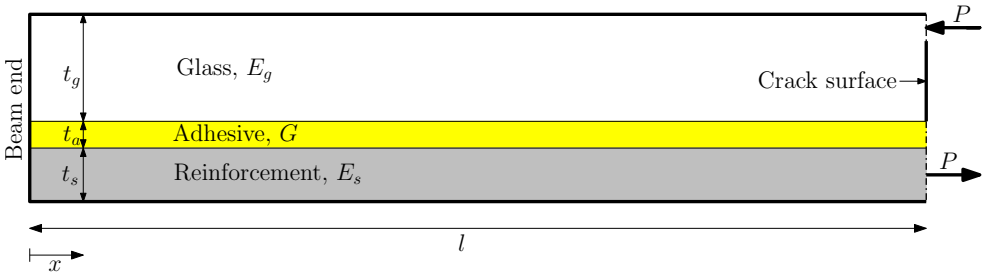

Figure 4.5: *Modified Volkersen analysis - Part of beam from crack to end.*

The maximum shear stress can be calculated from:

$$\tau_{max} = \omega P \coth(\omega l) \quad , \quad \omega = \sqrt{\frac{G}{t_a}\left(\frac{1}{E_g t_g} + \frac{1}{E_s t_s}\right)} \tag{4.3}$$

where l is the distance from the crack to the nearest beam end, G is the shear modulus of the adhesive, and E_g and E_s are Young's modulus of the glass and reinforcement respectively. The heights of the glass, adhesive and reinforcement are denoted t_g, t_a and t_s respectively.

It is seen from (4.3) that the distance to the beam end has to be estimated; however, the crack has to be located relatively close to the beam end before the influence is of any practical interest (see Appendix C).

The above formulas constitute the basics for designing a normal reinforced glass beam; however, only few experimental tests have been carried out in order to verify the formulas, see Paper VI.

[1] Volkersen (1938) derived an analytical expression for an adhesive single lap-joint.

4.2 Experiments

In Paper V experiments with four mechanically reinforced glass beams are reported. The dimensions for the beams are 1700 mm × 100 mm × 40 mm, where the adhesive and the steel strip have to be added to the height. The glass beam consists of 4×10 mm float glass panes laminated together. The beam layout, load and measurement setup is sketched in Figure 4.6 and more detailed information for each beam is given in Table 4.1.

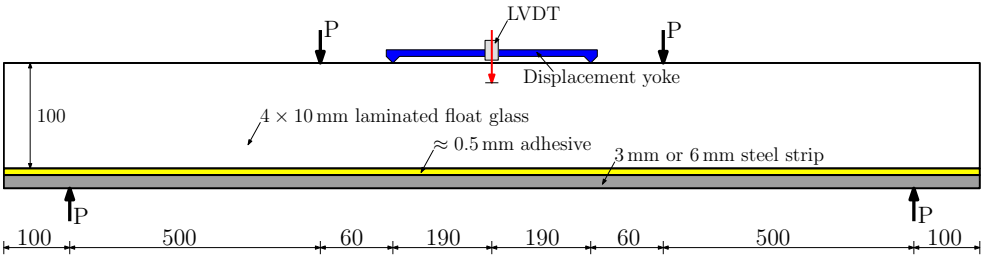

Figure 4.6: *Sketch of experimental setup (all measures in* mm*).*

Table 4.1: *Experimentally tested reinforced beams.*

	Beam 1	*Beam 2*	*Beam 3*	*Beam 4*
Length [mm]	1700	1700	1700	1700
Height (glass) [mm]	100	100	100	100
Thickness (glass) [mm]	40	40	40	40
Height (steel) [mm]	3	6	6	6
Yield stress (steel) [MPa]	330	390	390	390
Height (adhesive) [mm]	0.5	0.5	0.5	0.5
Stiffness (adhesive) [GPa]	2.4	2.4	2.4	2.4

The tests were displacement-controlled and the load-displacement curves are seen in Figure 4.7. It should be noted that the displacements on the graphs are the relative vertical measures between the LVDT[2] and the end of the displacement yoke (Figure 4.6).

Beam 1 demonstrates an extremely ductile behaviour with an increasing load[3] (Figure 4.9(b)). This behaviour indicates a normal-reinforcement of the beam. The other beams did not show any comparable ductility and the failure mode is characterised as anchorage failure. However, the ultimate load was considerably higher than the load at which the glass started cracking and thereby the beam displayed a warning before failure (Figure 4.9(a)).

It is seen that too much reinforcement reduces the ductility, which again emphasises the need for the design formulas presented above and numerical models as the one described in the following.

[2]Linear Voltage Displacement Transducer

[3]The test was stopped due to maximum travel of the test rig.

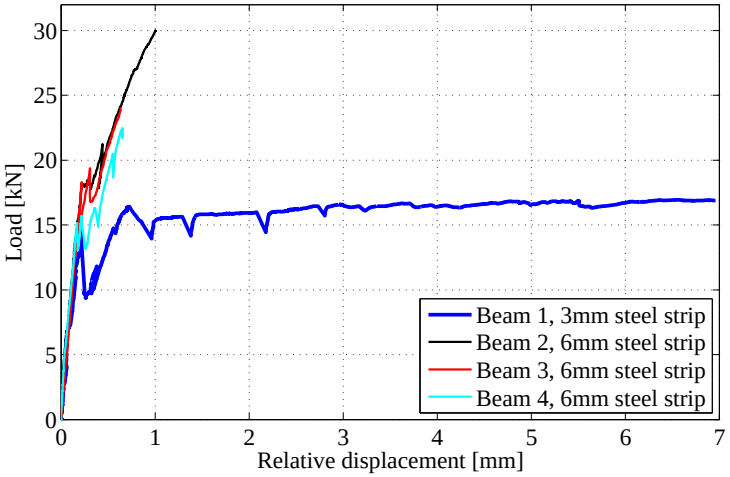

Figure 4.7: *Experimental load-displacement curves for reinforced float glass beams. Details for the beams can be found in Table 4.1.*

4.3 Modelling

In order to investigate other geometries and material parameters, a numerical model predicting the global behaviour is beneficial. A brief description of a simple modelling approach for the beam behaviour, including the cracking of glass, is given in the following. A more elaborate description is given in Paper V.

For the FE-model, plane stress was assumed and elements with a first-order displacement field were used.

4.3.1 Material Model

The adhesive layer was modelled as linear elastic using the stiffness provided by the manufacturer ($E = 2.4\,\text{GPa}$) and a Poisson's ratio of 0.4.

The steel strip was modelled using von Mises plasticity with isotropic hardening. The material data were found by inverse analysis on tensile tests of the steel.

The glass was modelled as linear elastic until fracture. The fracture criterion used in the model is based on the maximum principal strain, $\varepsilon_{I,cr}$, not the maximum principal stress, which is the most common criterion. The advantage of using the maximum principal strain is that information on the opening and closure of the crack is inherently available. Furthermore, for a beam in bending, the difference between the criteria is small. When the first principal strain exceeds $\varepsilon_{I,cr}$ the element containing that particular material point will lose its stiffness and the stress will be set to zero. Algorithm 1 shows a pseudocode of the material model just described.

Algorithm 1 Glass constitutive model

1: $\boldsymbol{D} = \boldsymbol{D}_g$
2: $\varepsilon_{I,cr} = f_{tg}/E_g$
3: $\varepsilon_I = 0.5(\varepsilon_{11} + \varepsilon_{22}) + \sqrt{0.5(\varepsilon_{11} - \varepsilon_{22})^2 + \varepsilon_{12}^2}$
4: **if** $\varepsilon_I \geq \varepsilon_{I,cr}$ **then**
5: $\quad \boldsymbol{D} = \boldsymbol{D}_{red}$
6: $\quad \boldsymbol{\sigma} = \boldsymbol{0}$
7: **end if**
8: $\boldsymbol{\sigma} = \boldsymbol{\sigma} + \boldsymbol{D}d\boldsymbol{\varepsilon}$

Here $\boldsymbol{\sigma} = \boldsymbol{D}\boldsymbol{\varepsilon}$ is the constitutive relationship for plane stress defined by:

$$\begin{bmatrix} \sigma_x \\ \sigma_y \\ \tau_{xy} \end{bmatrix} = \frac{E}{1-\nu^2} \begin{bmatrix} 1 & \nu & 0 \\ \nu & 1 & 0 \\ 0 & 0 & \frac{1-\nu}{2} \end{bmatrix} \begin{bmatrix} \varepsilon_x \\ \varepsilon_y \\ \gamma_{xy} \end{bmatrix} \tag{4.4}$$

4.3.2 Verification of Material Model

In order to initiate the cracking of the glass, the strength of some of the elements at the bottom face of the glass is reduced according to the strengths found from tests on similar reinforced glass beams. Reasonable results can also be obtained by just reducing the strength of a single element located at the bottom face of the glass in the centre. A random reduction of the elements along the bottom face also provides reasonable results (see e.g. Paper VI) and is more realistic considering the surface flaw distribution of the glass.

Six float glass beams with the same measures as specified in Table 4.1 but without any reinforcement were tested in order to find the strength of the glass. From the experiments the minimum, mean and maximum strengths were found, see Paper V. Applying these three values to the numerical model, the three curves along with the experimentally obtained results for the normal-reinforced beam are shown in Figure 4.8. It is seen that the numerical prediction of the global behaviour is reasonable.

In Figure 4.9 the reinforced glass beams are compared with a concrete beam and with the numerical model.

From Figure 4.9 it is seen that the crack patterns of the reinforced glass and the concrete beams are similar.

The crack pattern from the numerical model (Figure 4.9(d)) deviates from the experimentally obtained crack patterns (Figure 4.9(b)). This could be caused by the simple modelling approach. A more refined model, where the direction of the crack were taken into account, might provide a better crack pattern.

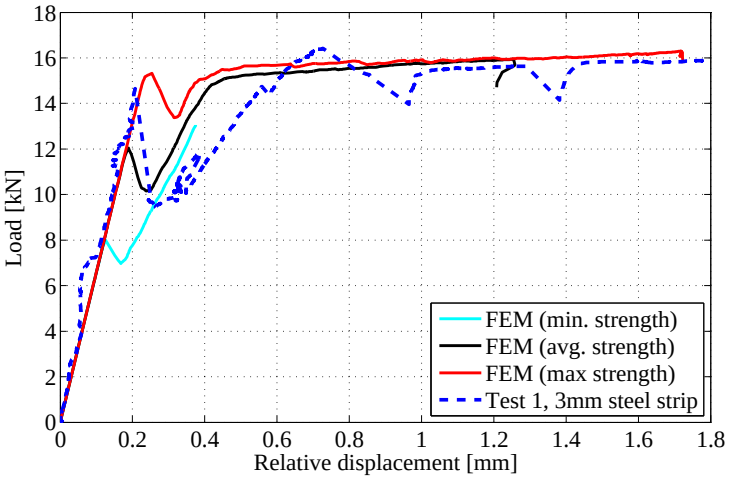

Figure 4.8: *Comparison of FE-modelling and experiments.*

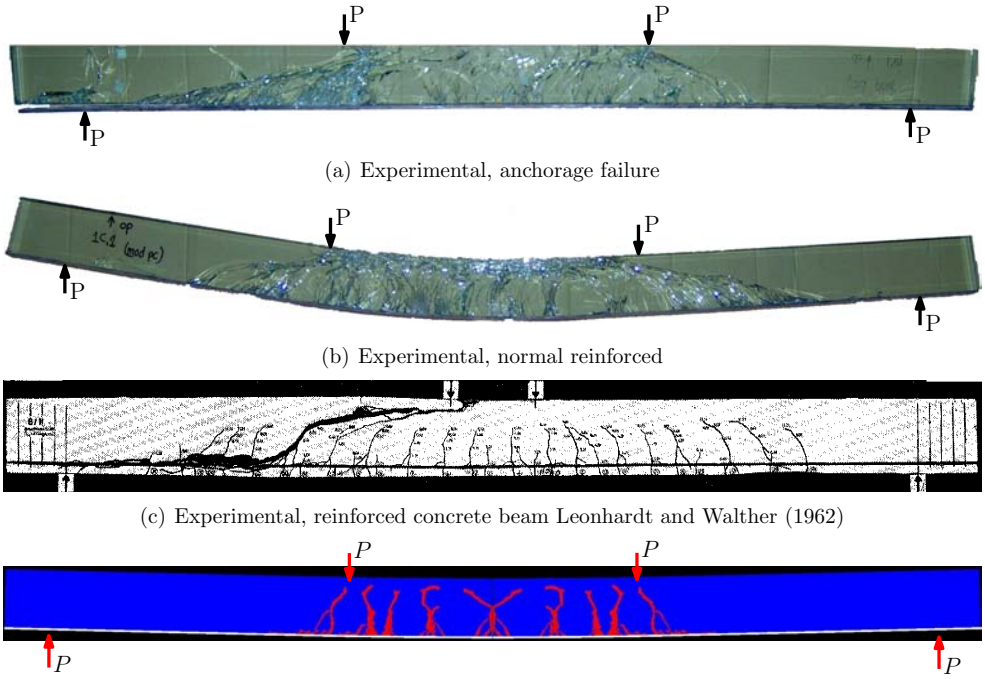

(a) Experimental, anchorage failure

(b) Experimental, normal reinforced

(c) Experimental, reinforced concrete beam Leonhardt and Walther (1962)

(d) Numerical model (results are mirrored about the symmetry line)

Figure 4.9: *Crack patterns from experiments on glass and concrete compared with the FE-model.*

4.4 Comments on Long-Term Behaviour

It is well known that most adhesives exhibit time-dependent behaviour. Therefore, dog-bone specimens of the adhesive (two-component epoxy) used for the beams were tested.

The test was conducted by loading and unloading the specimen stepwise. The results are plotted in Figure 4.10 along with the corresponding elastic response. From the graph, extensive creep is seen even for relatively low stress levels. Furthermore, the creep rate is dependent on the stress level, indicating a non-linear material behaviour. Other tests on the adhesives used are reported in Ølgaard et al. (2008a).

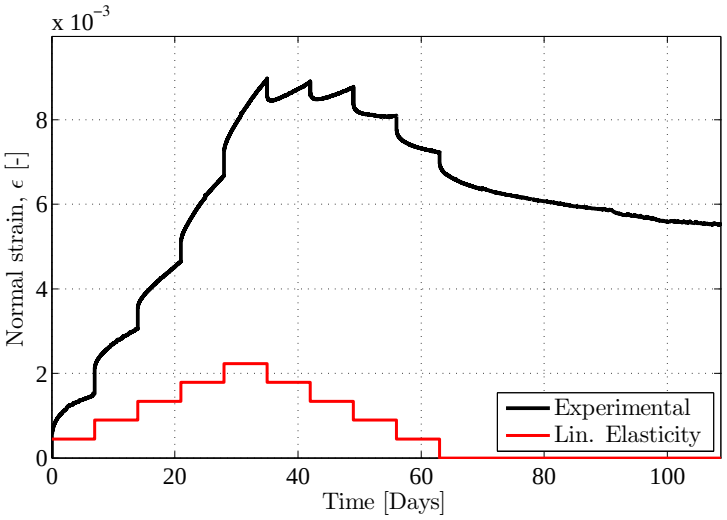

Figure 4.10: *Time-dependent behaviour of the adhesive, see e.g. Paper VI.*

Due to the extensive creep, the long-term strength of glass beams reinforced as shown in the preceding might be relatively low. This is caused by a reduction of transferred shear stresses by the adhesive along with a reduction of the strength of float glass over time. Therefore, the truly composite cross-section can only be considered for short-term loading.

Developing and investigating new design possibilities for reinforced glass beams is therefore important.

Interesting topics would be to incorporate tempered glass in the beams for carrying the long-term loading while the float glass keeps the integrity of the beam when cracked. Another possibility is to avoid using the adhesive and instead rely on transferring the force by means of bolts and contact pressure as sketched in Figure 4.11. In such a design tempered glass should be used and the results from Chapter 2 and Chapter 3 can be applied.

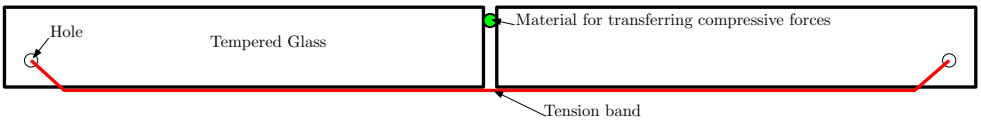

Figure 4.11: *Three-point reinforced glass beam.*

Chapter 5

Conclusion

The work within this thesis contributes to the use of in-plane loaded pinned joints in tempered glass. The strength of the tempered glass was investigated by photoelastic measurements and numerical simulations of the tempering process providing the residual stress state. The influence from nearby edges, corners and other holes on the residual stresses generated during the tempering process is given along with a parametric study of the stresses arising from the external loading of the pinned joint. The superposition of residual stresses, the material strength of float glass and the tensile stresses arising from the external load were used for estimating the strength of a given joint. This approach was verified by comparison with experimental data.

An experimental investigation of the residual stresses in commercially tempered glass revealed variations in the surface stresses of 35 MPa. Furthermore, the investigation showed a significant variation in the average residual surface stress with the thickness of the specimen. This variation is ascribed to an unadjusted tempering process, which is supported by numerical simulations of the tempering process.

The measurements were compared to the results of a fragmentation test and it was shown that the fragmentation test was dubious and unable to reveal local variations in the residual stress state. It must be concluded that classifying tempered glass for structural use on basis of a fragmentation test may be inaccurate and in the worst case unsafe.

Investigations on the fragmentation process were carried out using high-speed cameras for capturing the fragmentation. The fragments were also analysed in order to estimate the local crack directions. From these studies the in-plane shape of the fragmentation front was determined and a hypothesis on how the fragmentation is developed locally was given. Furthermore, the fragmentation velocity was accurately determined to be 1466 m/s and the so-called whirl-fragments were defined and discussed.

A state-of-the-art numerical model for the tempering process was established. Utilising the model, charts for estimating the cooling rate in order to obtain equal residual stresses for different thicknesses in tempered glass was derived.

Furthermore, the model was used for a parametric study on the residual stresses at holes. It was concluded that the lowest compressive residual stress was found on the perimeter of the hole in the panel mid-plane. It was concluded, on basis of the parametric study, that the residual stress state at the hole was governed by the cooling rate and the structural stiffness for carrying the stresses. Design tables providing measures and

minimum values for the compressive residual stresses at the holes were derived from the investigation.

For in-plane loaded pinned joints in tempered glass, a parametric investigation on the maximum principal stresses was carried out. The parametric study showed a significant difference in the residual stresses for different properties of the insert. The optimal insert material would have a relatively low stiffness and a high Poisson's ratio, while the coefficients of friction in the glass/insert and insert/bolt interfaces should be high and low respectively. Examples on how the strength of in-plane loaded pinned joints could be estimated from the FE-model and design charts for the residual stresses were given and compared to experiments.

The concept of reinforcing float glass beams was explored in order to improve the ductility of structural members. It was found that by gluing a steel strip to the bottom face of the glass, a ductile behaviour could be achieved. Analytical design formulas and a simple FE-model were developed for predicting the behaviour of such a beam. Both analytical and numerical models were verified by experiments.

The adhesive used for the beams was tested and extensive creeping behaviour was found, even at low stress levels. This indicates an issue for long-term loading of such beams. Alternative designs were discussed and a design without the use of adhesives was suggested.

5.1 Recommendations for Future Work

There are several recommendations for future work within the described areas of research.

5.1.1 Tempered Glass

It is an important task to optimise the tempering process in order to increase the apparent strength and provide a more uniform residual stress state for all possible geometries of the glass panes. Thereby, tempered glass could be used for structural applications with a much higher safety.

In the process of achieving such knowledge, numerical simulations of the tempering process will provide a powerful tool for estimating the optimal cooling scheme.

5.1.2 Pinned Joints

The long-term behaviour of insert materials used for the pinned joints is an important aspect, since the stress distribution at the hole is likely to change if the insert material creeps. A very interesting topic would be to investigate different insert materials under long-term loading exposed to different humidity, temperature and sunlight conditions.

Extending the research done here to consider groups of bolts for building moment stiff structures is also an interesting option. The basic tools for such an investigation are given here in terms of a model for estimating the residual stresses when several holes are located closely.

Finally, the present work is only concerned with the strength of in-plane loaded pinned joints. The influence from out-of-plane loading should also be investigated.

5.1.3 Reinforced Glass Beams

Due to the time-dependent strength properties of float glass along with the creeping behaviour of the adhesives, there is a need for more thorough investigation of such beams. Furthermore, a new design of a glass beam using tempered glass and no adhesives (at least for the permanent loads) is suggested in the present work. More experimental and numerical work should be done in order to prove that concept.

Bibliography

ABAQUS. *Theory manual v6.8*. Simulia, 2008.

H. Aben and C. Guillemet. *Photoelasticity of Glass*. Springer-Verlag, 1993.

H. Aben, J. Anton, and A. Errapart. Modern photoelasticity for residual stress measurement in glass. *Strain*, 44(1):40–48, 2008. ISSN 00392103.

P. Acloque. High speed cinematographic study of the fracture process in toughened glass. In *Symposium on Mechanical Strength of Glass and Ways of Improving it*, pages 851–886, 1962. in french.

L.H. Adams and E.D. Williamson. The annealing of glass. *Journal of the Franklin Institute*, 190:597–632, 1920.

U. Ankergren and A. Bak-Jensen. Structural glazing exposed to fire. Master's thesis, Department of Civil Engineering, Technical University of Denmark, 2008.

J. Anton. *Scattered Light Polariscope SCALP-03 -Instruction manual*, 2006.

J. Anton and H. Aben. A compact scattered light polariscope for residual stress measurement in glass plates. In *Glass Processing Days*, 2003.

J.M. Barsom. Fracture of tempered glass. *Journal of the American Ceramic Society*, 51 (2):75–78, 1968.

G.M. Bartenev. The phenomenon of the hardening of glass. *Journal of Technical Physics*, 18, 1948. in russian.

T. Bernard, R. Gy, and L. Daudeville. Finite element computation of transient and residual stresses near holes in tempered glass plates. *19th International Congress on Glass*, pages 445–6, 2001. ISSN noissn1040459583.

F.P. Bos, F.A. Veer, G.J. Hobbelman, and P.C. Louter. Stainless steel reinforced and post-tensioned glass beams. In *ICEM12- 12th International Conference on Experimental Mechanics*, 2004.

M.P. Brungs and X.Y. Sugeng. Some solutions to the nickel sulphide problem in toughened glass. *Glass Technology*, 36(4):107–110, 1995. ISSN 00171050.

R. M. Christensen. *Theory of Viscoelasticity*. Dover, 2 ed. edition, 2003.

EN12150-1. *Glass in building - Thermally toughened soda lime silicate safety glass - part1: Definition and descriptions*, 11 2004.

EN572-2. *Glass in Building - Basic soda lime silica glass products - Part 2: Float glass.* CEN, 2004.

B. Fay. Designing glass holes for bearing: An approach from first principles adapted for the practising structural glass engineer. In *Glass Processing Days*, 2001.

M. Feldmann, M. Pilsl, and C.C. Segura. Strength of bearing connections in toughened glass plates for the structural use. *Stahlbau*, 77(1):17–25, 2008. ISSN 00389145.

L. B. Freund. *Dynamic fracture mechanics.* Cambridge University Press, 1990.

B. Freytag. Glass-concrete composite technology. *Structural Engineering International: Journal of the International Association for Bridge and Structural Engineering (IABSE)*, 14(2):111–117, 2004. ISSN 10168664.

M. Goland and E. Reissner. The stresses in cemented joints. *Journal of Applied Mechanics*, 11:A17–A27, 1944. ISSN noissn1188306090.

D. J. Green, R. Tandon, and V. M. Sglavo. Crack arrest and multiple cracking in glass through the use of designed residual stress profiles. *Science*, 283(5406):1295–1297 and 2896580, 1999. ISSN 00368075.

M. Haldimann, A. Luible, and M Overend. *Structural Use of Glass.* IABSE, 2008.

L.J. Hart-Smith. Adhesive-bonded single-lap joints. Technical report, NASA, 1973.

R. Hess. Material glass. *Structural Engineering International: Journal of the International Association for Bridge and Structural Engineering (IABSE)*, 14(2):76–79, 2004. ISSN 10168664.

D. Hull. *Fractography - Observing, Measuring and Interpreting Fracture Surface Topography.* Cambridge University press, 1999.

L. Jacob. A review of the nickel sulphide induced fracture in tempered glass. In *Glass processing days*, 2001.

L.K. Jepsen and M.N. Svendsen. Modelling contact - bolted joints in steel structures. Technical report, Technical University of Denmark, Department of Civil Engineering, 2006. in danish.

A. J. Kinloch, editor. *Developments in Adhesive - 2.* Applied Science Publishers, 1981.

K. Køppen and M. Munck. Bolted connections in toughened glass. Master's thesis, DTU, 2005.

E.H. Lee and T.G. Rogers. On generation of residual stresses in thermoviscoelastic bodies. *American Society of Mechanical Engineers – Transactions – Journal of Applied Mechanics*, 32(4):874–880, 1965.

F. Leonhardt and R. Walther. Shear tests of beams with and without shear reinforcement for determining maximum allowable shearing stresses. *Deutscher Ausschuss fuer Stahlbeton*, (151), 1962. ISSN noissn1191484888.

D. Lochegnies, E. Romero, J. Anton, A. Errapart, and H. Aben. Measurement of complete residual stress fields in tempered glass plates. In *Glass Processing Days*, 2005.

C. Louter and F. Veer. Experimental research on scale 1:4 models of an 18m reinforced glass beam, part i. In *Glass Performance Days*, 2007.

C. Louter and F. Veer. Redundancy of reinforced glass beams; temperature, moisture and time dependent behaviour of the adhesive bond. In *Challenging Glass*, 2008.

C. Louter, J. Belis, F. Bos, F. Veer, and G. Hobbelman. Reinforced glass cantilever beams. In *Glass Processing Days*, 2005.

C. Louter, J.F. van Heusden, J.N.J.A. Vambersky F. Veer, H.R. de Boer, and J. Versteegen. Post-tensioned glass beams. In *16th European Conference of Fracture*, 2006.

C. Louter, F. Veer, and G. Hobbelman. Reinforced glass, effects of reinforcement geometry and bonding technology. In *Glass Performance Days*, 2007.

I. Maniatis. *Numerical and Experimental Investigations on the stress Distribution of Bolted Glass Connections under In-Plane Loads*. PhD thesis, TU München, 2005.

I. Maniatis. Determination of the stress distribution of point positioned glazings for stresses in the disk plane. *VDI Berichte*, (1933):393–398, 2006. ISSN 00835560.

A. Markovsky and T.F. Soules. An efficient and stable algorithm for calculating fictive temperatures. *Journal of the American Ceramic Society*, 67(4):C56–C57, 1984. ISSN 00027820.

K. Morcant, A. Panait, M. Cossavella, and Q. He. Friction-grip bolted connections for structural glass elements: Practical solutions using an experimental and numerical coupled approach. In *Glass Processing Days*, 2005.

O.S. Narayanaswamy. A model of structural relaxation in glass. *Journal of the American Ceramic Society*, 54(10):491–8, 1971. ISSN 00027820.

O.S. Narayanaswamy. Evolution of glass tempering models. In *Glass Processing Days*, 2001.

R. Nijsse. Special steel and adhesively bonded connections for glass structures. *Structural Engineering International: Journal of the International Association for Bridge and Structural Engineering (IABSE)*, 14(2):104–106, 2004. ISSN 10168664.

A.B. Ølgaard, J.H. Nielsen, J.F. Olesen, and H. Stang. Properties of an adhesive for structural glass applications. In *Challenging Glass*, 2008a.

A.B. Ølgaard, J.H. Nielsen, J.F. Olesen, and H. Stang. Properties of an adhesive for structural glass applications. In *Challenging Glass*, 2008b.

W.D. Pilkey, editor. *Peterson's Stress Concentration Factors*. Wiley, 1997.

R. J. et al. Saunders. *Structural use of glass in buildings*. The Institutuion of Structural Engineers, 1999.

C. Schittich, G. Staib, D. Balkow, M. Schuler, and W. Sobek. *Glass Construction Manual*. Birkhäuser, 1999.

J. Schneider. Glass strength of annealed and tempered structural glass in the area of drilled holes. In *Glass Processing Days*, 2001.

J.E. Shelby. *Introduction to Glass Science and Technology*. The Royal Society of Chemistry, 2nd edition, 2005.

B. Siebert. *Beitrag zur Berechnung punktgehaltener Gläser*. PhD thesis, Technische Universität München, 2004.

K. Takahashi. Fast fracture in tempered glass. *Key Engineering Materials*, 166:9–18, 1999. ISSN 10139826.

S. P. Timoshenko and J. N. Goodier. *Theory of Elasticity*. McGraw - Hill, 3 edition, 1970. 567p, english.

Q.D. To and Q.-C. He. On the conforming contact problem in a reinforced pin-loaded structure with a non-zero second dundurs" constant. *International Journal of Solids and Structures*, 45(14-15):3935–3950, 2008. ISSN 00207683.

Q.D. To, Q.C. He, M. Cossavella, K. Morcant, and A. Panait. Closed-form solution for the contact problem of reinforced pin-loaded joints used in glass structures. *International Journal of Solids and Structures*, 44(11-12):3887–3903, 2007. ISSN 00207683.

A.Q. Tool. Relation between inelastic deformability and thermal expansion of glass in its annealing range. *Journal of the American Ceramic Society*, 29(9):240–253, 1946.

D. R. Uhlmann and N. J. Kreidl. *Glass Science and technology. 5: Elasticity and strength in glasses*. Academic Press, 1980.

J.R. Varner and H.J. Oel. Surface defects: their origin, characterization and effects on strength. *Journal of Non-Crystalline Solids*, 19:321–33, 1975. ISSN 00223093.

O. Volkersen. Die nietkraftverteilung in zugbeanspruchten nietverbindungen mit konstanten laschenguerschnitten. *Luftfahrtforschung*, 15(1):41–47, 1938. ISSN noissn1188306229.

Wikipedia. *http://en.wikipedia.org/*, December 2008. URL `http://en.wikipedia.org/wiki/Viscosity`.

E.H. Yoffe. The moving griffith crack. *Philosophical Magazine*, 42:739–750, 1951.

Appendix A

User-subroutine for ABAQUS

```
      SUBROUTINE UMAT(STRESS,STATEV,DDSDDE,SSE,SPD,SCD,
     1 RPL,DDSDDT,DRPLDE,DRPLDT,STRAN,DSTRAN,
     2 TIME,DTIME,TEMP,DTEMP,PREDEF,DPRED,MATERL,NDI,NSHR,NTENS,
     3 NSTATV,PROPS,NPROPS,COORDS,DROT,PNEWDT,CELENT,
     4 DFGRD0,DFGRD1,NOEL,NPT,KSLAY,KSPT,KSTEP,KINC)
!
      implicit double precision (a-h,o-z)
      parameter (j_sys_Dimension = 2); parameter( n_vec_Length = 544 )
      parameter( maxblk = n_vec_Length ); parameter(i_ipm_sta = -6)
      character*5 j_ipm_Error
      parameter(j_ipm_Error = "Error"); parameter(j_ipm_Aborted = 20)
!
      CHARACTER*80 MATERL
      DIMENSION STRESS(NTENS),STATEV(NSTATV),
     1 DDSDDE(NTENS,NTENS),DDSDDT(NTENS),DRPLDE(NTENS),
     2 STRAN(NTENS),DSTRAN(NTENS),TIME(2),PREDEF(1),DPRED(1),
     3 PROPS(NPROPS),COORDS(3),DROT(3,3),
     4 DFGRD0(3,3),DFGRD1(3,3)

      DOUBLE PRECISION G(6), lamG(6), K(7), lamK(7), M(6),
     1 lamM(6), x, alpg, alpl, HRg, TB, dRtime, depsth, depsK,
     2 depsG(NTENS), dSincG(NTENS,SIZE(G)), dSincK(SIZE(K)),
     3 dStotG(NTENS,SIZE(G)), dStotK(SIZE(K)), StotG(NTENS,SIZE(G)),
     4 StotK(SIZE(K)), A, B, f1G(SIZE(G)), f1K(SIZE(K)),
     5 f2G(SIZE(G)), f2K(SIZE(K)), phiM, Tf(2), Tfi(SIZE(M))

      Integer i, n, j, stNM

! ****************** Subroutine begins **********************
! *** Material Parameters
      G=(/1.5845D9, 2.3539D9, 3.4857D9, 6.5582D9, 8.2049D9, 6.4980D9/)
      lamG=(/6.658D-5, 1.197D-3, 15.14D-3, 167.2D-3, 749.7D-3, 3.292D0/)
      K=(/758.8D6, 765.0D6, 980.6D6, 7.301D9, 13.47D9, 10.9D9, 7.5D9/)
      lamK=(/5.009D-5, 9.945D-4, 2.022D-3, 1.925D-2, 1.199D-1,
```

```
35      1 2.033D0, 1D100/)
36       M=(/5.523D-2, 8.205D-2, 1.215D-1, 2.286D-1, 2.860D-1, 2.265D-1/)
37       lamM=(/5.965D-4, 1.077D-2, 1.362D-1, 1.505D-1, 6.747D0, 29.63D0/)
38       x=0.5D0
39
40       alpg = 9.1D-6  ! solid coeff. of expansion
41       alpl = 25.1D-6 ! Liquid coefficient of thermal expansion
42       HRg = 55000D0 ! H/Rg in the shift function
43       TB = 869D0 ! Reference temperature in K
44
45  ! *** Structural relaxation (Markovsky algorithm)
46       stNM = NTENS*SIZE(G)+SIZE(K)+1! place in STATEV where Tf starts
47       IF (TIME(2) .EQ. 0D0) THEN
48         STATEV(stNM:stNM+SIZE(M)+1)=TEMP
49       ELSE
50         Tf(1) = STATEV(stNM+SIZE(M)+1) ! Tf from previos step
51         phiM = DTIME*EXP(HRg*(1/TB-x/(TEMP)-(1-x)/(Tf(1))))
52         Tfi = (lamM*STATEV(stNM:stNM+SIZE(M))+TEMP*phiM)/(lamM+phiM)
53         Tf(2) = SUM(M*Tfi)
54         STATEV(stNM:stNM+SIZE(M))=Tfi
55         STATEV(stNM+SIZE(M)+1)=Tf(2)
56       ENDIF
57  ! *** Thermal strain increment
58       depsth = alpg*DTEMP+(alpl-alpg)*(Tf(2)-Tf(1))
59       dRtime = 0.5D0*DTIME*EXP(HRg/TB)*(EXP(-HRg/(TEMP+DTEMP))
60      1        +EXP(-HRg/TEMP))
61  ! *** deviatoric strain and hydrostatic strain increments
62       depsK = SUM(DSTRAN(1:NDI)-depsth) ! sums the direct strains, e11+e22+e33
63       depsG(1:NDI) = DSTRAN(1:NDI)-depsth-1D0/3D0*depsK ! deviatoric strains -
             diagonal terms
64       depsG(NDI+1:NTENS) = 0.5D0*DSTRAN(NDI+1:NTENS)      ! deviatoric strains
             - off-diagonal terms
65  ! *** Viscoelastic stress increments and decay of total stress
66       f1G = EXP(-dRtime/lamG)
67       f1K = EXP(-dRtime/lamK)
68       IF (dRtime<1D-7) THEN
69         f2G = 1D0-1D0/2D0*(dRtime/lamG)+1D0/6D0*(dRtime/lamG)**2D0
70         f2K = 1D0-1D0/2D0*(dRtime/lamK)+1D0/6D0*(dRtime/lamK)**2D0
71       ELSE
72         f2G = lamG/dRtime*(1D0-f1G)
73         f2K = lamK/dRtime*(1D0-f1K)
74       ENDIF
75       DO i=1, NTENS
76         DO n=1, SIZE(G)
77           dSincG(i,n)=2.0D0*G(n)*depsG(i)*f2G(n)
78           dStotG(i,n)= STATEV(n+(i-1)*SIZE(G))*f1G(n) ! decay of total
                 stresses (shear)
79         END DO
```

```
80        END DO
81        DO n=1, SIZE(K)
82          dSincK(n)=K(n)*depsK*f2K(n) ! Viscoelastic increment (Hydrostatic)
83          dStotK(n) = STATEV(NTENS*SIZE(G)+n)*f1K(n) ! decay of total stress
              (Hydrostatic)
84        END DO
85  ! *** Updating the stresses in each branch
86        StotG = dSincG+dStotG
87        StotK = dSincK+dStotK
88  ! *** Updating the state variables
89        DO i=1, NTENS
90          DO n=1, SIZE(G)
91            STATEV(n+(i-1)*SIZE(G))=StotG(i,n)
92          END DO
93        END DO
94        DO n=1, SIZE(K)
95          STATEV(NTENS*SIZE(G)+n)=StotK(n)
96        END DO
97  ! *** Calculating the total stress tensor
98        STRESS=SUM(StotG,2)
99        STRESS(1:NDI)=STRESS(1:NDI)+SUM(StotK)
100 ! *** Deriving the material tangent stiffness matrix
101       A = 2D0/3D0*SUM(G*f2G)  ! Terms for the instantanous constitutive matrix
102       B = SUM(K*f2K)
103 !      DDSDDE(:,:)=0D0
104       Do i=1,NDI            ! Generates the inst. const. matrix
105         Do j=1,NDI
106           DDSDDE(i,j)=-A+B    ! upper left 3x3 matrix = 1/3*(K-2G)
107         end do
108         DDSDDE(i,i)= DDSDDE(i,i) + 3D0*A     ! first 3 diagonal: K+4/3G
109         DDSDDE(i+NDI,i+NDI)=3D0/2D0*A          ! last 3 diagonal terms = G0
110       end do
111 ! *** Ending the subroutine
112       RETURN
113       END
```

Appendix B

Pinned Joints - Parametric Study

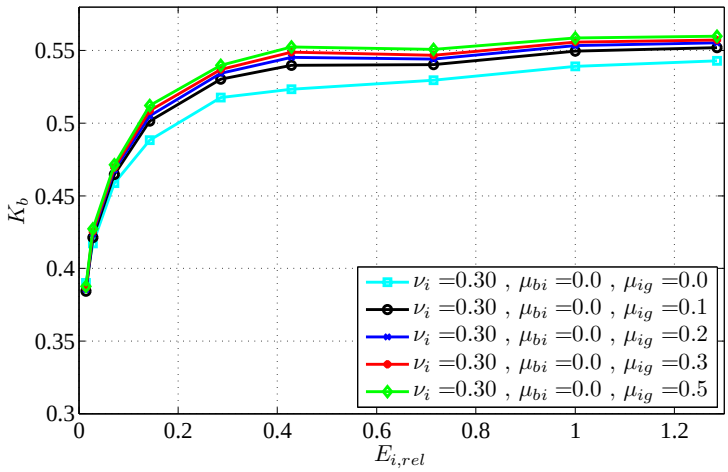

Figure B.1: *Stress concentration factor against relative stiffness of the insert.*

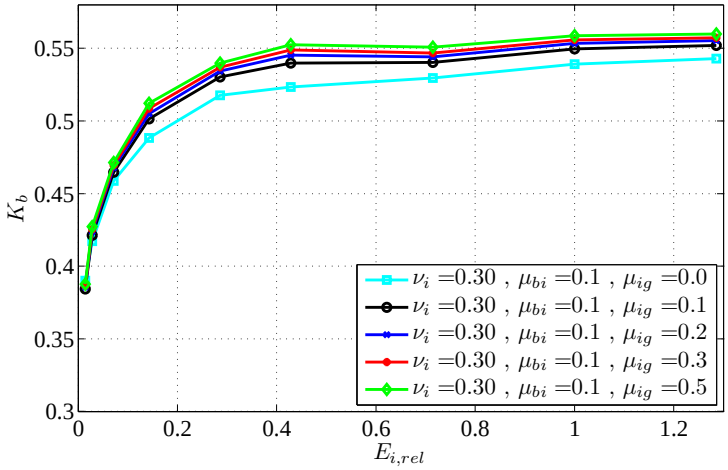

Figure B.2: *Stress concentration factor against relative stiffness of the insert.*

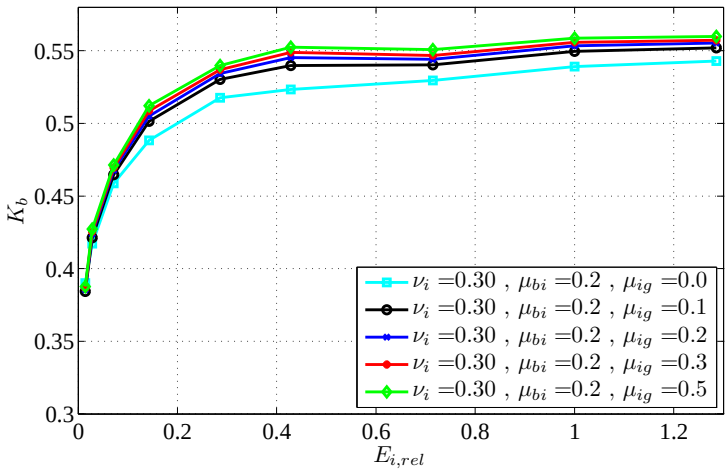

Figure B.3: *Stress concentration factor against relative stiffness of the insert.*

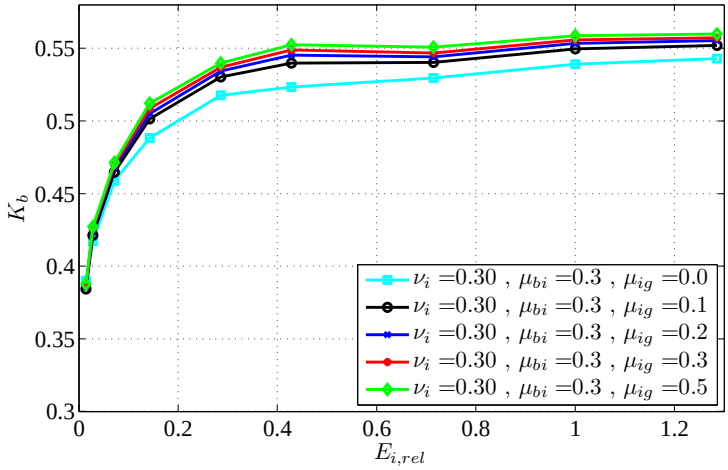

Figure B.4: *Stress concentration factor against relative stiffness of the insert.*

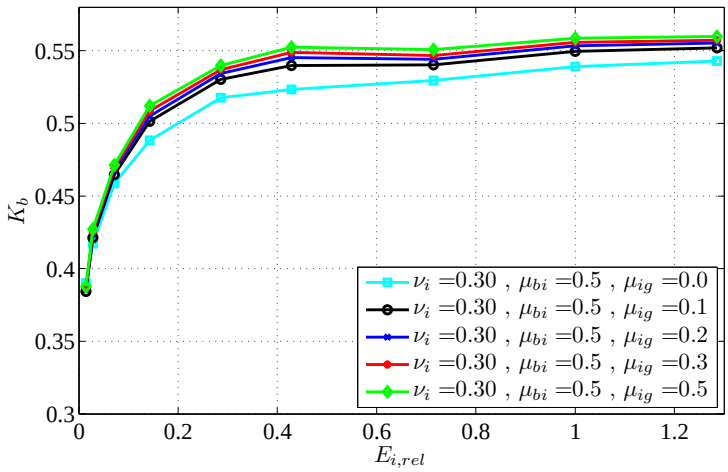

Figure B.5: *Stress concentration factor against relative stiffness of the insert.*

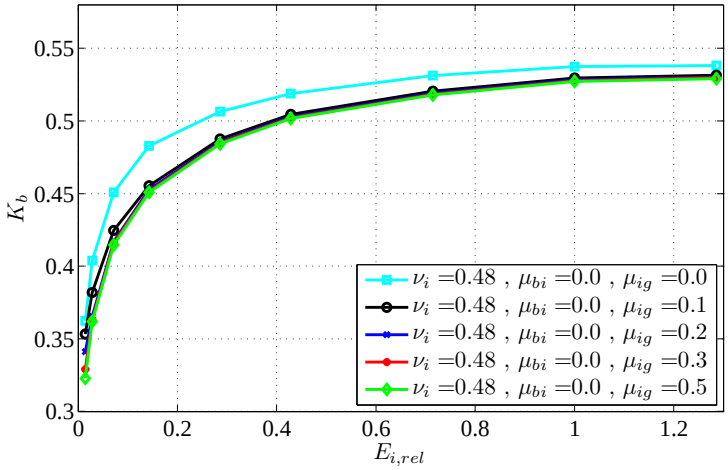

Figure B.6: *Stress concentration factor against relative stiffness of the insert.*

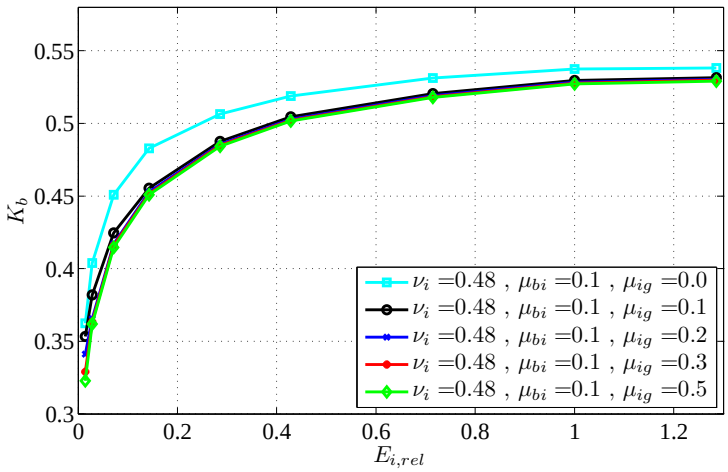

Figure B.7: *Stress concentration factor against relative stiffness of the insert.*

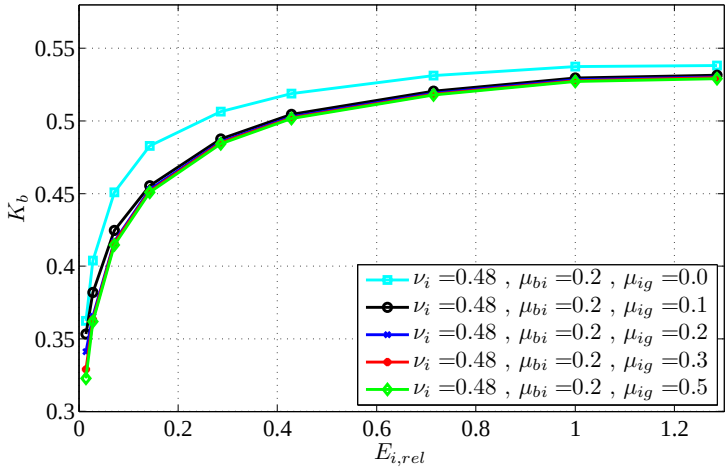

Figure B.8: *Stress concentration factor against relative stiffness of the insert.*

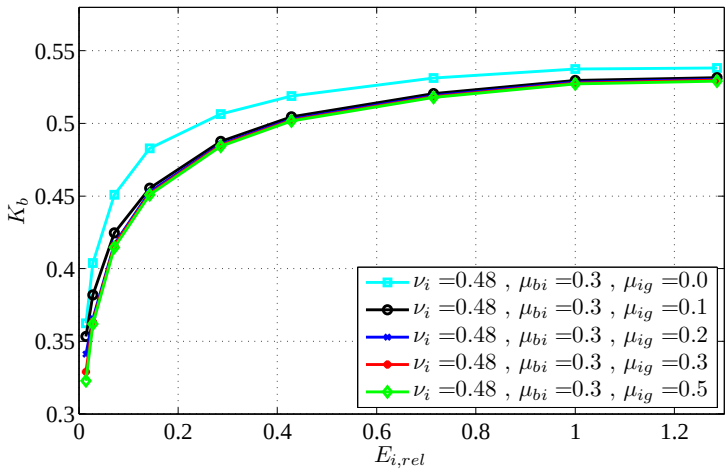

Figure B.9: *Stress concentration factor against relative stiffness of the insert.*

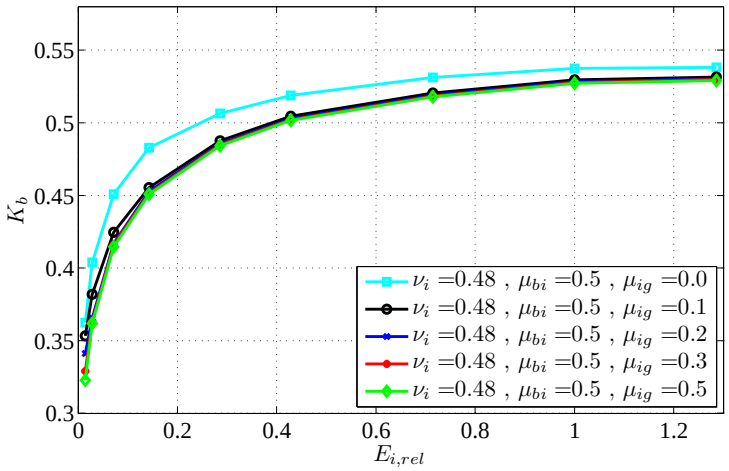

Figure B.10: *Stress concentration factor against relative stiffness of the insert.*

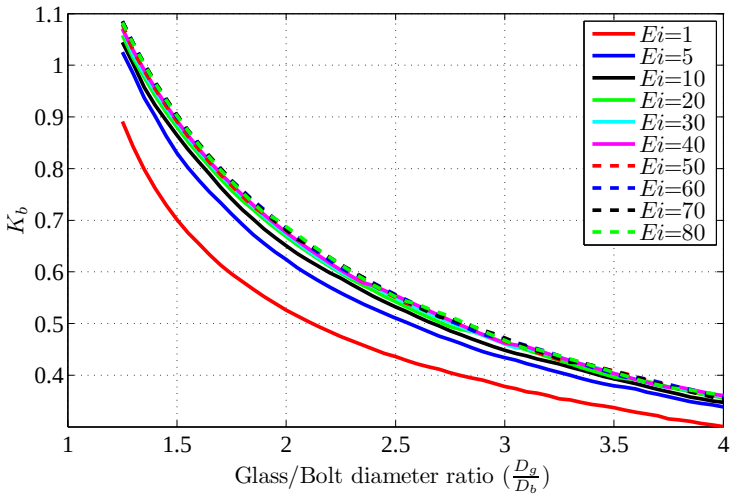

Figure B.11: *Variation of hole diameter in a large panel.*

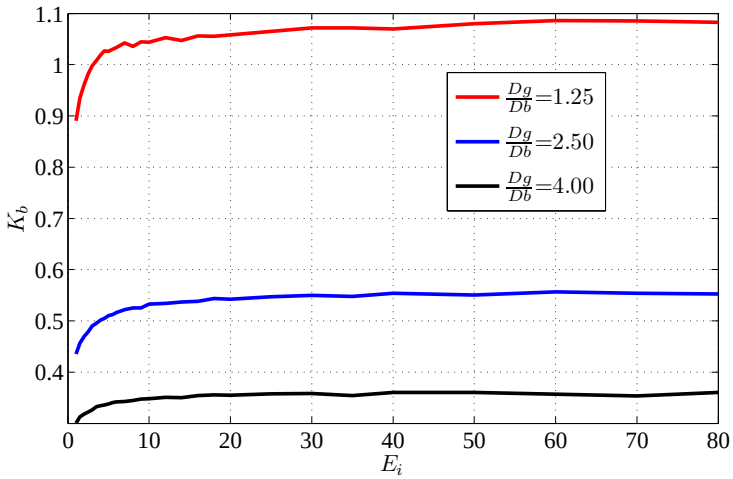

Figure B.12: *Influence of insert stiffness for different hole diameters.*

Appendix C

Derivation of Design Formulas for Reinforced Beams

In this appendix, the derivation of the design formulas from Chapter 4 is given.

Un-cracked State

The cross-section can be treated as a composite cross-section, i.e. each part of the cross-section is weighted with its own stiffness relative to a chosen reference. The analysis is simplified by assuming the adhesive layer as insignificant due to its small area and relatively low stiffness. It is assumed that the strain distribution is linear.

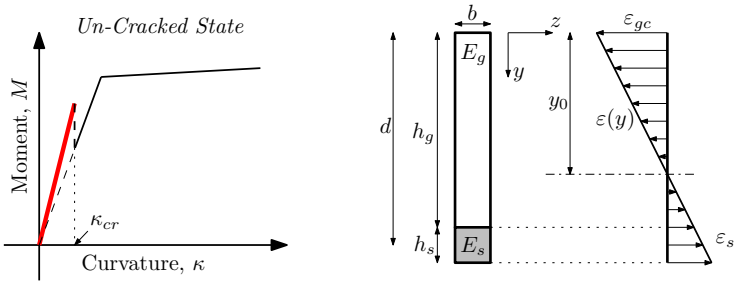

Figure C.1: *Composite cross-section for the un-cracked state.*

The formulas derived in this subsection can be used for estimating the red part of the curve shown in Figure C.1. The figure also shows the un-cracked composite cross-section.

The stiffness of the glass, E_g, is chosen to be the reference stiffness and the relative stiffness, n, of the reinforcement is:

$$n = \frac{E_s}{E_g} \tag{C.1}$$

The transformed cross-sectional area, A_t, is:

$$A_t = h_g b + n h_s b \tag{C.2}$$

The transformed static moment, S_t, is given by:

$$S_t = \frac{1}{2} h_g b h_g + n h_s b d = \frac{1}{2} b \left(h_g^2 + 2 n h_s d \right) \tag{C.3}$$

The depth of the neutral axis, y_0, can now be found:

$$y_0 = \frac{S_t}{A_t} = \frac{h_g^2 + 2 n h_s d}{2 \left(h_g + n h_s \right)} \tag{C.4}$$

The transformed moment of inertia is:

$$I_t = b h_g \left(\frac{1}{12} h_g^2 + (\frac{1}{2} h_g - y_0)^2 \right) + n b h_s \left(\frac{1}{12} h_s^2 + (d - y_0)^2 \right) \tag{C.5}$$

The curvature, κ_z, the strain distribution, $\varepsilon(y)$, and the moment, M, can now be found by the relation:

$$\kappa = \frac{M}{I_t E_g} = -\frac{\varepsilon(y)}{y_0 - y} \quad \Leftrightarrow \quad \varepsilon(y) = -\left(y_0 - y \right) \kappa \tag{C.6}$$

The formulas derived above are valid until cracking occurs, eg. $\varepsilon_g^{max} = \varepsilon(h_g) \leq \frac{f_{tg}}{E_g}$. The maximum curvature in the glass at fracture, κ_{cr}, can be found from:

$$\kappa_{cr} = -\frac{f_{tg}}{E_g (y_0 - h_g)} \tag{C.7}$$

Utilisation of the above formulas can provide estimates for the moment at which the glass is fracturing.

Cracked State - Linear Elastic

This subsection provides the equations for estimating the part of the moment-curvature curve marked with red in Figure C.2. The cross-section is assumed to be partly cracked and it is furthermore assumed that no tensile stresses are transferred in the glass. Again the linear strain distribution is assumed; however, the force in the reinforcement is assumed to be located in the centre of the reinforcement in order to simplify the equations further.

The depth of the neutral axis can be found from equilibrium and geometric considerations. The equilibrium equation becomes:

$$-\frac{1}{2} \varepsilon_{gc} y_{0,cr} b E_g + h_s b \varepsilon_s E_s = 0 \tag{C.8}$$

From geometric considerations it is found that $\varepsilon_s = \varepsilon_{gc} \left(\frac{d}{y_{0,cr}} - 1 \right)$ which can be substituted into (C.8), yielding a second order polynomial.

$$y_{0,cr}^2 + 2 n h_s y_{0,cr} - 2 n h_s d = 0 \quad , \quad n = \frac{E_s}{E_g} \tag{C.9}$$

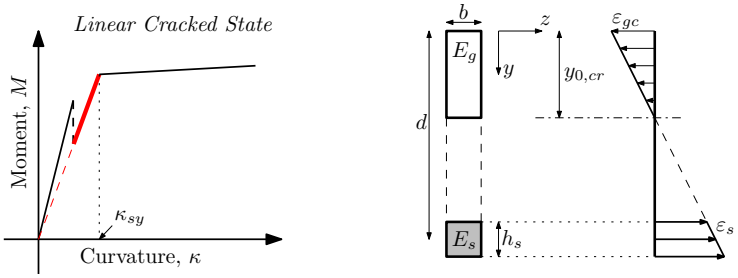

Figure C.2: *Composite cross-section for the cracked and linear state.*

The solution to this equation yields:

$$y_{0,cr} = nh_s\left(-1 \pm \sqrt{1+\frac{2d}{nh_s}}\right) \tag{C.10}$$

where only the positive solution is of interests.

The curvature moment relation is derived in the following:

$$M = h_s b E_s \varepsilon_s \left(d - \frac{1}{3}y_{0,cr}\right) \quad \Leftrightarrow \quad \varepsilon_s = \frac{M}{h_s b E_s \left(d - \frac{1}{3}y_{0,cr}\right)} \tag{C.11}$$

$$\kappa = \frac{\varepsilon_s}{d - y_{0,cr}} = \frac{M}{(d - y_{0,cr}) h_s b E_s \left(d - \frac{1}{3}y_{0,cr}\right)} \tag{C.12}$$

Substituting $\varepsilon_s = \varepsilon_{sy} = \frac{f_y}{Es}$ in the equation above the yield curvature, κ_{sy}, can be determined. Substituting κ_{cr} yields the point at which the load is dropping (if displacement control is assumed).

Cracked State - Yielding

The following formulas are covering the yield stage of the reinforcement as indicated with red in Figure C.3. Ideal plasticity of the reinforcement is assumed.

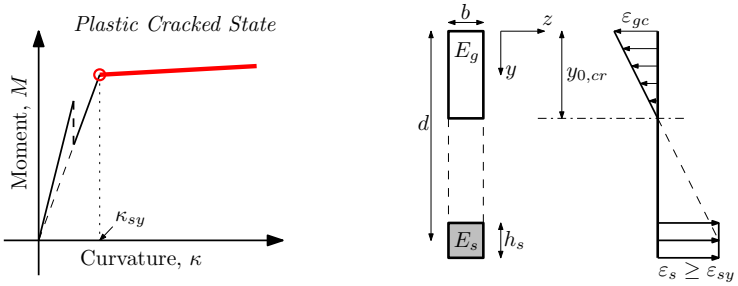

Figure C.3: *Composite cross-section for the cracked state with yielding in the reinforcement.*

Equilibrium:

$$h_s b f_y - \frac{1}{2} b y_{0,cr} \varepsilon_{gc} E_g = 0 \quad \Leftrightarrow \quad y_{0,cr} = \frac{2 h_s f_y}{\varepsilon_{gc} E_g} \tag{C.13}$$

From the geometric considerations and substitution of (C.13):

$$y_{0,cr} = \frac{\varepsilon_{gc}}{\varepsilon_{gc} + \varepsilon_s} d = \frac{2 h_s f_y}{\varepsilon_{gc} E_g} \tag{C.14}$$

By rearrangement the following second order polynomial can be found:

$$\varepsilon_{gc}^2 - k \varepsilon_{gc} - k \varepsilon_s = 0 \quad , \quad k = \frac{2 h_s f_y}{E_g d} \tag{C.15}$$

The solution is

$$\varepsilon_{gc} = \frac{1}{2} \left(k \pm \sqrt{k^2 + 4 k \varepsilon_s} \right) \tag{C.16}$$

Where only the positive value is of interest, yielding:

$$\varepsilon_{gc} = \frac{h_s f_y}{E_g d} \left(1 + \sqrt{1 + \frac{2 E_g d}{h_s f_y} \varepsilon_s} \right) \tag{C.17}$$

The moment can be written as a function of ε_s:

$$\begin{aligned} M(\varepsilon_s) &= b h_s f_y \left(d - \frac{1}{3} y_{0,cr} \right) = b h_s f_y \left(d - \frac{2 h_s f_y}{3 \varepsilon_{gc} E_g} \right) \\ &= b d h_s f_y \left(1 - \frac{2}{1 + \sqrt{1 + \frac{2 E_g d}{h_s f_y} \varepsilon_s}} \right) \end{aligned} \tag{C.18}$$

The initial yield moment (marked with a circle in Figure C.3) can be found by substituting $\varepsilon_s = \varepsilon_{sy} = \frac{f_y}{E_s}$ in (C.18). Due to different assumptions this yield point is not exactly equal with the estimate from (C.12).

Examples and experimental verification of the formulas given above can be found in Paper VI. It is show that the design formulas are able to estimate the behaviour of the beam very well. From the formulas given, it is possible to design the beam for being normal-reinforced; however, it should be noted that knowledge of the reinforcement yield stress and the tensile strength of the glass is needed.

Anchorage Failure

The above formulas does not consider anchorage failure. A simple failure criterion for the adhesive is to specify a maximum shear stress. A modified Volkersen[1] formula for the adhesive layer is derived in the following under the assumption that all materials behave linear elastic, that the steel and reinforcement only deform in the longitudinal direction and the adhesive only deforms in pure shear.

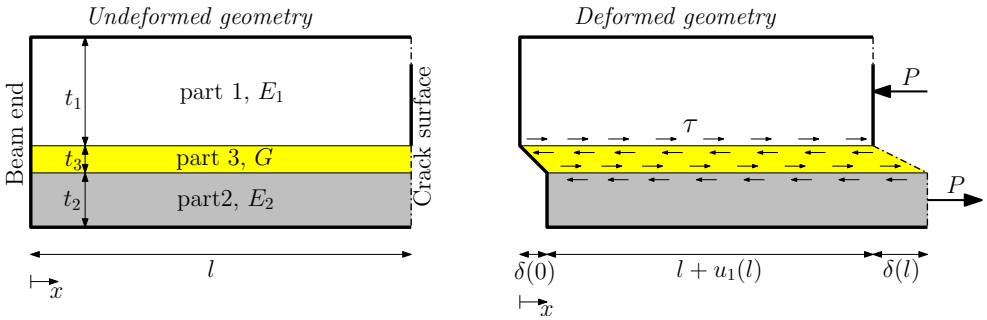

Figure C.4: *Modified Volkersen analysis - Part of beam from crack to end.*

Considering a cracked part of the beam (Figure C.4), an equation for the adhesive shear stress can be derived.

The shear deformation, $\delta(x)$, can be written as:

$$\delta(x) = \frac{t_3}{G}\tau(x) = u_2(x) - u_1(x) = \delta(0) + \int_0^x \varepsilon_2(\xi)d\xi - \int_0^x \varepsilon_1(\xi)d\xi \tag{C.19}$$

where u_1 and u_2 are the axial displacements in Part 1 and Part 2 respectively. The strains in Part 1 and Part 2 are denoted ε_1 and ε_2.

The normal force in the two parts (N_1 and N_2) can be found by equilibrium:

$$N_1(x) = -\int_0^x \tau(\eta)d\eta = -N_2(x) \tag{C.20}$$

From the normal force, the strains can be derived

$$\begin{aligned} \varepsilon_1(\xi) &= \frac{N_1(\xi)}{E_1 t_1} = -\frac{1}{E_1 t_1}\int_0^\xi \tau(\eta)d\eta \\ \varepsilon_2(\xi) &= \frac{N_2(\xi)}{E_2 t_2} = \frac{1}{E_2 t_2}\int_0^\xi \tau(\eta)d\eta \end{aligned} \tag{C.21}$$

Substituting (C.21) in (C.19) and rearranging yield:

$$\tau(x) = \frac{G}{t_3}\left[\delta(0) + \left(\frac{1}{E_1 t_1} - \frac{1}{E_2 t_2}\right)\int_0^x \int_0^\xi \tau(\eta)d\eta d\xi\right] \tag{C.22}$$

Differentiating twice yields

$$\tau(x)'' - \omega^2\tau = 0 \quad , \quad \omega^2 = \frac{G}{t_3}\left(\frac{1}{E_1 t_1} + \frac{1}{E_2 t_2}\right) \tag{C.23}$$

A general solution to such a second order differential equation can be written as:

$$\tau(x) = A\cosh(\omega x) + B\sinh(\omega x) \tag{C.24}$$

[1]Volkersen (1938) derived analytical expression for an adhesive single lap-joint.

Two boundary conditions are needed:

$$N_2(l) = P \tag{C.25}$$

$$u_1(l) + \delta(l) = \delta(0) + u_2(l) \tag{C.26}$$

Applying (C.25):

$$\begin{aligned} N_2(l) &= \int_0^l \tau(x)dx = \frac{A}{\omega}\sinh(\omega l) + \frac{B}{\omega}\left(\cosh(\omega l) - 1\right) = P \\ &\Updownarrow \\ A &= \frac{\omega P - B\left(\cosh(\omega l) - 1\right)}{\sinh(\omega l)} \end{aligned} \tag{C.27}$$

Applying (C.26) and utilising $\delta(x) = t_3\frac{\tau(x)}{G}$:

$$\begin{aligned} 0 &= u_1(l) + \delta(l) - \delta(0) - u_2(l) = u_1(l) - u_2(l) + t_3\frac{\tau(l)}{G} - t_3\frac{\tau(0)}{G} \\ &= \frac{\omega l t_3}{G}B \qquad \Rightarrow \qquad B = 0 \end{aligned} \tag{C.28}$$

Substituting $B = 0$ in (C.27) yields:

$$A = \frac{\omega P}{\sinh(\omega l)} \tag{C.29}$$

Substituting (C.29) into (C.24) yields:

$$\boxed{\tau(x) = \omega P\frac{\cosh(\omega x)}{\sinh\left(\omega l\right)} \quad , \quad \omega = \sqrt{\frac{G}{t_3}\left(\frac{1}{E_1 t_1} + \frac{1}{E_2 t_2}\right)}} \tag{C.30}$$

The equation above can be used for estimating the maximum elastic shear stress in the adhesive layer, τ_{max}, which is located at the crack ($x = l$):

$$\tau_{max} = \tau(l) = \omega P\coth(\omega l) \tag{C.31}$$

The shear stress distribution estimated from (C.30) for a given beam with four different thicknesses of the reinforcement is shown in Figure C.5. From this plot it is clearly seen that the maximum shear stress is found where the glass is cracked (at $x = l$).

Plotting τ_{max} at yielding in the steel as a function of the edge-to-crack distance, l, it is seen that the influence from the edge is only pronounced for relatively short distances, see Figure C.6. From the figure it is seen that for the specified layout the height of the steel strip should not exceed 2 mm, assuming an adhesive shear strength of about 30 MPa. However, the adhesive is likely to be able to redistribute the stresses by plastic deformations and thereby the estimates by (C.30) should be conservative.

The above formulas constitute the basics for designing a normal reinforced glass beam; however, only few experimental tests have been carried out in order to verify the formulas, see Paper VI.

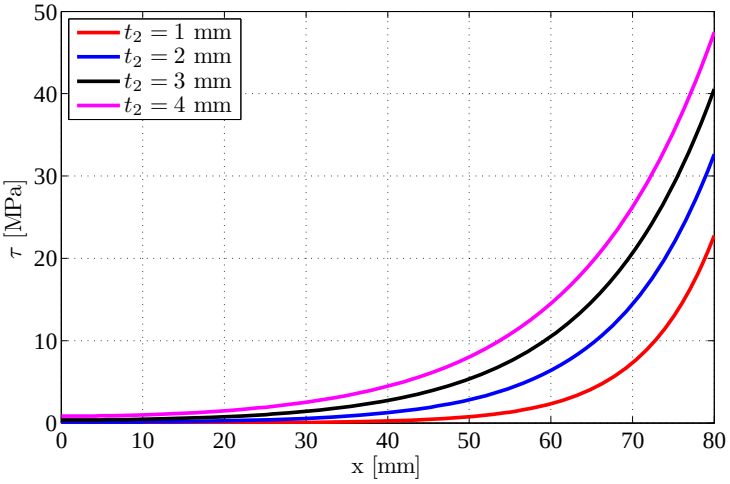

Figure C.5: *Shear stress at yielding in the reinforcement. The parameters used are:* $t_1 = 100\,\text{mm}, t_3 = 0.5\,\text{mm}, E_1 = 70\,\text{GPa}, E_2 = 210\,\text{GPa}, G = 1.32\,\text{GPa}$ *and* $f_y = 200\,\text{MPa}$

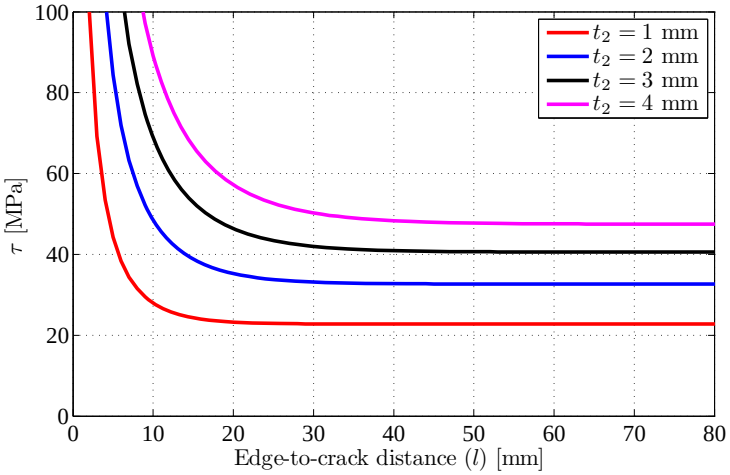

Figure C.6: *The maximum shear stress at yielding in the reinforcement as function of the edge-to-crack length. The parameters used are:* $t_1 = 100\,\text{mm}, t_3 = 0.5\,\text{mm}, E_1 = 70\,\text{GPa}, E_2 = 210\,\text{GPa}, G = 1.32\,\text{GPa}$ *and* $f_y = 200\,\text{MPa}$

Part II

Appended papers

Paper I

"Characterization of the Residual Stress State in Commercially Fully Toughened Glass"

J.H. Nielsen, J.F. Olesen & H. Stang

Accepted for publication in: *Journal of Materials in Civil Engineering - ASCE*

Characterization of the Residual Stress State in Commercially Fully Toughened Glass

Jens Henrik Nielsen, John Forbes Olesen, Henrik Stang
Department of Civil Engineering, Technical University Denmark
Corresponding author: jhn@byg.dtu.dk

Abstract: Toughened glass is often used in load carrying elements due to the relatively high tensile strength compared with float glass. The apparent tensile strength of toughened glass is a combination of the pure material strength and the residual stresses imposed by the toughening process. This paper is concerned with an experimental characterization of the residual stress state for toughened glass. Results for the variation of residual stresses within 32 square specimens with a side length of 300 mm are investigated. The specimens varied in thickness and one group was glass with low iron content. The photoelastic constant was estimated from a four-point bending test. The experimental results revealed large variations in the residual stress state within each specimen and between groups of different thicknesses. The results are compared with a non-standard fragmentation test, showing that the fragment size does not seem to be dependent on the local variations of the residual stress state in a specimen.

Introduction

There seems to be an increasing use of glass in structural load carrying elements. The reason for this is the transparent nature of glass combined with excellent properties such as high resistance to environmental loads high compressive strength and a relatively high stiffness compared with more commonly used building materials. Unfortunately glass is extremely brittle and the tensile strength is primarily governed by flaws in the material surface. Furthermore, the strength of float glass exhibits considerable time dependency (Beason and Morgan 1984).

A well known technology for improving the apparent strength of glass is thermal toughening. This process may increase the apparent strength more than 5 times and furthermore it reduces the time dependency of the strength. The principle of this process is to heat up float glass to a temperature near the glass transition temperature and then to quench it. The surface of the glass specimen will then contract and stiffen while the core is still hot and soft so that it is unable to carry any stresses. The "transition line" progresses towards the center plane of the glass and stresses build up in the outer layers, see Fig. 1.

More elaborate descriptions of the toughening process and mathematical models for the thermal toughening process may be found in the literature, see e.g. (Lee et al. 1965), (Narayanaswamy 1971), (Narayanaswamy 1978), (Daudeville et al. 2002) and (Nielsen et al. 2007).

When glass is toughened the apparent strength is increased drastically due to the compressive stress state in the surface. This compressive stress has to be exceeded by the external load before any flaw in the surface may open and act as a crack initiator. A very straightforward hypothesis for the apparent strength of toughened glass is that it consists of a contribution from the residual stresses and a contribution from the "pure" glass strength. However, one must realize that the "pure" glass strength is the strength of annealed glass (not float glass) without any residual stresses. Furthermore some crack healing may occur during the toughening process which might increase the "pure" glass strength.

According to Eurocode (EN12150-1 2001), glass can be regarded as fully toughened when the number of fragments within a given area in a standard specimen exceeds a certain limit. This is a very rough characterization considering the importance of this measure in relation to strengths up to an apparent strength of 120 MPa.

In this paper the intention is to characterize the residual stress state in specimens ordered as fully toughened glass obtained from a commercial manufacturer. The residual stress state is investigated using a scattered light polariscope.

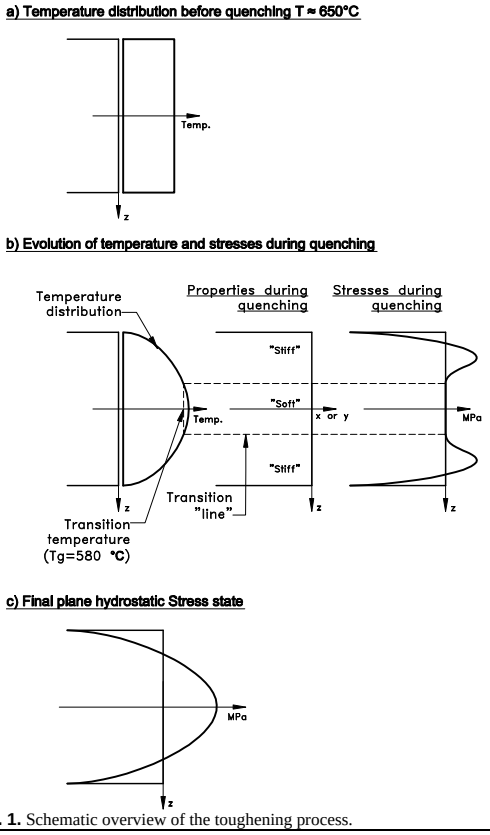

Fig. 1. Schematic overview of the toughening process.

Theory of the Measurement Technique

Structural glass belongs to a group of so-called photo elastic materials which exhibit the ability to affect light when stressed. The instrument used for measuring stresses in the tests presented in this paper is a scattered light polariscope (SCALP) developed by GlasStress Ltd. in Tallinn. Here we will briefly describe the method, for more detailed information the reader is referred to (Anton and Aben 2003) and (Aben 1993).

The instrument basically consists of a light source (a laser) and a camera. A laser beam is sent into the glass specimen and the intensity of the scattered light at different points through the thickness is recorded, see Fig. 2. The data for the intensity are post-processed by a computer fitting to a polynomium. A 3rd order polynomium has been chosen throughout this paper because this will provide a 2nd order stress distribution which is reasonable comparing with numerical models for toughened glass, see e.g. (Nielsen et al. 2007).

Assuming plane stress, the retardation of light (δ) can be expressed as (1), which is an integration of the so-called Wertheim law, see (Aben 1993).

$$\delta(\eta) = C\int_{\eta_0}^{\eta} (\sigma_x - \sigma_y \cos^2 \alpha)\, d\eta \tag{1}$$

Here C is the photoelastic constant (2.70 TPa^{-1} for float glass (Anton 2006)), σ_x and σ_y are normal stresses in perpendicular directions, α is the laser beam inclination, see Fig. 2. The path for the laser beam is denoted η, and η_0 indicates the coordinate at the top surface of the glass specimen. Equation (1) can be rewritten by differentiation

$$\frac{1}{C}\frac{d\delta(\eta)}{d\eta} = \sigma_x - \sigma_y \cos^2 \alpha \tag{2}$$

Since we have two unknowns in this equation we need either to make an assumption, e.g. hydrostatic plane stress (σ_x=σ_y) or make two orthogonal measurements at each point. The latter approach has been used for the results presented in this paper. However, the results will not be exact throughout thickness; since the laser beams are inclined they can at most coincide in a single point.

Denoting the measurements by δ_x and δ_y we get two equations analogous to (2). Solving these equations for σ_x and σ_y we find

$$\sigma_x = \frac{\delta_x' + \delta_y' \cos^2 \alpha}{C(1-\cos^4 \alpha)} \quad , \quad \sigma_y = \frac{\delta_y' + \delta_x' \cos^2 \alpha}{C(1-\cos^4 \alpha)} \tag{3}$$

where the derivative of δ is written as δ'. Utilizing $\alpha=\pi/4$ for the SCALP we find

$$\sigma_x = \frac{4\delta_x' + 2\delta_y'}{3C} \quad , \quad \sigma_y = \frac{4\delta_y' + 2\delta_x'}{3C} \tag{4}$$

Equation (4) is used for determining the stress distribution in both directions from two measurements.

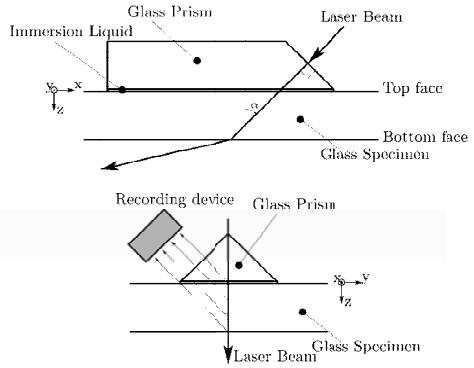

Fig. 2. Principal sketch of the SCALP instrument. The top figure shows a sketch seen perpendicular to the measuring direction (x). The bottom figure is the same, seen along the measuring direction including the recording device (after (Anton and Aben 2003)).

Experimental Result – The Photo-Elastic Constant

Experimental Variation of the Measuring Technique

The standard deviation (SD) of results from the method used was estimated by 20 measurements at the same location of a 12 mm specimen. Fig. 3 shows the results as a function through the thickness of the specimen.

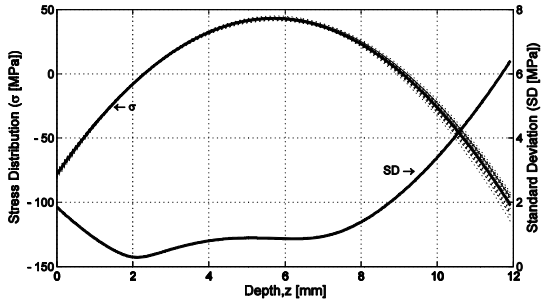

Fig. 3. Stress distribution (left axis) and standard deviation (right axis) for the measurements, carried out on a 12mm plate (C=3.01TPa^{-1}).

It is seen that the largest (absolute) standard deviation is found at the bottom of the plate where the light beam exits the glass. The exit of the laser beam causes some scatter in the light intensity which is one reason for the high SD. The estimated SD of the measurements includes both the error of the method and the possibility that SCALP is not placed at the exact same location for each measurement. However, the positioning of SCALP is done within an accuracy of ±1mm. The standard deviation for the compressive stresses at the top face is found to be 1.8 MPa, see Fig. 3.

Four Point Bending Test – Determination of the Photoelastic Constant

The photoelastic constant (C) was determined by measuring the change in surface stress for a glass specimen subjected to four point bending. In this test we have used a

toughened glass beam with the dimensions 15 mm x 150 mm x 1500 mm. The beam was supported and loaded as sketched in Fig. 4.

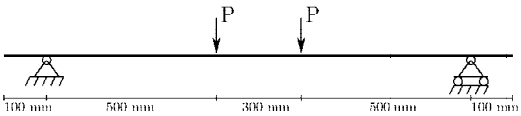

Fig. 4. Sketch of the four-point bending test.

Four levels of loading were used and at each level five measurements of the stress state were made. Only the top face stress in the beam direction was considered. Plotting the measured change of stress as a function of the stress, found from the load using Bernoulli beam theory, we should, ideally, find a straight line with a slope equal to one, and intersecting the axis at the origin. From this knowledge we can estimate the photoelastic constant, since C is our only free parameter. The results are shown in Fig. 5, where it is found that C=3.01 TPa^{-1} for this specimen of toughened glass.

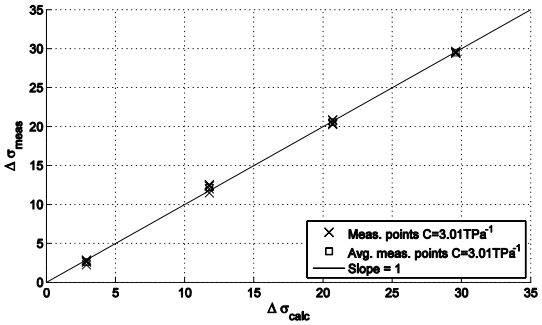

Fig. 5. Results for the four point bending test, C=2.70 TPa^{-1} is the default value for SCALP (typically for float glass).

The photoelastic constant found here is assumed to apply for the tested specimens and is used throughout this paper.

Experimental Results – The Residual Stress State

In this section, only stresses at the top face are considered. It should be noted that all specimens were stamped at the bottom right corner on the top face by the manufacturer. This stamp has been used for fixing the coordinate system as sketched in Fig. 6. All specimens were specified as fully toughened glass and delivered by the same manufacture.

In the experiment 32 specimens divided in 4 groups were investigated, see Table 1. All specimens were cut as squares with a side length of 300 mm.

Table 1. Data for groups investigated.

Group	Thickness [mm]	Number of specimens	Low iron content
A	19	8	No
B	19	8	Yes
C	12	8	No
D	8	8	No

For each plate σ_x and σ_y were measured at 9 locations (measurement points a,b,…,i) as indicated in Fig. 6.

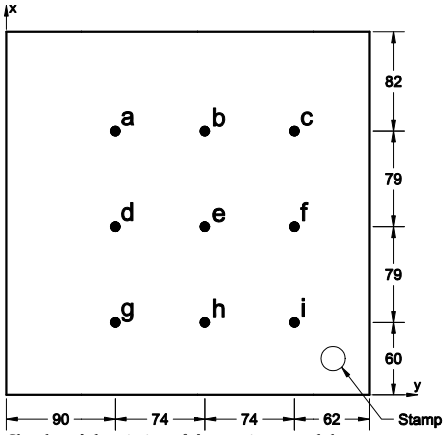

Fig. 6. Sketch and description of the specimens and the measurement points a,b,…,i. Note that the vertical axis for the coordinate system is denoted x.

Mean Values and Variation of Stresses within Groups

Table 2 shows measured data summarized within groups, meaning that mean values and standard deviations are calculated from measurements on 8 different specimens within the same group at the same measurement point. The bottom row shows the mean value and standard deviation of all measurements in the same direction within each group.

Table 2. Mean value (compressive stress) and standard deviation in MPa.

	A		B		C		D	
	σ_x	σ_y	σ_x	σ_y	σ_x	σ_y	σ_x	σ_y
a	71.59 (2.29)	73.95 (3.23)	65.81 (2.60)	67.56 (1.72)	81.77 (2.84)	82.17 (2.50)	96.61 (5.79)	95.98 (5.67)
b	69.31 (1.78)	70.69 (1.34)	64.42 (2.13)	64.55 (2.68)	80.49 (2.74)	80.10 (1.85)	93.49 (5.75)	93.42 (4.45)
c	47.31 (4.79)	57.00 (2.73)	55.43 (13.29)	59.39 (7.79)	81.84 (2.76)	81.31 (3.58)	98.50 (6.32)	94.49 (4.06)
d	71.64 (1.53)	69.99 (1.25)	64.99 (3.09)	64.63 (1.78)	79.70 (1.40)	79.77 (1.52)	94.25 (4.55)	94.51 (2.87)
e	69.19 (1.61)	69.53 (1.63)	64.42 (2.66)	64.41 (2.43)	77.13 (3.52)	77.66 (3.08)	92.54 (4.24)	93.45 (2.37)
f	71.49 (1.75)	69.51 (1.74)	66.08 (3.43)	65.66 (2.55)	79.90 (2.93)	80.16 (2.62)	93.53 (3.27)	94.15 (3.26)
g	71.56 (3.44)	71.63 (3.74)	67.16 (1.84)	67.08 (2.03)	81.51 (2.16)	80.99 (2.18)	93.89 (3.56)	91.69 (4.67)
h	70.15 (1.18)	72.46 (1.15)	65.23 (2.73)	66.23 (3.14)	80.19 (2.56)	81.09 (2.44)	96.57 (7.69)	95.29 (4.84)
i	69.34 5.99)	64.38 (11.14)	66.52 (8.52)	64.24 (12.95)	84.96 (2.53)	84.69 (2.77)	96.61 (4.12)	98.32 (4.32)
mean	**67.95 (2.71)**	**68.79 (3.11)**	**64.45 (4.48)**	**64.86 (4.12)**	**80.83 (2.60)**	**80.88 (2.50)**	**95.11 (5.03)**	**94.59 (4.06)**

Investigation of the Plane Hydrostatic Stress State

In this section the probability that the measured state of stress is plane hydrostatic ($\sigma_x = \sigma_y$) is investigated. If we have a plane hydrostatic stress state, only one measurement is needed in order to estimate the stress distribution across the thickness of the specimen. Furthermore it is a very common assumption for locations far from edges. In Table 3 the probability for measuring a hydrostatic stress state is shown. The probabilities are calculated under the assumption that the observations follow a normal distribution. The probability, *P*, used for Table 3 is specified in (5).

$$P\left\{SD_{meas} > \left|\sigma_x - \sigma_y\right|\right\} \tag{5}$$

Here SD_{meas} is the standard deviation for the measuring method.

Table 3. Probability for measuring equal stresses ($\sigma_x = \sigma_y$) for each measuring location and for each group.

	A	B	C	D	Point
a	0.38	0.53	0.56	0.63	**0.53**
b	0.73	0.87	0.91	0.55	**0.77**
c	0.00	0.20	0.90	0.20	**0.32**
d	0.66	0.71	0.95	0.56	**0.72**
e	0.99	0.98	0.68	0.45	**0.78**
f	0.44	0.80	0.80	0.60	**0.66**
g	0.70	0.81	0.83	0.40	**0.69**
h	0.16	0.81	0.70	0.36	**0.51**
i	0.18	0.25	0.96	0.48	**0.47**
Group	**0.47**	**0.66**	**0.81**	**0.47**	**0.60**

It is seen that when measuring at point e, the probability for measuring a hydrostatic stress state is highest with a likelihood of 78%. In general it can be verified that when approaching corners, e.g. point c (32%) and i (47%), there is a low probability for measuring a hydrostatic stress state. It can also be seen that measuring in an arbitrary location (within the measurement points) on an arbitrary specimen, the probability for finding a hydrostatic stress state is 60%. The values shown in the bottom row describe the probability of measuring a hydrostatic stress state within that particular group.

The Mean Value of the Residual Stress in a Specimen

In order to investigate the differences in stresses within each specimen, the total mean value of the stress within one specimen is defined as a measure for the degree of toughening. We will now investigate how likely it is that one measurement on the specimen is representative for the degree of toughening.

Testing the degree of toughening against the mean value found in the different specimens at the different measuring points using a two-sided t-test, we are able to determine those measurements that are significantly different from the degree of toughening of the specimen. The results are presented in Table 4, where the number of specimens which are significantly different from the degree of toughening is shown. The results are shown at 3 different levels of significance.

Table 4. Number of specimens which are different from the degree of toughening at significance level α.

	α	a	b	c	d	e	f	g	h	i
	0.01	4	0	8	0	0	0	1	2	0
A	***0.05***	8	1	8	1	0	0	2	5	1
	0.1	8	2	8	1	1	1	3	6	3
	0.01	4	2	5	2	2	4	3	3	0
B	***0.05***	4	4	6	5	5	5	4	3	0
	0.1	4	8	6	8	5	5	5	4	0
	0.01	2	1	0	2	5	1	1	0	8
C	***0.05***	4	2	0	4	8	1	1	1	8
	0.1	4	3	3	4	8	2	3	3	8
	0.01	2	1	2	2	5	2	4	1	4
D	***0.05***	4	4	3	5	5	5	4	4	4
	0.1	5	5	5	8	6	6	4	5	5

In total 288 comparisons were made at each level of significance. For a significance level of $\alpha=0.01$, 82 of the measures were significantly different from the degree of toughening. For $\alpha=0.05$ the number was 127 and for $\alpha=0.1$ the number was 161. Looking more into details, there seems to be some tendency for the 19 mm specimens (Group A and B) that measuring at point d, e or f gives reasonable estimate for the mean value of the residual stress in the specimen. For Group C and D only the points d and f show similar tendencies. However, it does not seem possible to find one measurement which is representative for the average stress in the specimen.

Differences of Residual Stresses within each Specimen

In this section the differences in stresses within each specimen is calculated as the largest difference between the 9 measurement points. Table 5 summarizes the results within the different groups in columns.

Table 5. Differences between highest and lowest compressive surface stress (MPa) for each specimen.

	A	B	C	D
1	34.7	26.7	12.3	11.6
2	35.3	34.3	9.4	23.0
3	22.9	6.2	8.2	15.8
4	30.5	4.9	8.1	15.0
5	25.9	29.7	15.4	9.1
6	35.0	7.5	6.8	8.1
7	27.7	22.0	11.5	15.2
8	19.8	6.1	7.3	13.8
Mean	**29.0**	**17.2**	**9.9**	**13.9**
Max	**35.3**	**34.3**	**15.4**	**23.0**

It is seen that the stresses deviate with up to approximately 35 MPa (within the tested area) for Group A and Group B, and 23 MPa for Group D and 15 MPa for Group C. These values seem to be independent of the degree of toughening, since groups A and B have the lowest degree of toughening, see Table 2.

Residual Stress as a Function of Specimen Thickness

The effect of the specimen thickness on the measured stress is analyzed in this section. The results for Group A (19 mm), Group C (12 mm) and Group D (8 mm) are shown in Fig. 7. Group B is excluded since these specimens are made of glass with low iron content.

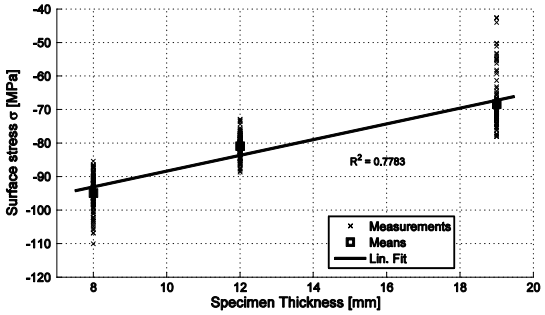

Fig. 7. Linear fit of the stress thickness relation.

From Fig. 7 there seems to be a relationship between the thickness of the specimen and the stress state. This indicates that the toughening process is not correctly adjusted for the different thicknesses of the specimens. At least "fully toughened" does not imply the same level of residual stress.

The Effect of Toughened Glass with Low Iron Content

Group B was geometrically similar to Group A, however Group B was cut from glass with low iron content. The effect of the low iron content on the residual stresses is investigated by comparing the mean values for all measurements in a particular geometric point (a,b,…) between the two groups. A plot showing the measurements for the groups can be seen in Fig. 8.

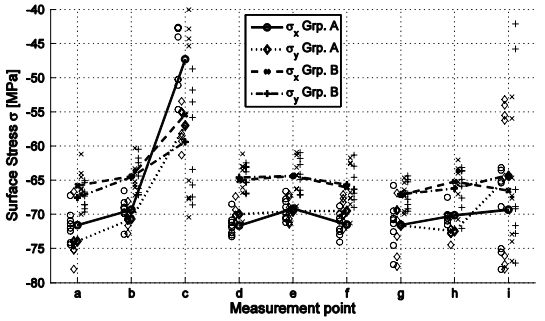

Fig. 8. Measurements of σ_x and σ_y for Group A and B. The lines connect the mean values of the measurements. Note that the data points for Group A is shown to the left of the grid line for the particular measurement point and the data points for Group B is shown to the right.

The comparison is evaluated using a t-test where the mean value of the stresses for Group A is compared with the mean value of the stresses for Group B. The results for the t-test rejected the null-hypothesis (the two mean values are equal) for both σ_x and σ_y with P-values of 0.0042 and 0.0001. From this it can be concluded that there are significant differences in the stresses measured for Group A and Group B. However, it should be noticed that the same photoelastic constant is used for measurements on both types of glass which might not be correct.

Fragmentation Test

According to Eurocode (EN12150-1 2001) toughened glasses is classified by a destructive test where the fragments in a standard area of the fragmentized specimen are counted. In the standardized test, the specimen is 1100mm x 360mm and the fracture is initiated by an impact of a pointed steel tool perpendicular to the plane of the specimen.

For the fragmentation test described in this paper, the size of the specimen was 300 mm x 300 mm with a thickness of 19 mm. The fracture was initiated by drilling a hole from the edge into the center plane of the specimen as indicated in Fig. 9. This approach for initiating the crack has been used in order to minimize the amount of energy added to the specimen. This means that the source of energy for the fracture propagation is the internal elastic energy originating from the residual stresses.

The fractured specimen is shown in Fig. 9, and squares of 50 mm x 50 mm are shown. The squares are placed with their center located at the measurement points shown in Fig. 6, and are used for calculating the number of fragments according to Eurocode (EN12150-1 2001).

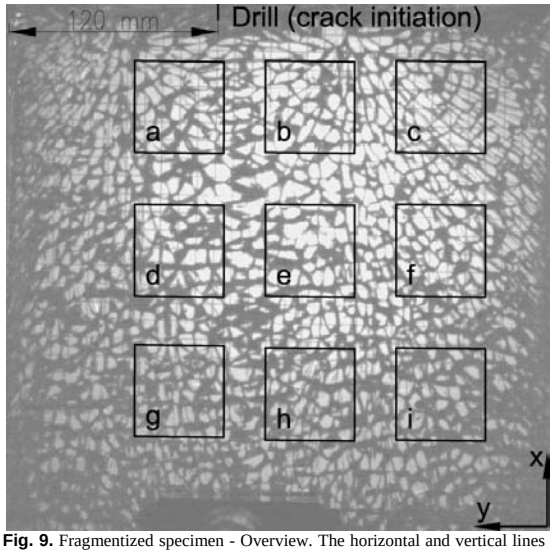

Fig. 9. Fragmentized specimen - Overview. The horizontal and vertical lines are a grid (10mm) placed behind the specimen in order to estimate sizes on the picture.

An example of how the numbers of fragments are counted for location e is given in Fig. 10. The dots are counted as one fragment and the cross-lines are counted as half a fragment. It should be noted that the number of fragments might be larger due to the shadows from the cracks which might hide small fragments.

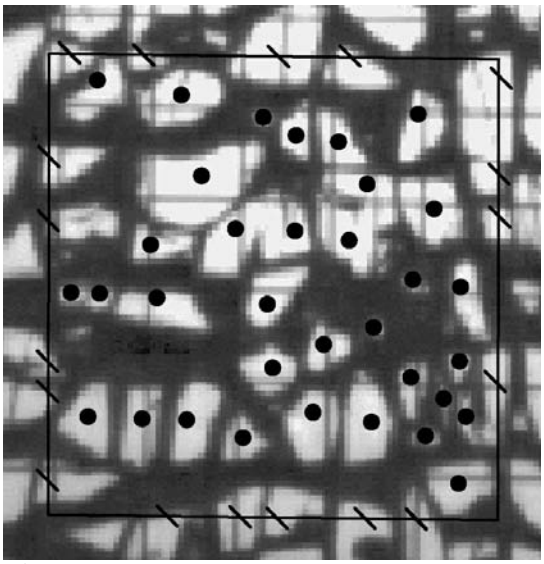

Fig. 10. Fragmentized specimen – particle count at point e.

According to the fragmentation test described in Eurocode (EN12150-1 2001) the number of fragments in order to classify a 19 mm specimen to be fully toughened (apparent strength of 120 MPa) is 30 fragments. The apparent strength includes both the residual stresses and the material strength of the glass. From Eurocode (prEN13474-3 2005) the short term material strength can be extracted from a formula describing the allowable stress in a toughened glass plate. The characteristic material strength is then 45 MPa according to this approach, which again indicates that the compressive residual stresses at the surface of the specimens should be at least 75 MPa in order to comply with the apparent strength of 120 MPa.

The number of counted fragments normalized with 30 and the stresses in both directions normalized with 75 MPa as function of the measurement points are shown in Fig. 11.

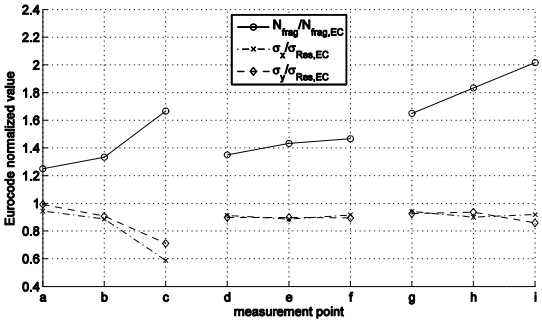

Fig. 11. Comparison between the counted number of particles and the measured stress. $\sigma_{Res,EC}$ is the residual stress determined from the EuroCode (75 MPa) and $N_{frag,EC}$ is the minimum number of fragments to classify the glass as fully toughened according to EuroCode.

It is seen that in general the residual stress is measured about 10% lower than the 75 MPa derived from Eurocode. Furthermore, there does not seem to be any indication of a correlation between the number of fragments and the local degree of toughening within the plate. This seems to be a reasonable conclusion due to the fact that the crack propagation is dynamic. Furthermore, the influence of the relatively small variations in the residual stress state is properly overruled by the influence of the forces of inertia. The curve for the fragmentation count shows that the number of fragments is more than 20% higher at all locations than needed for the specimen to be classified as fully toughened in accordance with Eurocode (EN12150-1 2001). This observation – and the observation that deviations from the average residual stress of more than 30% cannot be revealed by counting the number of fragments – indicates that the fragmentation test used today might not be accurate enough to comply with modern needs for glass as a structural material.

Conclusion

The residual stresses in toughened glass were investigated using a scattered light polariscope developed by GlasStress Ltd. in Tallinn. This device is able to estimate the stress distribution through the thickness of a planar glass specimen assuming plane stress. The standard deviation of the measurements was estimated from 20 measurements at the same spot and the value was found to be 1.8 MPa for surface stresses at the measurement side.

The photoelastic constant for toughened glass was determined using a four point bending test. Testing a 15 mm x 150 mm x 1500 mm glass beam and comparing the measured stress changes with analytical values, the photoelastic constant was estimated to $C=3.01\ TPa^{-1}$.

An investigation of 4 different groups of square glass specimen with a side length of 300 mm was carried out in order to characterize the residual stress state in toughened glass. The 4 groups consisted of 32 specimens in total. Stresses in two orthogonal directions were determined in 9 points for each specimen. In order to limit the investigation only the surface stresses have been considered here.

It was investigated if the stresses in both directions were equal. The investigation revealed that when measuring on a arbitrary plate in an arbitrary point (within the investigated area) the probability of finding a plane hydrostatic stress state was 60%. It was also shown that when approaching corners the likelihood of having a plane hydrostatic stress state decreased.

Further, it was investigated if one measurement could give a quantitative measure for the degree of toughening for the full plate. This did not seem to be a reasonable assumption, since the variation of stresses within the specimens was too large. It was found that the stress at the top face could deviate with approximately 35 MPa for the 19 mm glass and 15 MPa and 23 MPa for the 12 mm and 8 mm specimens respectively. Furthermore, it was found that the specimen thickness and the mean value of the residual stress had an almost linear relationship. This observation may be explained by inaccurate adjustment of the toughening process to accommodate for different specimen thicknesses.

Finally, differences in the residual stress state between low iron content glass and standard glass was observed. The cause for this deviation may be that the photoelastic constant for glass with low iron content differs from the one found and used for standard toughened glass.

On the basis of the presented results it may be concluded that specimens with high variations of the residual stresses are to be expected when ordering fully toughened glass. A much more uniform distribution of the residual stresses had been expected both within each specimen, but also between the different groups. This must be considered as a serious problem for the structural use of toughened glass. The results indicate that more knowledge of the control of the toughening process for different geometries is needed.

One of the specimens was used for a destructive fragmentation test. The fragmentation process was initiated by a drill in order to minimize the energy added to the specimen. It was found that the number of fragments in different areas could not be related to the residual stresses measured in that particular area. Furthermore, it is questioned if the fragmentation test used today is accurate enough to comply with the increasing need for high quality of toughened glass required by structural engineers.

Acknowledgements

The authors would like to thank the COWI foundation and the Toubro Foundation for sponsoring the photoelastic measuring device.

References

Aben, H. (1993). Photoelasticity of Glass, Springer-Verlag.

Anton, J. (2006). "Scattered Light Polariscope SCALP-03." GlassStress Ltd., Tallinn.

Anton, J., and Aben, H. (2003). "A Compact Scattered Light Polariscope for Residual Stress Measurement in Glass Plates."

Beason, W. L., and Morgan, J. R. (1984). "Glass failure prediction model." Journal of Structural Engineering, 197-212.

Daudeville, L., Bernard, F., and Gy, R. (2002). "Residual stresses near holes in tempered glass plates." Materials Science Forum, 43-48.

Lee, E. H., Rogers, T. G., and Woo, T. C. (1965). "Residual stresses in a glass plate cooled symmetrically from both surfaces." Journal of the American Ceramic Society.

Narayanaswamy, O. S. (1971). "A model of structural relaxation in glass." Journal of the American Ceramic Society, 491-8.

Narayanaswamy, O. S. (1978). "Stress and structural relaxation in tempering glass." Journal of the American Ceramic Society, 146-52.

Nielsen, J. H., Olesen, J. F., H.Stang, and Poulsen, P. N. (2007). "An Implementation of 3D Viscoelastic Behavior for Glass During Toughening." Glass Performance Days, Finland.

EN12150-1 2001, "Glass in building – Thermally toughened soda lime silicate safety glass – Part1: Definition and description." European Standard EN 12150-1, June 2000.

prEN13474-3 2005, "Glass in building – Determination of the strength of glass panes – Part3: General method of calculation and determination of strength of glass by testing." European Standard prEN 13474-3, November 2005.

Paper II

"Finite Element Implementation of a Glass Tempering Model in Three Dimensions"

J.H. Nielsen, J.F. Olesen, P.N. Poulsen & H. Stang

Submitted to: *Computers & Structures*

Finite Element Implementation of a Glass Tempering Model in Three Dimensions

J.H. Nielsen[a,*], J.F. Olesen[a], P.N. Poulsen[a], H. Stang[a]

[a]*Department of Civil Engineering, Technical University of Denmark, Brovej Building 118, DK-2800 Kgs. Lyngby, Denmark*

Abstract

The present paper develops and validates a 3D model for the simulation of glass tempering. It is assembled from well-known models of temperature dependent viscoelasticity and structural relaxation and predicts both transient and steady-state stresses in complex 3D glass geometries. The theory and implementation of the model is comprehensively given and the model is carefully checked and validated. It is demonstrated that by adjusting a single parameter in the model, experimental results can be replicated accurately even for cooling rates far from normal.

Keywords: Residual Stresses, Toughened Glass, Structural Relaxation, Thermorheological Simple Material, Strength of Tempered Glass, soda-lime-silica Glass

1. Introduction

1.1. Motivation

Over the last couple of decades, glass[1] has gained an increasing popularity as a structural, load carrying material due to its transparency and high resistance to environmental loadings. However, glass lacks the capability of yielding and is extremely brittle. This indicates that the tensile strength is governed by small flaws in the surface which reduce the strength of ordinary float glass to approximately 50 MPa and give rise to huge variations in the strength value.

By imposing a compressive residual stress at the surface balanced with an internal tensile stress as shown in Figure 1, the surface flaws will be in a permanent state of compression which has to be exceeded by external loading before failure can occur. The tensile residual stresses are carried by the interior part of the material, which is (almost) flawless [3]. Such a distribution of the residual stresses can be obtained by the so-called tempering process of the glass. Glass with such a stress state is often referred to as tempered glass or toughened glass[2]. The strength of tempered glass is considerably higher than what is found for ordinary float glass and furthermore, the strength is more reliable and (almost) time-independent [3]. However, if the residual stress state is disturbed sufficiently, the tempered glass will fragmentize completely. The fragmentation process is experimentally investigated further in [1].

When a hot glass specimen is cooled rapidly (quenched) from temperatures above the glass transition temperature, residual stresses are developed. This process is referred to as the tempering process and increases the apparent strength of the glass considerably by introducing compressive residual stresses at the surface. However, the cooling rates in such a specimen will be spatially dependent indicating that spatial variations in the residual stresses will be present. This means that the apparent strength of a tempered glass specimen is spatially dependent as indicated in (1)

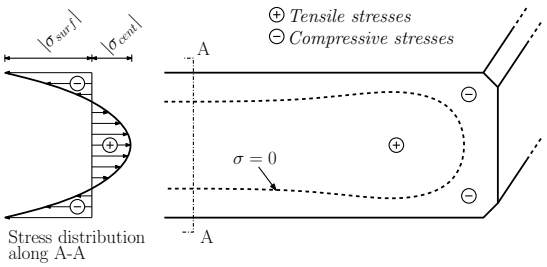

Figure 1: Residual stresses in tempered glass. The right drawing shows a line representing the location where the residual stresses equals zero near an edge. The left drawing shows the stress distribution far from any edges (cut A-A).

$$f_t^{app}(x_i) = f_t^{mat}(x_i) - \sigma_{rs}(x_i) + f_t^{other}(x_i) \tag{1}$$

where f_t^{app} is the apparent tensile strength, x_i are the spatial Cartesian coordinates with i ranging from 1 to 3, f_t^{mat} is the inherent material strength, σ_{rs} is the residual stress (compression is negative) and f_t^{other} is a contribution to the strength originating from secondary phenomenons such as crack healing during tempering. The inherent material strength, f_t^{mat}, is time dependent due to static fatigue [2] and the contribution from crack healing is relatively small. It is therefore common practice to assume the strength equal to the residual stress when designing with tempered glass [3]. Today, a simple destructive test is used for identifying the glass as tempered or not [4], however, this test does not reveal anything about local variations of

*Corresponding author

Email addresses: jhn@byg.dtu.dk (J.H. Nielsen), jfo@byg.dtu.dk (J.F. Olesen), pnp@byg.dtu.dk (P.N. Poulsen), hs@byg.dtu.dk (H. Stang)

[1]In this paper, only soda-lime-silica glass is considered.

[2]The stress state should be above a certain level before these names are used.

the residual stresses near corners, edges and holes . Another technique is more advanced and measures the residual stresses, however, this technique cannot be used close to corners, edges and holes, where the largest loads are often applied. A numerical tool for predicting the residual stresses in tempered glass will be valuable for optimizing the tempering process as well as an important tool when designing structures in tempered glass.

In commercially tempered glass, the residual compressive stresses at the surface are often in the order of magnitude of 100 MPa. However, the residual stresses are governed by the cooling rate, but unfortunately a brutal quenching of the glass will induce high transient tensile stresses which may lead to breakage of the glass during the process. A model capable of predicting the transient residual stresses is therefore a valuable tool for the manufacturer of tempered glass in order to optimize their product.

The present paper starts by describing the foundation for constructing a model capable of predicting the tempering process in a full 3D domain. The foundation is based on well known models, however, after the basis is formed a thorough description of how to combine and implement the models is given. The model is verified by comparison with experimental data and several examples of the use is given.

1.2. Evolution of Tempering Models

According to [5] the tempering process of glass was patented in 1877, however, it was not until 1920 that the first simple models were developed. Adams & Williamson[6] formulated a simple theory for the generation of residual stresses, stating that "*the strain remaining in a block of glass is equal and opposite in sign to the reverse strain lost by viscous yielding in the early stages of the cooling process*". The reverse strain is to be interpretated as the strain originating from the transient temperature gradient during cooling.

In 1948, Bartenev[7] utilized that the viscosity of molten glass increases very rapidly during cooling. By assuming the glass to be a fluid, without any capability to carry stresses for temperatures above the glass transition temperature, T_g, and a linear elastic solid below T_g. This is the basic concept of the so-called instant freeze theory. The next step was to include the relaxation of stresses during the glass transition temperature range. Experimental data was provided in several papers around 1950 and 1960, showing that the relaxation of glass at different temperatures can be treated in a simple manner, see e.g. [8]. It was shown that the relaxation curves for glass at different temperatures can be brought to coincide simply by changing the timescale; a material with such behavior is said to be thermorheologically simple (TS) [9]. In 1965, Lee, Rogers & Woo [10] introduced a model including the TS behavior of glass.

The most recent step in developing the theory for the tempering process was to include the so-called structural relaxation, which accounts for the fact that the slower a glass is cooled the more regular the long range order becomes which affects certain properties. A model for such behavior was proposed by Narayanaswamy [11] using the concept of fictive temperatures introduced by Tool in 1946 [12]. It was found that the volume change was by far the property that contributed the most to the residual stresses [13], and often the theory is referred to as volume relaxation. At the time of development, only the in-plane stress distribution through the thickness of a plate far from any edges was considered, i.e. the one-dimensional case, however, modern computers provide enough computational power for analyzing complex geometries in three dimensions.

Although, a theory for the tempering process is available, the application to engineering practice seems remote at the present time. However, it is the view of the authors, that this remoteness is caused by a lack of knowledge regarding the theory and its implementation using numerical methods.

Implementations of tempering models have been reported recently, see e.g. [14] or [15]. However, the focus of these papers is on particular results without a detailed description of the algorithm nor an extensive verification of the model is given.

The present paper provides the reader with the theory of the constitutive behavior of glass during quenching and provides detailed information on how to implement a full 3D algorithm in a Finite Element program. Furthermore, a verification and a finite element convergency analysis of the implementation is performed.

2. Theory

This section presents the basis for a tempering model capable of predicting both transient and steady-state residual stresses in tempered glass. The tempering model is formed by three main ingredients, namely temperature dependent viscoelasticity, structural volume relaxation and the temperature history. Only the two first will be considered in detail, the temperature history is assumed known. For the examples given, the temperature problem is solved using a simple convective boundary condition and the heat equation. A more detailed discussion on the temperature history during tempering is given in [15] and [16].

2.1. Viscoelasticity

For linear viscoelastic materials, the Boltzmann superposition principle holds and the constitutive law can be formulated by a convolution integral. Using index notation and assuming zero initial strain, the constitutive equations can be written as

$$\begin{aligned}\sigma_{ij}(t) =& 2\int_0^t G(t-t')\frac{de_{ij}(t')}{dt'}dt' \\ &+ \delta_{ij}\int_0^t K(t-t')\frac{d\varepsilon_{ii}(t')}{dt'}dt'\end{aligned} \tag{2}$$

where σ_{ij} is the stress tensor, t is the time, t' is a running parameter for the time, ε_{ii} is the trace of the strain tensor, e_{ij} is the deviatoric strains, $G(t)$ and $K(t)$ are relaxation functions representing the time dependent shear and bulk modulus, respectively. The first term of the right hand side of (2) represents the deviatoric stresses, s_{ij}, while the second term represents to the hydrostatic stress, σ_{kk}.

A simple approach to include the temperature dependence is by changing the time-scale associated with the relaxation functions. Such behaviour is often referred to as a thermorheological simple (TS) [9] and it has been shown experimentally that glass is well represented by such a behaviour [8].

Utilizing the TS property, the relaxation function obtained at one temperature can be transformed to be valid for an arbitrary temperature by substituting the real time, t, with a scaled time[3], ξ. The scaling factor is temperature dependent and is most often referred to as the shift function[4], $\phi(T)$. The scaled time, ξ, for varying temperatures is found by integrating the shift-function, $\phi(T)$, over time

$$\xi = \int_0^t \phi\left(T(t')\right)dt' \tag{3}$$

The temperature for which $\phi(T) = 1$ is referred to as the base temperature, T_B, indicating that $\phi(T_B) \equiv 1$. For most materials, the viscosity increases with decreasing temperature, corresponding to an extension of the time scale ($\phi(T) > 1$).

The shift-function relates the viscosity, η, at the base temperature, T_B, to the viscosity at the present temperature through a scaling in time

$$\eta(T_B)t = \eta(T)\xi \quad \Leftrightarrow \quad \xi = \frac{\eta(T_B)}{\eta(T)}t \quad \Rightarrow \quad \phi(T) = \frac{\eta(T_B)}{\eta(T)} \tag{4}$$

Several empirical shift functions have been proposed in order to fit the behavior of various materials, however, by assuming the behavior of a newtonian fluid, a shift function can be derived. The temperature variation of the viscosity follows a law of the Arrhenius type, see e.g. [17] and the shift function derived from the above assumptions can be written as

$$\ln\phi(T) = \ln\left(\frac{\eta(T_B)}{\eta(T)}\right) = \frac{H}{R_g}\left(\frac{1}{T_B} - \frac{1}{T}\right) \tag{5}$$

where H is the activation energy (627.8 kJ/mol for soda-lime glass [18]) and R_g is the universal gas constant (8.31 J/mol·K).

2.2. Structural Relaxation Model

It has been shown that the rate of cooling (or heating) has an effect on certain properties such as viscosity and density [18]. This effect is attributed to the structural arrangement of the atoms (long range order) and it has turned out that the structure dependent density change is, by far, the most important regarding the residual stresses [13]. Therefore, only the change in density is considered here. Such relaxation is referred to as the volume relaxation due to mass conservation.

Figure 2 sketches the development of the volume as a function of the temperature for different cooling rates. When the glass is cooled from above its melting temperature, T_m, it might crystallize when reaching T_m following Curve c in the figure, however, the rate of crystallization in silica glasses is very low and crystallization is unlikely to occur even for relatively slow cooling rates [19].

It is seen that for a relatively high cooling rate (Curve a), the density in the solid state becomes smaller (higher volume) than for a relatively lower cooling rate (Curve b). The dashed part on the curves indicate the glass transition range.

The phenomenon of structural relaxation was first treated by Tool [12] who introduced the fictive temperature, T_f, as a measure of the degree of non-equilibrated glass. The fictive temperature for a glass can be interpreted as the temperature where the extension lines of the solid state and the liquid state intersect [20]. The fictive temperatures for a glass following Curve a and Curve b in Figure 2 respectively are denoted T_f^a and T_f^b as indicated in the figure.

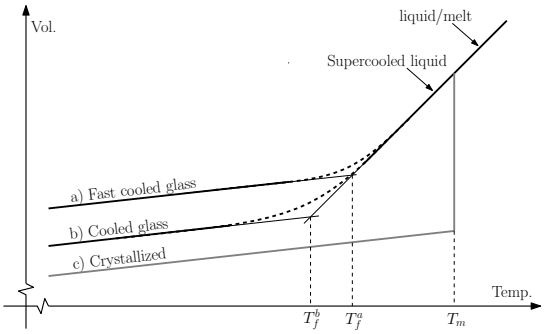

Figure 2: Variation of volume with temperature for different cooling rates. Curve c represents the crystalline state with an abrupt change in volume when the melting temperature, T_m, is passed.

In 1971 Narayanaswamy [11] proposed a mathematical formulation to be used in conjunction with the viscoelastic tempering model described in [10]. The structural model is capable of describing the property changes for different cooling rates, considerably improving the model based on viscoelasticity alone [13].

The fictive temperature for a specific property is found from the corresponding response function, $M(t)$, which is obtained experimentially. The equation for determining the fictive temperature from the response function is, see [11]:

$$T_f(t) = T(t) - \int_0^t M(\xi(t) - \xi'(t))\frac{\partial T(t')}{\partial t'}dt' \tag{6}$$

where the scaled time is given by (3) using a shift function dependent on the fictive temperature, given by:

$$\ln\left(\phi_v(T, T_f)\right) = \frac{H}{R_g}\left(\frac{1}{T_B} - \frac{x}{T} - \frac{1-x}{T_f}\right) \tag{7}$$

with

$$H = H_g + H_s \qquad , \qquad x = \frac{H_g}{H} \quad x \in [0; 1] \tag{8}$$

where H_g and H_s are the activation energies associated with temperature and structure (long range order), respectively and x is a factor controlling the relative influence of H_g and H_s.

[3] often the term *reduced time* is used for ξ. This might be misleading since the theory covers both contraction and extension of the time scale.

[4] The name "Shift function" refers to the derivation using a logarithmic time, where the scaling of linear time is represented by a shift.

When the fictive temperature is found from (6), the property associated with it can be derived. As stated before, only the volume relaxation is considered and due to the isotropy of the material this is accounted for by a change of the thermal strains. The thermal strains can now be found by the following relation

$$\Delta\varepsilon_{ij}^{th} = \delta_{ij}\Delta\varepsilon_{th} = \delta_{ij}\left(\alpha_g\Delta T + (\alpha_l - \alpha_g)\Delta T_f\right) \tag{9}$$

where α_l and α_g are the isotropic thermal expansion coefficients for the liquid and solid state, respectively.

When the temperature is high enough for the material to be in the liquid state the fictive temperature equals the real temperature, $T_f = T$, and the solid expansion coefficient, α_g cancels out in (9). During the transition, the fictive temperature is lacking behind the real temperature, $T < T_f$ (for cooling) and the expansion coefficient changes. When the temperature is low enough for the material to be solid, the fictive temperature is constant, $\Delta T_f = 0$, and the last term, including the liquid expansion coefficient α_l, vanishes.

3. Implementation

This section provides an implementation of the model described above, into a material routine for a finite element program. First the temperature independent linear viscoelastic model is treated, then it is extended to include the TS behavior, and finally, the structural volume relaxation is included. The algorithms are all well known from litterature such as [21, 22, 23, 24, 25].

3.1. Linear Viscoelasticity

In general, an integration of the load history is needed in order to evaluate (2), however, such time and memory consuming operations can be avoided if the scaling of the relaxation functions is independent of the time considered, see e.g. [23]. This condition can be written as:

$$\frac{R(t+\Delta t)}{R(t)} = f(\Delta t) \tag{10}$$

where $f(\Delta t)$ represents an arbitrary function, independent of the total time, t. This condition is satisfied for series of exponential functions which, therefore, with great advantage can be used for describing the viscoelastic behaviour of the shear and bulk relaxation moduli, $G(t)$ and $K(t)$, respectively.

$$\begin{aligned} G(t) &= \sum_{n=1}^{N_G} g_n \exp\left(-\frac{t}{\lambda_n^g}\right) \\ K(t) &= \sum_{n=1}^{N_K} k_n \exp\left(-\frac{t}{\lambda_n^k}\right) \end{aligned} \tag{11}$$

In Figure 3, a mechanical interpretation of $G(t)$ in (11) is shown. The mechanical model represents the *generalized Maxwell* material constructed by N_G single *Maxwell* elements in parallel. Each Maxwell element consists of a spring stiffness, g_n, and a dashpot with the relaxation time λ_n^g in a sequence. The exponential series might also include a constant term for describing the deferred moduli, and are often referred to as Prony series. However, here the deferred modulus will be represented by an extra exponential term with a large relaxation time, $\lambda \gg t$.

It should be noted that the strains in each branch of the generalized Maxwell element are equal, (12), and that the total stress equals the sum of the stress in each branch, (13).

$$e_{ij}^{(1)} = e_{ij}^{(2)} = \ldots = e_{ij}^{(N_G)} \tag{12}$$

$$s_{ij} = \sum_{n=1}^{N_G} s_{ij}^{(n)} \tag{13}$$

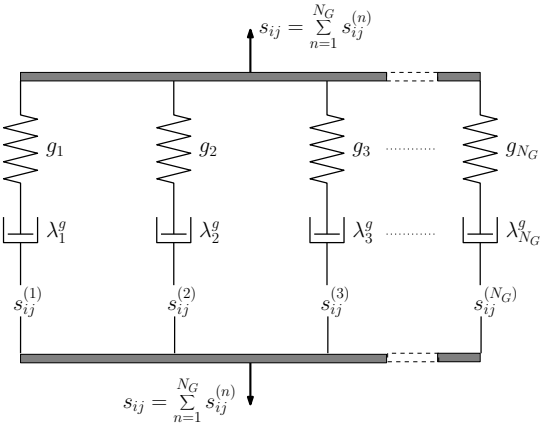

Figure 3: Generalized Maxwell element with N_G branches for the deviatoric stresses, s_{ij}.

An analogues interpretation can be made for $K(t)$ and the hydrostatic stress, σ_{ii}.

In Figure 4 a step in time from t to $t + \Delta t$ is shown on the horizontal axis and the stress associated with this increment is shown on the vertical axis. The stress increment is divided into two parts: one considering the viscoelastic response to the actual strain increment,$\Delta\breve{\sigma}_{ij}$, and another considering the relaxation of the current total stress state $\Delta\tilde{\sigma}_{ij}$, shown as Curve b and Curve d, respectively. Using (2) the viscoelastic response to the applied strain, $\Delta\breve{\sigma}_{ij}$, can be written as.

$$\begin{aligned} \Delta\breve{\sigma}_{ij} = 2\int_t^{t+\Delta t} G\left(t+\Delta t-t'\right)\frac{\partial e_{ij}(t')}{\partial t'}dt' \\ + \delta_{ij}\int_t^{t+\Delta t} K\left(t+\Delta t-t'\right)\frac{\partial \varepsilon_{ii}(t')}{\partial t'}dt' \end{aligned} \tag{14}$$

By assuming a linear strain variation in each time step and evaluating the integral of the exponential series analytically Equation (14) may, when writing the deviatoric and hydrostatic part separately, be written as

$$\Delta\breve{s}_{ij}^{(n)} = 2g_n\frac{\Delta e_{ij}}{\Delta t}\lambda_n^g\left(1-\exp\left(-\frac{\Delta t}{\lambda_n^g}\right)\right) \tag{15a}$$

$$\Delta\breve{\sigma}_{ii}^{(n)} = k_n\frac{\Delta \varepsilon_{ii}}{\Delta t}\lambda_n^k\left(1-\exp\left(-\frac{\Delta t}{\lambda_n^k}\right)\right) \tag{15b}$$

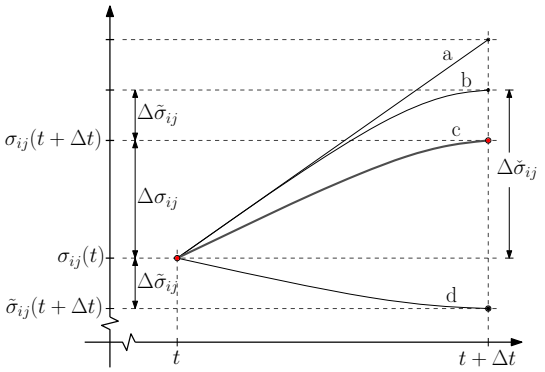

Figure 4: Incremental formulation for the viscoelastic stress response. The increment has been divided into two parts; the viscoelastic increment and the decay of the current stress state.

for each term in the exponential series in (11).

The stress relaxation of the current stress state, $\Delta\tilde{\sigma}_{ij}(t)$, is found by scaling, using the relaxation function. This scaling eliminates the need for an integration of the full load history and complies with (10) if it is done for each term in the exponential series. The new stress state at $t+\Delta t$ is denoted $\tilde{\sigma}_{ij}(t+\Delta t)$ which, in terms of deviatoric and hydrostatic stresses, can be written as

$$\tilde{s}_{ij}^{(n)}(t+\Delta t) = s_{ij}^{(n)}(t)\exp\left(-\frac{\Delta t}{\lambda_n^g}\right) \tag{16a}$$

$$\tilde{\sigma}_{ii}^{(n)}(t+\Delta t) = \sigma_{ii}^{(n)}(t)\exp\left(-\frac{\Delta t}{\lambda_n^k}\right) \tag{16b}$$

Hence, only the total stress for each term in (11) is needed from the previous time step, not the complete history.

The total stress increment for each branch in the generalized Maxwell material can now be calculated by adding (15) and (16).

$$s_{ij}^{(n)}(t+\Delta t) = \Delta\check{s}_{ij}^{(n)} + \tilde{s}_{ij}^{(n)}(t+\Delta t) \tag{17a}$$

$$\sigma_{ii}^{(n)}(t+\Delta t) = \Delta\check{\sigma}_{ii}^{(n)} + \tilde{\sigma}_{ii}^{(n)}(t+\Delta t) \tag{17b}$$

The total stress tensor, σ_{ij}, is found by summing over all branches.

$$\sigma_{ij}(t+\Delta t) = \sum_{n=1}^{N_G} s_{ij}^{(n)}(t+\Delta t) + \delta_{ij}\sum_{n=1}^{N_K}\sigma_{ii}^{(n)}(t+\Delta t) \tag{18}$$

The total stress is represented as Curve c in Figure 4.

3.2. Thermorheological Simplicity

In order to implement the TS material behavior the real time increment, Δt, has to be substituted with the scaled time increment, $\Delta\xi$. Rewriting (3) to an incremental form and using the trapeziodal integration rule (assuming linear temperature variation in the step), the scaled time step may be written as

$$\Delta\xi = \int_t^{t+\Delta t}\phi dt' \approx \frac{\Delta t}{2}\left(\phi(T+\Delta T)-\phi(T)\right) \tag{19}$$

where $\phi(T)$ is found from equation (5).

The value of the scaled time may vary with several orders of magnitude depending on the temperature, which might cause numerical problems when the material behaves almost like a linear elastic material and the scaled time step becomes small ($\Delta\xi \to 0$). A remedy for this problem is to use a Taylor expansion for the critical part of (15) when $\Delta\xi \to 0$

$$\frac{\lambda}{\Delta\xi}\left[1-\exp\left(-\frac{\Delta\xi}{\lambda}\right)\right] = \frac{\lambda}{\Delta\xi}\left(1-\sum_{k=0}^{\infty}\frac{1}{k!}\left(-\frac{\Delta\xi}{\lambda}\right)^k\right) \tag{20}$$

An investigation reveals that using the first three terms in the Taylor expansion for $\Delta\xi < 10^{-7}$ causes relative errors less than 10^{-10}.

For high temperatures a considerable decay of the stresses occurs and convergence will be slow if the linear elastic material tangent stiffness is used. By updating the material tangent stiffness matrix, D_T, using (15) the convergency rate can be improved. Curve a and b in Figure 4 represent the linear elastic step and the viscoelastic step, respectively. The viscoelastic material tangent stiffness matrix can be written as

$$\boldsymbol{D}_T = \begin{bmatrix} B+4A & B-2A & B-2A & 0 & 0 & 0 \\ B-2A & B+4A & B-2A & 0 & 0 & 0 \\ B-2A & B-2A & B+4A & 0 & 0 & 0 \\ 0 & 0 & 0 & 3A & 0 & 0 \\ 0 & 0 & 0 & 0 & 3A & 0 \\ 0 & 0 & 0 & 0 & 0 & 3A \end{bmatrix} \tag{21}$$

where

$$A = \frac{1}{3}\sum_{n=1}^{N_G} g_n\frac{\lambda_n^g}{\Delta t}\left(1-e^{-\frac{\Delta t}{\lambda_n^g}}\right) \quad , \quad B = \sum_{n=1}^{N_K} k_n\frac{\lambda_n^g}{\Delta t}\left(1-e^{-\frac{\Delta t}{\lambda_n^g}}\right) \tag{22}$$

3.3. Structural Volume Relaxation

The structural relaxation is inherently non-linear as seen from (6) and (7), however, by describing the response function $M(\xi)$ by an exponential series, an efficient and stable algorithm as proposed by Markovsky & Soules [26] may be utilized for solving the equations, and thereby determining the fictive temperature T_f. The exponential series reads:

$$M(\xi) = \sum_{n=1}^{N_M} m_n\exp\left(-\frac{\xi(T,T_f)}{\lambda_n^m}\right) \quad , \quad \sum_{n=1}^{N_M} m_n = 1 \tag{23}$$

where ξ depends on both T and T_f, and can be found from (7). In the algorithm for obtaining T_f from (6), a "partial fictive temperature" $T_f^{(n)}$ which is linked to the n'te term in the response function (23), is calculated from

$$T_f^{(n)}(t) = \frac{\lambda_n^m T_f^{(n)}(t-\Delta t) + T(t)\Delta t\phi_v}{\lambda_n^m + \Delta t\phi_v} \tag{24}$$

where

$$\phi_v = \exp\left[\frac{H}{Rg}\left(\frac{1}{T_B}-\frac{x}{T(t)}-\frac{1-x}{T_f(t-\Delta t)}\right)\right] \tag{25}$$

The fictive temperature at the current time, $T_f(t)$, is then given by the sum of the partial fictive temperatures weighted with m_n

$$T_f(t) = \sum_{n=1}^{N_M} m_n T_f^{(n)}(t) \tag{26}$$

The initial conditions for $T_f^{(n)}$ and T_f are:

$$T_f^{(n)}(0) = T(0) \qquad , \qquad T_f(0) = T(0) \tag{27}$$

It is seen that each partial fictive temperature, $T_f^{(n)}$, from the previous time step is needed together with the fictive temperature, T_f, from the previous time step.

The algorithm above can be shown to be stable for monotonic temperature changes [26].

The thermal strain increments, $\Delta\varepsilon_{ij}^{th}$, can now be found by the use of (9) and are subtracted from the normal strain increments originating from the mechanical boundary conditions, $\Delta\varepsilon_{ij}^{mech}$,

$$\Delta\varepsilon_{ij} = \Delta\varepsilon_{ij}^{mech} - \Delta\varepsilon_{ij}^{th} \tag{28}$$

From this strain increment tensor the deviatoric strain increment can be calculated as

$$\Delta e_{ij} = \Delta\varepsilon_{ij} - \frac{1}{3}\delta_{ij}\Delta\varepsilon_{ii} \tag{29}$$

In order to summarize this section, an overview of the implementation of the model is given in Figure 5. The parameters to the left of an arrow are needed in order to calculate the result provided to the right of the arrow. The numbers above the arrows refer to the relevant equations in the present paper.

4. Convergence, Verification and Application

The algorithm has been implemented as a material subroutine in the commercial finite element program Abaqus [27]. This section validates the model and investigates the discretization regarding time and geometry. Experimental validation of the tempering theory presented has been reported for a 1D model by [13] and a 3D model by [14]. However, the present paper presents a comparison with experiments and a discussion of the deviations for different cooling rates which has not, to the knowledge of the authors, been reported before.

4.1. Comparison with analytical solution

In order to verify the thermorheologically simple part of the implementation, an analytical one-dimensional model for a prescribed load– and temperature history has been derived, see Appendix Appendix A. The relaxation modulus, the load and the temperature used in the analytical solution have been fitted to a numerical simulation of the tempering process at the surface, however, it should be emphasized that the solution does not reflect any physical process and that the model only describes a single material point. The numerical solution is therefore independent of the number of elements used, however, it provides a convenient way to test the specific part of the implementation.

Figure 6 shows the analytical solution together with the solutions obtained from the implementation presented in Section 3 (without structural relaxation). From the figure it is seen that the simulation follows the analytical solution.

FICTIVE TEMPERATURE

for n=1 to N_m **do**

$\left.\begin{matrix}\lambda_n^m, T_f^{(n)}(t-\Delta t), T(t), \Delta t,\\ \phi_v(T(t), T_f(t-\Delta t))\end{matrix}\right\} \xrightarrow{(24)} T_f^{(n)}(t)$

$m_n, T_f^{(n)}(t) \xrightarrow{(26)} T_f(t)$

end for

STRAIN INCREMENTS

$\alpha_g, \alpha_l, \Delta T, \Delta T_f \xrightarrow{(9)} \Delta\varepsilon_{ij}^{th}$

$\Delta\varepsilon_{ij}^{mech}, \Delta\varepsilon_{ij}^{th} \xrightarrow{(28)} \Delta\varepsilon_{ii}$

$\Delta\varepsilon_{ij} \xrightarrow{(29)} \Delta e_{ij}$

SHIFTED TIME

$\Delta t, \phi(T(t), T(t+\Delta t)) \xrightarrow{(19)} \Delta\xi$

DEVIATORIC STRESSES

for n=1 to N_G **do**

$g_n, \lambda_n^g, \Delta e_{ij}, \Delta\xi \xrightarrow{(15a)/(20)} \Delta\check{s}_{ij}^{(n)}$

$\lambda_n^g, s_{ij}^{(n)}(t), \Delta\xi \xrightarrow{(16a)} \tilde{s}_{ij}^{(n)}(t+\Delta t)$

$\tilde{s}_{ij}^{(n)}(t+\Delta t), \Delta\check{s}_{ij}^{(n)} \xrightarrow{(17a)} s_{ij}^{(n)}(t+\Delta t)$

end for

HYDROSTATIC STRESS

for n=1 to N_K **do**

$k_n, \lambda_n^k, \Delta\varepsilon_{ii}, \Delta\xi \xrightarrow{(15b)/(20)} \Delta\check{\sigma}_{ii}^{(n)}$

$\lambda_n^k, \sigma_{ii}^{(n)}(t), \Delta\xi \xrightarrow{(16b)} \tilde{\sigma}_{ii}^{(n)}(t+\Delta t)$

$\tilde{\sigma}_{ii}^{(n)}(t+\Delta t), \Delta\check{\sigma}_{ii}^{(n)} \xrightarrow{(17b)} \sigma_{ii}^{(n)}(t+\Delta t)$

end for

TOTAL STRESSES

$s_{ij}^{(n)}(t+\Delta t), \sigma_{ii}^{(n)}(t+\Delta t) \xrightarrow{(18)} \sigma_{ij}(t+\Delta t)$

Figure 5: Overview of the implementation of the tempering model

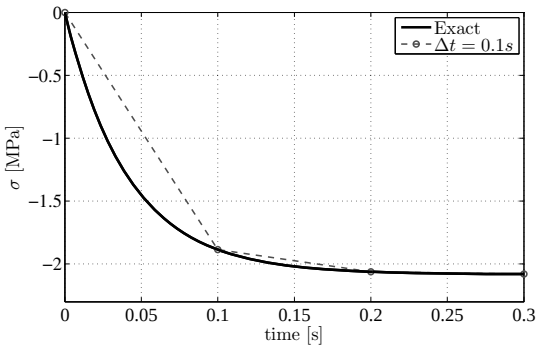

Figure 6: The analytical solution along with a run using $\Delta t = 0.1$ s.

4.2. Comparison with experimental results

Experimental results for the tempering process are rarely reported in the literature, however, [28] presents an experimental

investigation of the mid-plane stress for varying initial temperatures, T_{init} and forced convection constants, h.

In Figure 7 the model is compared with the test results. It is seen that the model captures the observed trend from the experiments quite well. It is worth noting that for $h = 222\,\mathrm{W/m^2{\cdot}K}$ there is a good correlation between the model and the experimental results. This value of h corresponds to what is needed for producing commercially tempered glass according to [28].

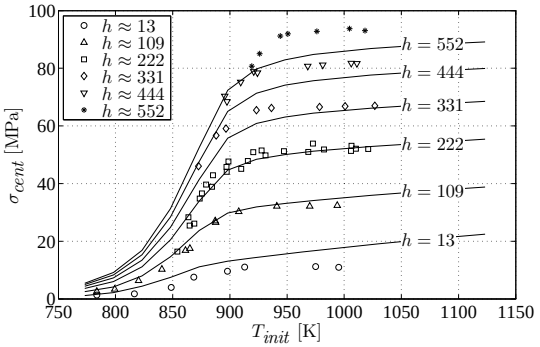

Figure 7: Experimental validation of model for different forced convection constants, h, and initial temperatures, T_{init}. Experimental results are found in [28]. The forced convection constants have the unit of $\mathrm{W/(m^2{\cdot}K)}$.

The experiments conducted in [28] are of a relatively complex nature and uncertainties on e.g. the determination of h and the residual stresses are present. In order to see if the model can be fitted in a simple manner to more accurately represent the experimental observations, a fit using h as the only parameter is performed. This is motivated by assuming that the there might be an error in the measurement of h which is a function of the air flow velocity (expressed by h itself). The fitted values of h are denoted h_{fit} and the obtained correlation between h and h_{fit} is shown in Figure 8.

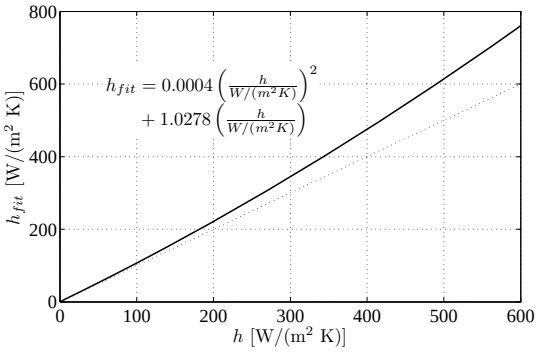

Figure 8: Fitted values of the forced convection constant h_{fit} as a function of the originally used forced convection constant, h.

Using the fitted values of h for the modeling and comparing with the experimental results, Figure 9 is obtained.

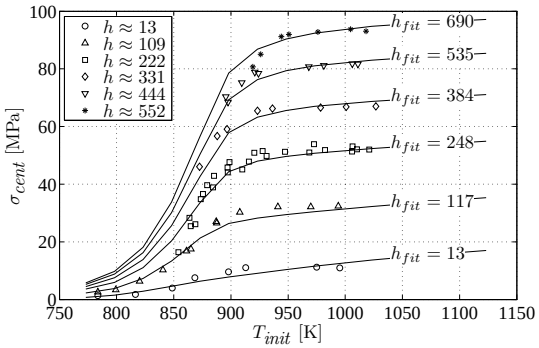

Figure 9: Comparison with experiments [28] using the fitted values for the forced convection constant, h_{fit}. The forced convection constants have the unit of $\mathrm{W/(m^2{\cdot}K)}$.

It is seen that with such simple adjustment, the model is capable of reproducing the experimental results quite accurately even for relatively extreme cooling rates. This indicates that there might be uncertainties in the experimental work in [28] and these may be accounted for (by modifying h).

4.3. Convergence

The implementation presented previously can be used for simulating the state of residual stress in complex 3D geometries modeled using solid elements. In general the convergence is dependent on the problem simulated. However, in this section, a model representing the stress state through the thickness of a glass plate is used for investigating the convergence. However, the presented curves are in principal only valid for the specific parameters used here.

The plate considered is 19 mm thick and cooled symmetrically from both sides. The models described in this section consists of solid elements with proper boundary conditions, representing the large distance to the edges, (see [29]). Relevant model parameters can be found in Appendix B.

The development of stresses over time at the surface and in the center is shown in Figure 10. It is seen that during the transition period the surface goes into tension. The maximum transient tensile surface stress is denoted $\sigma_{surf,max}$ as shown in the figure. When the plate has cooled to a uniform temperature in the solid state, the stresses will be constant and referred to as the steady state stresses, denoted σ_{cent} and σ_{surf} for the center and surface stresses, respectively, see Figure 10.

These three stresses are considered for convergency throughout this investigation. The model is implemented in a material user-subroutine in Abaqus and 20–node coupled displacement-temperature continuum elements with quadratic displacement fields and linear temperature field have been applied. The results in this section are normalized using the most trustworthy solution, meaning the solution with most elements and/or smallest time-steps.

The curves in Figure 11 show the convergence for perfectly cubic shaped solid elements, uniformly distributed. The cooling

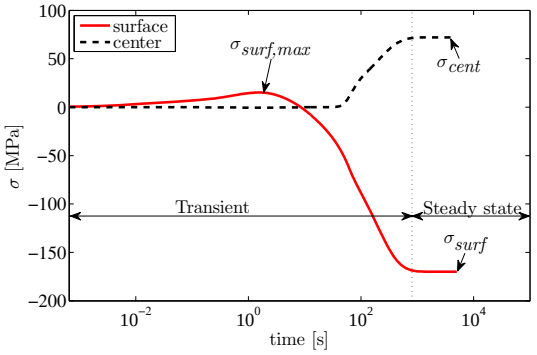

Figure 10: Typical development of the surface and center stresses during the cooling process.

rate is controlled by the forced convection constant, h. A convergency analysis for three different values of h is performed and shown in Figure 11. The value $h = 280.1\,\mathrm{W/m^2K}$ is reported by [14] for a 6 mm thick plate and must be considered quite high for a 19 mm plate, indicating a more severe cooling than required for obtaining a reasonable level of residual stress values.

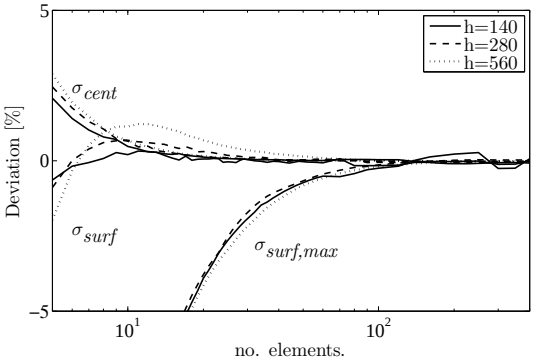

Figure 11: Convergency for uniformly distributed 20-node hexahedron elements for different cooling rates.

In Figure 11 it is seen that for an increasing cooling rate; the deviation for σ_{surf} is slightly increased for an equal number of elements. It is furthermore seen that for the steady state stresses, five elements through half the thickness provides a reasonable convergence, however, for the transient stress more than fifteen uniformly distributed elements are required for reaching convergence within 5 %.

An investigation on the influence of the time step has been carried out. The step size was controlled by setting a limit to the maximum temperature change, ΔT_{max}, within an increment. From Figure 12 it is seen that care should be taken when allowing for too large temperature changes in each step (large time steps).

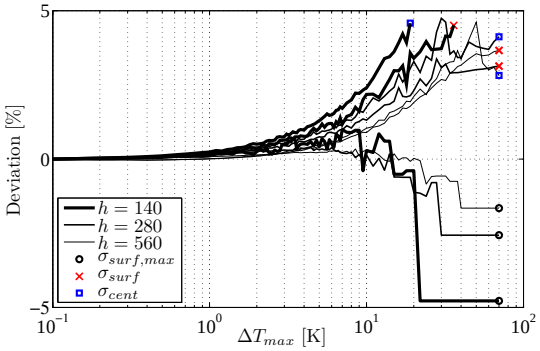

Figure 12: Step size convergency, regulated using a maximum temperature change, $\Delta\, T_{max}$, in the increment.

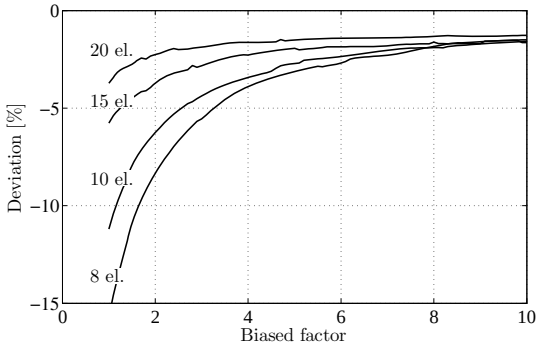

Figure 13: Biased element convergency for the transient surface stress, $\sigma_{surf,max}$.

In order to minimize the number of elements, an investigation on how the transient stresses converge towards the best solution (1200 elements) is shown in Figure 11. From this figure it is seen that convergence is reached for the residual steady-state stresses (far from any edges) with quite few elements through the thickness. However, the transient surface tensile stresses require more elements for reaching convergence due to the more complex transient stress distribution.

By increasing the mesh density near the surface, convergence can be reached with fewer elements. For investigating this we define the bias factor as the ratio between the length of the center element and the length of the surface element in the direction along the surface normal.

These investigations revealed that the biased mesh had a major positive effect on the convergence of the transient stresses, a small effect on the steady state center stresses and an insignificant effect on the steady state surface stress. In Figure 13 (only showing the transient stresses) it is seen that the convergence improve with higher bias ratio, however, since the steady state center stresses diverge for an increased bias ratio, an optimum exists.

As a result of the diverging tensile stresses, the curves in the figure do not approach the solution obtained for 1200 uniformly distributed elements. A recommended bias ratio for this type of problem would be between 4 and 8, with the element size decreasing towards the surface. However, it should be emphasized that the stress state at corners and edges is more complex and requires more elements.

4.4. 3D Residual Stress Field - Example

The possible applications for the model described and validated in the preceding are numerous. This example shows the evolution of tempering stresses in a square glass plate with a centrally located hole (see Figure 14(a)), during the process. In Figure 14, 1/16 of the geometry is shown at three different times. In this case the maximum transient stress is found at the edge after approximately 20 s of cooling (Figure 14(b)). After approximately 100 s the surface is in compression and the compression zones are seen to expand, increasing the tensile stresses in the interior (Figure 14(c)). Finally the temperature is uniformly distributed and the residual (steady-state) stresses are shown in Figure 14(d). Due to the variation in the residual stresses, a spatial dependency of the apparent strength is a consequence. Stresses far away from the edges approach a planar hydrostatic stress state corresponding to the results found in the previous section.

For plates with holes, the largest compressive stresses are typically found in the surface of the hole near the surface of the plate and most far away from the corner. A parametric investigation of the residual stresses at holes for different geometries may be found in [30].

5. Conclusion

The theory and implementation of a model predicting the evolution of 3D stress state during the glass tempering process is developed. The model is based on thermorheological simplicity and structural relaxation. The thermorheologically simplicity relates the decay of stresses to the temperature history, while the structural relaxation relates the density change to the history of the cooling rate. The theory and implementation of these models is comprehensively described in order to enable the reader to easily understand and implement such model in own code.

The implemented model is capable of predicting transient stresses as well as steady-state stresses for complex geometries and thereby provides a strong tool for optimization of the tempering process as well as estimating the steady-state residual stresses in tempered glass in order to evaluate the spatially dependent apparent strength. An analytical expression for testing the thermorheologically part of the model have been derived and used for verifying that part of the model.

The model has also been validated against experimental data showing that for commonly used convection constants for tempered glass, the model is quite accurate. For high or low cooling rates the model deviates more from the experimental results, however, it is shown that this can be accounted for by adjusting a single parameter, namely the forced convection constant.

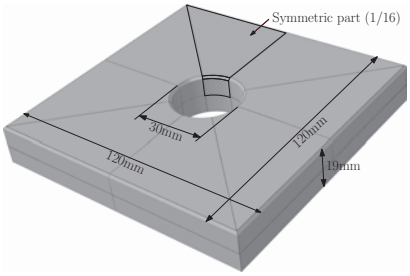

(a) 1/16 symmetry.

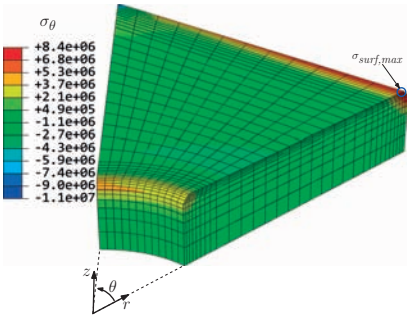

(b) $t \approx 20\,\mathrm{s}$

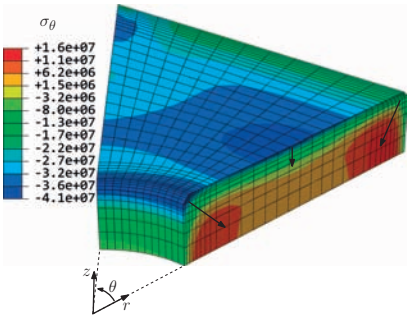

(c) $t \approx 100\,\mathrm{s}$

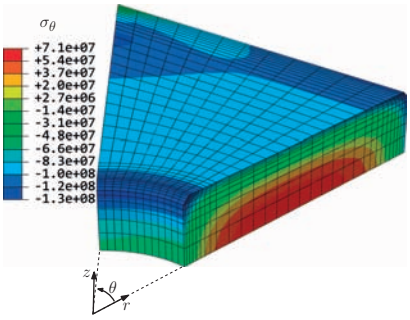

(d) $t \to \infty$

Figure 14: The development of (tangential) stresses, σ_θ during tempering.

Convergence analyses have been performed on a model representing a symmetrically cooled glass plate far from any edge. It was found that the convergence depends on the cooling rate, however, the dependency is weak for realistic values of the cooling rate quantified by the forced convection constant h.

Finally, an example showing the stress state at three different stages for a square glass plate with a centrally located hole is given.

Appendix A. Analytical Solution

The solid considered has a known temperature history, independent of the spatial coordinates, x_i, and without any thermal contraction.

$$T(x_i, t) = T(t) = \frac{c}{\ln(at + b)} \tag{A.1}$$

where t is the time and a, b, c are constants to be defined. Using the shift function defined in (5), and substituting the temperature relation from (A.1) we find

$$\ln(\phi(T)) = H\left(\frac{1}{T_B} - \frac{\ln(at + b)}{c}\right) \tag{A.2}$$

where T_B and H are constants to be defined.

The relaxation modulus for uniaxial load is described by a single exponential term:

$$E(t) = E_0 e^{-\frac{t}{\lambda}} \tag{A.3}$$

where E_0 and λ are constants to be defined.

The material is exposed uniaxially to a prescribed strain, which is a known function of time.

$$\frac{d\varepsilon(t)}{dt} = \begin{cases} k\,(at + b)^{\left(-\frac{H}{c}\right)} & \text{for } t \geq 0 \\ 0 & \text{for } t < 0 \end{cases} \tag{A.4}$$

where k is the only constant to be defined, since the rest are known from the previous equations.

Due to the uniaxial load and the independency of the spatial coordinates the convolution integral can be written as

$$\sigma(t) = \int_0^t E\left(\xi - \xi'\right) \frac{d\varepsilon\left(t'\right)}{dt'} dt' \tag{A.5}$$

where ξ and ξ' are defined by (3) by using t and t' as the upper integration bound, respectively. The integration of (A.5) can be done analytically and yields

$$\begin{aligned} A_1\sigma(t) = \exp\Big[&A_5 b T_B (at + b)^{A_3} - A_5 T_B b^{A_3+1} \\ &+ A_5 t a T_B (at + b)^{A_3} - A_2 H a \lambda\Big] + A_4 \end{aligned} \tag{A.6}$$

where

$$\begin{aligned} A_1 &= \frac{-1}{\lambda E_0 k} \exp\left(\frac{H(H - 2c)}{T_B(H - c)}\right) \\ A_2 &= \frac{c}{a\lambda T_B(H - c)} \\ A_3 &= -\frac{H}{c} \\ A_4 &= -\exp\left(\frac{-Hc}{T_B(H - c)}\right) \\ A_5 &= A_2 \exp\left(\frac{H}{T_B}\right) \end{aligned}$$

Table A.1: Constants

$a = 0.2957\ 1/\mathrm{s}$	$b = 6.937$
$c = 1.676 \times 10^3\ \mathrm{K}$	$H = 22.380 \times 10^3\ \mathrm{K}$
$T_B = 779.9\ \mathrm{K}$	$k = -1.231 \times 10^8\ 1/\mathrm{s}$
$E_0 = 70 \times 10^9\ \mathrm{Pa}$	$\lambda = 0.7012\ \mathrm{s}$

Appendix B. Modeling Parameters

Table B.2: Material data for the generalized Maxwell material. The data is derived from [14]

n	g_n [GPa]	λ_n^g [s]	k_n [GPa]	λ_n^k [s]
1	1.585	6.658×10^{-5}	0.7588	5.009×10^{-5}
2	2.354	1.197×10^{-3}	0.7650	9.945×10^{-4}
3	3.486	1.514×10^{-2}	0.9806	2.022×10^{-3}
4	6.558	1.672×10^{-1}	7.301	1.925×10^{-2}
5	8.205	7.497×10^{-1}	13.470	1.199×10^{-1}
6	6.498	3.292	10.900	2.033
7			7.500	∞
sum	28.686		41.670	

Table B.3: Material data for the response function (23) for the structural volume relaxation. The data is derived from [14]

n	m_n [-]	λ_n^m [s]
1	5.523×10^{-2}	5.965×10^{-4}
2	8.205×10^{-2}	1.077×10^{-2}
3	1.215×10^{-1}	1.362×10^{-1}
4	2.286×10^{-1}	1.505×10^{-1}
5	2.860×10^{-1}	6.747
6	2.265×10^{-1}	29.630

Table B.4: Modeling parameters used.

Parameter	Value	Ref.
Plate thickness	19 mm	-
Activation energy (total), H	457.05 kJ/mol	[14]
structural/total ratio, x	0.5	[18]
Ideal Gas constant, R_g	8.31 J/mol	-
Base temperature, T_B	869 K	[14]
Solid thermal expansion, α_s	$9.10 \times 10^{-6}\ \mathrm{K}^{-1}$	[14]
Liquid thermal expansion, α_l	$25.10 \times 10^{-6}\ \mathrm{K}^{-1}$	[14]
Density, ρ	$2500\ \mathrm{kg/m^3}$	[3]
Initial Temperature, T_{init}	923.15 K	-
Ambient Temperature, T_∞	293.15 K	-
Forced convection constant, h	$280.1\ \mathrm{W/m^2{\cdot}K}$	[14]

The thermal conductivity, λ_{th}, and the specific heat, C, for soda-lime-silica glass as function of the temperature, T, is given in [14]:

$$\begin{aligned} \lambda_{th} &= 0.741\ \mathrm{W/m{\cdot}K} + T \cdot 8.58 \times 10^{-4}\ \mathrm{W/m{\cdot}K^2} \\ C &= \begin{cases} 1433 + 6.5 \times 10^{-3}\,T & T \geq 850K \\ 893 + 0.4\,T - 18 \times 10^{-8}\,T^{-2} & T < 850K \end{cases} \end{aligned} \tag{B.1}$$

The unit of C is j kg·K if the temperature is given in Kelvin.

[1] J. H. Nielsen, J. F. Olesen, H. Stang, The fracture process of tempered soda-lime-silica glass, Experimental Mechanics 49 (6) (2009) 855.

[2] J. Barsom, Fracture of tempered glass, Journal of the American Ceramic Society 51 (2) (1968) 75–78.

[3] M. Haldimann, A. Luible, M. Overend, Structural Use of Glass, IABSE, 2008.

[4] EN12150-1, Glass in building - Thermally toughened soda lime silicate safety glass - part1: Definition and descriptions (11 2004).

[5] O. Narayanaswamy, Evolution of glass tempering models, in: Glass Processing Days, 2001.

[6] L. Adams, E. Williamson, The annealing of glass, Journal of the Franklin Institute 190 (1920) 597–632.

[7] G. Bartenev, The phenomenon of the hardening of glass, Journal of Technical Physics 18, in russian.

[8] C. Kurkjian, Relaxation of torsional stress in transformation range of soda-lime-silica glass, Physics and Chemistry of Glasses 4 (4) (1963) 128–136.

[9] F. Schwarzl, A. Staverman, Time-temperature dependence of linear viscoelastic behavior, Journal of Applied Physics 23 (8) (1952) 838–843.

[10] E. Lee, T. Rogers, T. Woo, Residual stresses in a glass plate cooled symmetrically from both surfaces, Journal of the American Ceramic Society 48 (9).

[11] O. Narayanaswamy, A model of structural relaxation in glass, Journal of the American Ceramic Society 54 (10) (1971) 491–8.

[12] A. Tool, Relation between inelastic deformability and thermal expansion of glass in its annealing range, Journal of the American Ceramic Society 29 (9) (1946) 240–253.

[13] O. Narayanaswamy, Stress and structural relaxation in tempering glass, Journal of the American Ceramic Society 61 (3-4) (1978) 146–52.

[14] L. Daudeville, H. Carre, Thermal tempering simulation of glass plates: Inner and edge residual stresses, Journal of Thermal Stresses 21 (6) (1998) 667–689.

[15] W. Laufs, G. Sedlacek, Stress distribution in thermally tempered glass panes near the edges, corners and holes. part 1. temperature distributions during the tempering process of glass panes, Glass Science and Technology: Glastechnische Berichte 72 (1) (1999) 7–14.

[16] T. Bernard, R. Gy, L. Daudeville, Finite element computation of transient and residual stresses near holes in tempered glass plates, 19th International Congress on Glass (2001) 445–6.

[17] K. J. Laidler, J. H. Meiser, Physical Chemistry, 3rd Edition, Houghton Mifflin, 1999.

[18] D. R. Uhlmann, N. J. Kreidl, Glass Science and technology. 5: Elasticity and strength in glasses, Academic Press, 1980.

[19] K. J. Rao, Structural Chemistry of Glasses, Elsevier, 2002.

[20] J. Shelby, Introduction to Glass Science and Technology, 2nd Edition, The Royal Society of Chemistry, 2005.

[21] M. D. Snyder, K.-J. Bathe, A solution procedure for thermo-elastic-plastic and creep problems, Nuclear Engineering and Design 64 (1) (1981) 49–80.

[22] J. C. Simo, T. J. R. Hughes, Computational Inelasticity, Springer Science, 1998.

[23] O. Zienkiewicz, R. Taylor, The Finite Element Method - Solid Mechanics, 5th Edition, Vol. 2, Butterworth-Heinemann, 2000, 459 p, english.

[24] M. Kojic, K. J. Bathe, Inealstic Analysis of Solids and Structures, Springer, 2005.

[25] A. Ibrahimbegovic, Nonlinear Solid Mechanics, Springer Science, 2009.

[26] A. Markovsky, T. Soules, An efficient and stable algorithm for calculating fictive temperatures, Journal of the American Ceramic Society 67 (4) (1984) C56–C57.

[27] Abaqus User Subroutines Reference Manual (v.6.7) (2007).

[28] R. Gardon, The tempering of flat glass by forced convection, in: Proc. Int. Congr. Glastt, 7th, Institut National du Verre, Charleroi, Belgique, 1965, p. Paper No. 79.

[29] J. H. Nielsen, Tempered glass - bolted connections and related problems, Ph.D. thesis, Technical University of Denmark, Dept. of Civil Eng. (2010).

[30] J. H. Nielsen, J. F. Olesen, P. N. Poulsen, H. Stang, Simulation of residual stresses at holes in tempered glass, Materials and Structures, Accepted for publication.

Paper III

"Simulation of Residual Stresses at Holes in Tempered Glass - A Parametric Study"

J.H. Nielsen, J.F. Olesen, P.N. Poulsen & H. Stang

Accepted for Publication in: *Materials and Structures*

Materials and Structures
DOI 10.1617/s11527-009-9558-z

ORIGINAL ARTICLE

Simulation of residual stresses at holes in tempered glass: a parametric study

J. H. Nielsen · J. F. Olesen · P. N. Poulsen · H. Stang

Received: 3 December 2008 / Accepted: 14 October 2009

Abstract This work presents a full 3D numerical study of the residual stresses in tempered (toughened) glass near holes using Narayanaswamy's model for the tempering process. It is the objective of the paper to elucidate the influence on the minimal residual compressive stresses at holes from variations in: the far-field stress, plate thickness, hole diameter and the interaction between holes and edges and corners. The work presents novel results for the sensitivity of the residual stresses to geometric features and provides a design tool for estimating residual stresses at holes for different geometries. An example of how to extrapolate the results in terms of far-field stresses is given.

Keywords Toughened glass · Finite element simulation · Bolted connections

1 Introduction

In materials like steel, residual stresses are often disregarded in the design process due to the yielding capacity of the material. For glass, yielding is not possible and the residual stresses have a major (most often beneficial) influence on the apparent strength. Therefore, knowledge of the residual stress state around holes is of great importance for developing a safe design for bolted connections in tempered glass.

Establishment of a safe design for a bolted connection in tempered glass is a cumbersome process due to the complexity of the residual stresses near holes. Therefore, designers of structures in tempered glass need a simple tool for assisting in the design of bolted connections. The present paper provides guidelines for determining the residual stress distribution near holes in tempered glass.

Glass, unlike other materials, has unique properties such as transparency and a superior resistance against environmental conditions such as salts, acids and aerated water. Therefore glass has gained an increased attention as a structural material over the last couple of decades. Unfortunately, the brittleness of glass reduces the tensile strength due to small scratches and flaws in the surface originating from processing and handling. Furthermore, float glass is unfit for bolted connections due to its time dependent strength [5] and high sensitivity to point loads.

The process of quenching glass from above its glass transition temperature is named the tempering process and the apparent strength is typically increased 4–5 times [10], providing a better resistance to point loads. Furthermore, the part of the strength originating from the quenching process can

J. H. Nielsen (✉) · J. F. Olesen · P. N. Poulsen · H. Stang
Department of Structural Engineering, Technical University of Denmark, Kongens Lyngby, Denmark
e-mail: jhn@byg.dtu.dk

Published online: 25 October 2009

be considered time-independent. According to [11] it is therefore common practice for designers only to utilize the part of the apparent strength originating from the residual stresses.

The tempering process induces a superficial compressive residual stress state, closing the surface flaws and thereby increasing the strength. The compressive surface stresses are induced by the sudden increase in stiffness when the temperature is lowered from above the glass transition temperature. During cooling the temperature of the surface layers will decrease before the interior and thereby contract and solidify, without causing notable stresses in the interior. Afterwards, the interior part solidifies and tries to contract. This contraction is prevented by the surface layers, inducing compressive stresses at the surface and tensile stresses in the interior. Fortunately the interior regions are (nearly) flawless and capable of carrying the tensile stresses.

A common assumption for the apparent strength of tempered glass, f_{TG}, is that it can be written as the sum of the compressive residual surface stress, σ_{surf}, and the material strength of annealed glass,[1] f_{AG}

$$f_{TG} = |\sigma_{\text{surf}}| + f_{AG} \tag{1}$$

Due to the equilibrated residual stress state, drilling or cutting of tempered glass is not possible without a complete fragmentation of the specimen, see e.g. [22]. The residual stresses induced by the tempering process depend on the rate of cooling and the location of holes, and the general geometry of the specimen. This results in a geometric dependency of the apparent strength for tempered glass.

The size of tempered glass is limited due to both the handling and the manufacturing process, thus assembly of tempered glass panes is necessary to produce large structures. The assembly can be done using bolted connections which have to be designed in a safe manner.

To the best knowledge of the authors, the only existing guidelines for minimal distances between holes and edges, corners and other holes are found in the Eurocode [9], however, this code does not provide any guidelines for the apparent strength of tempered glass at holes. Designers are therefore often forced to do full-scale destructive testing in order to determine the strength of a design. Knowledge of the residual stresses at holes would assist the designer in developing a safe design. Due to the complex residual stress state near holes, commercial measuring methods covering these areas do not exists. However, measuring the residual stresses far from edges or holes is practically possible using e.g. a scattered light polariscope [1, 3, 21].

Estimating the residual stresses near edges and holes is possible using a numerical model of the tempering process. Such modeling requires in-depth knowledge of the mechanisms and the tempering conditions and is cumbersome, at least for 3D simulations.

According to [19] the tempering process of glass was patented in 1877, however, it was not until 1920 that the first simple models were developed by Adams and Williamson [2]. In 1948, Bartenev [4] utilized the relatively short transition temperature range for glass and formulated the instant freeze theory. This theory is based on the assumption that glass is fluid above the transition temperature and behaves like an elastic solid below the transition temperature. This model predicts the stresses far from any edges within 20% of the correct value [19]. However, the model is not capable of predicting reasonable transient stresses [10].

The instant freeze theory was enhanced by including the relaxation of stresses during the glass transition temperature range. Experimental data was provided in several papers around 1950 and 1960, showing that glass can be treated as a thermorheological simple material, see e.g. [12]. In 1965, Lee et al. [15] introduced a tempering model utilizing this material behavior. This model improved the results slightly, but inaccuracies for low initial temperatures were still present [10].

The last major development of the glass tempering theory was to include structural relaxation, which accounts for the fact that the slower glass is cooled the more regular the atomic structure becomes, affecting certain properties such as the thermal expansion coefficient and thereby the generated residual stresses. A model for the structural relaxation was proposed by Narayanaswamy in 1971 [17] utilizing the concept of fictive temperatures introduced by Tool in 1946 [24]. The change of expansion coefficients (volume change) has been identified as

[1] Experimental observations indicate crack healing during the tempering process which increases the strength further, see e.g. [11].

the property that contributes the most to the residual stresses [18] and the phenomenon is often referred to as volume relaxation. This model, including both viscous and structural effects is capable of predicting both transient and permanent stresses for both high and low initial temperatures and different cooling rates [10].

At the time when the theory was developed, only the stress distribution through the thickness of a plate far from any edge was considered, i.e. the one-dimensional case. However, modern computers provide enough computational power for analyzing geometries in three dimensions, see [6, 7, 13, 14]. An overview of the Narayanaswamy model and a thorough description of the implementation in 3D, as used in this work, is found in [20].

The present paper investigates the influence on the residual stresses at holes from variations in the location of the hole, the geometry and the cooling rate, providing the design engineer with a tool for designing of bolted connections in tempered glass. The results are presented relative to the stresses far away from edges where non-destructive measurement of residual stresses can be conducted, even at the construction site. This enables the designer to verify the load capacity in a particular joint after construction with reasonable accuracy.

It should be emphasized that these simulations are far from trivial and many parameters influence the residual stress state. It is therefore not possible to cover all cases and the authors have selected commonly used parameters for the models, providing the best basis for designing and further research.

It is emphasized that this paper does not consider stress concentrations originating from any external loading of the holes considered. Furthermore, the transient stresses arising during the tempering process is beyond the scope of this paper even though the model used is capable of predicting such stresses. It is therefore recommended only to use geometries which also complies with Eurocode [9] or to consult the manufacturer about which geometries they can temper.

2 Method

The tempering process is modeled using Narayanaswamy's model [17] for structural relaxation along with a thermorheological model. The implementation and a description of the model is carefully outlined in [20] where the theory is extended to three dimensions (solid elements). Here a brief description of the constitutive model will be given.

The constitutive model of the tempering process can be considered a combination of temperature dependent viscoelasticity and structural (volume) relaxation.

The temperature dependency of the viscoelasticity is accounted for by time shifting, i.e. contracting or extending the time scale when the temperature changes; this is known as a thermorheological simple material behavior. Soda-lime-silica glass belongs to this group of materials [12].

The constitutive equations describing such a material can be written in the form of a heredity integral and this integral can be split into a hydrostatic and a deviatoric part of the stress state:

$$\sigma_{ij}(t) = \underbrace{2\int_0^t G(\xi-\xi')\frac{\mathrm{de_{ij}(t')}}{\mathrm{d}t'}\mathrm{d}t'}_{\text{Deviatoric stress}} + \underbrace{\delta_{ij}\int_0^t K(\xi-\xi')\frac{\mathrm{d}\varepsilon_{ii}(t')}{\mathrm{d}t'}\mathrm{d}t'}_{\text{Hydrostatic stress}} \tag{2}$$

where σ_{ij} represents the stress tensor, G and K are the time-dependent shear and bulk moduli, respectively, e_{ij} is the deviatoric strain tensor, ε_{ii} is the trace of the strain tensor, t is the time, ξ is the shifted time, ξ' and t' are running parameters and δ_{ij} is Kronecker's delta. The shifted time is given by

$$\xi = \int_0^t \phi(T(t'))\mathrm{d}t' \tag{3}$$

where ϕ is a temperature-dependent time-scaling function, adjusting the time-scale according to the temperature. The principle of scaling the time yields a simple description of the relaxation moduli for all temperatures by providing one so-called "master" curve valid at a single base temperature.

It turns out that by choosing the functions G and K wisely, an integration of the complete strain history can be avoided (see [20]). It is therefore a huge advantage to write the relaxation moduli as

series of exponential functions—the so-called Prony series.

$$G(\xi) = \sum_{n=1}^{N_G} g_n \exp\left(-\frac{\xi}{\lambda_n^g}\right)$$
$$K(\xi) = \sum_{n=1}^{N_K} k_n \exp\left(-\frac{\xi}{\lambda_n^k}\right) \quad (4)$$

It has been shown that the rate of cooling (or heating) has an effect on certain properties such as viscosity and density [10]. This effect is attributed to the structural arrangement of the microstructure (long range order) and can be accounted for by the structural relaxation model proposed by Narayanaswamy [17]. It has been shown that the structure dependent density change is, by far, the most important regarding the residual stresses [18] and is therefore the only property considered for structural relaxation here. The effect on the density is included by modifying the thermal expansion coefficients during the cooling.

The structural relaxation model utilizes the concept of fictive temperature, T_f, as a measure of the degree of non-equilibrated glass [17, 20, 24]. The fictive temperature can be found from

$$T_f(t) = T(t) - \int_0^t M(\xi(t,T_f) - \xi'(t,T_f))\frac{\partial T(t')}{\partial t'}\mathrm{d}t' \quad (5)$$

Here M is the so-called response function for the given property (in this case thermal expansion), ξ is again used for the scaled time, however, the shift function is now different from the one used in (3), see e.g. [20].

When the fictive temperature is found, the thermal strains may be found from

$$\Delta\varepsilon_{\mathrm{th}} = \alpha_g \Delta T + (\alpha_l - \alpha_g)\Delta T_f \quad (6)$$

The presented theory for the tempering process has been validated against experimental data in [18].

An implementation of this model has been done as a user-subroutine for the commercial Finite Element software package ABAQUS and is described more thoroughly in [20]. The basic material properties used for the model can be found in Appendix.

The boundary conditions for the thermal part of the tempering are modeled using forced convection boundary conditions with varying coefficients dependent on the location of the considered surface as indicated in Fig. 1. The coefficients used are adopted from [6] and replicated in Appendix.

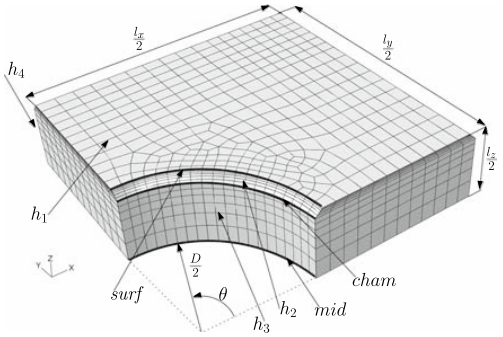

Fig. 1 Typical mesh for the models. The coefficients h_1, h_2, h_3 and h_4 refer to the forced convection boundary conditions and are given in Appendix

The elements used for this study are 20-node brick elements with a second order displacement field and a first order temperature field (C3D20T). In general, all symmetries have been utilized. The mesh consists of 10 elements through half the thickness, with increasing mesh density towards the surface, a typical mesh is seen in Fig. 1. From the figure it is seen that the side ratio for some of the elements (along the surf perimeter) is far from one. However, it has been investigated how this ratio effects the results and for this type of loading and the stress considered, the effect is insignificant.

In order to discretise the boundary of the hole, no less than 20 elements were used along the 90° segment of the hole perimeter (Fig. 1). The numerical model was verified in [20] and Narayanaswamy's model has been verified against experimental data in several publications, see e.g. [7, 8, 18].

Due to the one-way coupling between temperature and displacements, the system of equations is symmetric (7) and the solution can be achieved by solving the thermal and mechanical problems separately. The following matrix representation shows the coupled symmetric system governing the incremental behaviour.

$$\begin{bmatrix} K_{uu} & 0 \\ 0 & K_{TT} \end{bmatrix} \begin{Bmatrix} \Delta u \\ \Delta T \end{Bmatrix} = \begin{Bmatrix} R_u \\ R_T \end{Bmatrix} \quad (7)$$

Here Δu and ΔT are the respective corrections to the incremental displacement and temperature vectors,

K_{uu} and K_{TT} are submatrices representing stiffness matrices for the mechanical and thermal problems, respectively. The thermal and displacement increments are denoted ΔT and Δu, respectively, while R_u and R_T denote the incremental load vectors for the displacements and temperature, respectively.

This strategy increases the computational speed considerably compared to a solution of a fully coupled (and unsymmetric) equation system. It is also possible to solve the thermal problem first and then use that solution (by interpolation in time) for solving the mechanical problem, however, here the solutions for the two systems are obtained simultaneously in each time step without any need for interpolation of the transient solutions to the thermal problem.

Regarding the sensitivity of this model, Daudeville and Carre [7] reports a sensitivity analysis where it is shown that the reference temperature (a parameter which governs the viscoelastic material behavior) is the most influential parameter for the residual stress state. Furthermore, it should be mentioned, that obtaining material properties for the behavior of glass in the temperature transition range is difficult, and that the cooling rate in the tempering process is not uniform on the surfaces yielding a certain amount of fluctuation in the surface stress field [16] which should be taken into consideration when measuring or designing with tempered glass.

The reference geometry used throughout this paper is a plate with a thickness of 19 mm, a hole diameter of $D = 30$ mm and all edges chamfered by $a = 1$ mm (Fig. 2). Deviations from these reference values will be stated when necessary.

2.1 Definition of measures

The focus of this paper is the in-plane residual stress at the surface of the hole, and the term σ_{rc} is therefore defined here as "the residual compressive in-plane stress at the surface of the hole" (positive in compression). The minimal value of σ_{rc} is the most critical value regarding the apparent strength and is denoted $\sigma_{\mathrm{rc}}^{\mathrm{min}}$.

In order to relate the findings to more easily obtained measures, the far-field stress, σ_∞, is defined. The far-field stress for a given specimen is defined as "the undisturbed compressive surface stress observed far from edges or holes in a specimen of equal thickness and cooling history". The far-field stress used in this work is $\sigma_\infty = 83$ MPa unless otherwise specified. A value of 83 MPa for σ_∞ is experimentally supported, see e.g. [21] or [25]. Plates with this amount of residual stress will comply with the standard test procedure for classifying the glass as fully tempered [21].

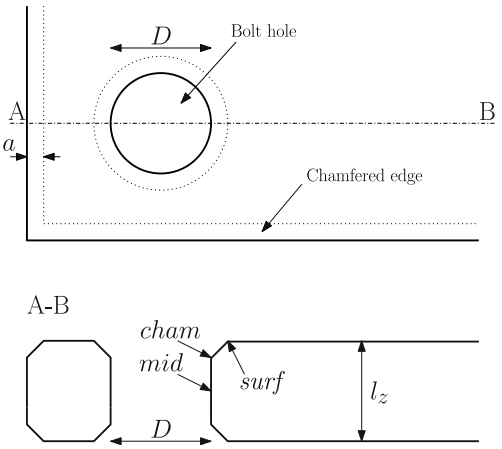

Fig. 2 Sketch of a bolt hole in a part of a glass plate with chamfered edges

The following terms are defined for later use:

$$\hat{\sigma}_{\mathrm{rc}} = \frac{\sigma_{\mathrm{rc}}}{\sigma_\infty}, \quad \text{and} \quad \hat{\sigma}_{\mathrm{rc}}^{\mathrm{min}} = \frac{\sigma_{\mathrm{rc}}^{\mathrm{min}}}{\sigma_\infty} \tag{8}$$

Hereby the actual residual stress state at the hole is related to the far-field stress, σ_∞.

3 Results

This study starts with an investigation of the correlation between σ_∞ and $\sigma_{\mathrm{rc}}^{\mathrm{min}}$. Finding such a relation is important in order for the presented results to cover cases where σ_∞ deviates from 83 MPa. When such a relation is established, a parametric investigation of a centrally located hole in a square plate is presented. For this geometry, variations of σ_∞, the size, the thickness, the diameter of the hole and a full scaling of the geometry is presented. The remaining parts of this section is concerned with the effect on σ_{rc} and $\sigma_{\mathrm{rc}}^{\mathrm{min}}$ of different locations of one or two holes and their interaction with the edges, corners and each other.

3.1 Correlation between the far-field stress and σ_{rc}

Determination of a relation between σ_∞ and σ_{rc}^{min} is interesting in order to extrapolate from σ_∞, obtained by e.g. measurements, to stresses at holes, σ_{rc}. The variation of σ_∞ was obtained by varying the forced convection coefficients between 50 and 175% of the reference values given in Appendix.

Three cases are considered here:

(1) a hole far from any edge ($l = 500$ mm, see Fig. 4),
(2) a hole close to a corner ($l_{xy} = 50$ mm, see Fig. 13), and
(3) a hole close to a single edge ($l_x = 2l_{y,s} = 700$ mm and $l_{y,e} = 75$ mm, see Fig. 9).

An almost linear correlation between σ_∞ and σ_{rc}^{min} is seen to exists for all locations of the hole, and results for (1) and (3) are almost coincident. It is noted that the slopes depend on the geometry considered, however, curve (2) represents an extreme, and in most reasonable designs, (1) will provide sufficient accuracy for an extrapolation.

If σ_∞ is known, e.g. by measurements, and the location of the hole is covered by the examples in the following, a simple extrapolation using the relations given in Fig. 3 can be made for determining σ_{rc}^{min} (see Example 1 in Sect. 4.1).

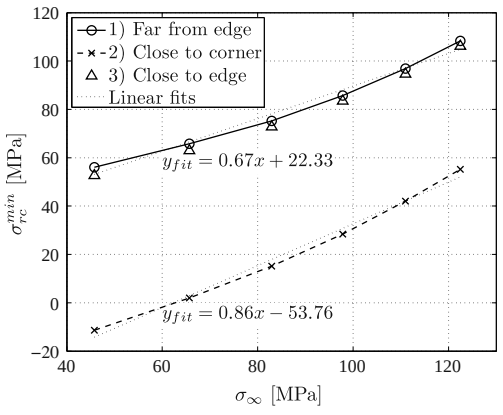

Fig. 3 Correlation between the σ_∞ stress and σ_{rc}^{min}

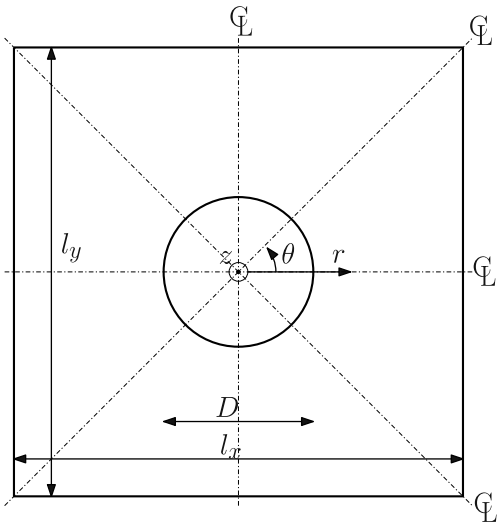

Fig. 4 Sketch of modeled plate. $D = 30$ mm, $l_z = 19$ mm and $l = l_x = l_y$, unless otherwise stated

3.2 Central hole in a square plate

A sketch of the model considered is shown in Fig. 4. As indicated in the figure only $\theta \in [0°;45°[$ needs to be modeled due to symmetry. For this model investigations on the specimen size and the scaling of the specimen has been conducted.

3.2.1 Size of the specimen

Plotting $\hat{\sigma}_{rc}^{min}$ found at the locations surf, cham and mid defined in Fig. 2, an influence from the edges is observed for relatively large plates (Fig. 5).

From this figure it is seen that $\hat{\sigma}_{rc}$ for the mid-plane, $\hat{\sigma}_{rc}^{mid}$, is most critical regarding the apparent strength and therefore $\hat{\sigma}_{rc}^{min}$ is located on the mid-plane perimeter. This is found for all the investigations carried out here and is supported by others, see e.g. the review in [11]. From Fig. 5 it is seen that $\hat{\sigma}_{rc}^{surf}$ and $\hat{\sigma}_{rc}^{cham}$ are approximately 75% higher than $\hat{\sigma}_{rc}^{mid}$. This is explained by the higher cooling rate due to cooling of two intersecting surfaces.

Comparing $\hat{\sigma}_{rc}^{mid}$ at $l = 500$ mm with $\hat{\sigma}_{rc}^{mid}$ at $l = 275$ mm a reduction of 5% is found, and for $l = 200$ mm the reduction is 10% (Fig. 5). These reductions can be attributed to the size of the

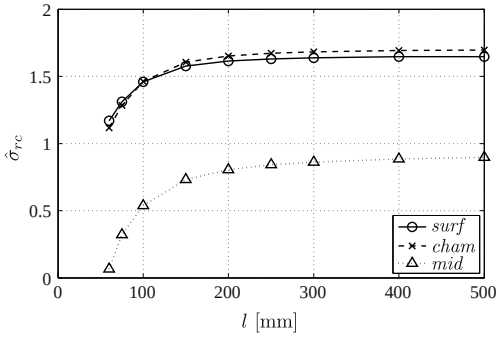

Fig. 5 Variation of the plate size. $\hat{\sigma}_{\mathrm{rc}}$ as a function of l for the locations surf, cham and mid

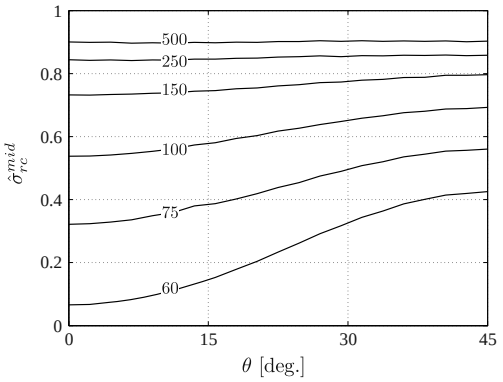

Fig. 6 The normalized stress $\hat{\sigma}_{\mathrm{rc}}^{\mathrm{mid}}$ as a function of θ for varying plate sizes, l from 60 to 500 mm

specimen. It is also seen that this effect is more pronounced for $\hat{\sigma}_{\mathrm{rc}}^{\mathrm{mid}}$, more than for $\hat{\sigma}_{\mathrm{rc}}^{\mathrm{surf}}$ and $\hat{\sigma}_{\mathrm{rc}}^{\mathrm{cham}}$.

Figure 6 shows the distribution of $\hat{\sigma}_{\mathrm{rc}}^{\mathrm{mid}}$ along the perimeter of the hole for varying length of the sides, l.

It is seen that the variation in $\hat{\sigma}_{\mathrm{rc}}^{\mathrm{mid}}$ with θ levels out for increasing plate size, and that $\hat{\sigma}_{\mathrm{rc}}^{\mathrm{mid}}$ converges towards 0.9 corresponding to 90% of σ_{∞}.

3.2.2 Scaling of the specimen

Due to the complexity of the time-dependencies in the material model and the heat transfer coefficients, a single unique scaling of the residual stress field with the geometry is impossible.

An investigation was carried out by choosing $l = 500$ mm as the specimen size and varying the

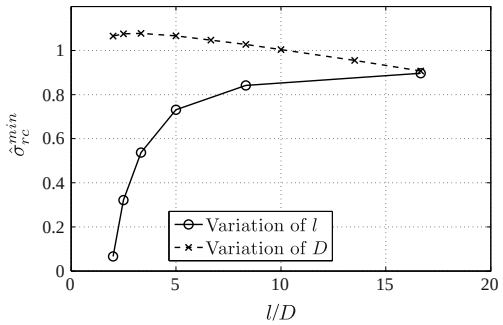

Fig. 7 Variation of l/D obtained by varying the diameter, D or the length l

diameter of the hole, D. The plot in Fig. 7 shows the results found from varying D and a curve from varying the length of the sides (Fig. 5).

It is seen that the influence from a change in D is relatively unimportant compared to a change in l. Furthermore, when decreasing the ratio l/D by increasing D an increase in $\sigma_{\mathrm{rc}}^{\mathrm{min}}$ is found as long as $l/D > 3.3$ where the curve peaks (Fig. 7).

Two phenomenons are seen to rule the generation of residual stresses: (1) the cooling rate, and (2) the amount of material available to build up and carry the stresses. In this case, the increased cooling rate when D increases and thereby the boundary of the hole approaches the edge increases the value of $\hat{\sigma}_{\mathrm{rc}}^{\mathrm{min}}$, but at some point there is a lack of material for generating and carrying the stresses and therefore, a decrease is observed for $l/D < 3.3$.

The variations of $\sigma_{\mathrm{rc}}^{\mathrm{min}}$ was also tested against a complete scaling of the geometry and a simple change of plate thickness. This was done by applying a cooling rate adjusted to obtain equal σ_{∞} for all models. A reference geometry with $l = 500$ mm and $D = 30$ mm was used for the complete scaling of the geometry while $l = 60$ mm was used for the thickness variation.

When scaling down, an increase in $\sigma_{\mathrm{rc}}^{\mathrm{min}}$ is observed (Fig. 8). This is also found for a reduction of the thickness alone where an almost linear relation is obtained.

One might be tempted to use the linear relation in Fig. 8 for extrapolating the data given in this paper to other thicknesses, however, such an approach yields results which might be unsafe (see Example 2 in

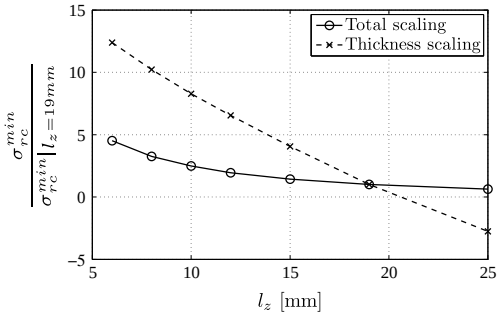

Fig. 8 Scaling of the complete model geometry expressed by the thickness, l_z, and a change of the thickness alone. Note that the curves are normalized with respect to the result for $l_z = 19$ mm

Sect. 4.1). Simple scaling of σ_{rc} with the geometry is therefore not possible.

3.3 Hole in a large pane close to edges

This section describes the influence of edges on the residual stress at a hole close to the edges. A model as sketched in Fig. 9 has been used for variations of the width, l_x, and the hole-to-edge distance, $l_{y,e}$. Three basic cases are studied:

(1) a hole close to an edge for varying widths, l_x,
(2) a variation of the hole-to-edge distance, l_y, e in a wide plate, and
(3) a hole close to a corner (Fig. 13).

3.3.1 Variation of plate width

In order to estimate the influence of l_x on σ_{rc}^{min}, a parametric study for $l_{y,e} = 53$ mm and $l_{y,s} = 350$ mm is carried out[2] and the distribution of $\hat{\sigma}_{rc}^{mid}$ is shown in Fig. 10.

Low values of $\hat{\sigma}_{rc}^{mid}$ are found at $\theta \approx 0°$ for the narrow specimens. For higher values of l_x a shift of this location is observed. The difference between the curve for $l_x = 500$ mm and $l_x = 700$ mm indicates that the sensitivity to the presence of these edges has not vanished.

[2] ly, $e = 53$ mm is the minimum distance to an edge according to [9]

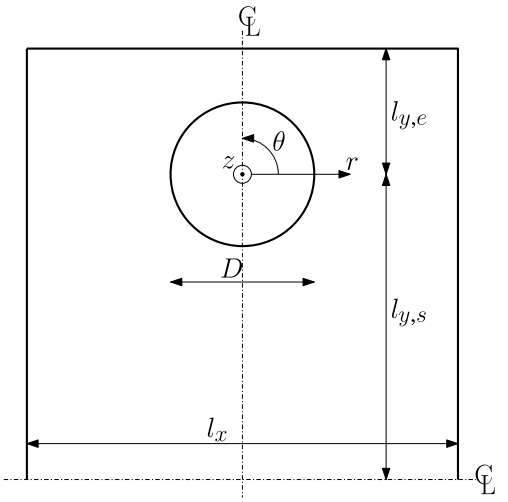

Fig. 9 Sketch of model for hole near an edge. $D = 30$ mm, $l_x = 700$ mm, l_y, $s = 350$ mm and $l_z = 19$ mm, unless otherwise stated

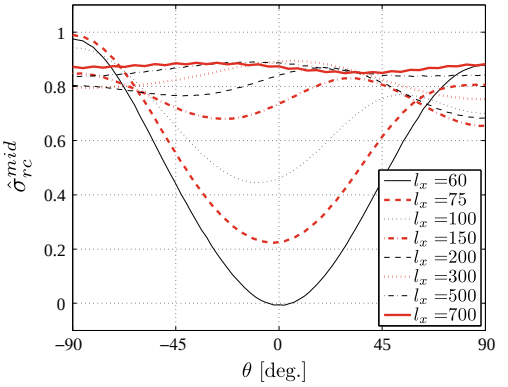

Fig. 10 The $\hat{\sigma}_{rc}^{mid}$ distribution for a variation of l_x with $l_{y,e} = 53$ mm

Plotting $\hat{\sigma}_{rc}^{min}$ as function of l_x for different $l_{y,e}$ shows that a short edge-to-hole distance, $l_{y,e}$, yields a low $\hat{\sigma}_{rc}^{min}$ (Fig. 11).

The irregularity of the curves is explained by the shift in location of $\hat{\sigma}_{rc}^{min}$. From this investigation it is seen that $\hat{\sigma}_{rc}^{min}$ for $l_x = 700$ mm has stabilized and the influence from l_x is reasonably small. However, it is worth noting that a long hole-to-edge distance increases the sensitivity to the width of the plate.

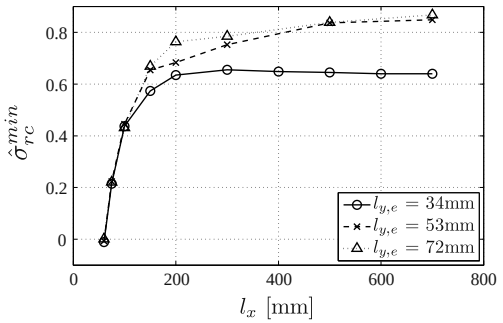

Fig. 11 Variation of l_x for three values of $l_{y,e}$

3.3.2 *Variation of the hole-to-edge distance in a wide plate*

In order to investigate the influence of the hole-to-edge distance more thoroughly, a parametric study of $l_{y,e}$ using a model with $l_{y,s} = 350$ mm was carried out.

The variation of $\hat{\sigma}_{\mathrm{rc}}^{\mathrm{min}}$ as a function of $l_{y,e}$ for two different values of l_x is shown in Fig. 12. Here it is seen that the magnitude of $\hat{\sigma}_{\mathrm{rc}}^{\mathrm{min}}$ stabilizes for $l_{y,e} > 50$ mm for the wide specimen and somewhat later for the narrow one. It should be emphasized that the lack of smoothness of the curves are caused by a change in the position of $\hat{\sigma}_{\mathrm{rc}}^{\mathrm{min}}$ on the perimeter of the hole. It is observed that for the smallest specimen ($l_x = 300$ mm) $\sigma_{\mathrm{rc}}^{\mathrm{min}}$ is lowest, which was also seen for the square specimens (Fig. 5). This indicates that if the calculations are carried out for a smaller model, then $\hat{\sigma}_{\mathrm{rc}}^{\mathrm{min}}$ will be underestimated and the predicted value of the apparent strength will be conservative.

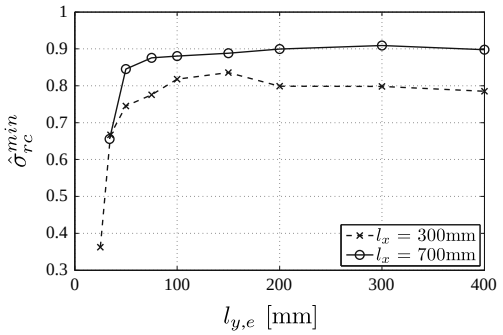

Fig. 12 Variation of $l_{y,e}$ for two values of l_x

3.3.3 *Variation of the hole-to-corner distance*

Holes in glass plates near corners are often used in the assembly of e.g. curtain walls. This section investigates such locations of the hole. The hole is located on the angular bisector of the corner, and the distance from the center of the hole to the tip of the corner is denoted l_{xy} (Fig. 13).

The location of $\hat{\sigma}_{\mathrm{rc}}^{\mathrm{min}}$ is approximately at $\theta = -35°$ (Fig. 14) and is not altered by the parametric variation due to the maintained symmetry. For $l_{xy} = 400$ mm, $\hat{\sigma}_{\mathrm{rc}}^{\mathrm{mid}}$ as a function of θ varies approximately 6%.

A graph of $\hat{\sigma}_{\mathrm{rc}}^{\mathrm{min}}$ as a function of the hole-to-corner distance, l_{xy}, is seen in Fig. 15. Comparing with the value for $\hat{\sigma}_{\mathrm{rc}}^{\mathrm{min}}$ at $l_{xy} = 400$ mm, a reduction of 7% is found for $l_{xy} = 200$ mm and a reduction of 25% is found for $l_{xy} = 100$ mm.

In the following, the found values are compared to the minimum distances given in Eurocode [9]. For $l_{xy} = 129$ mm, which is the minimum value according to Eurocode [9], $\hat{\sigma}_{\mathrm{rc}}^{\mathrm{min}}$ is found by interpolation in Fig. 15 using $\sigma_\infty = 83$ MPa to be 61 MPa. This

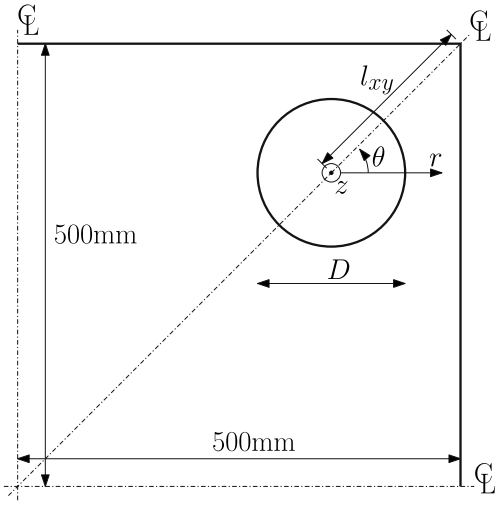

Fig. 13 Sketch of model for hole near a corner. $D = 30$ mm and $l_z = 19$ mm

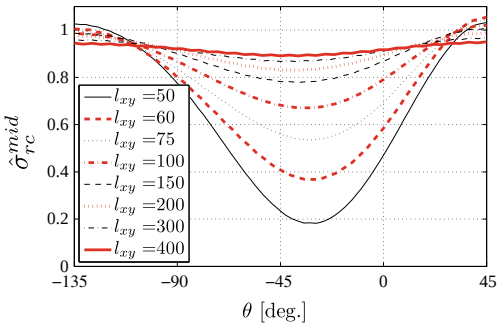

Fig. 14 Distribution of $\hat{\sigma}_{\mathrm{rc}}^{\mathrm{mid}}$ for a hole close to a corner. Note that for $l_{xy} > 129$ mm the geometry applies to [2]

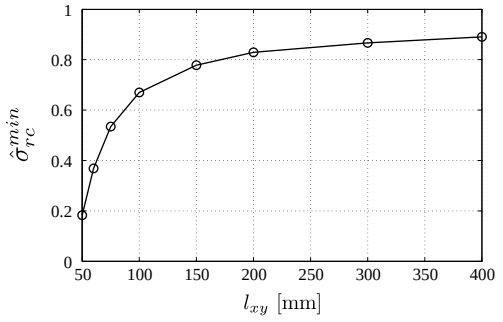

Fig. 15 Variation of the hole-to-corner distance, l_{xy}

value of σ_{∞} is higher than the 75 MPa implicitly given in Eurocode [23], see [11] or [21]. Using the curves in Fig. 3, $\sigma_{\mathrm{rc}}^{\mathrm{min}} \approx$ 55.6 MPa is found for a value of $\sigma_{\infty} = 75$ MPa complying with the Eurocode. Such a value for $\sigma_{\mathrm{rc}}^{\mathrm{min}}$ seems rather low compared to the 75 MPa assumed for the characteristic strength of 120 MPa given in Eurocode [23].

3.4 The interaction between two holes

Often more than one bolt is used in the same plate. Therefore, an investigation of the interaction between two holes has been carried out. This study consists of three cases:

(1) variation of the hole-to-hole distance, l_{h}, far from any edges,
(2) variation of l_{h} for two holes on a line parallel to an edge nearby, and
(3) variation of l_{h} for two holes on a line perpendicular to the edge.

3.4.1 *Variation of hole-to-hole distance far from edges*

For this investigation a model with $l_{x,e1} = l_{x,e2} = l_{y,e} = l_{y,s} = 350$ mm was used (Fig. 16). This model is also compared with a model where $l_{x,e1} = l_{x,e2} = 150$ mm and $l_{y,e} = l_{y,s} = 350$ mm.

In Fig. 17 the variation of $\hat{\sigma}_{\mathrm{rc}}^{\mathrm{mid}}$ along the perimeter of the hole is given. It is seen that $\hat{\sigma}_{\mathrm{rc}}^{\mathrm{min}}$ is located at $\theta = 180°$ corresponding to the point most close to the other hole. When the distance l_{h} is large, the small variation in the stress distribution is caused by the lack of symmetry, and thereby a high sensitivity to the directions in the specimen.

The variation of $\hat{\sigma}_{\mathrm{rc}}^{\mathrm{min}}$ as a function of l_{h} for two different widths is seen in Fig. 18.

In general, $\hat{\sigma}_{\mathrm{rc}}^{\mathrm{min}}$ is seen to increase for increasing hole-to-hole distance, however, the magnitude of $\hat{\sigma}_{\mathrm{rc}}^{\mathrm{min}}$ is in general lower for the more narrow plate (Fig. 18). The reduction of $\hat{\sigma}_{\mathrm{rc}}^{\mathrm{min}}$ compared to $l_{\mathrm{h}} = 220$ mm for the wide plate is less than 5% when $l_{\mathrm{h}} > 100$ mm. The corresponding value for $l_{\mathrm{h}} = 80$ mm is approximately 10% and for $l_{\mathrm{h}} = 60$ mm the reduction is more than 20%. For comparison, Eurocode [9] prescribes that $l_{\mathrm{h}} > 68$ mm where a deviation of approximately 15%.

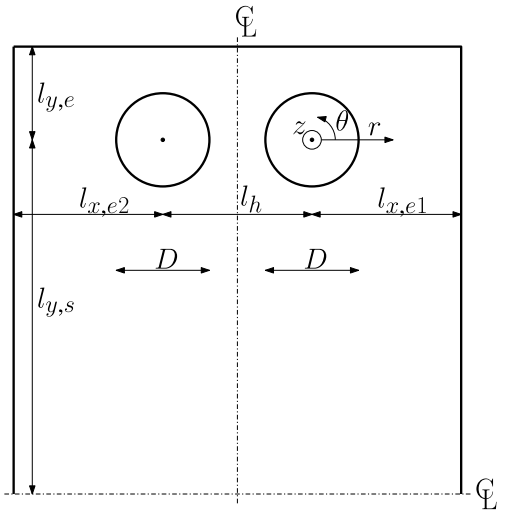

Fig. 16 Sketch of model for the interaction between two holes. $D = 30$ mm and $l_z = 19$ mm

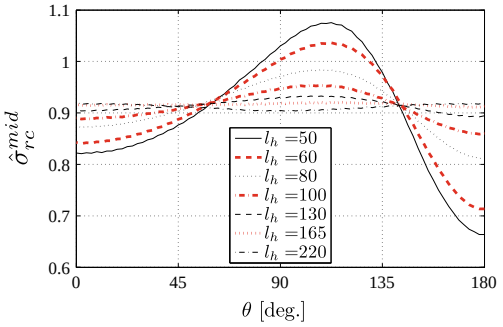

Fig. 17 Variation of the hole-to-hole distance far from edges

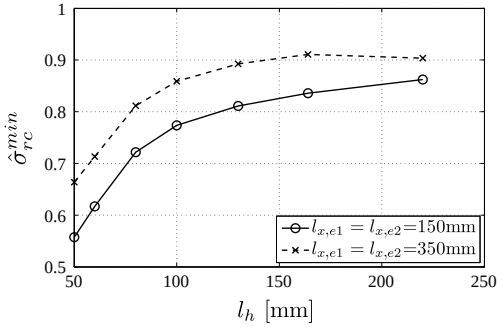

Fig. 18 Variation of the hole-to-hole distance for two holes relatively far from edges

3.4.2 *Hole-to-hole distance for two holes parallel to the edge*

A more complex example is the interaction between two holes on a line parallel to a nearby edge. A model with $l_{x,e1} = l_{x,e2} = l_{y,s} = 350$ mm and a variation of $l_{y,e}$ has been used for investigating the influence of l_h on $\hat{\sigma}_{rc}^{min}$.

The variations of $\hat{\sigma}_{rc}^{mid}$ along the perimeter of a hole located 53 mm from the edge for various hole-to-hole distances are shown in Fig. 19.

It is seen that the variation of $\hat{\sigma}_{rc}^{mid}$ is relatively complex, that the location of $\hat{\sigma}_{rc}^{min}$ is again found at $\theta = 180°$ and that the value of $\hat{\sigma}_{rc}^{min}$ is smaller compared to the holes far from edges (Fig. 17).

In Fig. 20 $\hat{\sigma}_{rc}^{min}$ is shown as a function of the hole-to-hole distance, l_h, for different values of the hole-to-edge distance, $l_{y,e}$.

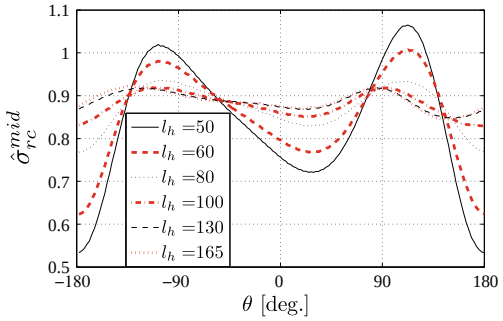

Fig. 19 The interaction between two holes close to an edge. Variation of l_h with $l_{y,e} = 53$ mm. For the geometry to comply with [2], $l_h \geq 68$ mm and $l_{y,e} \geq 53$ mm

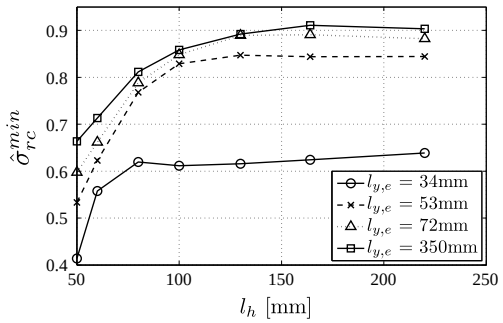

Fig. 20 Variation of hole-to-hole distance for holes parallel to the nearby edge

It is seen that for $l_{y,e} > 72$ mm or $l_h > 120$ mm not much is gained from increasing the respective distances further.

3.4.3 *Hole-to-hole distance for two holes perpendicular to the edge*

The final investigation considers the hole-to-hole distance for two holes on a line perpendicular to the edge. This geometric layout corresponds to Fig. 16 with $l_{y,e} = l_{y,s} = l_{x,e2} = 350$ mm, $l_{x,e1} = 53$ mm and varying l_h.

From Fig. 21 it is seen that the lowest value for $\hat{\sigma}_{rc}^{min}$ is found at the hole located nearest the edge, however, the difference is less than 5% between $\hat{\sigma}_{rc}^{min}$ in the two holes. Comparing these results with the results for two holes parallel to the edge (Fig. 20), $\hat{\sigma}_{rc}^{min}$ approaches the final stress level in a similar way. It is furthermore seen that $\hat{\sigma}_{rc}^{min}$ for the hole close to

the edge and $\hat{\sigma}_{rc}^{min}$ for the hole far from the edge approach the results given in Figs. 20 and 6, respectively, as expected.

4 General remarks on the results

For all the investigations carried out using $l_z = 19$ mm it has been found that σ_{rc}^{surf} and σ_{rc}^{cham} are always more than 50% higher than σ_{rc}^{mid}, regardless of the location of the holes. According to [11] this is an observation made by others and it is reported to be less distinct for thinner plates. These findings are all in agreement with the fact that near the top surfaces the cooling rate is higher which, in most cases, increases the generated compressive stresses. This situation is beneficial to bolted connections where the bending of the dowel typically will increase the stress concentration near the top- or bottom surface areas of the hole, however, detailed analysis should be considered in order to utilize this effect in the design.

From this parametric study, it is obvious that several geometries provide a certain value of σ_{rc}^{min} some examples are given in Table 1 for a single hole and Table 2 for two holes. It should be noted that even though such geometries can be used for the design they may not comply with Eurocode [9] and therefore be difficult to temper due to transient stresses. It is therefore recommended always to choose a geometry in compliance with Eurocode [9].

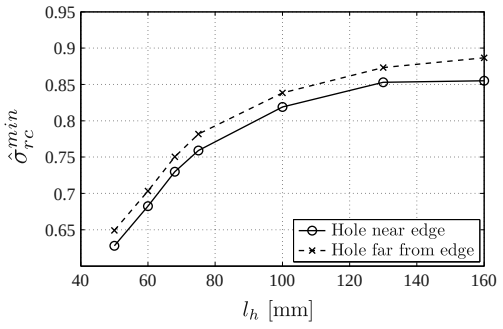

Fig. 21 Variation of hole-to-hole distance for two holes in-line perpendicular to the edge. The hole-to-edge distance for the hole close to the edge is $l_{x,e1} = 53$ mm

Table 1 Suggestion for minimum distances and corresponding $\hat{\sigma}_{rc}^{min}$ for a single hole ($l_z = 19$ mm)

$\hat{\sigma}_{rc}^{min}$	l_{min} (mm)	$l_{e,min}$ (mm)	$l_{xy,\ min}$ (mm)
0.90	350	200	400
0.85	350	53	250
0.80	150	100	170
0.75	150	53	150
0.65	75	53	90[a]

The symbols l_{min} denote the minimum distance from the center of the hole to the nearest straight edge

[a] Values that do not comply with [2]

Table 2 Suggestion for minimum distances and corresponding $\hat{\sigma}_{rc}^{min}$ for two holes ($l_z = 19$ mm)

$\hat{\sigma}_{rc}^{min}$	l_h (mm)	$l_{e,min1}$ (mm)	$l_{e,min2}$ (mm)
0.90	150	350	350
0.85	130	350	53
0.80	90	350	53
0.75	75	350	53
0.60	50[a]	350	53

l_h is the minimum distance between the two holes. The symbol $l_{e,min1}$ and $l_{e,min2}$ denotes the distances to the two nearby edges

[a] Values that do not comply with [2]

4.1 Extrapolation of results

The following examples show that a scaling of σ_{rc}^{min} with σ_∞ is possible while a scaling with respect to the thickness yields inaccurate results.

Example 1 Scaling σ_{rc}^{min} with σ_∞.

The geometry corresponds to the sketch in Fig. 13 with $l_{xy} = 75$ mm, and σ_{rc}^{min} for a far-field stress of $\sigma_\infty = 100$ MPa is sought for. Using Fig. 15, $\hat{\sigma}_{rc}^{min}$ for $\sigma_\infty = 83$ MPa is found to be 0.53. Using the slope for the "close to a corner" curve in Fig. 3 ($\alpha = 0.86\sigma_{rc}^{min}/\sigma_\infty$) the following extrapolation can be made

$$\begin{aligned}\tilde{\sigma}_{rc}^{min} &= \hat{\sigma}_{rc}^{min}\sigma_\infty + \alpha(\tilde{\sigma}_\infty - \sigma_\infty) \\ &= 0.53 \cdot 83\ \text{MPa} + 0.86 \cdot (100\ \text{MPa} - 83\ \text{MPa}) \\ &= 58.61\ \text{MPa} \end{aligned} \quad (9)$$

where a "$\sim$" denotes values corresponding to $\sigma_\infty = 100$ MPa. A FE model of the problem yields

the value $\tilde{\sigma}_{rc}^{min,FE} = 59.09$ MPa which is less than 1% higher than the scaled prediction.

Example 2 Scaling of σ_{rc}^{min} with l_z.

This example attempts to scale σ_{rc}^{min} with the thickness according to Fig. 8. The problem is the same as in Example 1, but the thickness is changed from 19 to 10 mm. From Fig. 8 it is seen that the stress for this thickness should be increased by a factor of 8.25. Applying this factor to the result given in Example 1 yields

$$\tilde{\sigma}_{rc,10\,mm}^{min} = 8.25 \cdot 55.38\ \text{MPa} = 456.89\,\text{MPa} \qquad (10)$$

A FE model yields $\tilde{\sigma}_{rc,10mm}^{min,FE} = 95.72$ MPa which gives a deviation of more than 375% from the scaled prediction. By this example it is demonstrated that a simple scaling of the thickness may yield unsafe results.

5 Conclusion

In general, the residual stress state in tempered glass is complex and, in general, numerical models are needed for estimating the stress fields. However, this study covers several cases for one and two holes which can be used as guidelines. Furthermore, some features of a general nature may be extracted from the simulations:

- The value of σ_{rc}^{min} converges towards 90% of the far-field stress for increasing plate size.
- Scaling of σ_{rc}^{min} with the geometry is not possible due to the complex tempering process. However, when scaling down the total geometry or the thickness alone, an increase in σ_{rc}^{min} is found for a constant far-field stress.
- The value of σ_{rc}^{min} is primarily governed by the total size of the plate over the size of the hole.
- The lowest in-plane compressive residual stress at the hole, σ_{rc}^{min}, is always located along the mid-plane perimeter and is always less than 50% of the corresponding stresses along the surface plane perimeter. The 50% is only valid for 19 mm thick plates, for thinner plates the effect is less distinct.
- Two phenomena seem to govern the magnitude of σ_{rc}^{min}: (1) The rate of cooling, (2) The amount of material available to carry the stresses.
- For hole geometries, the change in σ_{rc}^{min} is proportional to σ_{∞} with an almost unique proportionality factor. This provides a possibility to easily obtain results for plates with a different far-field stress.

When two holes are considered, it was found that for holes in wide plates, with an edge distance of 72 mm only a small increase in σ_{rc}^{min} is gained when increasing this distance further. No significant differences in σ_{rc}^{min} between holes parallel to and perpendicular to the nearest edge were found.

It was shown that σ_{rc}^{min} can be influenced by edges as far as 20 times the plate thickness away. However, using a distance of more than 350 mm to the edge for 19 mm plates, the effect of edges is, in most cases, insignificant.

Tables suggesting minimal distances and corresponding values of σ_{rc}^{min} are provided in the text.

It was found that, using the minimum distances provided in Eurocode [9], does not always yield a reasonable residual stress state at holes for structural use. Therefore, it is recommended to use numerical simulations when designing bolted connections in tempered glass that are not covered by the available literature.

Appendix: parameters for the model

The material parameters for the exponential series used for viscoelasticity and for the structural response function are found in Tables 3 and 4, respectively. Here (g_n, λ_n^g) is a set of constants used for the deviatoric part of the relaxation function and (k_n, λ_n^k) is used for the hydrostatic part of the relaxation function and (m_n, λ_n^m) defines the response function for the structural volume relaxation. A more in-depth explanation is given in [20].

The initial temperature used was 923.15 K and the ambient temperature was 293.15 K. The thermal conductivity, λ_{th}, and the specific heat, C, for soda-lime-silica glass are modeled as temperature dependent and may be found in [7][3]:

[3] The term $-T \cdot 1.8e-7$ J T^2/kg K found in [7] for (12) is omitted here due to insignificance for the considered temperatures.

Table 3 Material data for the generalized Maxwell material

n	g_n (GPa)	λ_n^g (s)	k_n (GPa)	λ_n^k (s)
1	1.585	6.658e−5	0.7588	5.009e−5
2	2.354	1.197e−3	0.7650	9.945e−4
3	3.486	1.514e−2	0.9806	2.022e−3
4	6.558	1.672e−1	7.301	1.925e−2
5	8.205	7.497e−1	13.470	1.199e−1
6	6.498	3.292	10.900	2.033
7			7.500	∞

The data are derived from [8], see [20]

Table 4 Material data for the response function for the structural volume relaxation

n	m_n	λ_n^m (s)
1	5.523e−2	5.965e−4
2	8.205e−2	1.077e−2
3	1.215e−1	1.362e−1
4	2.286e−1	1.505e−1
5	2.860e−1	6.747
6	2.265e−1	29.630

The data are derived from [8], see [20]

Table 5 Forced convection constants used for the model [7]

Symbol	Value (W/m^2K)	Note
h_1	77	The top surface
h_2	76	The chamfered edge of the hole
h_3	60	The surface of the hole
h_4	62	The surface of the edges

$$\lambda_{\text{th}} = 0.741\,\text{W/m K} + T \cdot 8.58\text{e} - 4\,\text{W/m K}^2 \qquad (11)$$

$$C = \begin{cases} 1433\,\text{J/kg K} + T \cdot 6.5\text{e} - 3\,\text{J/kg K}^2 & \text{for } T \geq 850\,\text{K} \\ 893\,\text{J/kg K} + T \cdot 0.4\,\text{J/kg K}^2 & \text{for } T < 850\,\text{K} \end{cases} \qquad (12)$$

The forced convection coefficients from Table 5 may be found in [6].

References

1. Aben H, Guillemet C (1993) Photoelasticity of glass. Springer, Berlin
2. Adams LH, Williamson ED (1920) The annealing of glass. J Frankl Inst 190:597–632
3. Anton J, Aben H (2003) A compact scattered light polariscope for residual stress measurement in glass plates. In Glass processing days
4. Bartenev GM (1948) The phenomenon of the hardening of glass. J Tech Phys 18:383–388 (in Russian)
5. Beason WL, Morgan JR (1984) Glass failure prediction model. J Struct Eng 110(2):197–212
6. Bernard T, Gy R, Daudeville L (2001) Finite element computation of transient and residual stresses near holes in tempered glass plates. In: 19th International congress on glass, pp 445–446
7. Daudeville L, Carre H (1998) Thermal tempering simulation of glass plates: inner and edge residual stresses. J Therm Stress 21(6):667–689
8. Daudeville L, Bernard F, Gy R (2002) Residual stresses near holes in tempered glass plates. Mater Sci Forum 404–407:43–48
9. EN 12150-1 (2004) Glass in building—thermally toughened soda lime silicate safety glass—part 1: definition and descriptions 11
10. Gardon R (1980) Glass science and technology, vol 5: elasticity and strength in glasses, Chap. 5. Academic Press, New York, pp 145–216
11. Haldimann M, Luible A, Overend M (2008) Structural use of glass. IABSE, Zurich
12. Kurkjian CR (1963) Relaxation of torsional stress in transformation range of soda-lime-silica glass. Phys Chem Glass 4(4):128–136
13. Laufs W, Sedlacek G (1999) Stress distribution in thermally tempered glass panes near the edges, corners and holes. Part 1. Temperature distributions during the tempering process of glass panes. Glass Sci Technol 72(1): 7–14
14. Laufs W, Sedlacek G (1999) Stress distribution in thermally tempered glass panes near the edges, corners and holes: part 2. Distribution of thermal stresses. Glass Sci Technol 72(2):42–48
15. Lee EH, Rogers TG, Woo TC (1965) Residual stresses in a glass plate cooled symmetrically from both surfaces. J Am Ceram Soc 48(9):480–487
16. Lochegnies D, Romero E, Anton J, Errapart A, Aben H (2005) Measurement of complete residual stress fields in tempered glass plates. In: Glass processing days
17. Narayanaswamy OS (1971) A model of structural relaxation in glass. J Am Ceram Soc 54(10):491–498
18. Narayanaswamy OS (1978) Stress and structural relaxation in tempering glass. J Am Ceram Soc 61(3–4):146–152
19. Narayanaswamy OS (2001) Evolution of glass tempering models. In: Glass processing days
20. Nielsen JH, Olesen JF, Poulsen PN, Stang H (2008) Implementation of a 3D glass tempering model. (submitted)
21. Nielsen JH, Olesen JF, Stang H (2008) Characterization of the residual stress state in commercially fully toughened glass. ASCE Mater (submitted)
22. Nielsen JH, Olesen JF, Stang H (2008) The fracture process of tempered soda-lime-silica glass. Exp Mech. doi: 10.1007/s11340-008-9200-y
23. prEN 13474-3 (2005) Glass in building—determination of the strength of glass panes—part 3: general method of

calculation and determination of the strength of glass by testing, November
24. Tool AQ (1946) Relation between inelastic deformability and thermal expansion of glass in its annealing range. J Am Ceram Soc 29(9):240–253
25. Veer FA, Louter C, Bos FP, Romein T, van Ginkel H, Riemslag AC (2008) The strength of architectural glass. In: Bos FP, Louter C, Veer FA (eds) Challenging glass. IOS Press, Amsterdam

Paper IV

"The Fracture Process of Tempered Soda-Lime-Silica Glass"

J.H. Nielsen, J.F. Olesen & H. Stang

Published in: *Experimental Mechanics*

Experimental Mechanics
DOI 10.1007/s11340-008-9200-y

The Fracture Process of Tempered Soda-Lime-Silica Glass

J.H. Nielsen · J.F. Olesen · H. Stang

Received: 21 June 2008 / Accepted: 17 October 2008

Abstract This work presents experimental observations of the characteristic fracture process of tempered glass. Square specimens with a side length of 300 mm, various thicknesses and a residual stress state characterized by photoelastic measurements were used. Fracture was initiated using a 2.5 mm diamond drill and the fragmentation process was captured using High-Speed digital cameras. From the images, the average speed of the fracture front propagation was determined within an accuracy of 1.0%. Two characteristic fragments were found to form on each side of the initiation point and are named *"Whirl-fragments"* referring to the way they are generated. An earlier estimation of the in-plane shape of the fracture front is corrected and a hypothesis on the development for the fracture front is offered. The hypothesis is supported by investigations of the fragments using a Scanning Electron Microscope (SEM) which also revealed a micro scale crack bridging effect.

Keywords Dynamic fracture · Residual stress · Experimental high-speed observations · Elastic material · Fracture process

Introduction

The fracture behavior of glass has been studied extensively along with the development of linear elastic fracture mechanics (LEFM) starting in 1920 with the fundamental paper by Griffith [16]. Griffith utilized the mathematical framework for an elliptic crack provided by Inglis [18] and experimentally verified the application of LEFM on glass fracture within 10% accuracy.

The present work is concerned with high-speed observations of the catastrophic fracture propagation in thermally toughened soda-lime-silica glass. The dynamic fragmentation process develops in a fractal manner by repeated branching of propagating cracks. Thermally toughened glass is characterized by a high level of residual stresses. The residual compressive stresses at the surfaces eliminate the effect of surface flaws and thereby increase the apparent tensile strength of the glass. European codes for the structural use of glass implicitly require that the compressive residual surface stress must exceed 75 MPa for the glass to qualify as fully toughened (see Nielsen et al., unpublished manuscript). The residual stress state may increase the apparent tensile strength of glass more than four times [see e.g. 15], without disturbing the transparency of it. A further advantage is that the increase in the apparent tensile strength due to the residual stress state is time-independent; this is in contrast to the tensile strength of float glass where a decrease in strength over time is well known, [see e.g. 10]. These properties generally make toughened glass more suitable for load carrying structures than float glass, and a trend towards using glass for transparent, load carrying structural elements is observed over the last decade.

Since the residual stresses are considered the very basis for the characteristic fragmentation process taking place in toughened glass, when first triggered, a brief introduction to the field of modeling of the toughening process and characterization of the residual stress state is offered here.

J.H. Nielsen (✉) · J.F. Olesen · H. Stang
Department of Civil Engineering, Technical University of Denmark, Brovej building 118, 2800 Kgs. Lyngby, Denmark
e-mail: jhn@byg.dtu.dk

Published online: 09 December 2008

Glass is typically toughened by a process most often referred to as thermal toughening, which is simply an air quenching of float glass from a temperature just below its glass transition temperature. The surface regions of the glass are hereby solidified while the core region remains soft, unable to sustain any stress. When the inner region subsequently cools down, the contraction is prevented by the already solidified outer regions. This generates an equilibrated stress state, where the surface regions are dominated by compressive stresses, and a state of tension is present in the center region. The resulting plane-hydrostatic stress distribution through the thickness in a symmetrically quenched glass plate, far away from edges, is sketched in Fig. 1.

The stress state near corners, holes and edges is more complex and beyond the scope of this paper, instead references to Laufs and Sedlacek [21], Daudeville and Carre [13] are made.

A symmetric second order polynomial is commonly used for the approximation of the variation of the residual stresses through the thickness, see e.g. [8]. Assuming that $\sigma(z=0)=\sigma_{rt}$ together with symmetry ($\sigma(z)=\sigma(-z)$) and stress equilibrium over the cross-section, a second order polynomial describing the residual stress distribution may be determined. For this distribution the surface stress equals twice the center stress with opposite sign ($\sigma_{rc}=-2\sigma_{rt}$), and the tensile zone is approximately 58% of the total thickness.

In the past the physical phenomena arising during the tempering process were thoroughly investigated, and mathematical models were developed to predict the generation of residual stresses. Adams and Williamson [6] started by investigating the quite opposite phenomenon, namely the annealing of float glass, however, the physics of annealing and thermal toughening are similar to some extent. The next step was the development of the so-called instant freeze theory by Bartenev [9], where it is assumed that the transition from liquid to solid state is instant and takes place at the glass transition temperature. In the 1950'ies and the beginning of the 1960'ies experimental data on the viscoelastic behavior of glass at high temperatures were published. In 1963 a fine set of experimental data for the viscoelastic behavior of soda-lime-silica glass, which shows that the glass transition is not instant, was published by Kurkjian [20]. His paper presented relaxation curves at seven different temperatures for specimens subjected to torsion and showed that these curves could be represented by a single mastercurve if a simple shift in the time scale was applied; this states glass as a thermorheologically simple material as defined by Schwarzl and Staverman [27]. A theory of the tempering process, including the viscoelastic behavior at high temperatures, was developed in the 1960'ies, [see e.g. 22]. The last major step in the development and understanding of the tempering process was to include atomic structure dependent properties. Such a model was developed by Narayanaswamy [23, 24].

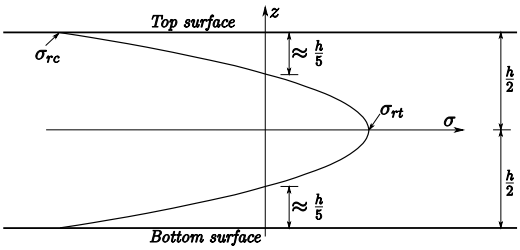

Fig. 1 Residual plane-hydrostatic stress distribution in a thermally toughened glass plate, far away from any edges. Tension exists in the interior, while compression is present in the surface layers. The stress neutral zone is located approximately 1/5 through the thickness

Later on, these theories have been implemented in finite element codes in order to investigate, among other subjects, the residual stress distribution near boundaries [see e.g. 13, 21, 26, 28]. An experimental characterization of the actual residual stress state present in commercially, fully toughened glass can be found in Nielsen et al. (unpublished manuscript). Here the stresses were measured by using a scattered light polariscope.

To describe the process of fracture in toughened glass, a few terms are defined: The word *crack* refers to the local development of a single crack before it *branches*. *Fragmentation* is used for describing the overall fracture process, including multiple crack- and crack branching processes.

When the equilibrated residual stress state in thermally toughened glass is disturbed sufficiently, the fragmentation process is initiated. The necessary degree of disturbance depends on the way in which it is introduced. Due to the residual stress state, energy is present at the crack tip at all times, capable of driving cracks into branches; this is observed as a fragmentation process.

According to Narayanaswamy [25] a U.S. patent on the tempering process was issued in 1877, however, the characteristic fracture behavior of toughened glass was first studied during the late 1950'ies and the early 1960'ies by Acloque, [see 1–3, 5]. Using the Cranz-Schardin high-speed photo technique with rotating mirrors [12], pictures of the fragmentation process were

obtained with a frame rate of 1μs. The fragmentation was initiated by the impact of a sharp steel point in order to penetrate the surface layers with compressive residual stresses, minimizing the external energy added to the system. Acloque [3] observed that two characteristic fragments, located on each side of the impact point, were generated. Acloque [1] also showed fragments with clearly visible markings from the fracture front (Wallner lines [31]) from which he estimated the in-plane shape of the crack front [1, 5].

Acloque [3] determined the velocity of the fracture propagation to be 1500 m/s by means of high-speed images. The velocity was also derived theoretically by energy considerations and verified experimentally by Kerkhof [19]. The expression for the velocity is: $v_\gamma = 2\sqrt{\frac{\gamma}{\rho \bar{r}}}$ where γ is the surface fracture energy, ρ is the density, and the average of the ion-distance for the material is denoted $\bar{r}$. According to Acloque [4] the material constants are $\rho = 2500\,\mathrm{kg/m^3}$, $\bar{r} = 21 \times 10^{-9}\mathrm{m}$ and $\gamma = 0.305\ \mathrm{J/m^2}$ which yields a velocity of $v_\gamma = 1524$ m/s. Several authors in the past have determined the fracture surface energy, however, with results ranging from 1.8 J/m^2 to 11 J/m^2 depending on the experimental method [32]. The magnitude of the fracture surface energy has a significant influence on the calculated velocity, and it should be noted that the value applied in Acloque [4] is well below the range found by others.

A paper on the failure of toughened glass caused by small-particle impact was published by Chaudhri and Liangyi [11], where images of the fragmentation process, captured with a framing speed of 1 μs, were shown. The authors estimated the velocity of the crack propagation to 1800 m/s in the tensile regions of their specimen, with a stated accuracy of 5%. The residual stress state was described as 100 MPa tensile stress in the center and 200 MPa compressive stress at the surface and a zero-stress depth of 1/5 of the thickness. Pictures captured through photo elastic folie reveal a change in the fringes at impact, and it can be seen that the fringes are influenced about 8 mm ahead of the fracture front, for a 10 mm thick specimen.

In 1992 Takahashi reported high-speed color pictures of the photoelastic fringes in 5 mm zone-tempered glass during the fracture propagation [30]. A more elaborate paper on these photos was published by Takahashi [29] were a small but, according to the authors, significant correlation between the crack velocity and the residual stress state was present. This dependency was also found earlier by Acloque [2]. Furthermore, Takahashi [29] found that cracks were capable of changing direction according to the maximum principal stress direction, with a minimum radius of curvature of 2 mm.

The main objective of the present work is to report observations of fracture and fragmentation phenomena which may arise in toughened glass. Observations were achieved by means of high-speed digital cameras, and the specimens used for the experiments were carefully characterized with respect to their individual residual stress state. In this work, the fragmentation was initiated by drilling into the tensile zone from the edge of the specimens. Similar to the observations in Acloque [3], two characteristic larger fragments were also observed here, however, our observations are markedly different from what has been reported earlier. The characteristic fragments are generated by a whirl-like crack propagation and will be referred to as the "Whirl-fragments" throughout the rest of this paper. Furthermore, unique pictures of the in-plane shape of the fracture front, captured during fragmentation are presented. From these pictures it is seen that the fracture front is more complex than what was derived from Wallner lines by Acloque. The fracture velocity is determined with a very high accuracy and Scanning Electron Microscope (SEM) images of the surfaces after fracture are analyzed to support the explanation of some of the observed phenomena.

The Experimental Setup

The specimens used for the present work were all 300 mm × 300 mm commercially toughened soda-lime-silica glass with various thicknesses. The specimens belong to four groups according to Table 1. The fragmentation process was initiated by drilling from the narrow surface into the specimen using a 2.5 mm diamond drill, water as cooling agent and a setup as indicated in Fig. 4. Each specimen was fixed at the bottom using a vice, loosely tightened in order to minimize the disturbance of the residual stress state.

The distribution of the residual stresses over the thickness, in two perpendicular directions at nine different locations on each specimen (see e.g. Nielsen

Table 1 Groups of specimens

	A	B	C	D
Thickness (nominal):	19 mm	19 mm	12 mm	8 mm
Low iron content:	No	Yes	No	No
Number of specimens:	6	3	10	5

Table 2 Characterization of the residual stresses (MPa) at three points through the depth, z (mm) and the average drill depth at fracture, $d_{avg.}$ (mm)

Spec. grp.	A	B	C	D
z_{rc}^{top}	0.0	0.0	0.0	0.0
$\sigma_{rc,x}^{top}$	−67.8(1.0)	−64.0(4.0)	−80.8(1.4)	−92.8(1.5)
$\sigma_{rc,y}^{top}$	−68.9(1.5)	−64.3(4.1)	−80.9(1.5)	−91.9(0.6)
$z_{rt,x}$	9.5	9.5	5.9	4.1
$\sigma_{rt,x}$	38.3(0.9)	36.5(2.9)	45.2(0.7)	49.9(1.0)
$\sigma_{rt,y}$	39.1(1.7)	36.8(3.4)	45.3(0.6)	49.7(0.8)
z_{rc}^{bot}	18.4	18.4	11.6	7.8
$\sigma_{rc,x}^{bot}$	−63.1(1.9)	−53.3(7.5)	−76.6(8.8)	67.3(13.9)
$\sigma_{rc,y}^{bot}$	−66.8(1.9)	−57.2(8.9)	−76.6(9.7)	−66.1(13.0)
d_{avg}	4.53(0.36)	5.37(1.74)	4.45(1.39)	4.85(1.59)

Numbers in parentheses are the sample standard deviations. The superscript refers to either the top, middle or bottom plane of the glass. The subscript refers to weather it is residual compressive stresses (rc) or residual tensile stresses (rt), and the x,y denotes two perpendicular directions.

et al., unpublished manuscript), were determined using a scattered light polariscope (SCALP) developed by GlasStress Ltd. in Tallin (Estonia), based the photoelastic response of glass [see. 7]. The results for the residual stress measurements are summarized by averaging values for each direction at three locations through the thickness (z) for each group of specimens as shown in Table 2. From these data, an approximate distribution of the residual stresses can be obtained using a second order polynomial. For the specific sets of specimens used in these tests, there is a strong correlation between the thickness and the residual stress state as indicated in Fig. 2. This means that it is not possible to distinguish if a particular effect arises from a variation in thickness or a variation in the magnitude of the residual stress state.

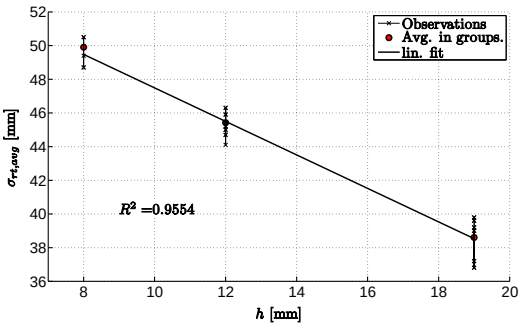

Fig. 2 Correlation between residual stresses and specimen thickness

The drilling depth at fracture initiation (d) was measured using a Linear Voltage Transducer attached to the drilling machine. The average depth at fracture initiation for each group is given in Table 2, and the value for each specimen can be found in Table 4. It should be noted that for the thin specimens, the edge of the specimen sometimes chipped off during drilling, without initiating the fragmentation process.

In order to investigate the characteristic fragmentation of toughened glass, two digital Photron FastCam-APX RS high-speed cameras were used. Each camera has a maximum frame rate of 250000 fps and a minimum shutter time of 1/1000000 s. However, due to limitations for the speed at which data can be written to the memory in the cameras, there is an optimum between the picture resolution and the frame rate. An advantage of using digital High-Speed cameras compared to the Cranz-Schardin type camera [12] is that the images are stored in endless loops, such that the last 2–3 s of recording are always available and the recording can be stopped using a simple handheld trigger. For high frame rates, it is not possible to capture the complete specimen in a reasonable resolution and different views for the cameras were chosen as sketched in Fig. 3.

Views A and B are used in order to derive the crack front velocity and View C is used for investigating the crack initiation and the generation of the Whirl-fragments. View D gives an overview of the fragmentation process and view E is used for determining the in-plane shape of the fragmentation front. The applied frame rates, shutter times, views and picture resolutions are stated in Table 3 for each specimen.

Two experimental setups were used as shown in Fig. 4, a standard setup for the views perpendicular to the specimen plane, Fig. 4(a), and a setup for the in-plane view of the fracture front where the specimens were rotated 90°, Fig. 4(b). As seen from Fig. 4, the cameras were pointed directly at the light source, passing through the specimen, a transparent sheet of plastic with a grid and a light disperser. The grid is used for quantifying observations and thereby extracting e.g. the velocity. The light disperser provides more uniform brightness to the pictures. The total retardation of light traveling through the plane of a specimen is high, which gives difficulties in capturing clear in-plane images of the fracture front. In order to reduce the total retardation, glass with high transparency (low iron content) was used for these tests, and the light was guided into the specimens using a shiny metal funnel. The light source for the in-plane view consisted of lamps with a total effect of 2.5 kW and for the standard setup the effect of the light source ranged from 1–2 kW, depending on the shutter time used.

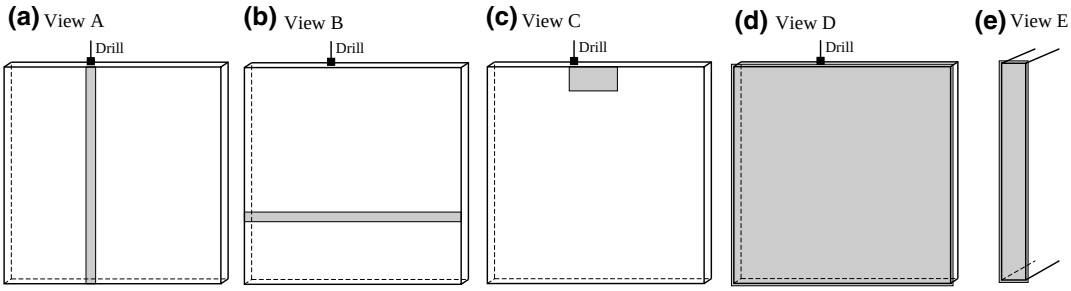

Fig. 3 Sketch of camera views. Viewing direction is perpendicular to the plane of the shaded area (**a**–**e**)

Experimental Results

Crack Propagation Mechanism

As described earlier, the residual stress state in toughened glass is unstable in the sense that if it is disturbed significantly a chain reaction is started and the specimen will fragmentize completely due to the embedded strain energy which will continuously feed the fracture propagation. Figure 5 shows a series of pictures of the fragmentation process at four different stages; *before fracture*, *initiation of fracture* (*generation of the Whirl-fragments*), the *propagation of fragmentation* and the *post fragmentation behavior*. From Fig. 5(d) it is seen that the sudden release of internal energy is large enough for the specimen to explode in groups of fragments which are kept together by micro scale crack bridging, as shown later.

When initiating the fragmentation process in toughened glass, the generation of two larger fragments located adjacently on each side of the initiation point are characteristic [see e.g. 2]. Here, however, fracture initiation from the edge into the center plate plane apparently causes these characteristic fragments to form several centimeters apart, symmetrically about the initiation point. This phenomenon has, to the best of the authors knowledge, never been reported before and, as stated earlier, will be referred to as formation of the "Whirl-fragments". A brief investigation has revealed that the Whirl-fragments are caused by the location of the fracture and not by the drilling process. The Whirl-fragments are clearly seen from the photo in Fig. 6. Experimental observations of the location of the Whirl-fragments are given in Table 4 for most of the specimens. The horizontal distance from the center of the Whirl-fragment to the drill is denoted e and the vertical distance from the edge surface is denoted b, with index corresponding to side, see Fig. 10. We will return to the description and discussion of the formation of the Whirl-fragments later.

Two simultaneous fragmentation processes were observed. The origin of a fragmentation process seems to coincide with the initiation of a Whirl-fragment, and it is seemingly located on its boundary at the point most far away from the drill as indicated in Fig. 6. Apparently the fragmentation processes are polar as indicated in this figure where the polar coordinates are defined. Two characteristic fragmentation patterns were observed in the specimens, as seen from Fig. 6, where the specimen has been divided into different areas with different patterns. In area type A the pattern seems arbitrary,

Table 3 Setup data for cameras

Spec.	View	fps [kHz]	Shutter [10^{-6}s]	Resolution [pixels]
A1	A/B	125	2.0	1024×16
A2	A/B	125	2.0	1024×16
A3	A/B	125	2.0	1024×16
A4	D/D	7.5	2.0	640×592
A5	C/A	150/5.6	4.1/3.9	128×48/768×672
A6	A/B	105	2.0	640×32
B1	E	21	2.0	1024×144
B2	E/E	31.5	1.0	896×96
B3	E/E	45	1.0	640×32
C0	C/C	21	4.1	640×208
C1	C/C	90	4.1	256×64
C2	A/B	125	4.0	1024×16
C3	A/B	125	2.0	1024×16
C4	A/B	125	2.0	1024×16
C5	C/D	150/7.5	4.1	128×48/640×592
C6	C/D	150/7.5	4.1	128×48/640×592
C7	C/D	150/5.6	4.1/3.9	128×48/768×672
C8	A/B	105	2.0	640×32
C9	C/C	21	4.1	640×208
D1	A/B	125	2.0	1024×16
D2	C/D	75/7.5	2.0/4.1	256×80/640×592
D3	D	5.6	3.9	768×672
D4	A/B	105	2.0	640×32
D5	A/B	105	2.0	640×32

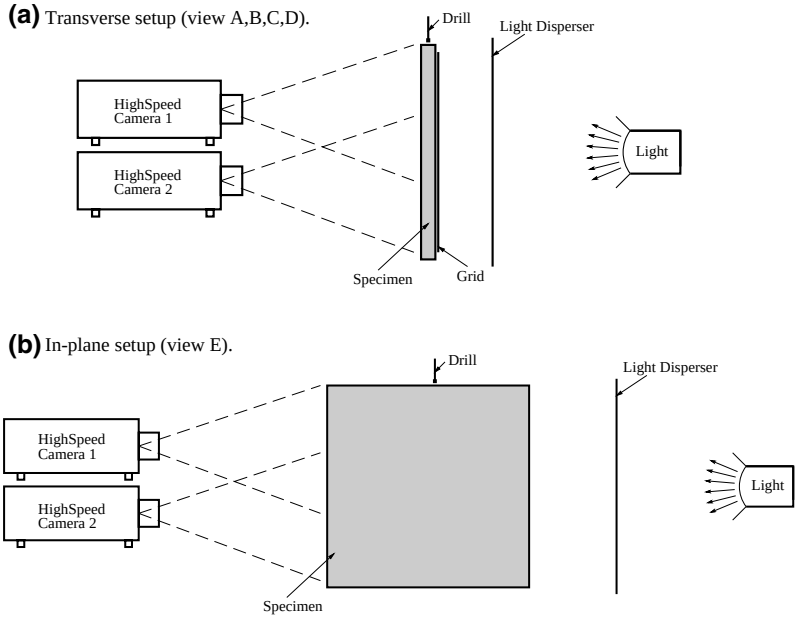

Fig. 4 Sketch of the test setup (**a**, **b**)

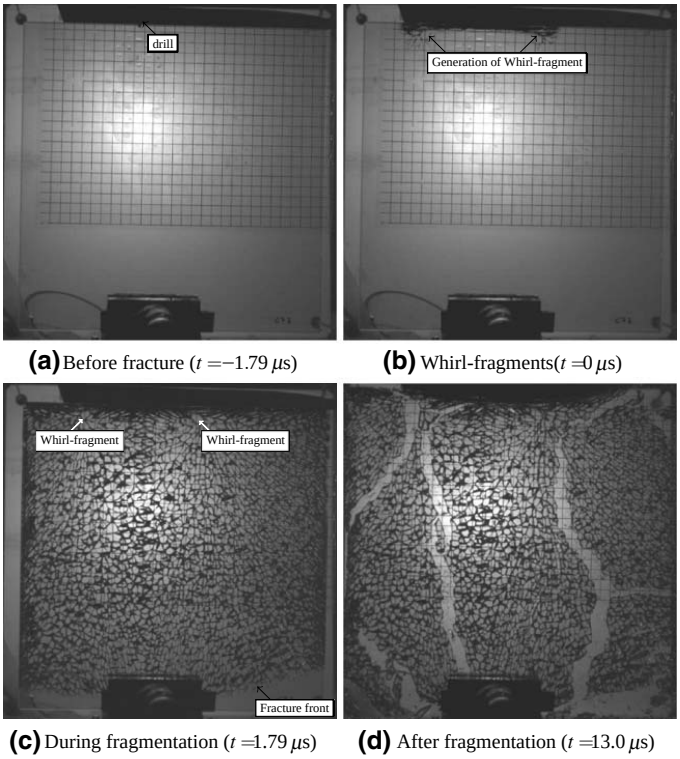

(a) Before fracture ($t = -1.79\,\mu$s) **(b)** Whirl-fragments($t = 0\,\mu$s)

(c) During fragmentation ($t = 1.79\,\mu$s) **(d)** After fragmentation ($t = 13.0\,\mu$s)

Fig. 5 Four stages of the fragmentation process (**a**–**d**). Note that fragmentation has not yet reached the bottom of the specimen in (**c**). Specimen C7, view D, Grid: 10 mm × 10 mm

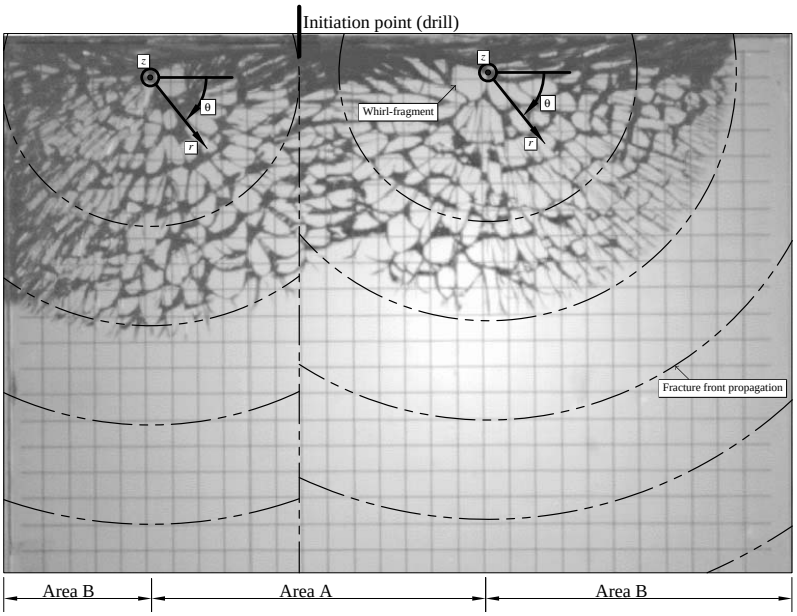

Fig. 6 The crack front propagation. The origin of the polar coordinate systems is referred to as the apparent center. Specimen A4, upper part of view D, Grid: 10 mm× 10 mm

whereas the polar nature of the fragmentation is clear in the areas of type B; also the direction of the propagation is evident in these areas.

An example of the generation of a Whirl-fragment is shown in Fig. 7, where it is seen that the initial cracks propagate perpendicular to the drill axis, seeking towards the surface of the edge. At some point, however, a crack enters into the bulk material (away from the edge) and initiates the generation of a Whirl-fragments and of the polar fragmentation process. This happens almost simultaneously to the right and to the left of the drill.

Table 4 Observations, see Fig. 10

Spec.	e_l/e_r [mm]	b_l/b_r [mm]	d [mm]	Spec.	e_l/e_r [mm]	b_l/b_r [mm]	d [mm]
A1	35/33	15/15	4.7	A4	50/65	15/15	4.2
A2	55/65	15/15	4.3	A5	30/32	15/15	5.2
A3	52/65	15/15	4.5	A6	35/45	15/15	4.3
B1	–	–	4.1	B3	–	–	7.4
B2	–	–	4.7				
C0	17/17	14/14	3.8	C5	*/40	*/12	2.8
C1	*/*	*/*	5.9	C6	20/17	13/13	5.5
C2	25/20	15/15	4.5	C7	55/55	12/12	2.9
C3	15/15	15/15	4.6	C8	35/73	13/14	4.7
C4	40/33	12/12	2.9	C9	6/10	14/14	6.9
D1	12/8	6/6	3.1	D4	*/15	*/8	5.5
D2	12/*	9/*	6.0	D5	10/9	8/9	3.2
D3	5/*	15/*	6.4				

The pictures in Fig. 8 show the formation of a Whirl-fragment in specimen A5. The drill is located to the left just outside the pictures, and it is seen how the cracks seem to be hurled away from the Whirl-fragment as it is formed. In the last picture [Fig. 8(g)], it is seen how cracks originating from the formation of the other (left) Whirl-fragment, meet at A with the cracks from the right one.

The Whirl-fragments are generated by the branching of cracks. The bifurcation half angles for these branching cracks are approximately 60° as shown in Fig. 8(h). This is in agreement with the direction for the max principal stress for cracks propagating with velocities above 60% of the elastic shear wave speed, as shown by Yoffe [33]. However, Freund [14], p. 166 states that the attainment of a critical velocity appears to be neither a necessary nor sufficient condition for bifurcation.

In order to determine parameters which might influence the generation of the Whirl-fragments, the correlation between $\sigma_{rt,avg}$, t, e and d has been investigated. A plot showing the distance from the center of the Whirl-fragments to the drill as a function of the thickness is found in Fig. 9. Here it is seen that there might be a weak correlation between the thickness and e, however, a similar plot is found for the residual stress versus e and as explained earlier these observations cannot be distinguished (Fig. 10). Further, plots of e versus d and d versus t did not reveal any correlation between these parameters.

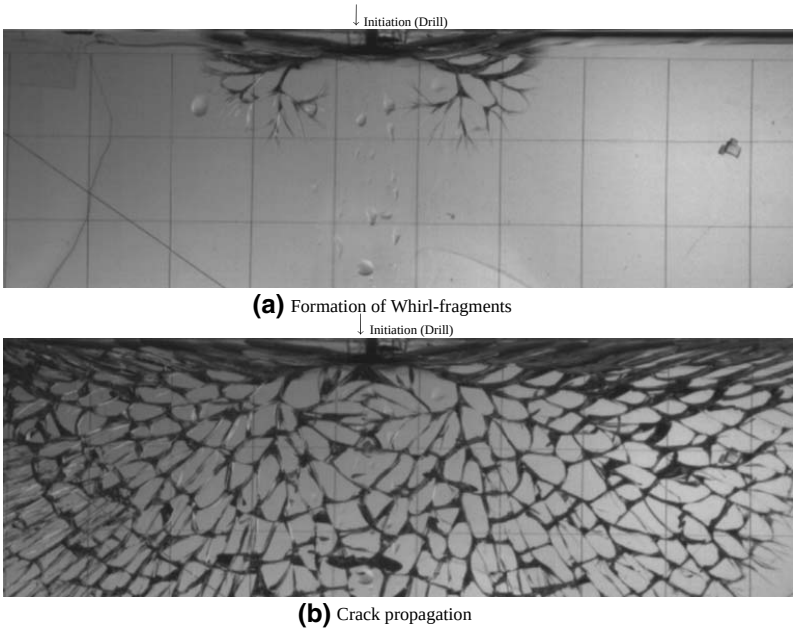

Fig. 7 Formation of Whirl-fragments. Specimen C0, view C, Grid: 20 mm× 20 mm (**a**, **b**)

(a) Formation of Whirl-fragments

(b) Crack propagation

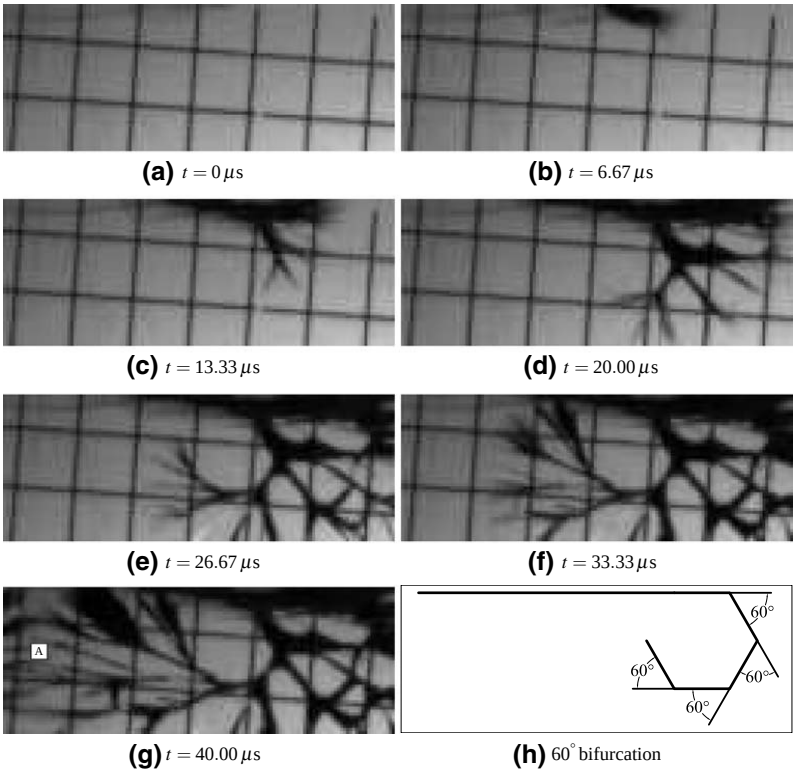

Fig. 8 A close view to the formation of a Whirl-fragment. The drill initiates the fragmentation just to the left of the pictures. Specimen A5, view C, Grid: 10 mm×10 mm (**a**–**h**)

(a) $t = 0\,\mu$s **(b)** $t = 6.67\,\mu$s

(c) $t = 13.33\,\mu$s **(d)** $t = 20.00\,\mu$s

(e) $t = 26.67\,\mu$s **(f)** $t = 33.33\,\mu$s

(g) $t = 40.00\,\mu$s **(h)** 60° bifurcation

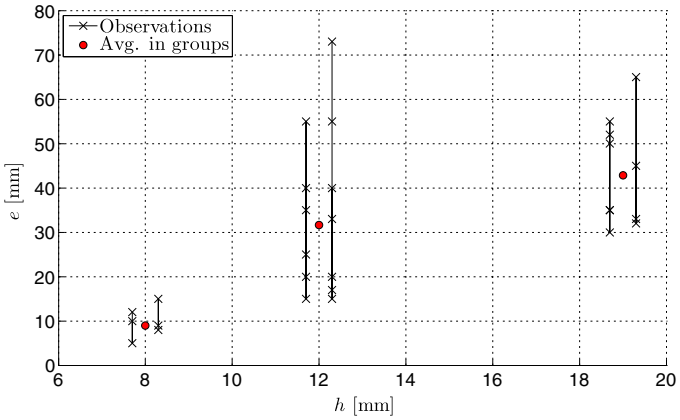

Fig. 9 Distance between Whirl-fragments and drill, e. Note that the observations are moved a bit to the left or right of the nominal thickness corresponding to observations of the left and right Whirl-fragments, respectively

Velocity of the Fracture Propagation Front

As indicated in the introduction, several authors have estimated the velocity of the fracture front in toughened glass. However, these velocity estimates seem to be determined on the basis of few specimens and few pictures. Here we have studied 11 specimens, and more than 15 pictures of each specimen were considered to determine the average velocity. Due to the high frame rate, the resolution for each picture was limited and View A and View B were used (see Fig. 3). An example of the set of pictures used for analyzing one specimen can be seen in Fig. 11. In order to determine the true velocity, the length direction of the pictures must coincide with the direction of the overall velocity, which, however, is not known beforehand.

In Fig. 11, the position of the fracture front is read from the pictures knowing that the grid is 10 mm× 10 mm, but in order to determine the true velocity, the pictures either have to include the apparent center of the polar crack propagation or a geometrical model must be setup for evaluating the pictures.

Since it is impossible to estimate the location of the apparent center before fracture, it is not possible to make sure that the pictures include this point. Thus, a geometrical model was applied, relating the position of the fracture front from the pictures at different times, $u(t)$, to the true velocity. Assuming the true velocity to be constant, and assuming a polar fracture propagation, such a relationship may be derived from geometrical considerations and is written as

$$u(t) = \sqrt{(v(t - t_0))^2 - a^2} - x_0 \tag{1}$$

where v is the true velocity, t is the time, a is the vertical distance from the nearest apparent center to the pictures and x_0 is the vertical distance between the apparent center and $u(0)$, t_0 is a time correction which is fitted along with the true velocity v.

From post fracture observations, x_0 is determined and from high-speed pictures of View B (see Fig. 12) and post fragmentation investigations, the position of the camera relative to the center, a, is determined.

Once these constants are estimated, the observations of $u(t)$ can be related to the true velocity v, by a least squares fit of v and t_0 in equation (1).

Figure 13 shows a fit of the model for a specific specimen, and it is seen that the model fits well to the measured data, providing a reasonable estimate for the true velocity.

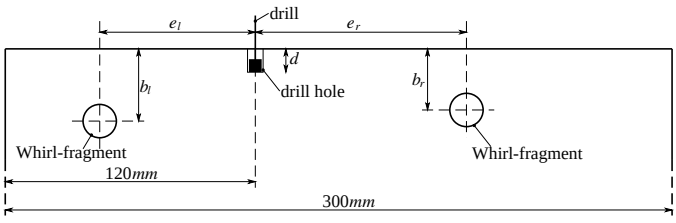

Fig. 10 Upper part of a specimen, defining the measures given in Table 4 and location of the initiation point (center of drill)

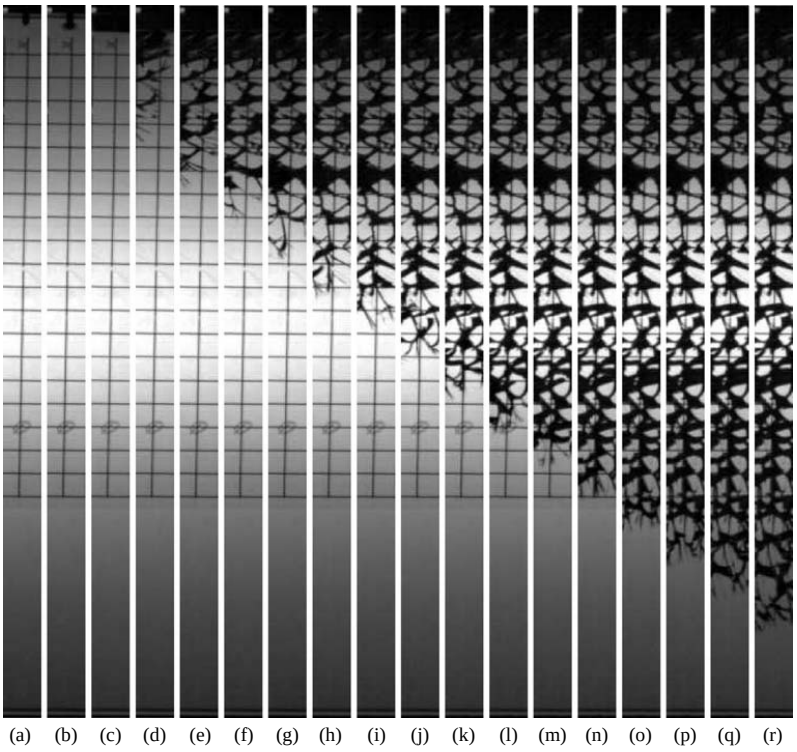

Fig. 11 Fracture front propagation in view A. There is 9.52 μs between each picture, except between (c) and (d) where 66.67μs has elapsed. Specimen A6, view A, Grid: 10 mm×10 mm

The fitted values of v and t_0, the goodness of the fit and parameters used for the model can be found in Table 5 for each specimen.

Furthermore, the table provides information on the residual stress state in each specimen by giving the average center stresses, $\sigma_{rt,avg}$ and the average stresses at the top surface, $\sigma^{top}_{rc,avg}$. The accuracy of the parameters a and x_0 is estimated conservatively to be ±2 mm and ±2.5 mm, respectively. A sensitivity analysis of the model parameters was carried out. Errors in determination of x_0 and a and systematic errors of ±2 mm in the estimation of u were considered simultaneously. The worst combination of the parameters in the sensitivity analysis changed the velocity by 1.0% corresponding to approximately 15 m/s, however, it must be emphasized that this worst case scenario is most unlikely to have occurred.

In Fig. 14 the measured average velocity is plotted against the measured residual tensile stress for each specimen used for determination of the average velocity, see Table 5. The figure does not significantly support a correlation between the average fracture front velocity and the residual stresses or the thickness, contrary to indications in earlier work by Takahashi [29], Acloque [2]. However, it should be noted that the specimens used throughout the present work

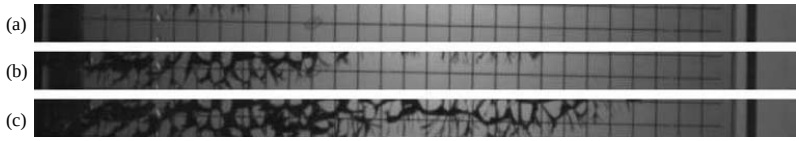

Fig. 12 Fracture front propagation in view B. The front emanating from the left apparent center emerges first, at the left top in (**a**). The front emanating from the second (right) apparent center emerges later in (**b**). Both fronts are seen at a more developed stage in (**c**). There is 9.52 μs between each picture. Specimen A6, view B, Grid: 10 mm×10 mm

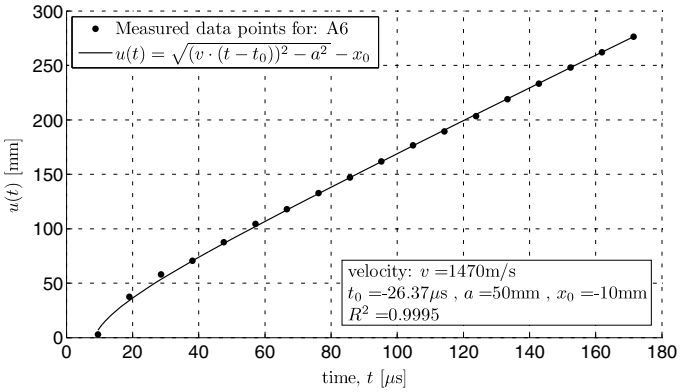

Fig. 13 Fit of fracture front propagation model assuming constant average fracture front velocity within one plate

only had a relatively small variation in the residual stresses.

Unfortunately the general residual stress state in the specimens vary significantly with the thickness. Therefore, it can not be excluded that there are simultaneous effects from both the thickness and the residual stress state, which cancel out each other, even though this is unlikely.

Shape of a Propagating Fracture Front

It is well known that the fracture process may propagate in a polar manner from an apparent center, as pointed out earlier and shown in Fig. 6. However, the in-plane shape of the fracture front has, to the best of the authors knowledge, never been captured before. In Fig. 15 photos of the in-plane fracture front are shown.

Table 5 Parameters for equation (1) and average measured residual stresses at the top surface and the center of each specimen

Spec.	v	t_0	a	x_0	R^2	$\sigma_{rt,avg}$	$\sigma^{top}_{rc,avg}$
A1	1472	−21.1	40	0	0.9998	39.6	−69.3
A2	1451	−37	60	0	0.9989	39.8	−69.3
A3	1469	−27.5	45	−5	0.9989	36.8	−67.9
A6	1470	−26.4	50	−10	0.9995	37.2	−68.0
C2	1471	−16	25	−4	0.9996	45.4	−80.0
C3	1471	−6.5	20	0	0.9994	46.3	−83.4
C4	1483	−25.6	42	−3	0.9992	45.9	−81.7
C8	1452	−20.4	38	−1	0.9996	45.0	−79.6
D1	1473	−1.9	10	−7	0.9997	50.5	−92.8
D4	1458	−6.9	18	−5	0.9997	49.4	−92.2
D5	1460	−7.1	13	−9	0.9998	48.7	−91.1
Avg.	1466	−17.9	33	−4	0.9995	–	–

Emphasized parameters are found by fitting the measured data.

These pictures were captured during fracture propagation in specimen B2, seen through the narrow 19 mm×300 mm face (view E).

In Fig. 15(a) the drill is clearly visible, however, there is no sign that cracks might have started. In Fig. 15(b) the fragmentation has just started, and Fig. 15(c) shows the in-plane view of the fracture process generating the Whirl-fragments. Figure 15(d) shows the fracture front at an early stage, and Fig. 15(e) and Fig. 15(f) show the in-plane shape of the fracture front. Here it is seen that the fracture front near the surfaces is delayed compared to the front in the interior, tensile zone. Furthermore, it is seen from Fig. 15(e) mark C that the surface crack at this point has developed deeper into the material than those just to the right. This observation justifies a hypothesis that the surface cracks start at the surface and propagate towards the center and not in the global direction of the crack propagation as the interior front does. This hypothesis is also supported by the post fracture investigation presented in Section Post Fracture Investigation.

The shape of the fracture front has been sketched in Fig. 16(b) for comparison with the shape suggested by Acloque [2] shown in Fig. 16(a).

It is seen that the actual fracture front is less blunted than the shape proposed by Acloque [2] and that fracture occurs at the surface giving a more complex shape of the front. The two zones marked with an A are the depth at which the residual stresses theoretically equals zero as marked on Fig. 2. The width of the zones is due to the perspective in the picture with the inner boundary representing the plane most far away from the cameras. It is observed that the surface-near fracture front actually meets the interior fracture front inside the theoretical compressive zone.

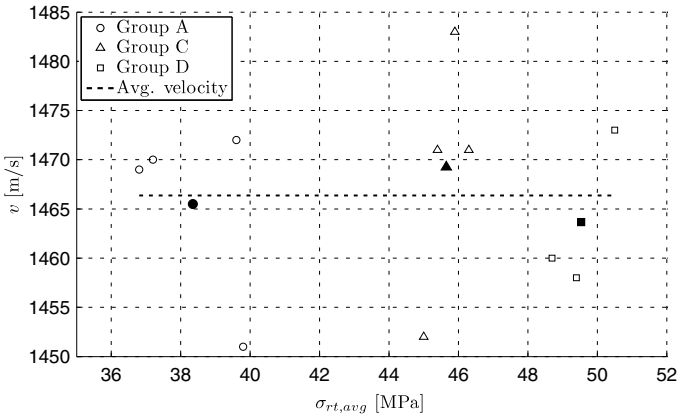

Fig. 14 True fracture front velocity vs. residual stresses. The filled markers are representing the average value within the respective groups

Post Fracture Investigation

When toughened glass fails, the fracture surfaces generated are rather characteristic due to the unique loading conditions originating from the residual stress state. Three different zones of the fracture surfaces are identified as characteristic; they are visible to the naked eye, see Fig. 17(a). Near the surfaces Zone 1, characterized by regular grooves, is present. This zone is about $h/5$ high and corresponds to the compressive zone in the theoretical residual stress distribution.

Zone 2 in Fig. 17(a) is characterized by being almost perfectly smooth, however, by an investigation of the fragment (using a stereo microscope) some characteristic lines are seen here. The lines run along the boundary of Zone 1 and then curve through Zone 2; such lines are called Wallner lines and they reveal that the crack propagation direction in this zone is from right to left

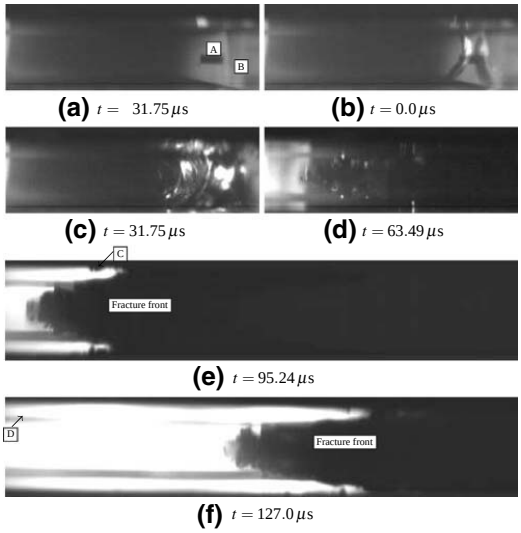

Fig. 15 Pictures of the initiation and shape of the crack front taken with 31500 fps and a shutter time of 1.0 μs. A is the drill, B is the narrow surface of the specimen and D is the edge of the narrow side opposite the cameras. C is the surface part of the crack front. Specimen B2, view E, rotated 90°

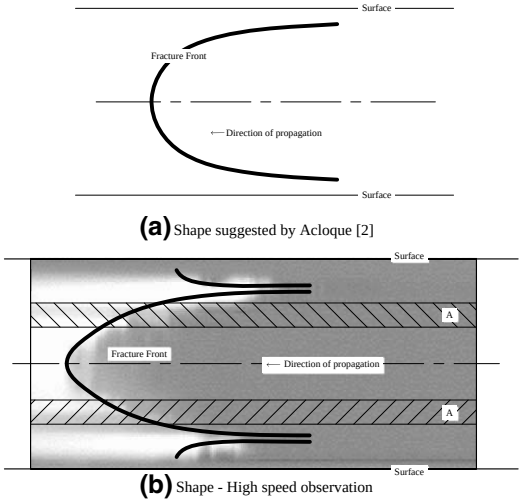

Fig. 16 Sketches of the in-plane shape of the crack front. (**a**) is suggested from Wallner lines by Acloque [1], (**b**) is based on high speed observations in the present work. View: (r,θ)-plane

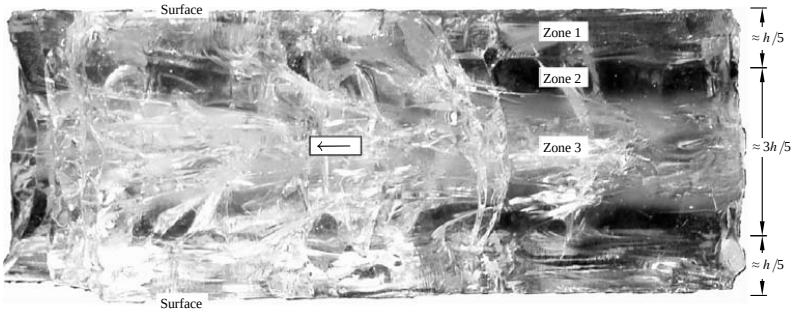

(a) View: (z,r)-plane, the arrow indicates the global crack propagation direction

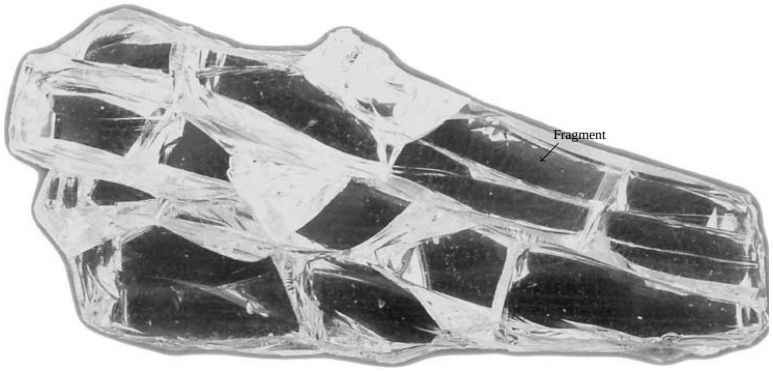

(b) View: (r,θ)-plane

Fig. 17 Pictures of fragments (**a**, **b**). The indication of picture planes refer to the coordinate system shown in Fig. 6

as indicated by the arrow in Fig. 17(a) indicates. The Wallner lines are not visible on the photo given here, however, very clear photos of such Wallner lines in tempered glass may be found in e.g. Acloque [1].

Zone 3 is characterized by being almost white, and represents the zone with the highest residual tensile stress. A close view of this zone reveals a complex fracture process, see Fig. 18(b).

The appearance of the zones is changed if the loading situation leading to fracture is changed, e.g. subjecting the specimens to bending by external loads will produce the same zone types, however, they will appear in other regions of the fracture surface.

In Fig. 17(b) we see a group of fragments viewed perpendicular to the (r,θ)-plane, i.e. the original specimen surface. It will be shown later that these fragments actually are kept together by crack bridging on the micro scale.

In order to investigate the fracture surfaces further, images from a Scanning Electron Microscope (SEM) have been analyzed. When investigating the fracture surface of transparent materials, the SEM has the advantage that only the surface is visible.

In Fig. 18, SEM images of Zone 1 near the edge and Zone 3 near the center of the fracture surface are shown. Figure 18(a) shows a SEM image of Zone 1 where the edge of the fracture surface is seen near the bottom of the image, marked with E. A radical change in the topography is marked with A and B. Above this boundary, so-called river lines are seen indicating a fracture propagation direction marked by the arrow, [17], supporting the hypothesis that the surface fracture fronts are developed from the surface towards the center. The river lines indicate that the fracture has propagated with an increasing Mode III component responsible for a more rough surface texture. This complies with the hypothesis that the interior fracture drives the fragmentation process. The area below the boundary A – B is more smooth indicating a lower velocity and a lower energy release rate according to Hull [17]. Furthermore, small scratches perpendicular to the edge are observed near D. The bright area C is due to large irregularities in the fracture surface caused by chips which have spalled off, and is not interpreted as a fractographic observation.

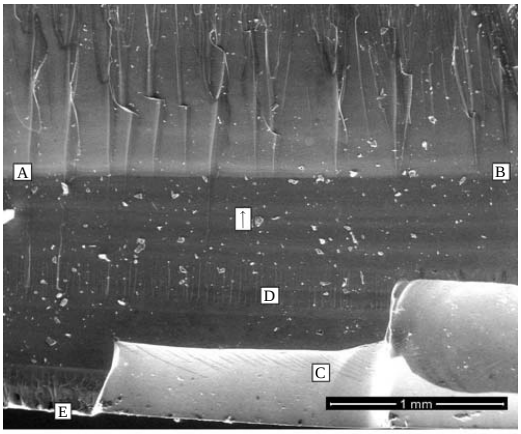

(a) Near the edge, Zone 1.

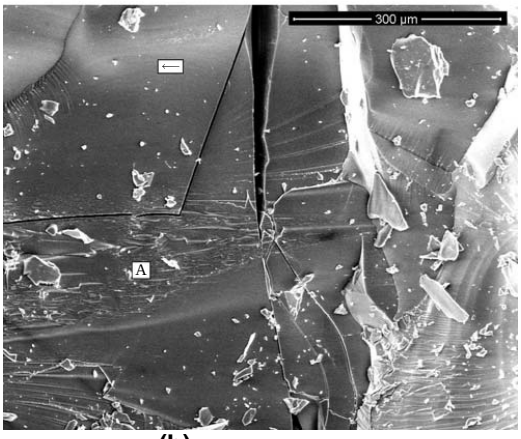

(b) Center area, Mist zone.

Fig. 18 Scanning Electron Microscope images of fracture surfaces in a (z,r)-plane (**a**, **b**)

A SEM image of Zone 3 is shown in Fig. 18(b) where it is seen that the fracture propagation in the central area is governed by many processes, which is seen from the very complex and irregular topography. It should be noted that the large vertical crack was formed at a late stage since some of the horizontal markings have been cut by it. The overall direction of the crack propagation in this zone is indicated in the figure by the arrow.

In Fig. 19 a SEM image of the regular surface of a fragment with a secondary crack is shown.

From this image, it is obvious that there are crack bridging effects on the micro scale which are partly responsible for keeping the fragments together in larger pieces after fracture, as seen in Fig. 5(d). This image also supports the hypothesis that the surface cracks are propagating in the global crack propagation direction in a stepwise manner, indicating that the surface cracks are generated by several single crack processes initiated when the interior crack has propagated a certain distance ahead of the surface fracture front, depending on the material strength at the current location.

The Crack Generation Mechanism

Based on the information provided in this article, a mechanism for the local development of the fracture front is offered here. From the pictures of the in-plane shape of the fracture front it is seen that the fracture propagates in the interior tensile zone and, with a small delay, is followed by the fracture front in the near surface regions, as shown in Fig. 16(b). From the fractographic analysis and the high-speed photographs, the direction of the surface fracture propagation is determined to be towards the center of the specimen. From this information, a novel hypothesis concerning the local development of the fracture front is derived and sketched in Fig. 20. The residual stress state before fragmentation is governed by compressive stresses near the surface and tension in the interior, see Fig. 20(a). When the interior fracture front appears [Fig. 20(b)], the tensile stresses are lost and in order to obtain equilibrium the compressive stresses must decrease to zero. Due to the loss of stresses, the material contracts where tensile stresses were present (interior) and expands momentarily where compressive stresses were present (surface) initiating the observed fracture front at the surface propagating towards the center, see Fig. 20(c). This process is repeated whenever the interior fracture front has developed too far ahead of the surface near fracture fronts, giving the impression of an overall

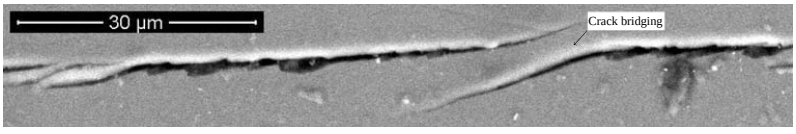

Fig. 19 SEM image of a crack on the surface in the (r,θ)-plane of a fractured specimen

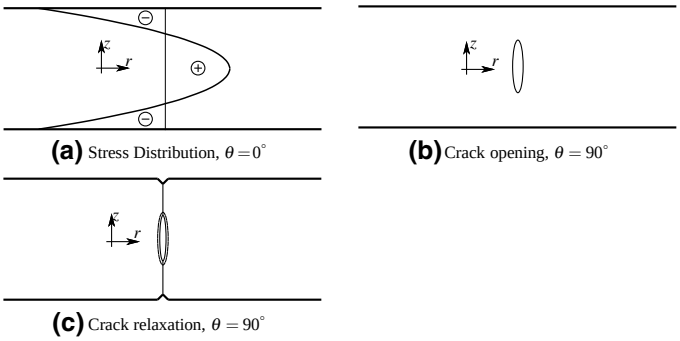

Fig. 20 Formation of zones in the fragments. Planes are indicated by a polar coordinate system where θ is constant in all figures (**a**–**c**)

surface fracture propagation in the same direction as the interior fracture front propagates.

Conclusion

The fracture of the toughened glass specimens was initiated from the edge using a 2.5 mm diamond drill in order to minimize the energy added. The drilling depth at fracture initiation, d, was observed and compared to the thickness, h, and the residual stress state of each specimen. These comparisons did not reveal any clear correlation between d and h or d and the residual stresses, however, a clear linear correlation between h and the residual stresses was observed. The fragmentation was observed to propagate along the edge on both sides of the initiation point for several centimeters before entering into the bulk material, producing two characteristic larger fragments. These two characteristic fragments formed regardless of the specimen thickness; they have not been reported before and are referred to as the *Whirl-fragments* of the fragmentation pattern. It was found that the generation of the Whirl-fragments is caused by the initiation of fracture on the narrow surface at the edge and not by the process of drilling.

From the two Whirl-fragments formed in each specimen, it was found that the origins of the polar crack front propagations were always located on the boundary of the Whirl-fragments at the point most far away from the drill. Further, it was observed that two distinct polar fracture propagation processes practically developed simultaneously.

The dependency of the 'Whirl-fragments-to-drill-distance' on the a) level of residual stresses, b) drill depth at fracture initiation and c) thickness of the specimen, was investigated. However, none of the cases indicated any significant correlation.

The average velocity of the fracture propagation front was determined for 11 specimens, using more than 15 pictures of each specimen. The velocity was found to be constant throughout the specimen and it was determined by a least squares fit to the measured data. An average velocity of the fracture front was found to be 1466 m/s and no correlation was found, neither with respect to thickness nor to the residual stress state. However, it should be noted that a weak correlation between the velocity and the residual stress state has been reported by other authors. A sensitivity analysis on the velocity reveals that it has been determined within an accuracy of 1%.

The in-plane shape of the fracture front was captured, and pictures reveal that the shape derived by only analyzing the so-called Wallner lines is dubious. Pictures showing the in-plane shape of the fracture front have been presented and the local development has been described. The pictures reveal that the actual fracture front consists of a governing front in the interior tensile zone driving a surface front in both compressive zones. SEM images of the fracture surfaces were provided and analyzed, revealing that fractures close to the surfaces were directed towards the center plane of the specimen. Furthermore, a SEM image showing micro-scale crack bridging on the original surface was presented and assumed to be partly responsible for the cohesion between fragments after fracture. At the present stage, only observations have been made of the fragmentation of toughened glass. Modeling of the fracture process is still needed in order to understand the phenomenon of crack development, and thus, to clarify if it is possible to temper glass in alternative ways in order to obtain a desired fracture pattern, or even preventing toughened glass from complete fragmentation.

Acknowledgements The authors would like to thank Mads Bonde at ScanGlas (DK) for providing the glass specimens, The Villum Kann Rasmussen foundation for sponsoring the digital high-speed cameras, and Ebba Cederberg Schnell at DTU Byg for assisting with the SEM images.

References

1. Acloque P (1956) Influence of strain-systems in glass upon the course of its fracture. In: Proc. 4th. international congress on Glass Chaix, Paris, pp 95–106 (in French)
2. Acloque P (1962) High speed cinematographic study of the fracture process in toughened glass. In: Symposium on mechanical strength of glass and ways of improving it. pp 851–886 (in French)
3. Acloque P (1963) La fracture du verre propagation - influence des précontraintes. Verres Refract 17(3):151–162 (in French)
4. Acloque P (1975) Déformation et rupture des verres. Ann Mines 2:57–66 (in French)
5. Acloque P, Guillemet C (1963) The course of fracture propagation in glass under varying strain. In: Advances in Glass Technology—Part 2 (in French)
6. Adams L, Williamson E (1920) The annealing of glass. J Franklin Inst 190:597–632
7. Anton J, Aben H (2003) A compact scattered light polariscope for residual stress measurement in glass plates. In: Glass processing days
8. Barsom J (1968) Fracture of tempered glass. J Am Ceram Soc 51(2):75–78
9. Bartenev G (1948) The phenomenon of the hardening of glass. J Tech Phys 18:383–388 (in Russian)
10. Beason WL, Morgan JR (1984) Glass failure prediction model. J Struct Eng 110(2):197–212
11. Chaudhri MM, Liangyi C (1986) The catastrophic failure of thermally tempered glass caused by small-particle impact. Nature 320(6057):48–50
12. Cranz C, Schardin H (1929) Kinematographie auf ruhendem film und mit extrem hoher bildfrequenz. Z Phys 56(3–4):147–183 (in German)
13. Daudeville L, Carre H (1998) Thermal tempering simulation of glass plates: inner and edge residual stresses. J Therm Stress 21(6):667–689
14. Freund LB (1990) Dynamic fracture mechanics. Cambridge University Press, Cambridge
15. Gardon R (1980) Glass Science and technology 5: elasticity and strength in glasses, chap 5. Academic, London, pp 145–216
16. Griffith A (1920) The phenomena of rupture and flow in solids. Philos Trans R Soc Lond 221:163–198
17. Hull D (1999) Fractography—observing, measuring and interpreting fracture surface topography. Cambridge University Press, Cambridge
18. Inglis CE (1913) Stresses in a plate due to the presence of cracks and sharp corners. In: Proc. Inst. Naval Architects
19. Kerkhof F (1963) Maximale bruchgeschwindigkeit und spezifische oberflächenenergie. Die Naturwissenschaften 50(17):565–566 (in German)
20. Kurkjian C (1963) Relaxation of torsional stress in transformation range of soda-lime-silica glass. Phys Chem Glasses 4(4):128–136
21. Laufs W, Sedlacek G (1999) Stress distribution in thermally tempered glass panes near the edges, corners and holes: Part 2. Distribution of thermal stresses. Glass Sci Technol Glastech Ber 72(2):42–48
22. Lee E, Rogers T, Woo T (1965) Residual stresses in a glass plate cooled symmetrically from both surfaces. J Am Ceram Soc 48(9):480–487
23. Narayanaswamy O (1971) A model of structural relaxation in glass. J Am Ceram Soc 54(10):491–498
24. Narayanaswamy O (1978) Stress and structural relaxation in tempering glass. J Am Ceram Soc 61(3–4):146–152
25. Narayanaswamy O (2001) Evolution of glass tempering models. In: Glass processing days
26. Nielsen J, Olesen J, Stang H, Poulsen P (2007) An implementation of 3d viscoelastic behavior for glass during toughening. In: Glass performance days
27. Schwarzl F, Staverman A (1952) Time-temperature dependence of linear viscoelastic behavior. J Appl Phys 23(8):838–843
28. Soules T, Busbey R, Rekhson S, Markovsky A, Burke M (1987) Finite-element calculation of stresses in glass parts undergoing viscous relaxation. J Am Ceram Soc 70(2):90–95
29. Takahashi K (1999) Fast fracture in tempered glass. Key Eng Mater 166:9–18
30. Takahashi K, Aratani SI, Yamauchi Y (1992) Dynamic fracture in zone-tempered glasses observed by high-speed photoelastic colour photography. J Mater Sci Lett 11(1):15–17
31. Wallner H (1939) Linienstructuren an bruchflächen. Z Phys 114(5–6):368–378 (in German)
32. Wiederhorn S (1969) Fracture surface energy of glass. J Am Ceram Soc 52(2):99–105
33. Yoffe E (1951) The moving griffith crack. Philos Mag 42:739–750

Paper V

"Mechanically Reinforced Glass Beams"

J.H. Nielsen & J.F. Olesen

Published in: *Proceedings of the 3rd Int. Conf. on Structural Engineering, Mechanics and Computations, Cape Town, South Africa*

Mechanically reinforced glass beams

J.H. Nielsen & J.F. Olesen
Technical University of Denmark, Department of Civil Engineering, jhn@byg.dtu.dk

Keywords: structural glass, reinforced glass beam, experiments, modeling

ABSTRACT: The use of glass as a load carrying material in structural elements is rarely seen even though glass is a popular material for many architects. This is owed to the unreliable and low tensile strength, which is due to surface flaws and high brittleness of the material. These properties lead to breakage without any warning or ductility, which can be catastrophic if no precautions are taken. One aspect of this issue is treated here by looking at the possibility of mechanically reinforcing glass beams in order to obtain ductile failure for such a structural component.

A mechanically reinforced laminated float glass beam is constructed and tested in four-point bending. The beam consist of 4 layers of glass laminated together with a slack steel band glued onto the bottom face of the beam. The glass parts of the tested beams are 1700 mm long and 100 mm high, and the total width of one beam is 4×10 mm. It is reinforced with a 3 mm high steel band covering the full width of the beam. The experimental setup is described and results for this beam are presented. Furthermore, the results for three similar experiments with a 6 mm steel band reinforcement are briefly presented. The experiments show that it is possible to obtain a very ductile structural behavior using the right amount of reinforcement.

A Finite Element Model including - in a simple manner - the effects of cracking of glass is presented. Based on a comparison between experimental and model results the mechanical behavior of the beam is explained. Finally, some design criterions for reinforced glass beams are discussed.

1 INTRODUCTION

Glass has been used in buildings for centuries but, until recently, not widely used as load carrying structural elements. Glass has many excellent properties such as high compressive strength, high stiffness and superior environmental resistance. However, glass is extremely brittle and the tensile strength, which is governed by flaws and fracture processes, is approximately 40 MPa. This is about 20 times less than the compressive strength, see eg. Hess (2004). Furthermore, the tensile strength is time-dependent, Beason & Morgan (1984) or Gioffre & Gusella (2002), and unreliable due to the random distribution of surface flaws and impurities, which induce cracks.

There are several ways of improving the strength of glass, and the most common is known as toughening, see e.g. Uhlmann & Kreidl (1980) or Mencik (1992). This is a quenching process where residual compressive stresses are introduced in the surfacenear parts and tensile stresses in the core, where the material is able to carry the tensile stresses. The quenching process improves the tensile strength up to more than 120 MPa, where the strength increase due residual stresses is not time dependent. However, the failure mode is still brittle and fracture based, and furthermore, the glass will break into small fragments due to the energy associated with the residual stresses, Uhlmann & Kreidl (1980), Narayanaswamy & Gardon (1969), Laufs & Sedlacek (1999) and Daudeville et al. (2002).

Due to the brittleness of glass as a material, the ductility must be ensured through the design of the structural components. The objective is to create safe transparent structures in glass by incorporating this ductility into the structural elements.

The idea presented here is to reinforce a glass beam in a way similar to what is known from reinforced concrete. Similar ideas have been reported recently by Louter et al. (2005), Louter et al. (2006) and Bos et al. (2004).

The glass beams treated in this paper is build from four pieces of 10 mm float glass laminated together and reinforced by a steel band glued onto the bottom face. The total length of the beam is 1700 mm, the height is 100 mm and the thickness is 40 mm,

disregarding the thickness of the laminates. The glass used is standard float glass with a thickness of 10 mm and polished edges. The adhesive is Delo-Duopox AD895 which is an epoxy with a shear strength of 32 MPa and a Young's modulus of 2.4 GPa according to the manufactures data sheet. The glass was cut and laminated by an industrial producer, but the steel band was glued onto the glass at the testing site using thin steel wires to control the thickness of the adhesive layer.

2 MECHANISM

The beam is loaded in four point bending as shown in Figure 3. The mechanism of the beam can be divided into three stages, the elastic stage, the cracked stage and the yield stage, assuming that there is no failure of the adhesive.

2.1 *Stage 1 - Elastic (pre-cracking)*

At this stage there are no cracks in the beam, and the reinforcement is in the linear elastic range.

The mechanism is that some of the tensile stresses are transferred to the relatively stiffer reinforcement through a shear deformation of the adhesive layer. The amount of stresses transferred depends on the stiffness of the adhesive layer and of the reinforcement. Shear stresses are primarily transferred in the part of the beam between the support and the concentrated load, since this is the only part subject to cross-sectional shear forces.

In this un-cracked stage where yielding of the reinforcement it not relevant, it seems reasonable to consider the beam to act in a linear elastic manner. The stresses in the adhesive are small and for this particular reinforcement arrangement the strains in the steel are far from the yield strain, since fracture in the glass occurs at a much lower strain level.

In order to estimate the magnitude of the shear stresses in the adhesive a linear elastic FE-model has been set up. A plot of the shear stresses in the adhesive layer as a function of the distance from the free end to the center is shown in Fig. 1 for two different steel band thicknesses. It is observed that the maximum absolute values for the shear stresses in the adhesive are near the support. This is due to the modeling of the reaction as a concentrated point load. It is also seen that the peak values are less for the thicker reinforcement. This is caused by the fact that the "contact" stresses from the support are spread to a larger area in the glass due to the larger reinforcement thickness.

The stress state in the reinforcement is depicted in Fig. 2 where the Von Mises stress is plotted along the length of the beam. From this figure it is seen that the stress level in the 3 mm thick reinforcement is relatively higher even though the total force in the reinforcement is lower.

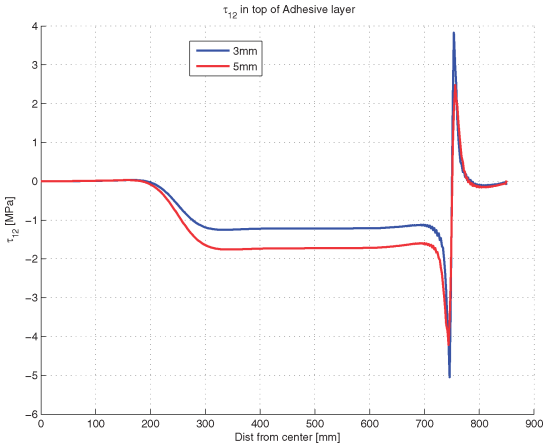

Figure 1. Shear stress in adhesive layer for steel reinforcement of 3 mm and 5 mm. The plot is based on a linear elastic FE-calculation.

2.2 *Stage 2 - Cracked cross-section*

In this stage cracks are developed in such a manner that hardly no shear stresses can be transferred through the cracked areas of the beam glass body. In order to increase the load further in this stage the uncracked part of the beam will have to transfer more shear in order to maintain equilibrium. The shear stresses in the cracked part will have large positive and negative peaks due to the remaining glass parts and the elongation of the reinforcement. However, in the adhesive these stresses are self-equilibrating.

In this stage the linear elastic FE model is no longer valid due to the development of cracks. In Section 4 a simple strategy for the inclusion of crack behavior in the FE model is presented.

2.3 *Stage 3 - Yielding (post-cracking)*

At the beginning of the third stage a lot of cracks have developed and the reinforcement starts yielding. The

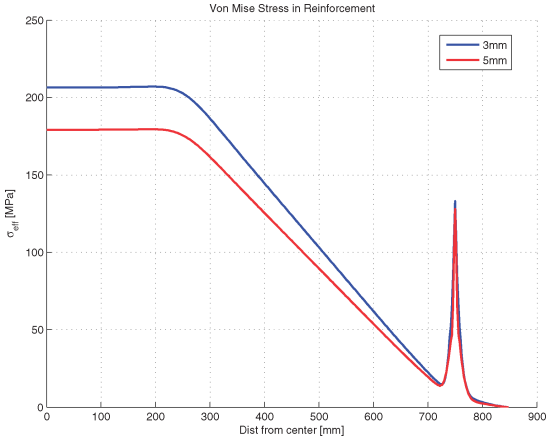

Figure 2. Von Mises stress in the steel for 3 mm and 5 mm reinforcement. The plot is based on a linear elastic FE-calculation.

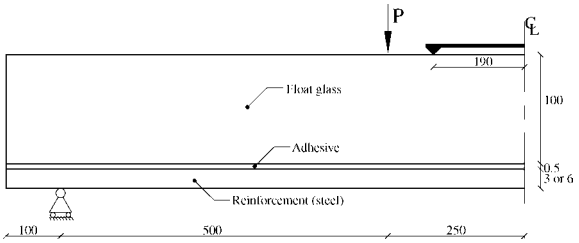

Figure 3. Sketch of the experimental setup. All measures are in mm (not in scale).

glass only transfers stresses in compression and serves as a separator maintaining the internal lever arm. The global behavior at this stage is very dependent on the plastic properties of the reinforcement steel.

3 EXPERIMENTAL VALIDATION

3.1 *Experimental setup*

Tests were performed on beams with a total length (L) of 1700 mm a height of 100 mm and a width of 40 mm (dimensions referring to the glass body only). They were tested with two different thicknesses of the steel band, 3 mm and 6 mm. In total four beams were tested; three with the 6 mm reinforcement and one with the 3 mm reinforcement. The beams were tested in a mechanical 100 kN 4-point bending machine at BYG·DTU. They were simply supported on the reinforced side with a span of 1500 mm and the load was transferred to the top of the glass body through a layer of rubber and aluminium at points 1/3*L* from the supports, see Fig. 3. The tests were displacement controlled with a crosshead speed of 0.5 mm=min. The mid-point deflection was measured relative to a rig placed on top of the beam in the center part between the loads. The measuring rig was supported at the two points located 190 mm from the center.

3.2 *Test of beams*

In Fig. 4 the load-deflection curves for the beams with 6 mm reinforcement are shown. It is seen that Stage 1 ends at approximately 0:2 mm. In Stage 2, when cracking of the glass has co mmenced, the slope of the curves change and the beams carry more than 30% extra load.

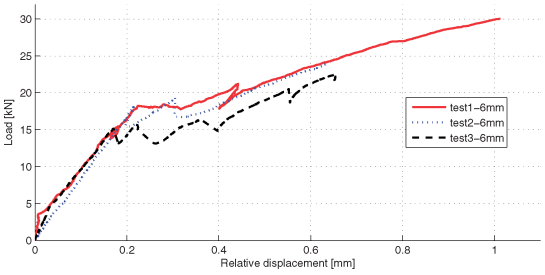

Figure 4. Load-deflection curve for the 6 mm reinforced beams.

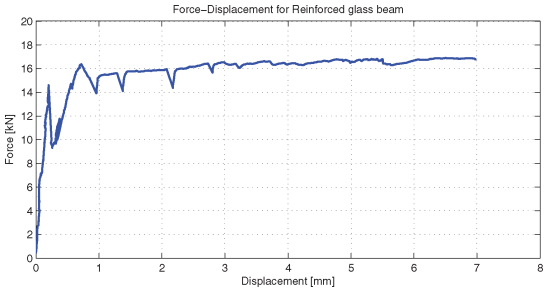

Figure 5. Load-deflection curve for the 3 mm reinforced beam.

Unfortunately the adhesive layer failed before yielding of the steel, and the ductility of these beams was limited by the abrupt failure of the adhesive, hence, Stage 3 was never reached for these beams. Some of the curves show a decrease in the deflection during the test, this is due to un-controlled set-out of the testing machine followed by manual restarting.

In order to provoke yielding in the reinforcement before failure of the adhesive the thickness of the reinforcement was reduced to 3 mm. The loaddeflection curve for this beam can be seen in Fig. 5. The load-deflection curve is almost linear in the beginning, until the glass begins to crack. At this point the stiffness of the structure changes suddenly and since the experiment is displacement controlled, the load is reduced. After this the load builds up again corresponding to the new stiffness of the structure. At approximately 0:7 mm of relative deflection another major crack is formed and the load decreases once more. Following this, a lot of secondary cracking takes place, and the reinforcement starts yielding in tension. The small load drops on this part of the curve (beyond 1 mmof deflection) are related to the set-out and restart of the testing machine.

Pictures of the specimens after failure are shown in Fig. 6, where the crack pattern in the reinforced beams can be seen. It is evident that the 3 mm reinforced beam exhibits a very ductile behavior. The delamination of the 6 mm reinforced beam may be observed, too. In general the crack pattern is rather interesting, since the compressive struts are clearly seen, and the multiple cracking is similar to what is seen in reinforced concrete beams.

3.3 *Material test*

Due to the extensive cracking of the glass, the postcracking (Stage 3) behavior of the 3 mm reinforced beam is mainly related to the material behavior of the reinforcement. The material parameters of the reinforcement steel were determined by a tensile test of a specimen cut from the same piece of steel. FE-modeling of the tensile test allowed for the determination of proper material parameters for the numerical modeling by fitting of the FE-result to the experimental curve. The result is shown in Fig. 7 and

Figure 6. Beams after test. left: 3 mm steel reinforcement, the crack patterns are similar to what is seen in concrete. right: 6 mm steel reinforcement, failure when delaminating in the adhesive layer.

the input for the FE-models is given in Table 1. The FE model assumes isotropic hardening and small strains. The use of isotropic hardening should be adequate since there is no change of the strain direction during yielding of the reinforcement. In order to determine the glass strength, six laminated reference beams with the same glass dimensions and without reinforcement were tested in bending. The average tensile strength

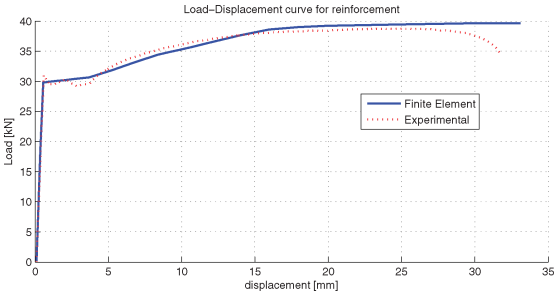

Figure 7. Load-displacement curve for material test of the reinforcement.

Table 1. Plastic stress-strain relation used for the reinforcement

σ [MPa]	ε^P [−]	σ [MPa]	ε^P [−]
330	0.000	435	0.120
340	0.028	440	0.200
430	0.090		

Table 2. Reference tests for the laminated glass beams

Specimen	$f_{tg,test}$ [MPa]	Specimen	$f_{tg,test}$ [MPa]
Ref.1	24.1	Ref.4	32.6
Ref.2	24.8	Ref.5	35.1
Ref.3	35.7	Ref.6	18.3

was found to be 28 MPa. Results from these tests are given in Table 2.

4 MODELING

4.1 *The general FEM modeling approach*

The beam is modeled with the co mmercial FEsoftware ABAQUS using first order displacement elements with a triangular shape (CST, constant strain). The stress state is assumed plane, and the mesh used for the calculations is shown in Fig. 8.

The cracking of the glass is modeled in a simple manner as described in Section 4.2, the adhesive is modeled using cohesive elements and the reinforcement is modeled as an isotropic hardening material.

The calculations are displacement controlled and the load acts over a length of 5 mm. This is done by coupling the nodes of the support with a single reference point, which is given the proper support conditions. The same principle is used for the support condition. This prevents unnecessary constraining and furnishes the same conditions as in the experiment. Another advantage of performing a displacement controlled analysis is that it allows for a decrease in the load-deflection curve.

4.2 *Constitutive modeling of the glass*

The glass part is modeled as a linear-elastic material in plane stress until the maximum principal strain reaches a critical value defined as:

$$\varepsilon_{I,cr} = \frac{f_{tg}}{E_g} \tag{1}$$

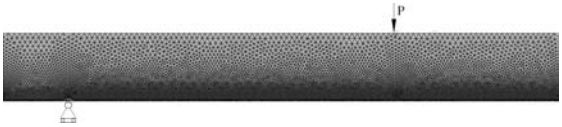

Figure 8. FE-mesh for the fully symmetric domain. The left half of the beam is modeled.

where f_{tg} is the tensile strength of the glass and E_g is the elastic modulus of the glass. After the strain has reached this critical level, the stiffness of the material point is reduced to E_{red}, and it is assumed that the laminates are not able to carry any stresses. The reason for not reducing the stiffness in the cracks to zero is to enhance convergence of the solution. The applied constitutive model is summarized in Algorithm 1, and it is supplied to ABAQUS as a user specified subroutine

Algorithm 1 Glass constitutive model
1: $\boldsymbol{D} = \boldsymbol{D}_g$
2: $\varepsilon_{I,cr} = f_{tg}/E_g$
3: $\varepsilon_I = 0.5(\varepsilon_{11} + \varepsilon_{22}) + \sqrt{0.5(\varepsilon_{11} + \varepsilon_{22})^2 + \varepsilon_{12}^2}$
4: **if** $\varepsilon_I \geq \varepsilon_{I,cr}$ **then**
5: $\boldsymbol{D} = \boldsymbol{D}_{red}$
6: $\boldsymbol{\sigma} = 0$
7: **end if**
8: $\boldsymbol{\sigma} = \boldsymbol{\sigma} + \boldsymbol{D}d\boldsymbol{\varepsilon}$

Here $\boldsymbol{\sigma} = \boldsymbol{D}\boldsymbol{\varepsilon}$ is the constitutive relationship for plane stress defined by:

$$\begin{bmatrix} \sigma_x \\ \sigma_y \\ \tau_{xy} \end{bmatrix} = \frac{E}{1-v^2} \begin{bmatrix} 1 & v & 0 \\ v & 1 & 0 \\ 0 & 0 & \frac{1-v}{2} \end{bmatrix} \begin{bmatrix} \varepsilon_x \\ \varepsilon_y \\ \gamma_{xy} \end{bmatrix} \quad (2)$$

In order to initiate cracks realistically, the critical strain value is based on a reduced glass strength, $f_{t,red}$ which is specified at equidistant points 30 mm apart in the bottom face of the glass beam.

It should be noted that the stiffness in the cracked material is reduced in all directions. This is a crude assumption, however, when the glass has cracked, the beam behavior in tension is primarily governed by the reinforcement and the adhesive.

4.3 *Constitutive modeling of the adhesive*

Due to the fact that the mechanical properties of the adhesive are not known in detail, the modeling is based on the adhesive being a simple linear elastic material with a Young's modulus of 2.4 GPa and a Poisson's ratio of 0.4. Although this might be inaccurate, it is assumed that it only has a secondary effect on the global response.

4.4 *Constitutive modeling of the reinforcement*

The reinforcement is modeled as a isotropic hardening material. The uni-axial plastic stress-strain relationship found by testing is specified in Table 1.

4.5 *The global behavior*

In Fig. 9 the beam model is shown at three different load stages after crack initiation. Regions with reduced stiffness simulate cracks and are shownin red. It is seen that the cracks are arrested by the compressive zone

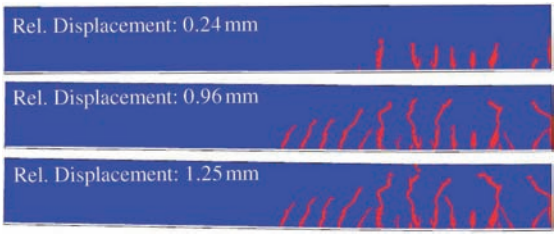

Figure 9. Plot of cracked elements for three different relative midpoint deflections.

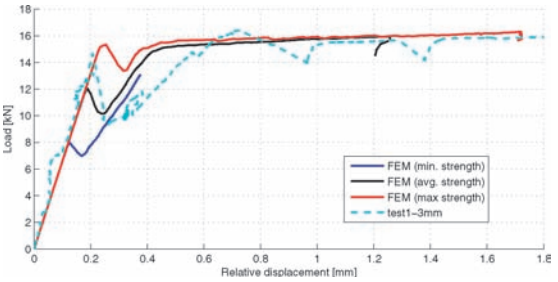

Figure 10. Load-Displacement curve for the 3 mm reinforced beam. Curves for the the highest, lowest and the mean glass strength found by the reference tests are also shown.

Table 3. Material Parameters for modeling the laminated glass

E_g	70 GPa	f_{tg}	40 MPa
v_g	0.23	$f_{t,red}$	28 MPa
E_{red}	0.5 GPa		

between the load and the support. Comparing Fig. 9 with the load-deflection curve in Fig. 10 it may be observed that when the crack reaches the top face of the glass, the calculations fail, which is due to the lack of element stiffness.

Table 3.

Considering Fig. 10 it is seen that the model prediction of the load-deflection behavior is fairly good, however, it is not able to followthe experimental curve all the way.

5 DISCUSSION

5.1 *Experiments*

All beams show some load carrying capacity after crack initiation, which means that residual load capacity may be obtained by the reinforcing arrangement, allowing for warning before total collapse. The most interesting beam is the one with 3 mm reinforcement which shows a very ductile behavior, even with a small hardening effect. By designing reinforced beams in this manner, it should be possible to create ductile structural elements with the visual advantages of glass. It should be mentioned that these experiments were

only performed as shortterm static tests, without taking into account long-term behavior or fatigue.

5.2 *Design criteria*

Several analogies exist between reinforced glass beams and reinforced concrete beams; therefore, it seems obvious to use similar definitions for the degree of reinforcement. Four different failure modes are identified and associated with different degrees of reinforcement and anchorage capacity:

- *Over-reinforced*: The reinforcement does not yield before crushing of the compression zone.
- *Normal-reinforced*: Yielding of the reinforcement begins after cracking of the glass and before failure of the compression zone. This situation is represented in Fig. 5.
- *Under-reinforced*: The reinforcement fails together with the glass and the maximum load capacity is the same as for the un-reinforced glass beam.
- *Anchorage*: The beam fails due to delamination of the reinforcement - i.e. failure of the adhesive. This type of failure is represented in Fig. 4.

5.3 *Finite element model*

The simple modeling of the cracking behavior is seen to give a good estimate of the global behavior and the crack pattern. However, convergency problems are encountered when the crack develops all the way through the cross section. This problem may be counteracted by the use of smaller elements or by the application of an anisotropic material model in the cracks.

6 CONCLUSIONS

It is shown by experiments that ductility in reinforced glass beams may be obtained using a glued slack steel band for transferring the tensile forces after cracking. This reinforcement is located on the bottom face of the beam without ruining the visual qualities of the glass beam.

Four tests are described in this paper, three with a high reinforcement degree and one with a normal reinforcement degree. The behavior of the highly reinforced beamswas linear until cracking of the glass, and after cracking they continued taking up more load with a moderate reduction in the stiffness. Failure was caused by delamination of the reinforcement band at a load level more than 30% above the cracking load.

The fourth test with a normal reinforcement degree shows almost linear behavior until cracking is initiated; here a drop in the load-deflection curve takes place. Following this drop the load increases and reaches a level a little higher than the cracking load. From this point it behaves in a plastic manner showing a small hardening effect.

The simple modeling of the cracking behavior is seen to fit the experiments very well. However, the model is not able to follow the load-deflection curve all the way, since cracks at large deflections develop all the way through the cross section.

Although the test results reported here have been obtained from pilot tests they are very promising as are the modeling results. Thus, there is certainly a potential for mechanically reinforcing glass beams to obtain ductile post cracking behavior without ruining the visual qualities of the beam.

ACKNOWLEDGEMENTS

The authors would like to thank COWI, Denmark, for sponsoring the manufacturing of test specimens, and students of civil engineering Charlotte M. Christensen and Michael H. Sass for carrying out the experiments.

REFERENCES

Beason, W.L., Morgan, J.R. 1984, Glass failure prediction model, *Journal of Structural Engineering* 110 (2): 197–212.

Bos, F., Veer, F., Hobbelman, G., Louter, P. 2004, Stainless steel reinforced and post-tensioned glass beams, *in* ICEM12-12th International Conference on Experimental Mechanics.

Daudeville, L., Bernard, F., Gy, R. 2002, Residual stresses near holes in tempered glass plates, *Materials Science Forum* 404–407: 43–48.

Gioffre, M. and Gusella, V. 2002, Damage accumulation in glass plates, *Journal of Engineering Mechanics* 128 (7): 801–805.

Hess, R. 2004. Material glass, Structural Engineering International: Journal of the International Association for Bridge and Structural Engineering (IABSE) 14 (2): 76–79.

Laufs, W., Sedlacek, G. 1999. Stress distribution in thermally tempered glass panes near the edges, corners and holes: Part 2. distribution of thermal stresses, *Glass Science and Technology: Glastechnische Berichte* 72(2): 42–48.

Louter, C., Belis, J., Bos, F., Veer, F., Hobbelman, G. 2005. Reinforced glass cantilever beams, *in* Glass Processing Days.

Louter, P., van Heusden, J., F.A. Veer, J. V., de Boer, H., Versteegen, J. 2006, Post-tensioned glass beams, *in* 16th European Conference of Fracture.

Mencik, J. 1992. Strength and fracture of glass and ceramics, Elsevier.

Narayanaswamy, O. and Gardon, R. 1969. Calculation of residual stresses in glass, *Journal of the American Ceramic Society* 52 (10): 554–8.

Uhlmann, D.R., Kreidl, N.J. 1980, Glass. Science and technology. 5: Elasticity and strenght in glasses, Academic Press.

Paper VI

"Design of Mechanically Reinforced Glass Beams - Modelling and Experiments"

A.B. Ølgaard, J.H. Nielsen & J.F. Olesen

Published in: *Structural Engineering International*

Design of Mechanically Reinforced Glass Beams: Modelling and Experiments

Andreas Breum Ølgaard, MSc, Civ. Eng., Research Asst.; **Jens Henrik Nielsen,** MSc, PhD Candidate and **John Forbes Olesen,** MSc, PhD, Assoc. Prof.; Dept. of Civil Engineering, Technical Univ. of Denmark. Contact: abo@radiusri.dk

Summary

The present paper is a study on how to obtain a ductile behaviour of a composite transparent structural element. The structural element is constructed by gluing a steel strip to the bottom face of a float glass beam using an epoxy adhesive. The composite beam is examined by four-point bending tests, and the mechanisms of the beam are discussed. Analogies to reinforced concrete beam theory are made; thus, four different design criteria, depending on the reinforcement ratio, are investigated. Analytical expressions are derived that are capable of describing the behaviour in an uncracked stage, a linear cracked stage and a yield stage. A finite element model, capable of handling the cracking of the glass by killing elements, is presented. Both analytical and numerical simulations are in fairly good agreement with the experimental observations. It appears that the reinforcement ratio is limited by the risk of anchorage failure and must be adjusted accordingly to obtain safe failure behaviour in a normal reinforced mode. Analysis of anchorage failure is made through a modified Volkersen stress analysis. Furthermore, different aspects of the design philosophy of reinforced glass beams are presented.

Keywords: structural glass; finite element method; killing elements; epoxy adhesive; design philosophy.

Introduction

The tendency in modern architecture to use more glass has resulted in a desire among architects to use glass even in load-carrying structural elements.

Glass has many excellent properties for use as a structural material, for example, a high compressive strength, high stiffness and superior environmental resistance. However, glass is extremely brittle, and the tensile strength, which is governed by small surface flaws, is relatively low and unreliable. It is commonly assumed that the tensile strength is approximately 40 MPa; however, considerably higher values are often observed, and much lower values may be found if the glass is scratched. Because of the distribution of flaws, a distinction must be made between edge strength and surface strength of a glass plate. The compressive strength of glass is often assumed to be 800 MPa, which is more than 20 times the tensile strength (see Hess[1]). Furthermore, the tensile strength is time dependent (Beason and Morgan[2] or Gioffre and Gusella[3]) and unreliable because of the random distribution of surface flaws and impurities, which induce cracks.

Because of the brittleness of glass, ductility must be ensured through the design of the structural component. The objective of the present work is to create safe transparent structures by incorporating this ductility into the structural elements. The idea presented here is to reinforce a glass beam in a way similar to reinforced concrete. Similar ideas have been reported by Louter *et al.*,[4] Louter *et al.*,[5] Bos *et al.*,[6] Nielsen and Olesen[7] and Freytag.[8]

The reinforced glass beams discussed in this paper are constructed by gluing a steel strip to the bottom face of a single-float glass beam by a two-component epoxy adhesive. The use of fully tempered glass for these beams is not considered because of its loss of integrity when fracturing. By reinforcing the bottom face (tensile side) of a float glass beam, the transparency of the structural element is hardly affected. 18 beams are constructed in the same size and are subjected to four-point bending tests.

In order to develop a design tool for such beams, material properties of the glass, the adhesive and the steel have been determined individually. The overall behaviour of the beam is described in three different stages: an uncracked stage, a cracked stage, and finally a yield stage. Furthermore, similar to reinforced concrete theory, design criteria defined by different ratios of reinforcement are outlined and discussed. The analytical model is supported by a finite element (FE) model capable of describing the behaviour in the three stages. The analytical and the FE model approach are compared with the experimental results.

Peer-reviewed by international experts and accepted for publication by SEI Editorial Board

Paper received: September 23, 2008
Paper accepted: December 24, 2008

Structural Beam—Concept and Design Philosophy

Beam Layout and Material Properties

The beams considered throughout this paper are constructed from a single piece of float glass reinforced by a steel strip glued onto the bottom face by an epoxy adhesive. The float glass has polished edges, and the reinforced beam is constructed using a special-made mould and devices that made it possible to construct a homogenous layer of adhesive with a thickness of 0,5 mm. The composite beam structure is sketched in *Fig. 1*.

Before testing the composite structural element, strength and stiffness properties of the three material components were determined. The properties, the standard deviations, s, and the number of specimens used in the investigations are presented in *Table 1*. The average glass tensile strength f_{gt} and the average Young's modulus of the glass E_g were determined by three four-point bending tests of pure glass beams. The yield strength f_{sy} and the Young's modulus E_s of the steel strip were determined by a tensile test giving the values f_{sy} = 400 MPa and E_s = 210 GPa. However, it should be noted that the plastic material-behaviour of the steel used

Fig. 1: Beam layout principle

for the FE model was found by inverse analysis of the steel tensile tests.

The adhesive is a two-component epoxy. In Ølgaard *et al.*,[8] material properties of this adhesive were examined. Here, the time dependency was found to be nonlinear and a curing time sensitivity was found. The average instantaneous Young's modulus of the adhesive E_a was determined for adhesive specimens with a curing time beyond 700 h. Furthermore, a joint of adhesive between toughened glass and steel was tested in combined load actions of normal and shear stresses[8]. From these tests, the average shear strength of the particular joint $f_{a,v}$ is presented here.

The time dependency of the adhesive has been further investigated. In a test rig similar to the one presented in [Ref. 9] an axisymmetric dog-bone specimen has been subjected to an increasing normal stress level. This is done by applying a load corresponding to an increase in normal stress of 1,0 MPa within 2 s. This procedure was repeated once a week for 5 weeks reaching a maximum normal stress of 5,0 MPa. Afterwards, unloading was conducted following a similar scheme and the experiment continues after reaching the normal stress level of zero. The magnitude of normal stress corresponds to the maximum shear stress level at failure load in an adhesive layer as given by a FE model of a reinforced glass beam in Nielsen and Olesen.[7]

	MPa	*s* (MPa)	No.
f_{gt}	77	0,6	3
E_g	75 100	5600	3
$f_{a,v}$	43,5	1,3	3
E_a	3434	79	4

Table 1: Material properties

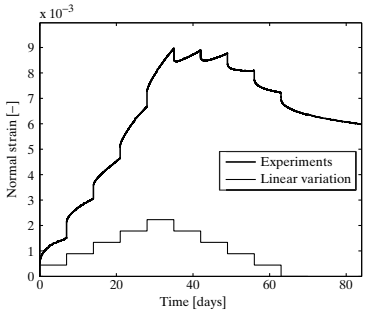

Fig. 2: Creep compliance of A1895. Normal strain

In *Fig. 2*, the normal strain obtained in this experiment as a function of time and the corresponding linear elastic response is plotted. An extensive creeping behaviour is clearly seen, and the increasing slope with increasing stress level indicates that the time dependency is nonlinear. A material model has not yet been extracted; however, it is seen that extensive creeping occurs even at relatively low stress levels. This implies that long-term composite action vanishes; thus, long-term loading of reinforced glass beams must be carried by the glass itself.

Characteristic Beam Behaviour

The mechanisms of the beam behaviour can be divided into three stages, see *Fig. 3*.

In the uncracked stage, Stage 1, there are no cracks and the reinforcement behaves linear elastic. The mechanisms of the beam are based on the shear stiffness of the adhesive. Because of this stiffness, deformations of the glass will activate the reinforcement, thus increasing the load capacity. Shear stresses are primarily transferred in that part of the beam between the support and the point load, because this is the only part subjected to cross-sectional shear forces. In the uncracked stage, where yielding of the reinforcement is not relevant, it is reasonable to consider the beam to act in a linear elastic manner. The stresses in the adhesive are small, and for this particular reinforcement arrangement, the strains in the glass until fracture are far below the yield strain of the reinforcement.

In Stage 2, cracks develop, preventing shear stresses from being transferred in the cracked areas. In order to increase the load further, the uncracked part of the beam must increase the transfer of shear to the reinforcement to maintain equilibrium. The shear stresses in the cracked part will have large positive and negative peaks because of the remaining glass parts and the elongation of the reinforcement; however, the integral of these stresses is zero and does not contribute to the overall shear transfer.

In Stage 3, extensive cracking of the glass has occurred and the reinforcement starts yielding. At this stage, the glass primarily transfers stresses in compression and serves as a separator maintaining the internal lever arm. The global behaviour at this stage is highly dependent on the plastic properties of the reinforcement steel.

In *Fig. 3*, the load–curvature relationship related to the beam defined in *Fig. 1* is sketched. The three stages are plotted for the short-term tensile strength of glass, $f_{gt,0}$ = 77 MPa, and the long-term tensile strength of glass $f_{gt,\infty}$ = 50 MPa. The load is applied by displacement control explaining the load drop.

If the load is applied by load control from a design point of view, ultimate failure for $f_{gt,0}$ will occur without any ductile behaviour. However, in practice, design ensures that failure does not happen until the tensile strength of glass is reduced over time to the design value that should be well below $f_{gt,0}$ corresponding to the lower curve in *Fig. 3*.

In relation to the serviceability limit state, the time dependency of the adhesive should be discussed. As a consequence of the extensive creeping behaviour, the stiffness of the adhesive joint will decrease with time; hence, the stiffness of the composite beam will also decrease. Because of the latter mechanism, the normal stresses in the glass will increase with time. These stresses must be compared with the decreasing strength of glass over time to avoid failure in the serviceability limit state. This is sketched in *Fig. 4*. From a design perspective, the development of the stresses in the glass must be kept below the glass strength as illustrated in *Fig. 4*. A conservative estimate of the development of the glass stress can be made assuming no composite action at the specified service life.

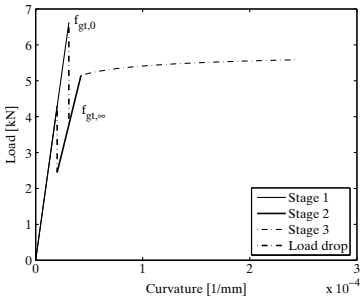

Fig. 3: Load–curvature relationship by displacement control for long term and short term tensile strength of glass

Theoretical Beam Model

Both Nielsen and Olesen[7] and Louter *et al.*[4] make the analogies between reinforced glass beams and reinforced concrete beams. Similar to reinforced concrete, design criteria or failure modes will be outlined for the reinforced glass beams. Four design criteria are associated with different degrees

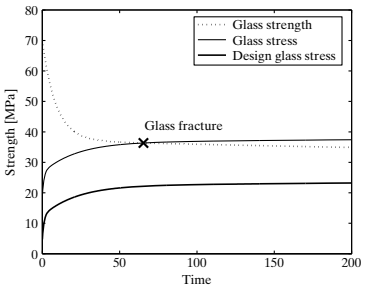

Fig. 4: Sketch of glass strength and glass stress as a function of time

of reinforcement. The load–curvature responses of the criteria are illustrated in *Fig. 5* for the specific beam.

1. The normal-reinforced state, where yielding of the reinforcement begins for increasing κ after cracking of the glass and before failure of the compressive zone.
2. The under-reinforced state, where the beam fails because of rupture of the reinforcement.
3. The over-reinforced state, where the reinforcement does not yield.
4. Ultimate failure can occur because of anchorage failure or failure of glass in compression. Anchorage failure describes the situation when the beam fails because of delamination of the reinforcement.

The beam must be designed to behave in the normal reinforced state, and the expected value of f_{gt} should be less than the long-term tensile strength of the glass.

The governing equations describing the load–curvature relationship (κ;M) in a normal-reinforced state will be presented in the following text for loading by displacement control.

When applying the principles of compound cross-sections describing Stage 1, the load–curvature relationship, Eqs. (1) and (2), can be derived from the parameters given in *Fig. 6*. The equations are simplified by assuming the stiffness of the adhesive to be equal to the stiffness of the glass. Therefore, the height of the adhesive h_a is added to the height of the glass h_g. I_{ztr} is the compound moment of inertia. A small simplification has been made with respect to the force resultant of the steel stresses, because it is assumed to act at $h_s/2$ from the bottom of the beam.

$$n = \frac{E_s}{E_g} \tag{1}$$

$$\kappa = \frac{M}{I_{ztr} E_g} \tag{2}$$

The analytical model describing Stage 2 assumes that no tensile stresses occur in the glass within the constant moment field of the beam and that the reinforcement strain ε_s is uniform over the height and that it is below the yield strain ε_{sy}. The Eqs. (3) and (4) are derived from *Fig. 7*.

$$x = \frac{A_s n}{b}\left(-1 + \sqrt{1 + \frac{2bd}{A_s n}}\right) \tag{3}$$

$$\kappa = \frac{M}{(d-x)\left\{A_s E_s\left[(d-x)/3\right]\right\}} \tag{4}$$

$$\varepsilon_s < \varepsilon_{sy} \tag{5}$$

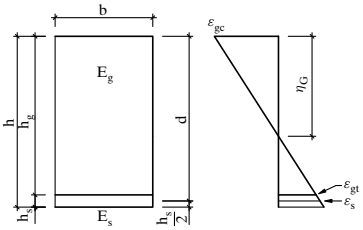

Fig. 6: Cross-section and strain distribution related to Stage 1

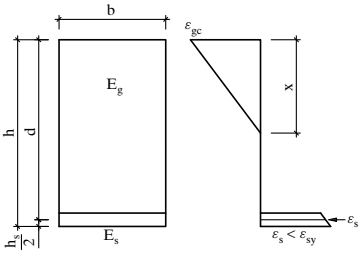

Fig. 7: Cross-section and strain distribution for Stage 2

The model describing Stage 3 assumes a plastic stress distribution in the reinforcement and that the compressive strains in the glass ε_{gc} are less than the ultimate compressive strain of the glass ε_{gcu}. No strain hardening is taken into account. The Eqs. (6), (7) and (8) are derived from *Fig. 8*.

$$\varepsilon_{gc} = \frac{A_s f_y + \sqrt{A_s}\sqrt{A_s f_y + 2bE_g d\varepsilon_s}\sqrt{f_y}}{bE_g d} \tag{6}$$

$$M = A_s f_y\left(d - \frac{2}{3}\frac{A_s f_y}{b \cdot \varepsilon_{gc} E_g}\right) \tag{7}$$

$$\kappa = \frac{\varepsilon_s}{d-x} \tag{8}$$

$$\varepsilon_s \geq \varepsilon_{sy} \tag{9}$$

Experimental Results and FE Modelling

Experiments

Reinforced beams with the geometry given in *Fig. 9* have been subjected to four-point bending tests in a 10 kN testing machine. Experimental details may be found in [Ref. 10].

The total length of each beam is 1000 mm, the thickness is 10 mm and the total height is approximately 73 mm. The load was applied with displacement control at a rate of 0,037 mm/s. For the uncracked beam in the linear elastic range, assuming a rigid adhesive connection, this induces a normal stress rate of 0,65 MPa/s.

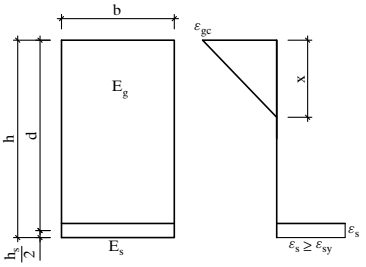

Fig. 8: Cross-section and strain distribution for Stage 3

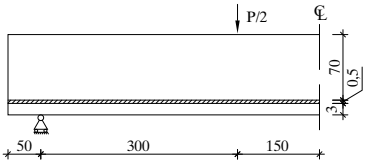

Fig. 9: Beam layout for one half of the beam (mm)

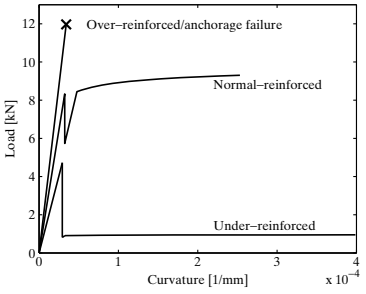

Fig. 5: Load–curvature response by displacement control for different degrees of reinforcement

The design of the beams is aimed at producing failure in the normal-reinforced mode. However, this design is performed without knowledge of the glass tensile strength. The beams have been cured for a minimum of 600 h in agreement with the experience from material tests of the adhesive. The displacement of the beam was measured by a measuring yoke in the area of the constant bending moment. From these measurements, the curvature κ is derived.

The typical load–curvature relationship from the experiments is shown in *Fig. 10* along with the corresponding analytical prediction. The glass strength used in the analytical prediction is obtained from the actual experiment.

On the basis of the typical curvature–load response of the beam, the global behaviour can be described by the five characteristic points indicated in *Fig. 11*. The corresponding development of cracks is sketched in *Fig. 12* and supported by the pictures shown in *Fig. 13* representing the crack development from Point B to Point D.

Point A represents the occurrence of the first crack in the glass. Because of a loss of beam stiffness, the load drops until Point B is reached. Typically, the first crack occurs below the loading point. This is explained by the local influence of the point load on the stress state at this point.

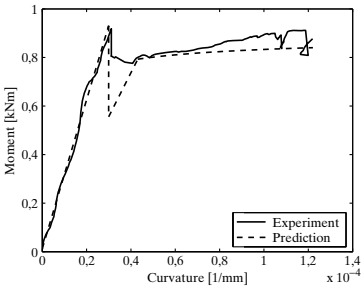

Fig. 10: Typical load–curvature response from experiments and the corresponding analytical prediction

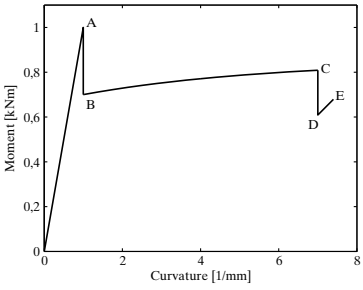

Fig. 11: Definition of characteristic points describing the load–curvature response of the reinforced glass beams

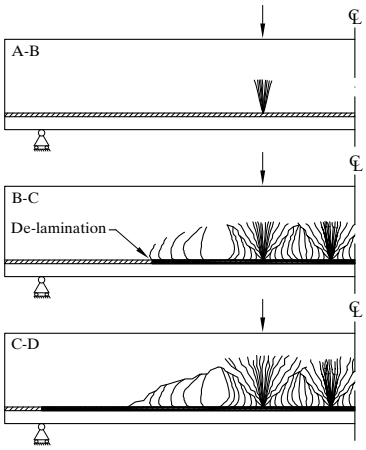

Fig. 12: Sketch of crack development in the reinforced glass beam at different stages

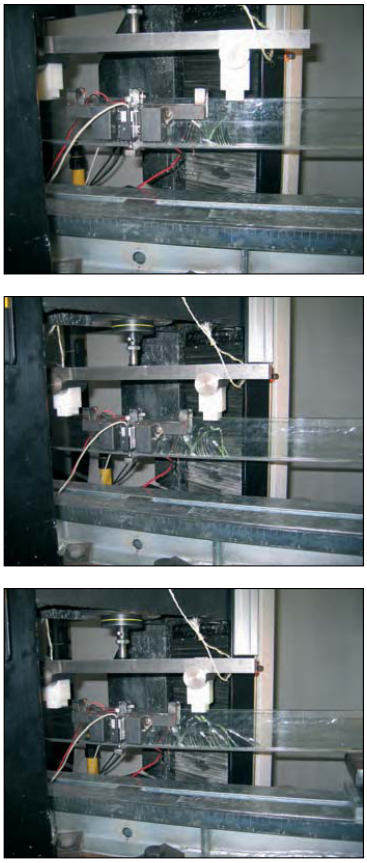

Fig. 13: Pictures of the crack development in the reinforced glass beam from Point B to Point D

The description of the beam behaviour in *Fig. 11* does not show the cracked linear stage as in the analytical prediction (see *Fig. 10*). The reason for this is that the prediction is based on a sectional analysis, whereas in the experiment the cracks develop discretely providing a more stiff behaviour.

Between Point B and Point C, secondary cracks develop in the constant bending moment field (and also outside this field towards the supports). The slope of the analytical prediction in this stage is not in agreement with the experiment. This is probably due to strain hardening of the reinforcement, which is not considered in the analytical model. At Point C, a shear crack occurs and delamination in the adhesive layer develops until reaching the support. The latter mechanisms take place within very short time and correspond to the load drop from Point C to Point D. The reason why the delamination stops at the support might be explained by two phenomena: (a) the bi-axial stress state or (b) the change of sign in the shear stresses at the middle of the support (see Nielsen and Olesen[7]). From Point D to Point E, the beam is again able to sustain an increasing load until reaching the final failure by delamination of the reinforcement.

From *Figs. 10* and *11*, it appears that the maximum load-carrying capacity of the beam is reached at Point A. This is a consequence of assuming a glass tensile strength of 50 MPa in the design phase, which was actually quite low compared with the experimentally obtained values. On the basis of the experimentally obtained values and the theory of compounded cross-sections, the average glass tensile strength in the composite element is derived and shown in *Table 2*. It appears that the average glass tensile strength has increased from 77,0 to 81,1 MPa as a result of gluing the reinforcement onto the glass. The initial crack occurs at the same location in non-reinforced and reinforced beams. The increasing strength tendency was also discovered through earlier pilot tests. The phenomenon may be explained by assuming the epoxy to have a sealing effect on the glass, leading to a deceleration of the static fatigue of the glass

	MPa	***s* (MPa)**	**No.**
f_{gt}	81,1	7,5	16

Table 2: Average glass tensile strength, standard deviation and number of investigated reinforced glass beams

caused by the humidity in the ambient environment.

FE Modelling

The beam is modelled using a FE software with a user subroutine for the glass behaviour. Constant strain triangle elements and a plane stress assumption were used.

The adhesive is modelled as linear elastic using cohesive elements, and the reinforcement is modelled as an isotropic hardening material. The calculations are displacement controlled and the load acts over a length of 5 mm with allowance for the loaded part to rotate. This is done by coupling the nodes of the support with a single reference point, which is given the proper support conditions. The same principle is used for the supports.

The glass part is modelled as a linear elastic material until fracture. The fracture criterion is when the maximum principal strain in a material point reaches a critical value ε_{gt} defined by Hooke's law respecting the tensile strength and the Young's modulus of the glass given in *Table 3*. After the strain has reached this critical level, the stiffness of the material point is reduced to $E_{red} << Eg$. The principle of the method is often referred to as killing elements or element death, see, for example, Refs. [11 and 12] where the technique is used for modelling the sawing of timber. Using the principal strain for the fracture criterion simplifies the implementation related to the closure of cracks. In the present application, the difference between a principal strain and a principal stress criterion is insignificant.

In order to initiate cracks realistically, the critical strain at the bottom of the glass is applied randomly with values from ε_{gt} (derived from experimentally measured values) to $\varepsilon_{gt}/0{,}75$. It should be noted that the stiffness in the cracked material is reduced in all directions. This is a crude assumption; however, when a crack has formed, it tends to continue opening and the global beam behaviour will, primarily, be governed by the reinforcement and the adhesive.

Because of the fact that the constitutive behaviour of the adhesive is not known in detail, the modelling is based on the adhesive being a simple linear elastic material with a Young's modulus of 3,4 GPa and a Poisson's ratio of 0,2. Although this might be inaccurate, it is assumed that it only has a secondary effect on the global response by short-term loading.

E_g	75,1 GPa
v_g	0,23
f_{gt}	81,1 MPa
E_{red}	0,05 GPa

Table 3: Material parameters for modelling the single layer of glass

In *Fig. 14*, the beam model is shown after crack initiation at three different load stages (Circle 1–Circle 3 in *Fig. 15*). Regions with reduced stiffness simulate cracks. It is seen that the cracks are arrested by the compressive zone between the load and the support. Comparing *Fig. 14* with the load–deflection curves for the experiments in *Fig. 15* and the location of the three load stages, the development of cracks seems reasonable. However, the location and the shape of the cracks simulated in the FE model do not completely correspond to the experimental observations (see *Figs. 12* and *13*).

Considering *Fig. 15*, it is seen that the FE model prediction and the experiments with $h_s = 3$ mm are in fairly good agreement. In addition, a FE model and an analytical prediction with $h_s = 6$ mm are presented in *Fig. 15*. These seem to be in fairly good agreement too; however, the yield plateau of the analytical prediction appears to be slightly below the FE prediction.

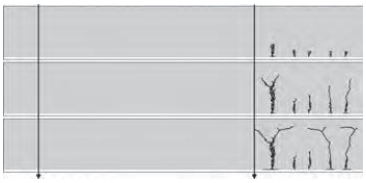

Fig. 14: Plot of cracked elements for three different relative midpoint deflections. Top: Circle 1; middle: Circle 2; bottom: Circle 3. The vertical line to the left represents the support and the vertical line to the right represents the position of load application

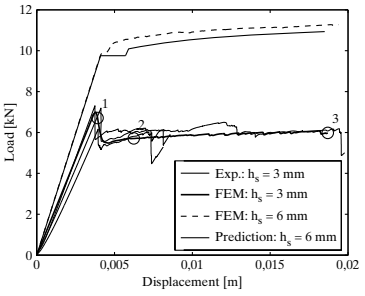

Fig. 15: Load–displacement curves for the 3 and 6 mm reinforced beams by FEM, 3 mm reinforced beam by experiments and 6 mm reinforced beam by analytical model. The circles are related to the three load stages defined in Fig. 14

Experiments on a Laminated Reinforced Glass Beam

Additionally, the analytical prediction is compared with experiments on a reinforced glass beam that consists of four layers of laminated glass each 10 mm thick. The experiments were carried out as pilot tests and were reported by Nielsen and Olesen.[7] The load–curvature curve for such a beam, along with an analytical solution, is given in *Fig. 16*.

The analytical prediction is seen to be in fairly good agreement with the experimentally determined curve; however, strain hardening is not included in the analytical solution, which is the reason for the increasing difference in the yielding range. In contrast to the single-layer glass beam, the linear cracked stage, before yielding of the reinforcement, is clearly seen for this experiment. The reason for this is the development of several cracks within

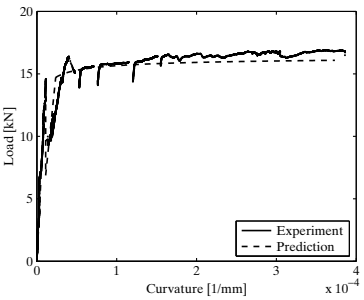

Fig. 16: Load–curvature relationship for a 3 mm reinforced laminated glass beam and the corresponding analytical prediction

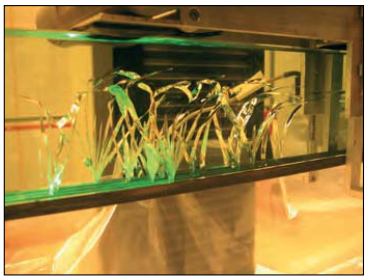

Fig. 17: Cracks developing within the constant bending moment zone when the laminated beam is acting in the linear cracked stage

the constant moment zone in all four glass layers before the yielding occurs. The laminate provides a higher level of beam integrity compared with the single-layer glass beam. In *Fig. 17*, a picture showing the cracking within the constant bending moment zone of the four-layered laminated beam is presented.

Anchorage Failure

Anchorage failure by delamination of the adhesive layer is investigated on the basis of the Volkersen analysis.[13] This approach provides the shear stress distribution in the adhesive for a linear elastic adhesive in a single lap joint. However, the load application in the single lap joint does not exactly correspond to the forces acting in the beam model; hence, the Volkersen approach must be modified.

Modified Volkersen Analysis

From *Fig. 18* a modified Volkersen shear stress distribution in the adhesive layer is derived (Eq. (12)).

The relative displacement δ is defined as

$$\delta = u_2 - u_1 \tag{10}$$

hence, the shear stress is defined as

$$\tau = G\frac{\delta}{h_a} \tag{11}$$

The modified Volkersen shear stress distribution is given by

$$\tau(x)^{\text{Volk.}} = A\omega\cosh(\omega x) \tag{12}$$

where

$$A = \frac{P}{\sinh(\omega l)} \tag{13}$$

and

$$\omega = \sqrt{\frac{G}{h_a}\left(\frac{1}{E_g h_g} + \frac{1}{E_s h_s}\right)} \tag{14}$$

The modified Volkersen solution yields an increase in shear stresses when approaching the cracked section from one of the beam ends. The maximum Volkersen shear stress at the cracked section $\tau_{max}^{Volk.}$ is determined for the beam experiments, where ultimate failure occurs as delamination of the adhesive layer. The results for $\tau_{max}^{Volk.}$ at the first crack in the glass and $\tau_{max}^{Volk.}$ at delamination are shown in *Figs. 19* and *20* as functions of the strain in the reinforcement.

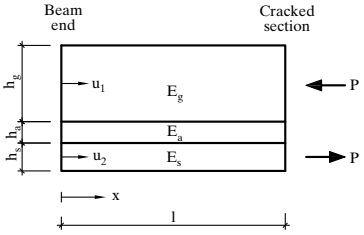

Fig. 18: Geometry and definitions for deriving a modified Volkersen shear stress distribution in the adhesive layer

The two lines representing reinforcement height equal to 3 and 4 mm are based on ideal plastic material behaviour of the reinforcement.

From *Figs. 19* and *20* it is noted that an increasing reinforcement ratio causes an increasing shear stress and this reduces the ability for a ductile behaviour. It is also seen that the adhesive delaminates at stresses almost twice as high as the adhesive shear strength $f_{a,v}$. This might be explained by the fact that the calculation is based on linear elasticity, which might be inaccurate in the light of the results presented in Ref. [9] where a ductile behaviour is observed for the adhesive subjected to shear.

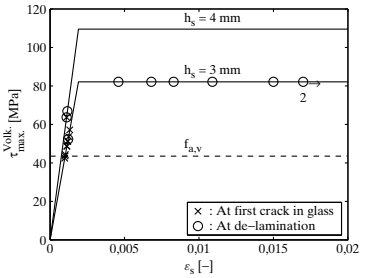

Fig. 19: Modified Volkersen shear stress at the cracked section at two different stages

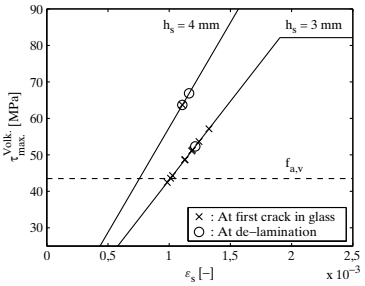

Fig. 20: Zoom of modified Volkersen shear stress at the cracked section at two different stages

Conclusion

Experiments have shown that reinforcing a glass beam by gluing a steel strip to the bottom face of a float glass plate can provide a transparent and yet ductile structural element with a relatively safe failure mode. However, it is important to note that the reinforcement ratio is limited by the risk of anchorage failure and must be adjusted accordingly to obtain safe failure behaviour in a normal-reinforced mode.

In the present work, a safe design through the use of a modified Volkersen stress analysis is developed to avoid anchorage failure.

Because of the creeping behaviour of the adhesive, long-term composite action vanishes. Thus, in the serviceability limit state, long-term loading of reinforced glass beams must be sustained by the glass itself. Here, the reduced tensile strength of glass over time becomes an important aspect that must be taken into account.

Analytical expressions with an analogy to reinforced concrete theory have been set up, to describe the composite beam behaviour in three stages: the fully rigid uncracked stage, the linear cracked stage and the yield stage assuming ideal plastic behaviour of the reinforcement. The analytical predictions show fairly good agreement with the experiments, especially for beams consisting of multiple layers of laminated glass. FE modelling shows a fine compliance with both the experiments and the analytical predictions.

The present work supplies tools for the design of a ductile transparent structural composite element made from glass, adhesive and steel. However, the limited number of test results published for such beams suggests that verification tests might be needed for designs deviating from those reported in the literature.

References

[1] HESS R. Material glass. *Struct. Eng. Int.: J. Int. Assoc. Bridge Struct. Eng. (IABSE)* 2004; **14**(2): 76–79.

[2] Beason WL, Morgan JR. Glass failure prediction model. *J. Struct. Eng.* 1984; **110**(2): 197–212.

[3] Gioffre M, Gusella V. Damage accumulation in glass plates. *J. Eng. Mech.* 2002; **128**(7): 801–805.

[4] Louter C, Belis J, Bos F, Veer F, Hobbelman G. *Reinforced Glass Cantilever Beams*, in Glass Processing Days, 2005.

[5] Louter C, van Heusden JF, Veer F, Vambersky JNJA, De Boer HR, Verstegen J. Post-tensioned glass beams, *16th European Conference of Fracture*, Alexandroupolis, Greece, 2006.

[6] Bos F, Veer F, Hobbelman G, Louter C. Stainless steel reinforced and post-tensioned glass beams, *ICEM12-12th International Conference on Experimental Mechanics*, Politecnico Di Bari, Italy, 2004.

[7] Nielsen JH, Olesen JF Mechanically reinforced glass beams. In *Structural Engineering, Mechanics and Computation, SEMC*, Zingoni A (ed.). Millpress, Cape Town, South Africa, 2007.

[8] Freytag B. Glass-concrete composite technology. *Struct. Eng. Int.* 2004; **14**(2): 111–117.

[9] ØLgaard AB, Nielsen JH, Olesen JF, Stang H. Properties of an adhesive for structural glass applications. In *Challenging Glass Conference*, Bos F, Louter CH, Veer F (eds). IOS Press, Delft, Holland, 2008.

[10] ØLgaard AB. *Application of an Adhesive in a Mechanically Reinforced Glass Beam*, Master Thesis, DTUBYG, 2008.

[11] *ANSYS Release 11.0 Documentation*, 2008.

[12] Omarson S, Dalblom O, Johansson M. *Finite Element Study of Growth Stress Formation in Wood and Related Distortion of Sawn Timber*. Wood Science and Technology, 2008.

[13] Volkersen O. Die nietkraft-verteilung in zugbeanspruchten nietverbindungen mit konstanten laschenguerschnitten. *Luftfahrtforschung* 1938; **15**(1): 41–47.